Development of Advanced Phosphate-based Cathode Materials for Na/K-ion Batteries by Spray-Drying Process.

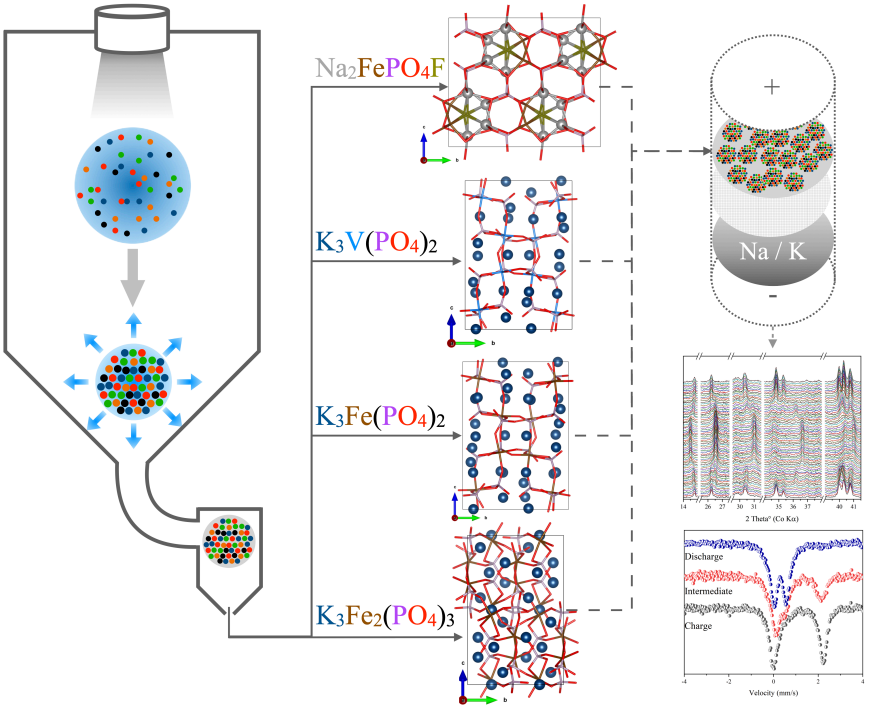

*Thesis submitted by **Jérôme Bodart***

for the degree of Doctor in Sciences at

Department of Chemistry

University of Liège

Supervisors:

Dr. Frédéric Boschini

Dr. Abdelfattah Mahmoud

Assessment Committee:

President: Prof. Christine Jérôme, University of Liège

Secretary: Dr. Abdelfattah Mahmoud, , University of Liège

Promoter: Dr. Frédéric Boschini, University of Liège

Members: Prof. Frédéric Hatert, University of Liège

Dr. Frank Tietz, Forschungszentrum Jülich, Deutschland

Dr. Moulay Tahar Sougrati, Institut Charles Gerhardt de Montpellier, France

The work presented in this thesis was funded by the University of Liège, the Group of Research in Energy and Environment from Materials, the Walloon Region under “PE PlanMarshall2.vert” program (BATWAL – 1318146), and personal travel grants from the FRS-FNRS and the University of Liège.

« The only way of discovering the limits of the possible is to venture a little way past them into the impossible »

Sir Arthur Charles Clarke

Abstract

Our future is threatened by the cataclysmic effects of global warming. In addition, the energy supply problems linked to the Russo-Ukrainian War and the ever-increasing demand for green and renewable energies are casting a shadow over our energy future. The energy transition will require using efficient, high-yield, low-cost energy storage systems with the least possible environmental impact to allow the durability and longevity of the used systems.

Electrochemical batteries are one of the most promising technologies to store energy efficiently. Current commercial Li-ion batteries, with high energy density and long cycle life, are used in a wide range of applications such as mobile phones, electric vehicles, or household storage. Current batteries are based on critical raw materials such as lithium and cobalt. The electrode materials' performance is highly impacted by their microstructure and composition, mainly dictated by the synthesis method. Also, developing a synthesis method that can be easily scaled up is a matter of importance to respond to future needs.

In this work, we specifically focus on the use of the spray-drying synthesis method of low-critical raw materials cathode materials for Na-ion and K-ion batteries. The spray-drying is a highly versatile, easily up-scalable, and cost-effective method. This work is divided into two main parts.

The first part of this work concerns the optimization of Na_2FePO_4F (NFPF) and Na_2FePO_4F/CNT materials by spray-drying method (Chapter 2). The influence of synthesis conditions on the structure and morphology was investigated. The particle size reduction has slightly enhanced the electrochemical performance. The *in situ* addition of carbon nanotubes in one step, using a spray-drying process to prepare NFPF/CNT composites, leads to the formation of impurities. Therefore, the synthesis is optimized to prevent these impurities, and the pure NFPF-15CNT with enhanced performance as cathode in NIB was

obtained: discharge capacity of 123 mAh/g at C/15. The precharged NFPF-15CNT (removing Na) also showed promising performance in KIB. The third chapter gives important insights on the electrochemical mechanisms of NFPF materials in both Na-ion batteries and K-ion batteries using *operando* ^{57}Fe Mössbauer combined with *operando* X-Ray diffraction. The obtained datasets are treated using chemometrics and particularly principal component analysis and multivariate curve resolution – alternating least square. A double biphasic mechanism is evidenced in Na-ion batteries with a mixed valence intermediate, while in K-ion batteries the cycling mechanism shows clear differences such as the absence of an intermediate state leading to a single biphasic mechanism.

The second part (Chapter 4 and 5) of this thesis present the development of three new cathode materials for KIB: $K_3V(PO_4)_2$, $K_3Fe(PO_4)_2$, and $K_3Fe_2(PO_4)_3$ for K-ion batteries. The spray-drying synthesis method was successfully optimized to prepare these materials with a heat treatment afterward. KVP with 20wt% of carbon nanotubes, with 20wt% graphene oxide, or with 10% of carbon nanotubes + 10wt% of graphene oxide composites were also prepared in one step using spray-drying and then tested as cathode materials for K-ion batteries. Without grinding, composite with a mix of carbon nanotubes and graphene oxide demonstrated the best performance with a discharge capacity of 100mAh/g at C/40. An increase of the cycling-rate leads to a rapid decay of the capacity; thus, the grinding of the materials was studied. After grinding, carbon nanotubes -based composite exhibited enhanced electrochemical properties even at higher C-rate thanks to the great reduction of the particle size and good carbon nanotubes dispersion in KVP material. The fifth chapter presents the synthesis and characterization of KFPx cathode materials for K-ion batteries. Contrary to others, these materials have not been obtained under argon atmosphere, preventing us from obtaining composite materials with carbon. Despite that, new strategies to enhance the electrochemical performance were studied: diminution of particle size, change of iron precursors, and addition of *ex situ* carbon nanotubes.

Our approach allowed us to achieve promising performance in K-ion batteries, with good initial discharge capacities: 70mAh/g for KFP_2 and 100mAh/g for KFP_3.

Résumé

Notre avenir est menacé par les effets cataclysmiques du réchauffement climatique. Les problèmes d'approvisionnement énergétique liés à la guerre russo-ukrainienne et la demande, sans cesse croissante, d'énergies vertes et renouvelables jettent un voile sur notre avenir énergétique. La transition énergétique se fera par l'utilisation de systèmes de stockage d'énergie efficaces, à haut rendement, à faible coût et avec le moins d'impact environnemental possible, pour permettre la pérennité et la longévité des systèmes utilisés.

Les batteries rechargeables sont l'une des technologies les plus prometteuses pour stocker efficacement l'énergie. Les batteries Li-ion commerciales actuelles, ayant une densité d'énergie élevée et une longue durée de vie, sont utilisées dans un large éventail d'applications, telles que les téléphones portables, les voitures électriques ou le stockage domestique. Malgré cela, celles-ci sont basées sur des matières premières critiques telles que le cobalt ou le lithium. Les performances des matériaux d'électrode sont fortement influencées par leur microstructure et leur composition, qui sont principalement dictées par la méthode de synthèse. Dès lors, le développement d'une méthode de synthèse facilement industrialisable est un enjeu important pour répondre aux besoins futurs.

Dans ce travail, nous nous concentrons spécifiquement sur l'utilisation de la méthode de synthèse de séchage par atomisation de matériaux de cathode, avec peu de matériaux critiques, pour les batteries Na-ion et K-ion. Le séchage par atomisation est une méthode très polyvalente, facilement industrialisable et peu coûteuse.

Ce travail est divisé en deux parties principales :

La première partie de ce travail concerne l'optimisation des matériaux Na_2FePO_4F (NFPF) et Na_2FePO_4F/NTC par la méthode de séchage par atomisation

(chapitre 2). L'influence des conditions de synthèse sur la structure et la morphologie a été étudiée. La réduction de la taille des particules a légèrement amélioré les performances électrochimiques. L'ajout *in situ* des nanotubes de carbone, en une seule étape, par le procédé de séchage par atomisation, pour préparer des composites NFPF/NTC conduit à la formation d'impuretés. Par conséquent, la synthèse est optimisée pour éviter ces impuretés et le NFPF-15NTC pur, avec des performances améliorées comme cathode pour batteries sodium-ion, a été obtenu avec une capacité de décharge de 123 mAh/g à C/15. Le NFPF-15NTC préchargé (pour enlever les ions de Na) a également montré des performances prometteuses dans les batteries K-ion. Le troisième chapitre présente des informations importantes sur le mécanisme réactionnel électrochimique des matériaux NFPF dans les batteries sodium-ion et potassium-ion en utilisant la technique de spectroscopie ^{57}Fe Mössbauer combinée avec la diffraction de rayons-X, tous deux en mode *operando*. Les données obtenues sont traitées par chimiométrie et notamment l'analyse de composantes principales et résolution de courbes multivariées. Un mécanisme de double biphasage est mis en évidence dans les batteries sodium-ion avec un intermédiaire de valence mixte ; tandis que, dans les batteries potassium-ion, le mécanisme réactionnel au cours cyclage montre des différences claires, telles que l'absence d'un état intermédiaire conduisant à un mécanisme biphasique simple.

La deuxième partie de cette thèse (chapitres 4 et 5) présente le développement de trois nouveaux matériaux cathodiques pour batteries potassium-ion : $K_3V(PO_4)_2$, $K_3Fe(PO_4)_2$ et $K_3Fe(PO_4)_3$. La méthode de séchage par atomisation a été optimisée avec succès pour préparer ces matériaux après traitement thermique. Des composites de KVP avec 20 % de nanotubes de carbone, avec 20 % d'oxyde de graphène ou avec 10 % de nanotubes de carbone + 10 % d'oxyde de graphène en masse, ont également été préparés, en une seule étape, en utilisant le séchage par atomisation, puis testés comme matériaux de cathode pour les batteries potassium-ion. Sans broyage, le composite avec un mélange de nanotubes de carbone et de

d'oxyde de graphène a démontré les meilleures performances électrochimiques avec une capacité de décharge de 100mAh/g à C/40. L'augmentation de la vitesse de cyclage conduit à une décroissance rapide de la capacité. Pour y remédier, le broyage des matériaux a été étudié. Après broyage, le composite à base de nanotubes de carbone présentait des propriétés électrochimiques améliorées, même à une plus grande vitesse de cyclage, grâce à la grande réduction de la taille des particules et à la bonne dispersion des nanotubes de carbone dans les particules de KVP. Le cinquième chapitre présente la synthèse et la caractérisation des matériaux cathodiques KFPx pour batterie K-ion. Contrairement aux autres, ces matériaux n'ont pas été obtenus sous atmosphère inerte, empêchant l'obtention de matériaux composites avec du carbone. Malgré cela, de nouvelles stratégies d'amélioration des performances électrochimiques ont été étudiées : diminution de la taille des particules, changement de précurseurs de fer et ajout de nanotubes de carbone *ex situ*. Cette approche a permis d'atteindre des performances prometteuses dans les batteries K-ion, avec de bonnes capacités initiales de décharge de l'ordre de 70mAh/g pour KFP_2, et 100mAh/g pour KFP_3.

Content

List of publications

Articles:

1. **Bodart, J.**, Eshraghi, N., Sougrati, M. T., Boschini, F., Lippens, P-E., Vertruyen, B., & Mahmoud, A. (July 2022) $NaKFePO_4F$/CNT composite as advanced cathode material for K-ion batteries (Under review at *Journal of Power Sources)*
2. **Bodart, J.**, Eshraghi, N., Carabin, T., Vertruyen, B., Cloots, R., Boschini, F., & Mahmoud, A. (19 October 2020). Spray-dried K3V(PO4)2/C composites as novel cathode materials for K-ion batteries with superior electrochemical performance. *Journal of Power Sources, 480*, 229057. doi:10.1016/j.jpowsour.2020.229057
3. Mahmoud, A., Karegeya, C., Moulay Tahar, S., **Bodart, J.**, Vertruyen, B., Cloots, R., Lippens, P.-E., & Boschini, F. (14 September 2018). Electrochemical Mechanism and Effect of Carbon Nanotubes on the Electrochemical Performance of Fe1.19(PO4)(OH)0.57(H2O)0.43 Cathode Material for Li-Ion Batteries. *ACS Applied Materials and Interfaces, 10* (40), 34202–34211. doi:10.1021/acsami.8b10663
4. Trabelsi, K., **Bodart, J.**, Karoui, K., Boschini, F., Ben Rhaiem, A., & Mahmoud, A. (22 July 2021). Electrochemical mechanism and effects of Fe doping and grinding process on the microstructural and electrochemical properties of Na2Co1-xFexSiO4 cathode material for sodium-ion batteries. *Electrochimica Acta, 391*, 138935. doi:10.1016/j.electacta.2021.138935
5. Trabelsi, K., Karoui, K., Mahmoud, A., **Bodart, J.**, Boschini, F., & Ben Rhaiem, A. (22 July 2020). The dielectric relaxation behavior induced by sodium migration in the Na2CoSiO4 structure within a three-dimensional Co–O–Si framework. *RSC Advances, 10*, 27456-27473. doi:10.1039/D0RA04912C
6. Vertruyen, B., Eshraghi, N., Piffet, C., **Bodart, J.**, Mahmoud, A., & Boschini, F. (2018). Spray-drying of electrode materials for lithium- and sodium-ion batteries. *Materials, 11* (7), 1076. doi:10.3390/ma11071076

Patent:

1. **Bodart, J.**, Boschini, F., Cloots, R. “Preparation of magnetic core-shell particles” WO 2021/198289 A1

Conference proceeding

Oral communications:

1. **Bodart, J**., Eshraghi, N., Carabin, T., Vertruyen, B., Cloots, R., Boschini, F., & Mahmoud, A. (25 November 2020). K3V(PO4)2/C: a New Cathode Material for Advanced Potassium-ion Batteries. **Oral presentation** at 8th International Renewable and Sustainable Energy Conference (IRSEC'20.
2. **Bodart, J.**, Eshraghi, N., Mahmoud, A., Vertruyen, B., Cloots, R., & Boschini, F. (22 July 2019). *Spray-drying as a versatile synthesis method for fluorophosphate-based compounds as cathodes material for Na-ion batteries*. **Oral presentation** at Electrochemical Conference on Energy and the Environment: Bioelectrochemistry and Energy Storage, Glasgow, United Kingdom.
3. **Bodart, J.**, Eshraghi, N., Piffet, C., Roex, E., Berardo, L., Vertruyen, B., Boschini, F., & Mahmoud, A. (05 May 2021). *Development of advanced electrodes materials for alkali- ions batteries by spray-drying method* . **Oral presentation** at 2021 Annual Meeting of Belgian Ceramics Society.
4. **Bodart, J.**, Mahmoud, A., Vertruyen, B., & Boschini, F. (05 July 2018). *Spray-Drying Synthesis of Na2FePO4F as Positive Electrode for Na-ion Batteries*. **Oral presentation** at Chemistry Department Day, Liege, Belgium.
5. **Bodart, J.**, Mahmoud, A., Vertruyen, B., Cloots, R., & Boschini, F. (May 2018). *Synthèse par Spray-Drying de Na2FePO4F comme matériaux d'électrode positives pour batteries Na-ion*. **Oral presentation** at 40e journées du groupe francophone de spectroscopie Mossbauer, Bordeaux, France.
6. **Bodart, J.**, Sougrati, M. T., Lippens, P.-E., Boschini, F., & Mahmoud, A. (18 May 2022). *Etude Mössbauer de la redox du fer dans NaFePO4F, obtenu via un séchage par atomisation*. **Oral presentation** at les journées du Groupe Francophone de Spectrométrie Mössbauer (GFSM).
7. Eshraghi, N., **Bodart, J.**, Mahmoud, A., Vertruyen, B., Malherbe, C., Cloots, R., & Boschini, F. (September 2018). Study the influence of carbon source on morphology and electrochemical behavior of Na3V2(PO4)2F3 carbon composites used as positive electrode material in Na-ion batteries. **Oral presentation** at 69th Annual Meeting of International Society of Electrochemistry, Bologna, Italy.
8. Eshraghi, N., **Bodart, J.**, Mahmoud, A., Vertruyen, B., Malherbe, C., Cloots, R., & Boschini, F. (10 July 2018). Effect of carbon source on electrochemical properties of spray-dried Na3V2(PO4)2F3/carbon

composites as cathode material for Na-ion batteries. Paper presented at Electroceramics XVI, Hasselt, Belgium.

9. Eshraghi, N., **Bodart, J.**, Vertruyen, B., M. Meyer III, H., Nanda, J., Belharouak, I., Boschini, F., & Mahmoud, A. (26 November 2020). *Spray dried Na3V2(PO4)2F3 and Na3V2(PO4)2F3/C composites as cathode materials for Na-ion batteries*. **Oral presentation** at International Renewable and Sustainable Energy Conference (IRSEC), Morocco.
10. Mahmoud, A., **Bodart, J.**, Karegeya, C., Sougrati, M. T., Hermann, R., Cloots, R., Vertruyen, B., Lippens, P. E., & Boschini, F. (21 May 2019). *Electrode materials for Li-ion and Na-ion batteries prepared by hydrothermal and spray drying methods*. **Oral presentation** at 5th Mediterranean Conference on the Applications of the Mössbauer Effect (MECAME) and 41st French speaking group of Mössbauer spectroscopy (GFSM), Montpellier, France.
11. Mahmoud, A., Eshraghi, N., **Bodart, J.**, Cloots, R., Vertruyen, B., & Boschini, F. (24 March 2021). *Spray drying method for high-performance phosphate-based cathode materials for Na-ion and K-ion batteries*. **Oral presentation** at International symposium on Energy and Materials (Second Edition), Benguerir, Morocco.
12. Mahmoud, A., Eshraghi, N., **Bodart, J.**, Vertruyen, B., Cloots, R., & Boschini, F. (01 February 2021). *Spray Drying of Phosphate based Cathode Materials for Na-ion and K-ion Batteries with Advanced Electrochemical Performance*. **Oral presentation** at 6th International Conference on Nanoscience and Nanotechnology (ICONN2021), Chennai, India.
13. Mahmoud, A., karegeya, C., Sougrati, M. T., **Bodart, J.**, Vertruyen, B., Cloots, R., Lippens, P.-E., & Boschini, F. (17 May 2018). *Composites Fe1.19(PO4)(OH)0.57(H2O)0.43/C comme matériaux d'électrode positive pour batteries Li-ion*. **Oral presentation** at 40èmes Journées du Groupe Francophone de Spectrométrie Mössbauer, Bordeaux, France.

Poster communications:

1. **Bodart, J**., Eshraghi, N., Carabin, T., Vertruyen, B., Boschini, F., & Mahmoud, A. (22 January 2020). Spray-dried K3V(PO4)2 and K3V(PO4)2/carbon as new cathode materials for potassium-ion batteries. **Poster** session presented at LE STUDIUM Conference - Towards Futuristic Energy Storage; paving its way through Supercapacitors, Li-ion batteries and beyond, Tours, France. Best poster certificate awarded for this presentation.
2. **Bodart, J**., Eshraghi, N., Vertruyen, B., Boschini, F., & Mahmoud, A. (15 March 2022). Le spray drying comme méthode de synthèse versatile des matériaux de cathodes polyanioniques à base de phosphate pour batteries Na-ion et K-ion. **Poster** session presented at Réunion annuelle du Groupe Français d'Etude des composés d'insertion, SETE, France.
3. **Bodart, J**, Violle, D., Mahmoud, A., Vertruyen, B., & Boschini, F. (13 December 2018). Synthesis of Na2FePO4F by spray *drying in order to optimise the composition and morphology for Na-ion batteries applications*. **Poster** session presented at BCers Annual Meeting, Liege, Belgium.
4. Berardo, L., Mahmoud, A., Caes, S., Brisbois, M., Hermann, R., **Bodart, J.**, Eshraghi, N., Schrijnemakers, A., Colson, P., Malherbe, C., Eppe, G., Cloots, R., Vertruyen, B., & Boschini, F. (02 October 2018). *Dispersion of conductive carbon allotropes inside Na2FePO4F particles by spray-drying*. **Poster** session presented at Batteries event 2018, Nice, France.
5. Eshraghi, N., **Bodart, J.**, Mahmoud, A., Vertruyen, B., Cloots, R., & Boschini, F. (13 December 2018). *Study of the effect of the carbon source on the properties of spraydried Na3V2(PO4)2F3 /C cathode material for Na-ion batteries*. **Poster** session presented at 2018 BCerS Annual Meeting, Liege, Belgium.
6. Eshraghi, N., **Bodart, J.**, Mahmoud, A., Vertruyen, B., Cloots, R., & Boschini, F. (25 November 2018). Spray drying synthesis of Na3V2(PO4)2F3/C cathode material for Na-ion batteries: study of the effect of the carbon source on electrochemical performance. **Poster** session presented at 2018 MRS Fall Meeting, Boston, United States.
7. Eshraghi, N., **Bodart, J.**, Mahmoud, A., Vertruyen, B., Cloots, R., Malherbe, C., Boschini, F., Meyer III, H. M. (Other coll.), & Nanda, J. (Other coll.). (28 May 2019). *XPS and Raman study of spray-dried Na3V2(PO4)2F3/C as cathode material for sodium ion batteries*. **Poster** session presented at Spring Meeting of the European Materials Research Society (E-MRS), Congress & Exhibition Centre Acropolis, NICE, France.
8. Mahmoud, A., **Bodart, J.**, Karegeya, C., Sougrati, M. T., Lippens, P. E., Cloots, R., Vertruyen, B., & Boschini, F. (05 May 2021). *Mössbauer spectroscopy studies of Fe-based electrode material for Li-ion and Na-*

ion batteries. **Poster** session presented at Annual Meeting BCerS 2021, Belgium.

9. Mahmoud, A., Karegeya, C., Eshraghi, N., Piffet, C., Berardo, L., Jungers, T., Costanza, T., **Bodart, J.**, Cloots, R., Vertruyen, B., & Boschini, F. (12 October 2017). *Electrode materials for Li/Na-ion batteries: Improving electrochemical performance through carbon addition during synthesis*. Poster session presented at Seminar: From Hard Grains To Soft Matter, Liege, Belgium.
10. Mahmoud, A., karegeya, C., Sougrati, M. T., **Bodart, J.**, Vertruyen, B., Cloots, R., Lippens, P.-E., & Boschini, F. (25 November 2018). *Electrochemical mechanism and effect of carbon addition during hydrothermal synthesis to improve the electrochemical performance of Fe1.19(PO4)(OH)0.57(H2O)0.43 cathode material for Li-ion batteries*. **Poster** session presented at 2018 MRS Fall Meeting, Boston, United States.

List of abbreviations

ΔEq	Quadrupole Splitting
A-ion	Alkali-ion battery
Ar flow	Argon Flow
at%	Atomic percentage
ATEX	Explosive Atmosphere
BET	Brunauer–Emmett–Teller (for determining the surface area)
BN	Bifluid Nozzle
C	Carbon
C-rate	1C Means the discharge current will discharge the entire battery in 1 hour
CB	Carbon Black
CNT	Carbon NanoTubes
CPE	Constant Phase Element
CRM	Critical Raw Materials
CS	Crystallite Size
CV	Cyclic Voltammetry
DEC	Diethyl Carbonate
DFT	Density Functional Theory
DMC	Dimethyl Carbonate
DSC	Differential Scanning Calorimetry
DTG	Derivative Thermogravimetric
EC	Ethylene Carbonate
EIS	Electrochemical Impedance Spectroscopy
EOC	End of Charge
EOD	End of Discharge
FEC	FluoroEthylene Carbonate
GO	Graphene Oxide
ICA	Independent Component Analysis
IS (or δ)	Isomer Shift
KFP_2	$K_3Fe(PO_4)_2$

KFP_3	$K_3Fe_2(PO_4)_3$
KIB	K-Ion Battery
KVP	$K_3V(PO_4)_2$
LCO	$LiCoO_2$
LFP	$LiFePO_4$
LIB	Li-Ion Battery
LLO	Lithium-rich Layered Oxides
LMO	$LiMn_2O_4$
LNMO	$LiNi_{0.5}Mn_{1.5}O_4$
LTO	$Li_4Ti_5O_{12}$
MCR-ALS	Multivariate Curve Resolution by Alternating Least Square
NASICON	Na Super Ionic Conductor
NCA	$LiNi_{0.8}Co_{0.15}Al_{0.05}O_2$
NFPF	Na_2FePO_4F
Ni-Cd	Nickel-Cadmium battery
Ni-MH	Nickel Metal hydride battery
NIB	Na-Ion Battery
NLLSQ	Non-Linear Least-Square
NMC	$LiNi_xMn_yCo_zO_2$
NMP	N-Methyl-2-Pyrrolidone
NMR	Nuclear Magnetic Resonance
OCV	Open Circuit Voltage
PBA	Prussian Blue Analogues
PC	Propylene Carbonate
PCA	Principal Component Analysis
PEDOT	poly(3,4-ethylene dioxythiophene)
ppm	part per million
PVDF	PolyVinyliDene Fluoride
PWA	Prussian White Analogues
R_{CT}	Charge Transfer Resistance
R_e	Electrolyte Resistance
RN	Rotary Nozzle
RNA	Ribonucleic Acid
RT-PCR	Reverse Transcription–Polymerase Chain Reaction

SEI	Solid Electrolyte Interface
SEM	Scanning Electron Microscopy
TEM	Transmission Electron Microscopy
TEOS	TetraEthyl OrthoSilicate
TGA	ThermoGravimetric Analysis
TMO	Transition Metal Oxides
TMS	Transition Metal Sulfides
vs.	versus
wt%	Weight percentage
XRD	X-ray Diffractions
Γ	Linewidth

List of figures

List of tables

Chapter I

Introduction

1. General introduction

Recent events have demonstrated the necessity of finding urgent and sustainable solutions to encounter energy needs. Whether it is the extreme climatic changes of these years, the pandemic supposedly linked to global warming, which promotes the appearance of new diseases [1], or the very recent war in Ukraine, which is undermining our entire economic system and the energy supply. Despite these evidences, in the coming years, the world's annual energy consumption will double from 14TW in 2010 to 28TW in 2050 (see Figure I-1), leading to more energetic challenges [2].

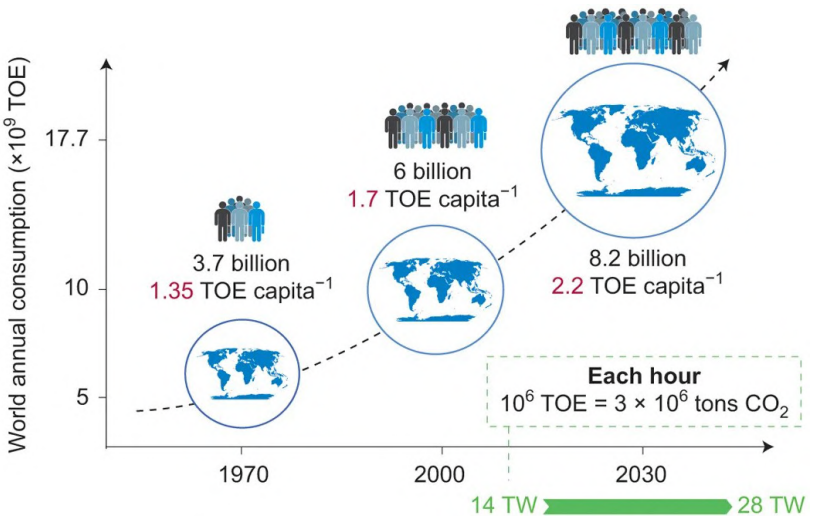

Figure I-1: Evolution of the world's energy consumption and prediction up to 2050, TOE = ton of oil equivalent [2]

In the past, the growing energy demand was met by exploiting fossil fuels such as coal, oil, and gas. These fossil sources are, by definition, non-renewable, therefore limited, and take an enormous amount of time to reconstitute, which does not make them a sustainable solution for future needs. In addition, tragic events linked to global warming and climate change continue to recur, raising public awareness of climate issues. It is our duty to change our habits and find a solution to these changes that our planet is facing. This is why the development of so-called

renewable energy is growing rapidly. The advantages of these energy sources are multiple: they are unlimited, do not cause greenhouse gas emissions, their production can be located almost anywhere, and they are clean. The best-known renewable energy sources are wind, solar, hydroelectric, and geothermal energy. Due to their intermittency, it is necessary to find a way to store them to respond to the demand whenever needed. These energy storage systems may be installed either at the power plant location or elsewhere in the grid distribution system, including the customer side.

Different energy storage technologies already exist. These include batteries, fuel cells, or supercapacitors. These various technologies can be classified according to the energy density or the power density they can deliver. As the name indicates, capacitors use capacitive and electrostatic interactions to exchange electrical energy; they provide high power with low energy. The batteries and fuel cells, on the contrary, provide low power but high energy and store the energy under chemical forms and restore it through redox reaction.

Among the various energy storage systems, the Li-ion battery is one of the most competitive and attractive technologies, since it has a high energy density, very good efficiency, and long cycle life. These batteries already have plenty of applications. Among them, it is transportation that has the fastest development. The electrification of transportation is not new as the trains, tram, and metro already use it for many years, but these transportation systems are always connected to the power source. The personal transport that uses diesel or petrol to operate, since their invention, is now moving toward a greener way using batteries. The rapid expansion of this market and other markets where everything has to be mobile puts increased pressure on battery requirements and development.

In the years to come, Li-ion technology may find itself unable to meet the colossal demand for energy storage systems. The interest in new systems based on a more abundant element has emerged for a few years. Sodium has rapidly attracted much

interest as a candidate to replace lithium since it has similar physical and chemical properties. In addition, it is highly abundant in the earth's crust, and the ocean and seas are considered an infinite source of sodium [3]. More recently, for a similar reason, potassium has attracted increased interest in the scientific community. For both of them, the energy density cannot be, for now, as high as their lithium counterpart, but they could be used for stationary applications [4]. Although the idea of replacing Li with Na or K may seem simple, the effects on chemistry are complicated and still poorly understood. That’s why the future of electricity storage will not be solved using only one system. These systems must be complementary, and research on the three systems Li, Na, and K-ion batteries should continue to improve these systems.

2. Electrochemical energy: history and development

Batteries' story began with Alessandro Volta, who experimented the combination of different metal plates with liquid electrolytes and invented the first known pile. This battery and all the other stays on the same basic principle, which is converting chemical energy into electricity through a redox reaction. After this discovery, other systems were developed, such as manganese-based batteries, but all these systems are single-use. Indeed, primary batteries are characterized by their single discharge and, once there is no more active material, the battery cannot be recharged and reused. These systems are then not able to store electricity that is produced by another system. Secondary batteries were invented a little later and, contrary to the primary batteries, they can be reused and recharged by applying an electric current to reverse the redox reaction and regenerate the material reversibly.

The four major commercial battery technologies: Lead-acid, Nickel-cadmium, Nickel-metal Hybrid, and Lithium-ion, can be classified according to their gravimetric and volumetric energy density. These two parameters have guided the development of batteries since the discovery of the lead-acid battery until the advent of Li-ion batteries. Figure I-2 presents the gravimetric and volumetric energy densities of the different battery technologies. The development of batteries has always tried to increase these two values. In 1859, Gaston Planté invented Lead-acid batteries. It is characterized by a low value of energy densities (~30 Wh/kg or 80 Wh/L). It is still widely used and particularly for starting thermal motors in cars because they can provide a high current intensity.

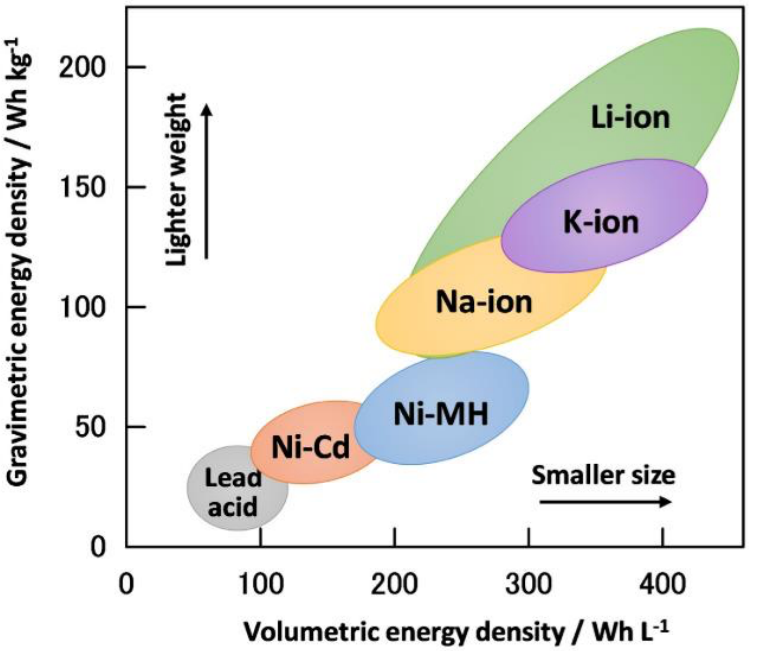

Figure I-2: Gravimetric and volumetric energy densities of common battery technologies [4].

A few years later, in 1899, Waldemar Jungner invented the Nickel-Cadmium batteries that present higher power density with less weight than the lead-acid battery increasing their gravimetric and volumetric energy densities (~40 Wh/kg or 150 Wh/L). However, the toxicity of cadmium quickly led to their marketing being reserved for professional applications [5]. A 27 MW, 6.75 MWh battery energy storage system with Ni-Cd batteries, connected to the Golden Valley Electric Association's grid near Fairbanks, Alaska, illustrates the applications [6].

The Nickel-metal hydride batteries were invented in 1967 and present even higher energy densities (~60 Wh/kg or 220 Wh/L) and have rapidly been used to develop the first portable applications with its commercialization in 1990. But only a year later, the commercialization by Sony of the first Li-ion battery completely revolutionized the battery market. Indeed, with energy densities more than twice those of Ni-MH batteries, Li-ion batteries quickly flooded the market, reaching today more than 200 Wh/kg (Figure I-2). Li-ion batteries are considered the most

efficient system for now. It can provide high energy density as well as high power density. These performances can be attributed to the unique properties of lithium. Indeed, with a molar mass of 6.941 g/mol and an ionic radius of 0.76 Å, lithium allows to store a large amount of energy in a minimum volume and weight. The small ionic radius also induces a rapid diffusion of Li^+ ions at the interfaces, which makes it possible to reach high powers. This technology is still unbeatable, but new technologies, based on sodium or potassium, so-called "beyond Li-ion batteries", can reach properties interesting in other energy storage applications. In the present work, we strongly believe that no technology, for now, is sufficient to respond alone to all the electrical energy storage demand. That's why we do not only focus on one kind of technology, as a combination of multiple energy storage systems for different applications may be the solution to fulfill the market growth and requirements.

3. The alkali-ion batteries: Fundamental concepts.

All alkali-ion (A-ion) batteries work through the same principle, illustrated in Figure I-3. The batteries work through the movement of A-ion across the electrolyte from the cathode material, which is the source of A-ion, to the anode, which stores the ion during the charging process. To avoid short circuits, the two electrodes are separated by a porous membrane soaked with the electrolyte.

During the charge, the A^+ ions are extracted from the cathode and migrate through the electrolyte to be inserted into the anode material. To allow the A^+ to be extracted from the positive electrode, the material is oxidized and produces one electron which flows, using the external circuit, to finish at the anode side and allow the reduction of the negative material during the insertion of the A^+ ion.

During the discharge, the exact reverse process is observed. The A^+ ions migrate through the electrolyte from the anode to the cathode, and the electrons flow from the anode to the cathode using the external circuit. Pay attention that the term anode and cathode are only correct when talking about the discharge process, but as a convention, the term cathode is used for the positive electrode and anode for the negative electrode.

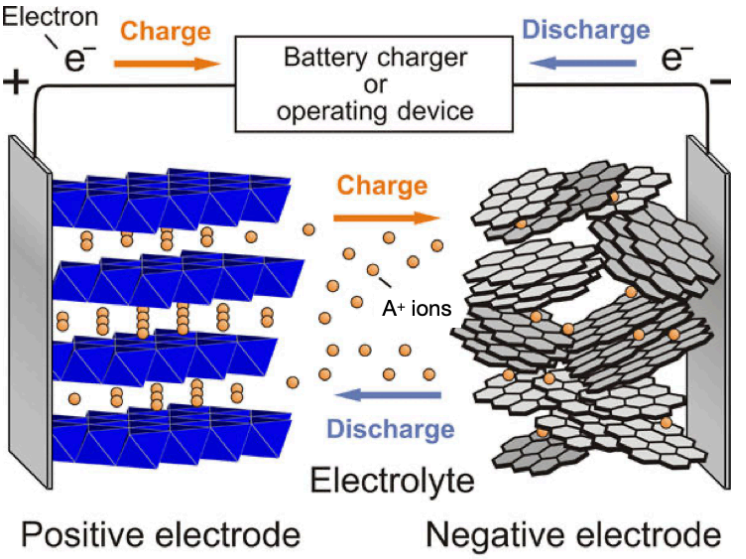

Figure I-3: Schematic representation of the functioning of an A-ion battery [7].

The battery performance depends mainly on the electrode material properties, but it is also strongly influenced by the electrolyte and the interface [8]. Before explaining these different components, it is important to remind some typical characteristic values.

3.1. Characteristic values.

The electrochemical performance of electrode material is evaluated and described using specific parameters detailed here below.

The capacity represents the amount of charge stored in a battery. It is defined by the integration of the current intensity as a function of time.

$$\int_0^t I(t)dt = Q(A.h) = nzF$$

Where I is the current intensity, n is the number of ions exchanged, z is the valence of the exchange ion, and F is the Faraday constant.

To compare results, the capacity is usually normalized by the mass. In this case, the specific capacity (Ah/g) is used and represents the capacity normalized by the

active material mass. The capacity can also be normalized by the volume of active material to give the density of charge (Ah/L).

The working potential of a battery represents the difference in potential between the two electrodes

$$E = E_{Cathode} - E_{Anode}$$

It can be evaluated by the Nernst equation but generally, it is simply measured. It is the potential at which the material will undergo the redox process, and it is independent of the quantity of material.

The energy (E) is obtained by multiplying the capacity and the potential (U) of the battery.

$$E = Q.U$$

When the energy is calculated with the specific capacity or density of charge, it is called energy density (Wh/g or Wh/L)

The coulombic efficiency is the ratio of the capacities obtained during the charge and the discharge. It is a percentage that represents the irreversibility of a cycle. In other words, it represents the amount of capacity not recovered during a cycle. The industrial rule for battery commercialization is that after 1000 cycles, the obtained capacity should be at least 80% of the initial capacity which means that at each cycle, the coulombic efficiency should be at least 99.98%.

The cycling rate represents the “speed” of cycling of a battery. To evaluate the corresponding current, the following formula is used:

$$I = \frac{C_{theoric}\left(\frac{Ah}{g}\right).m_{active\ material}(g)}{t_{time\ for\ a\ complete\ (dis)charge}\ (h)}$$

It is noted C/t, where t represents the theoretical number of hours necessary for a complete charge or discharge. If we note 1C, theoretically, one charge takes 1 hour as well as one discharge, 4C for 15 min, and C/4 for 4 h.

3.2. *Materials for batteries*

If efficient, all battery materials should have a high capacity, good structural and thermal stability during cycling, and good electronic and ionic conductivity. The insertion/exertion of lithium into material causes changes in bond length, thus in the volume of the cell unit of the materials. The different materials can be classified regarding their insertion mechanisms: intercalation, alloying, and conversion [9,10]. These mechanisms are illustrated in Figure I-4. The properties of the main materials for LIB are reported in Table I-1.

3.2.1. Intercalation

The term intercalation refers to a tunnel-like framework. The intercalation is a reversible insertion of the ion into the crystal site (1D), between layers (2D), or into tunnels (3D) of the electrode materials with low volume expansion. The structure of the host material is maintained in most cases, but a reversible phase change can occur during the intercalation process. It has been reported for $LiFePO_4$ or $Li_4Ti_5O_{12}$ materials [11].

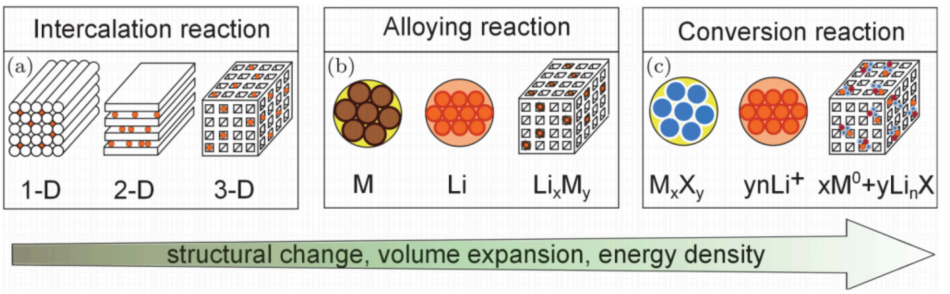

*Figure I-4: Possible lithium insertion reaction [*11].

3.2.2. Alloying

The alloying insertion mechanism is based on the formation of a solid solution between the ion and a metal (M) or semimetal, leading to the formation of Li_xM_y alloy. This kind of material has advantages such as a higher energy density, low cost, and safe operating conditions [12]. Therefore, intensive research is carried out on these materials to become the next generation batteries. However, this kind of reaction is linked with a huge volume expansion and structural change of the materials during cycling. The insertion of Li^+ into Sn induces a volume expansion of 255% [13]. These drawbacks can result in a loss of contact between the material particles and the current collector and the formation of an unstable solid electrolyte interface (SEI), leading to excessive ion consumption and poor cycling performance. The volume expansion can be reduced using different strategies, such as carbon coating [14] or nano structuration [9].

3.2.3. Conversion materials

Conversion electrodes have been widely used and are still commercialized for primary batteries. The main challenge of conversion materials is the reversibility of the reaction. Conversion electrodes have the general formula MaXb, where M is a transition metal (either Fe, Mn, Ni, Co, Cu,…). These transition metals can be in the form of an oxide (X=O), a sulfide (X=S), a fluoride (X=F), a nitride (X=N), a phosphate (X=PO4), or a hydride (X=H). During the insertion of the alkali-ion, the metal is reduced to its metallic state and the lithium reacts with the X atoms. This result in a matrix of Li_yX with nanoparticles of metallic nanoparticles dispersed in it. The problem of these materials is related to their volume expansion as for the alloying material and the unstable SEI. The higher the oxidation state of the starting material, the more ions can be inserted, thus the higher energy density. But the more ion insertion, the more volume changes and thus the less stability of the electrode during cycling [28].

*Table I-1: Volume Strain and Potential versus Li^+/Li of lithium-ion electrode materials reproduced from [*11,27]

Lithium Storage Compound	Limiting Composition	Volume strain $\Delta V/V_0$ (%)	Insertion Reaction	Potential *vs.* Li/Li^+(V)	Ref
Cathode materials (Li-extraction)					
$LiCoO_2$ (LCO)	$Li_{0.5}CoO_2$	+1.9	2D-intercalation	3.9	[17]
$LiNi_{0.8}Co_{0.2}O_2$	$Li_{0.5}Ni_{0.8}Co_{0.2}O_2$	-2.04	2D-intercalation	3.6	[18]
$LiNi_{0.8}Co_{0.15}Al_{0.05}O_2$ (NCA)	$Li_{0.5}Ni_{0.8}Co_{0.15}Al_{0.05}O_2$ (NCA)	-1.16	2D-intercalation	3.7	[19]
$LiNi_{1/3}Mn_{1/3}Co_{1/3}O_2$ (NMC)	$Li_{0.47}Ni_{1/3}Mn_{1/3}Co_{1/3}O_2$ (NMC)	2.44	2D-intercalation	3.7	[20]
$LiFePO_4$ (LFP)	$FePO_4$ (LFP)	-6.6	1D-intercalation	3.4	[21]
$LiMn_2O_4$ (LMO)	Mn_2O_4 (LMO)	-7.3	3D-intercalation	4.0	[22]
$LiNi_{0.5}Mn_{1.5}O_4$ (LNMO)	$Ni_{0.5}Mn_{1.5}O_4$ (LNMO)	-6.2	3D-intercalation	4.7	[23]
S	Li_2S	80	Conversion	2.4	[24]
Anode materials (Li Insertion)					
C_6 (graphite)	LiC_6	12.8	2D-intercalation	0.1	[25]
$Li_4Ti_5O_{12}$ (LTO)	$Li_7Ti_5O_{12}$ (LTO)	0	3D-intercalation	1.5	[26]
Si	$Li_{4.4}Si$	310	Alloying	0.3	[27]
Sn	$Li_{4.4}Sn$	255	Alloying	0.58	[13]
Li	Li_2O_2	30	Conversion	2.96	[26]

3.3. Lithium-ion batteries: electrode materials

3.3.1. Cathode materials

Figure I-5a presents the most common developed intercalation electrode materials, and Figure I-5b shows a future perspective for the conversion type materials. Different intercalation materials have been developed, and some layered, spinel, and olivine type materials have already been commercialized.

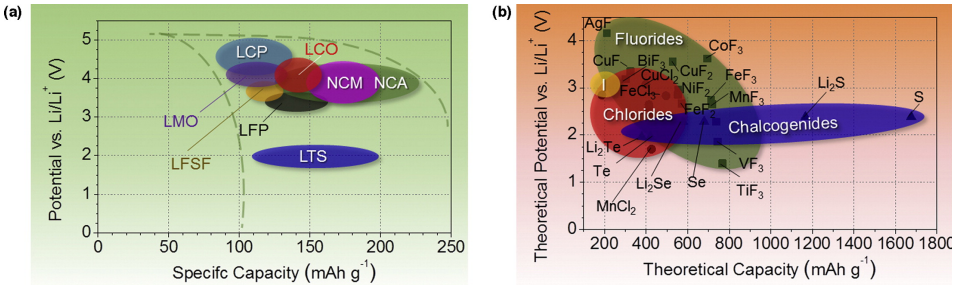

Figure I-5: Approximate range of average discharge potential of some of the most common a) intercalation type cathode material b) conversion type cathodes (theoretical) [29].

a. Layered oxide

In 1991, Sony commercialized the first Li-ion battery, which uses lithium cobalt oxide ($LiCoO_2$) at the cathode side. LCO was first introduced by Goodenough, which proved its interest [30–32]. Li-ions occupy free interlayer space. The main hexagonal structure is formed by CoO_2. This specific layered structure allows the reversible extraction/insertion of Li^+ at a high voltage of 3.8 V *vs.* Li^+/Li. It also shows a high theoretical capacity of 274 mAh/g and good cycling performance. Despite these promising properties, the use of LCO tends to disappear for several reasons. Among them are the high toxicity of the Co and its high cost. It also suffers from poor structural stability, which avoids reaching this material's theoretical capacity. When more than 50% of the Li^+ is extracted, there is an

irreversible structural change that induces a huge capacity fading. This phenomenon also occurs at high cycling rate [15].

The partial substitution of Co by Ni, Mn, and/or Al has proven to be efficient in stabilizing the structure during Li-ions extraction/insertion. The obtained $LiNi_xMn_yCo_zO_2$ (NMC) or $LiNi_xCo_yAl_zO_2$ (NCA) are already used in the market for many applications, including electric vehicles. The standard composition of NMC is a 6:2:2 ratio of each transition metal. Thanks to its enhanced thermal and structural stabilities, it has significantly increased the achievable specific capacity without changing the working potential. The cost and toxicity are also reduced due to the lower amount of cobalt. NCA, with an optimal composition of $LiNi_{0.8}Co_{0.15}Al_{0.05}O_2$ shows the same enhancement of its stability with a theoretical capacity of 280 mAh/g and a specific capacity that can reach 225 mAh/g [9,29].

In recent years, a new category of layered oxide has appeared with great interest. These are lithium-rich layered oxides (LLO), $Li_{1+x}M_{1-x}O_2$ (M = Ni, Co, Mn). They are considered to be among the highest-capacity cathodes. Indeed, LLOs possess possible capacities in the range of ~280 to 310 mAh/g with a high working potential of ~3.7 V (*vs.* Li^+/Li^0) and an energy density of ~900 Wh/kg [33–35]. These promising cathodes have not yet been successfully commercialized due to low initial coulombic efficiency, as well as continuous structural changes during the cycling that induce capacity and voltage fading.

b. Spinel compounds

The spinel group combines the minerals with the gross formula AB_2X_4 in which the X anions form a compact face-centered cubic stack, and the A and B cations share part of the octahedral and tetrahedral sites provided by the stack of anions. $LiMn_2O_4$ (LMO) is part of the spinel compounds. It has retained attention and is used due to the abundance, low toxicity, and low cost of the manganese. Also, it has interesting theoretical properties with a capacity of 148 mAh/g and a high insertion potential of 3.9 V. However, its long-term stability is insufficient due to

irreversible side reactions with the electrolyte, oxygen loss when delithiated, dissolution of manganese, and structural change at the surface [36]. Among the strategies tested to solve these problems, the doping to stabilize the structure with Nickel, chrome, iron, or boron has proven its interest and led to enhancement of the electrochemical performance of the material [29,37,38].

c. *Polyanionic compounds*

The polyanionic compounds have a structure with lattice positions occupied by large polyanions $(AO_4)^{3-}$(A=S, P, Si, As, Mo, W). These polyanions increase the cathode redox potential and stabilize the structure. The olivine $LiFePO_4$ is the most representative of the polyanionic compound for LIBs. It demonstrates high thermal and structural stability with long cycle life. However, it shows a lower potential (3.5 V) and lowers electronic conductivity than other LIB cathode materials. The problem of conductivity can be solved either by nanosizing or by the carbon coating of the material [29,39,40].

3.3.2. *Anode materials*

The use of metallic lithium as anode material for LIBs is theoretically the most interesting choice. It has the lowest voltage and is, by nature, an unlimited source of Li-ions. However, lithium is very reactive, and during cycling, its deposition is not homogeneous forming aggregates called dendrites (Figure I-6), which can grow and create short circuits in the battery. In addition, the use of metallic lithium in commercialized batteries has obvious safety issues due to the high reactivity of the metal with air and humidity. For all these reasons, alternative anode materials are necessary to develop safe batteries. At lab scale, the metallic alkaline is still used as a reference. Figure I-7 presents the average operating potentials and specific capacities of the main anode materials for LIBs.

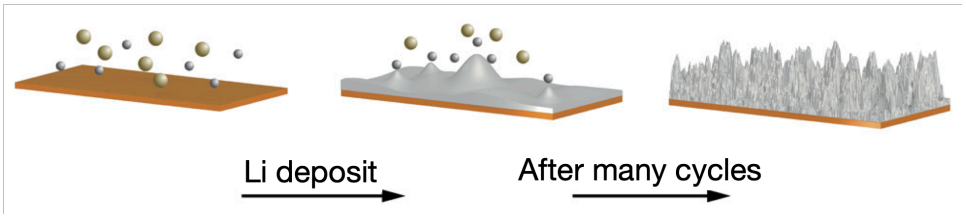

Figure I-6: Schematic representation of Li^+ deposition and formation of dendrites [41].

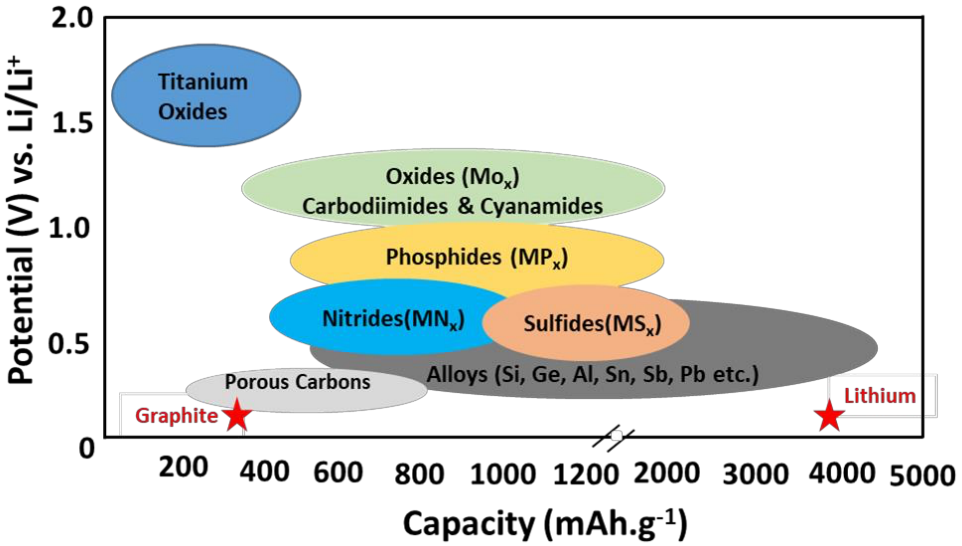

*Figure I-7: Average operating potentials and specific capacities of commonly used anode materials [*42].

a. Carbonaceous material

Since more than 30 years, carbon graphite is the most successful anode material of commercialized LIBs [4,43]. The carbon is abundant, safe, cheap, has a low insertion potential (0.1 V *vs.* Li^+/Li), and has a high electronic and ionic conductivity. Theoretically, one Li^+ can be stored by six carbon leading to a gravimetric capacity of 372 mAh/g. The lithium intercalates between the graphene inducing a volume expansion of about 10%. This volume expansion is one of the only drawbacks of this material for its current applications. The gravimetric capacity of graphite is still higher than any commercialized cathode material.

The development of new high-capacity cathode materials based on Li-rich materials or conversion materials like sulfur and also the technical demand for higher energy, such as electric vehicles, require new anodes with higher capacities.

b. Oxide

Lithium titanium oxide (LTO) is the only oxide anode material commercialized for now. Its commercialization is due to its high thermal, structural stability, and safe working potential of 1.5 V, which avoids the formation of SEI and thus the excessive consumption of Li during cycling. $Li_4Ti_5O_{12}$ can intercalate up to 3 Li^+ in its structure, leading to a gravimetric capacity of 172 mAh/g with no volume change [24,44]. This led to outstanding cycle life of more than 10,000 cycles with high stability. Due to its high voltage, it has a lower energy density. The conductivities of this material are also relatively low. This material is still interesting for lower energy applications but with high power and long cycle life [44].

c. Alloying and conversion materials

The alloying or conversion materials are characterized by an important gravimetric and volumetric capacity.: 4200 mAh/g for silicon ($Li_{4.4}Si$), 1600 mAh/g for germanium ($Li_{4.4}Ge$), 992 mAh/g for tin ($Li_{4.4}Sn$), and 660 mAh/ for antimony (Li_3Sb)[45]. The main drawback of all these materials is their volume expansion (up to 400%) during cycling. Alloying materials are also often associated with a low coulombic efficiency, mainly during the first lithiation attributed to the formation of SEI. Silicon has attracted more attention, Si is non-toxic, has a low cost, is the second most abundant element in the earth's crust after oxygen, and has an incredibly high theoretical capacity. However, during cycling Si expands when alloying with lithium to more than 300% of its initial volume. The electrochemical cycle is associated with a swelling and shrinking cycle and an unstable SEI, which consumes all the electrolytes of the cell and leads to poor cycle life.

Conversion-type materials such as Fe_2O_3, CO_2O_3, and CuO exhibit high theoretical capacities but suffer from several problems, including volume expansions. Other drawbacks of these materials are the low kinetic of insertion of Li^+ resulting in a huge hysteresis in their charge/discharge voltage profile and the presence of side reaction at low potential that can lead to the loss of contact between the particles in the active material [46–49].

3.3.3. *Electrolyte*

The battery performance doesn't depend only on the electrode material. The electrolyte is an essential component of batteries. It ensures the ion's transportation between the two electrodes. There are different types of electrolytes: liquid, solid, polymeric, aqueous, ionic liquid, super-concentrated… The most common electrolyte in batteries is made of lithium salt dissolved in an organic solvent such as alkyl carbonate or ether-based solvent. The concentration of the electrolyte is an important factor: a too low concentration will induce a too low ionic conductivity, and a too high concentration will increase the viscosity and reduce the ion mobility. The commonly used electrolyte salt is $LiPF_6$. It dissolves easily in different solvents and allows good ionic conductivity. Other salts also exist, like LiTFSI, $LiClO_4$, LiFSI… having some drawbacks, including reaction with the aluminum at the cathode current collector [50]. The choice of solvent is also important regarding its anodic stability. Indeed, the used solvent should be stable in a potential window higher than the batteries' working potential window. It means that the solvent or the salt can be reduced at low potentials on the anode side and oxidized at the high potential on the cathode side. The decomposition of the electrolyte results in the formation of a passivation layer on the electrodes called the solid electrolyte interface (SEI). Ideally, this passivation layer should be stable, protect the electrode and should be an electronic insulator, insoluble in the electrolyte solvent, and a good ionic conductor [51]. Unfortunately, in some cases, the SEI is unstable and continuously degrades the

electrolyte, reducing the cycle life of the battery. As explained before, this SEI layer can also break during cycling due to volume expansion. The new electrode surface may be in direct contact with electrolyte forming a new SEI layer.

The ideal electrolyte should have a high ionic conductivity (3.10^{-3} to 2.10^{-2} S/cm) at room temperature. This conductivity should be lowly affected by temperature variation, have high stability working potential window, be an electronic insulator, and have low toxicity and low cost [8,52,53].

4. Beyond lithium ions batteries

The growing energy demand and the development of new technology systems have increased the need for battery production. Conventional LIBs seem to reach a limit in energy density[54,55]. The LIBs market is fully expanding due to the development of smartphones and electric vehicles [56,57]. Therefore, the need for cheap batteries with high energy density is more than ever a priority. The prices related to the transition metal composing the cathode, such as cobalt, are one of the issues in making affordable batteries[58]. But the costs of the lithium precursors also become critical. As shown in Figure I-8, the lithium resources are unevenly distributed, with almost 90% of lithium production coming from Australia and South America. The price of lithium precursor (Li_2CO_3) has increased significantly from $6,000 per ton in 2015 to $17,000 in 2021[59]. The search for cheaper, higher energy density, and longer-lasting battery technology has led to an explosion of research activities centered on new technologies such as Na-ion, K-ion, metal-air (Li, Na, Zn), Li–S, multivalent ions, and redox flux[60]. Research on Li-ion and Na-ion batteries started in the 1980s [4,31,61], NIBs have first been overlooked by LIB technologies due to their outstanding performance, and now there are commercialized by different companies such as Tiamat, Natron energy, Faradion or Hina Battery. More recently, K-ion batteries have attracted an increased interest of scientific communities [4,62].

The sodium-metal battery (SMB) is a new high-energy battery technology.[63,64] Due to its higher theoretical specific capacity (1160 mAh/g) and lowest redox potential (-2.714 V *vs*. standard hydrogen electrode), Na metal is used directly in this system as an exceptionally attractive anode. Due to their high theoretical energy densities, oxygen (O_2), carbon dioxide (CO_2), sulfur dioxide (SO_2), or sulfur (S) show considerable promising performance as cathode candidates (See Figure I-9). Four SMBs share similar cell designs, including Na-O_2, Na-CO_2,

Na-SO_2, and room-temperature Na-S (RT-Na/S) batteries, which couple metallic Na anodes with gaseous O_2, CO_2, SO_2, or solid S cathodes.

These cathodes can only exhibit high electroactivity when housed in porous conductive cathode hosts, which act as charge-mass-transfer media and reservoirs for the active materials O_2, CO_2, SO_2, and S but are not involved in electrochemical reactions. These SMBs are appealing because of their low price and extremely high theoretical specific energy [64].

$$Na + O_2 \leftrightarrow NaO_2 \rightarrow (1108 \frac{Wh}{Kg})$$

$$4Na + 3CO_2 \leftrightarrow Na_2CO_3 \rightarrow (1876 \frac{Wh}{Kg})$$

$$2Na + 2SO_2 \leftrightarrow Na_2S_2O_4 \rightarrow (863 \frac{Wh}{Kg})$$

$$2Na + S \leftrightarrow Na_2S \rightarrow (1273 \frac{Wh}{Kg})$$

However, because they are still in their early stage of development and rely on pure Na metal and liquid electrolytes, they suffer from major safety concerns as well as drawbacks like low reaction kinetics, high overpotential, poor cycle performance, and complex reaction mechanisms [63,64].

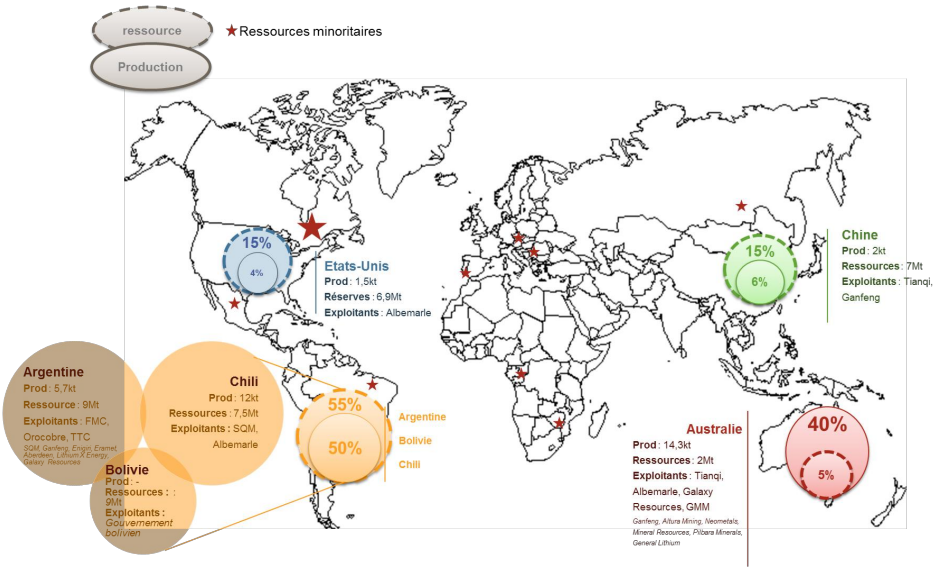

Figure I-8: Distribution of lithium world primary reserves (dotted circles) and production (solid circles)[65].

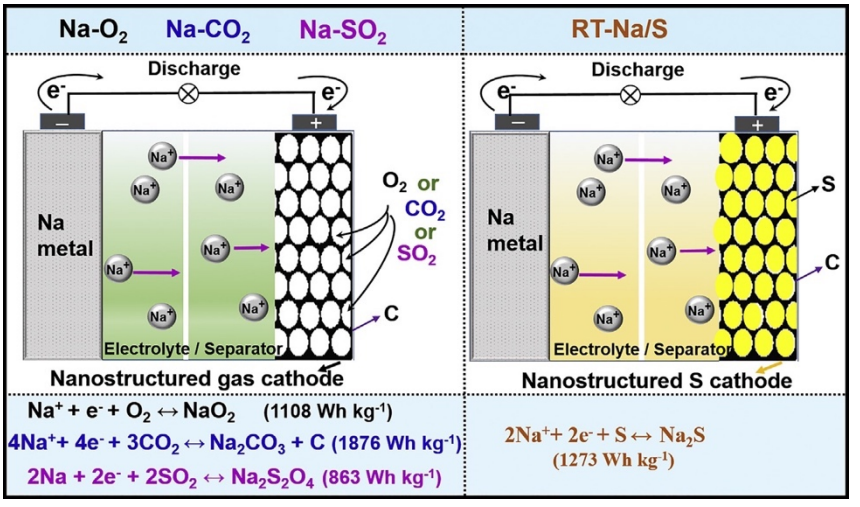

Figure I-9: Schematic Representations of SMBs Cell configurations of Na-O_2, Na-CO_2, Na-SO_2, and RT-Na/S batteries with cell chemistries and theoretical energy densities.[64]

4.1. Sodium-ion battery and potassium ion batteries

Both sodium and potassium are evenly distributed on the earth's crust, with a proportion 10 to 1000 times higher than lithium (Figure I-10). Firstly, criticized for being larger, heavier, and more reactive than lithium, both sodium and potassium are proving to be attractive candidates for the next generation of alkaline ion batteries. Indeed, these two elements have chemistry close to lithium and specific properties that counterbalance their disadvantage compared to lithium.

First, the energy density and the global cost of a battery cannot be calculated without counting all the elements that compose it. A major difference between Li and Na or K is that there is no electrochemical formation of alloy with aluminum for the two heavier ions. It is then possible to use aluminum foil as both cathode and anode current collector [4]. Therefore, cheaper and lighter batteries are expected for NIB and KIB technologies by avoiding the use of expensive elements such as Li, Co, and Cu.

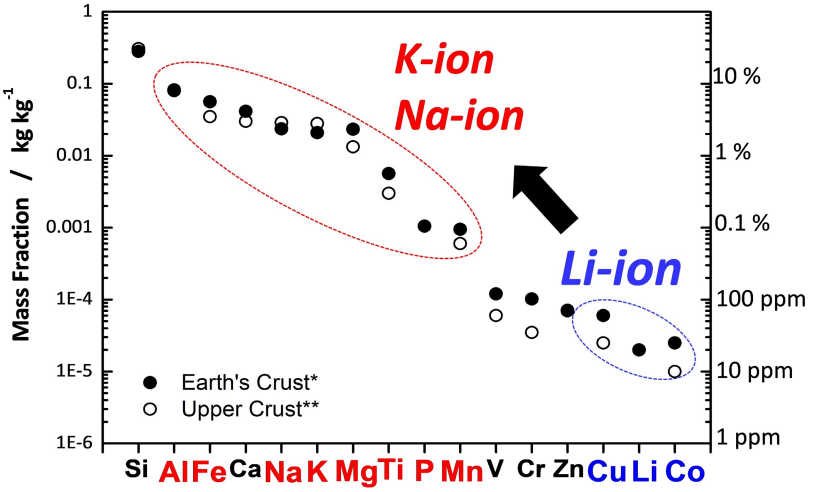

Figure I-10: Abundance of elements in Earth's crust [4].

Because of their larger ionic radii, KIB and NIB can seem unattractive. Figure I-11 presents the physical properties of the three ions. The standard potential of lithium is the lowest standard potential for metals, and this is one of the reasons for the high energy density of LIB. As a reminder, the energy is then calculated by multiplying the working voltage by the capacity. This only stands in aqueous conditions. Indeed in battery conditions, in propylene carbonate solvent, the potassium has potential even lower than Li^+. Studies also reported a potassium stripping/plating at -0.15V *vs.* Li^+/Li for KPF_6 in EC:DEC solution [4,66]. Therefore K-ion batteries have the potential to reach a high-voltage energy system as an alternative to LIB.

	Li^+	Na^+	K^+
Relative atomic mass	6.94	23.00	39.10
Mass-to-electron ratio	6.94	23.00	39.10
Shannon's ionic radii/Å	0.76	1.02	1.38
E^0 ($A^+_{aq.}$/A)/V vs. SHE	−3.04	−2.71	−2.93
E^0 (A^+_{PC}/A)/V vs. Li^+_{PC}/Li	0	0.23	−0.09
Melting point/°C	180.5	97.7	63.4
Desolvation energy in PC/ kJ mol^{-1}	215.8	158.2	119.2
Coordination preference of A^+ in $AMeO_2$	Octa-hedral and tetrahedral	Octa-hedral and prismatic	Prismatic

Figure I-11: Comparison of physical properties for Li^+, Na^+, and K^+ for secondary batteries [4].

Another important property of the battery system is the rate performance. This is linked to the ionic conductivity and transference number of the ion in the electrolyte. The transference number is defined as the ratio of the electric current derived from the cation to the total electric current. Na^+ has been reported to have a higher transference number than Li^+. This was evidenced in Na/Li hexafluorophosphate with EC:DEC solution [4,67]. Figure I-12 compares the ionic radius of the three alkali-metal ions. As expected, the Li^+ shows a lower

ionic radius of 0.68Å while Na^+ has 0.97Å and K^+ has a radius about two times higher of 1.33Å [68]. Nevertheless, Na^+ and K^+ have a smaller Stokes' radius in Propylene Carbonate (PC) due to their lower Lewis acidity. This tends to demonstrate higher ionic mobility of Na^+ and K^+ in electrolyte solution than Li^+ [69]. Therefore, replacing Li^+ with Na^+ or K^+ is expected to show superior transport properties than Li^+, thus allowing a higher current rate and mass loading of electrodes.

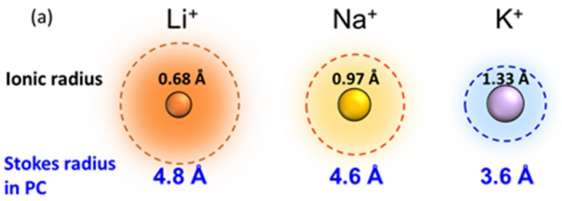

Figure I-12: Comparison of the ionic radius and Stokes radius in PC of Li, Na, and K ions [4].

For all these reasons, in addition to their lower cost and higher abundance, NIBs and KIBs are expected to reach the same performance or even higher than LIBS.

4.1.1. Anode material for NIBs and KIBs

To increase the energy density of future batteries, an optimum between high capacity and low insertion potential anode has to be found[70]. Different negative electrode materials have been developed for NIB and KIB technologies. Figure I-13 presents an overview of the recently reported materials. Among them, the carbon-based and the alloying materials show better and more promising prospects.

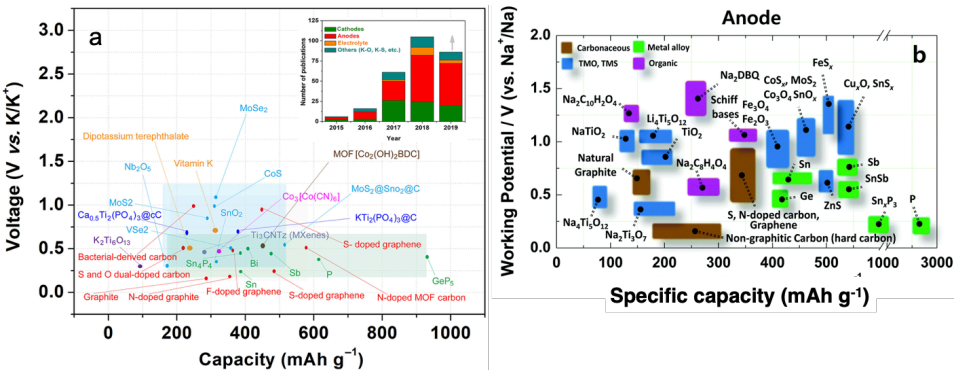

Figure I-13: Recent research of anode materials for (a) Potassium-ion [71] *and (b) Sodium-ion batteries* [72].

a. Carbon-based materials

Graphite is the reference anode material for LIB systems because of its low cost and good properties[73]. Unfortunately, non-modified graphite cannot intercalate sodium, contrary to potassium, which has shown great reversibility and good performance using graphite as anode material. Indeed, the capacity of 273 mAh/g [74] has been reported, which represents 87.5% of the theoretical capacity. Recently, some articles presented the possibility of inserting Na into graphite through co-intercalation reactions [75,76]. The reaction of potassium with graphite leads to the formation of KC_8, which induces a lower alkali to carbon ratio than in lithium, but enables the simple transfer of the anode material commercialized in LIBs to the future KIBs [66]. Unfortunately, the insertion of potassium in graphite is also associated with a huge volume expansion of 1.61 times its initial volumes, which can lead to a poor cycle life [4].

Hard carbon is electrochemically active for the three alkali-metal ions[74,77–83]. Figure I-14 shows the typical charges discharge profiles of Li, Na, and K insertion into hard carbon. The Li^+ (i) and K^+ (ii) show the same insertion profile, with a reversible capacity of 215 mAh/g. The Na^+ (iii) shows, in its case, a different profile with a sloping curve until 0.15 V, followed by a long insertion plateau at around 0.1 V, leading to a reversible capacity of 262 mAh/g. By optimizing the hard carbon, for example, by heat treatment of activated carbon at 2100°C,

a reversible capacity of about 420 mAh/g is achievable[84]. Kano *et al*., reported a similar process with a reversible capacity of more than 435 mAh/g[85]. It is still believed that better capacity can be achieved by optimizing this hard carbon. It is to note that, in the case of NIB and KIB, the result can be obtained using either a copper foil as the current collector or aluminum foil. The substitution of copper for aluminum has the great advantage of reducing both the global weight and cost of batteries.

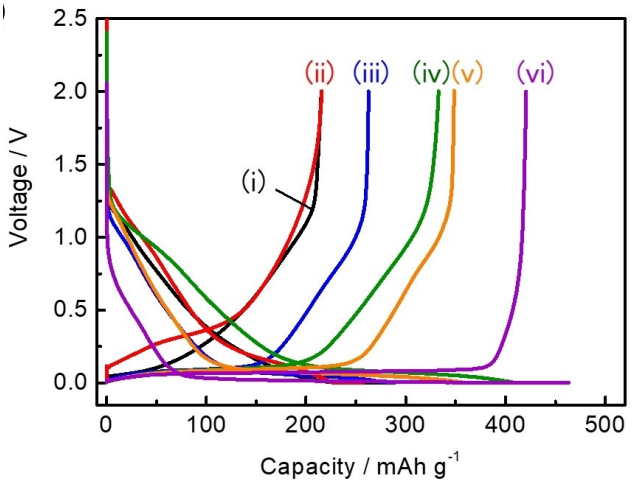

Figure I-14: Charges/discharge profiles of commercial hard carbon (Carbotron) in (i) Li Cell, (ii) K cell, (iii) Na cell, (iv) Na-cell with Argan hard carbon, (v) Na-cell with cellulose hard carbon, and (vi) Na-cell with activated carbon heat-treated at 2100°C.

b. *Alloying and conversion materials*

As already mentioned, alloying materials are generally characterized by a huge capacity. Silicon is one of the most interesting alloying materials for LIBs and has also attracted attention for its uses in NIBs and KIBs. Reversible capacities of 160 mAh/g and 510 mAh/g have been reported for the insertion of Na and K in silicon, respectively[4,86,87]. It is far more than 1300 mAh/g generally obtained for Li alloying with Si, but for the KIBs, it is already two times the obtained capacity with graphite. Another interesting alloying material is the antimony

which has proved its efficiency in both NIB and KIB, leading to capacities of 655 mAh/g and 660 mAh/g, respectively [88]. The expected problem of huge volumetric expansion still has to be solved in both cases [88]. Some transition metal oxide (TMO) or transition metal sulfide have also been tested for NIB and KIB, for example, Co_3O_4 and Fe_2O_3. These materials are also associated with the different problems of volume expansion and nanosizing of metallic particles, as explained. However, the TMS compound benefits from a weaker metal-sulfur bond, and the reversibility is better than in TMO, leading to better cycle life [72].

4.1.2. Cathode

The same aim of increasing the energy density of the battery has guided the research around the development of new cathode materials. Figure I-15 presents the recent cathode materials. These materials can be divided into four main categories: layered oxide compounds, organic compounds, Prussian blue analogs, and polyanionic compounds. This research of cathode materials has been hugely inspired by previous research on LIBs and also NIBs for the KIBs.

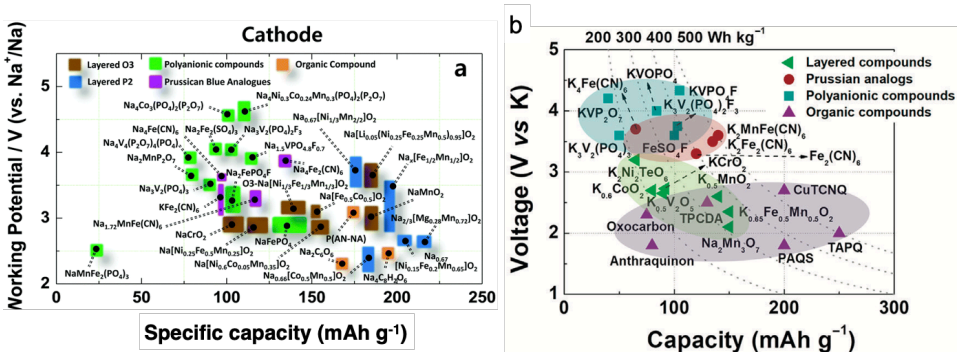

Figure I-15: Recent research of anode materials for (a) Sodium-ion batteries [72] *and (b) Potassium-ion* [89].

a. Layered oxide compounds

The typical structure of A_XMO_2 phases (A= Li, Na, K, and M= a transition metal, $x \leq 1$) is described as stacked layers of MO_6 sharing corners and with the alkali metal inserted between those layers. The alkali metal is on specific sites depending

on its nature, quantity, and synthesis method. A notation system was proposed by Delmas *et al.*, in 1980, to define the different structures. A schematic presentation of the layered oxide structure is presented in Figure I-16. The notation P is given for a material in which the alkali is in a prismatic site, and the notation O for an octahedral site. The numbers after the letter define the number of sheets per unit cell. Among the layered oxide for the KIBs, K_xCO_2 [90] has a reported capacity of 60 mAh/g with a potential window of 2-3.9 V, $K_{0.3}MnO_2$ [91] has a better capacity (110 mAh/g) but with really low capacity retention, and $K_{0.7}Fe_{0.5}Mn_{0.5}O_2$ gives a better capacity of 125 mAh/g, but the working potential is only 2.2 V [92]. In the case of NIB, some compounds, such as Na_xCoO_2[90] and $NaMnO_2$ [93–95] are also reported, but all these materials suffer from the same drawbacks. Despite their promise, in theory, their experimental capacity is low, as is their operating voltage. Moreover, their sensitivity to air and humidity leads to manufacturing problems. Some A-rich materials have also been developed, but the problem of stability is still observed [96].

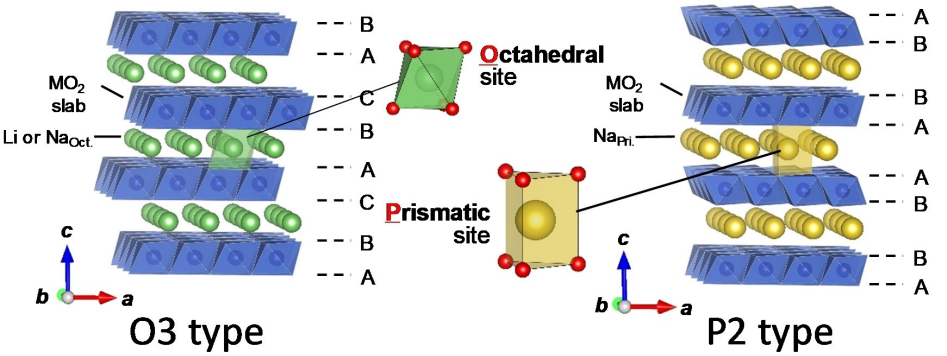

Figure I-16: Schematic illustrations of an O3 and P2 type structure [4]

b. Organic compound

Organic compounds have a flexible structure with large crystallite holes suitable for receiving larger ions like K^+ or Na^+ [97]. Perylene-3,4,9,10-tetracarboxylic dianhydride (PTCDA) and Poly-Anthraquinone Sulfide (PAQS) can be mentioned here as a reversible capacity of 130 mAh/g and 200 mAh/g can be obtained in KIBs[98,99]. PAQIS has been reported for NIBs with a reversible

capacity of 190 mAh/g with a capacity retention of 93% after 150 cycles [100]. Recently, polydopamine stabilized by grafting sulfonate groups has been reported for both LIBs and KIBs, showing storage capacities of 206 mAh/g and 82 mAh/g, respectively, at high current density of 1000 mA/g [101]. The disadvantage of these materials is the low voltage which makes them poor candidates in terms of energy density despite their viability and high capacity. In addition, these materials do not contain native potassium or sodium, which implies a precycling of these materials, which is difficult to set up within an accumulator.

c. *Prussian blue analogs*

The Prussian blue is a hexacyanoferrate ($Fe_4[Fe(CN)_6]_3$) compound that was at the origin used as a pigment. It is a non-toxic compound despite the presence of extremely stable cyanide groups. The Prussian blue analogs have a general formula $A_xM1[M2(CN)_6]_y .nH_2O$, where A is an alkali metal and M1 and M2 are transition metals. The typical open 3D cubic framework of Prussian blues analogs is presented in Figure I-17. The transition metals are coordinated octahedrally by the cyanide and have large diffusion tunnels suitable for the mobility of Na^+ or K^+ ions. The PBAs have attracted much interest as cathode materials for NIBs and KIBs [62,102–105].

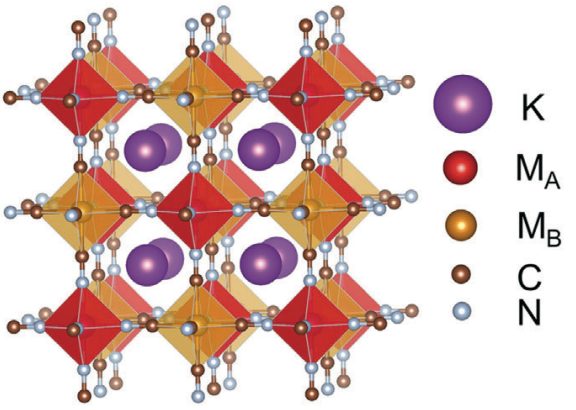

Figure I-17: Typical crystal structure of PBAs [89]

The influence of the transition metal [102], of the $[Fe(CN)_6]$ vacancies[106], the amount of Na [106–108], and water content in the interstitial site[109] has been widely investigated and are known to influence the electrochemical performance of the material.

In 2004, the first report of $KFe^{III}[Fe^{II}(CN)_6]$ (Prussian blues analog) used in KIBs was done by Eftekhari[62] in a thin film configuration. It can either be oxidized in the Prussian green $Fe^{III}[Fe^{III}(CN)_6]$ or reduced in the Prussian white $K_2Fe^{II}[Fe^{II}(CN)_6]$. Since that, the use of PBAs has been reported many times. The PBAs ($K_2Fe[Fe(CN)6].2H_2O$ [110], $K_{1.89}Mn[Fe(CN)_6]_{0.92}.0.75H_2O$ [111], and $K_{1.75}Mn[Fe(CN)_6]_{0.93}$. $0.16H_2O$ [112]) under powders forms have for example exhibit a reversible capacity of 120–140 mAh/g. Those results prove the interest of the PBAs as high energy density materials for KIBs and NIBs [111,112]. These materials are sensitive to synthesis, and a small change can significantly impact the electrochemical performance.

The Altris company in Uppsala aims to build a cathode material factory with an annual production of 2000 tons of Prussian Blue/White analog and to take the following steps for commercial production of sodium-ion batteries.

d. Polyanionic compounds

Polyanionic materials have been widely studied since the discovery by Padhi and Goodenough of Li insertion in $LiFePO_4$[113]. This material is of great interest for the next generation batteries due to their high capacity, excellent thermal and chemical stability, and long cycle life. Plenty of different polyanionic compounds have been reported made of sulfate[114–116], pyrophosphate[117–120], silicate [121], and phosphate [122–125]. The thesis aims the development of phosphate-based cathode materials thanks to their attractive performance and high stability. In the next section, we will present a quick overview of the polyanionic compounds made for NIBs and KIBs cathode materials, focusing on phosphate-based materials as they are the most widely studied materials of this kind.

- For NIBs Cathode

Polyanionic compounds have attracted a lot of interest in the past decades for NIBs. Figure I-18 present an overview of the different compounds. One of the best-known materials is the $Na_3V_2(PO_4)_2F_3$. It has attracted a lot of interest over the past years [122,124-128] due to its high theoretical capacity of 192 mAh/g, its high working potential of about 3.7 V and 4.2 V leading to a high theoretical energy density of 500 Wh/kg similar to LFP [131]. It has a Na^+ Super Ionic CONductor structure (NASICON) and crystallizes in a tetragonal crystal shape. Its structure (Figure I-19) presents large interstitial spaces that allow the fast diffusion and mobility of Na^+ ions inside the structure. The dioctahedral unit of VO_4F_2 is bridged with $V_2O_8F_3$ by the fluorine atoms and the oxygens are connected through the phosphate group. The inductive effect of both phosphate and fluorine increases the working potential of this material, but the space between the vanadium atoms in the structure, due to the large phosphate group, induces a poor electronic conductivity of the material[132]. This material is already used in commercial or nearly commercialized batteries. For example, the French company Tiamat successfully uses this cathode material.

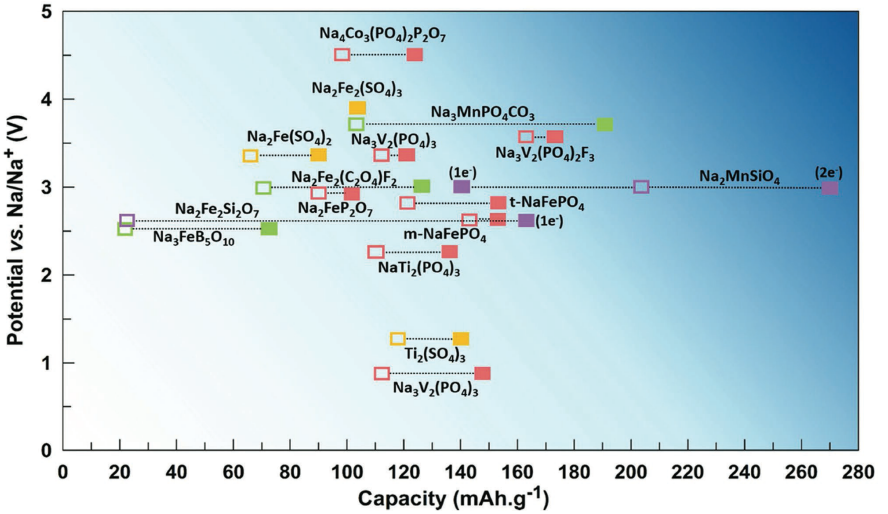

Figure I-18: Overview of reported polyanionic compounds for Na-ions batteries [133].

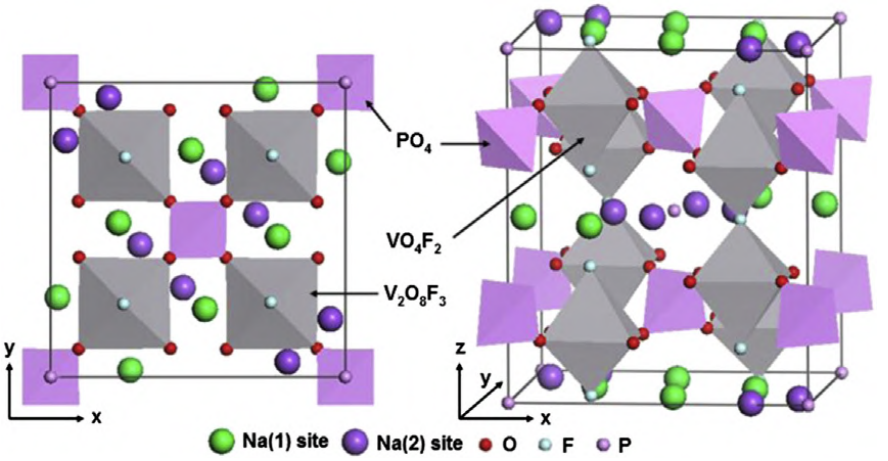

Figure I-19: Crystallographic structure of $Na_3V_2(PO_4)_2F_3$ material [134].

Other fluorophosphate-based materials have been developed. For example, $NaVPO_4F$/C made by hydrothermal synthesis shows 121 mAh/g at 3.7 V [135], Na_2MnPO_4F/C made by ball-milling shows 120.7 mAh/g[136], Na_2CoPO_4F shows 100 mAh/g at 4.3 V when made by solid-state reaction [137].

Despite these outstanding properties, problems of price and toxicity of the transition metal (except for the manganese) remain a major limitation. Another eco-friendly material has also been developed, which is Na_2FePO_4F(NFPF). First discovered in 2007 by Ellis *et al*. [138], its eco-friendliness due to the iron replacing cobalt or vanadium has rapidly made it attractive. It presents good electrochemical properties (124 mAh/g and 3 V) and excellent stability upon cycling, the volume expansion between the desodiated and pristine phase is only 4% [139].

Figure I-20 shows the orthorhombic structure of the NFPF material. The space group is Pbcn, and the iron atoms are coordinated from 2 fluorine atoms and 4 oxygen atoms, making an octahedral unit. These octahedra are connected by pairs sharing a face, and these dioctahedral units are connected to the others by corners along the *a* directions and to the tetrahedral phosphate by other corners along the *c* directions. These connections make the rigid structure of the NFPF materials. Between those layers are found two crystallite site of Na that shows a facile

diffusion in bidimensional pathways along the ac plane [140,141]. This material has been investigated for LIBs [142–146] and NIBs [138,145–148], demonstrating great performances. More details about the performance of this material are reported in chapter 2. In this dissertation, we present an optimized synthesis method of NFPF/C composite and its application as cathode material in NIBs and KIBs (chapter2). In chapter 3, the cycling mechanism of the reaction of this material both in NIBs and KIBs using *operando* X-ray diffraction combined with *operando* Mössbauer spectroscopy is presented.

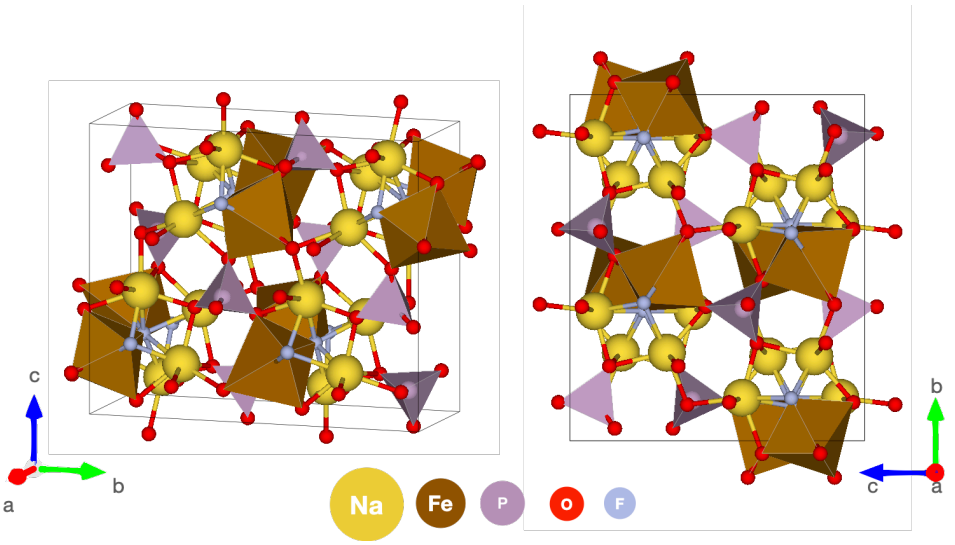

Figure I-20: Crystallographic structure of Na_2FePO_4F.

- For KIBs Cathode

The promising results obtained with polyanionic compounds for LIBS and NIBs have motivated researchers to study these compounds for K-ion batteries. Figure I-21 presents an overview of the polyanionic compounds reported in the literature and compares the theoretical performance to the experimental one.

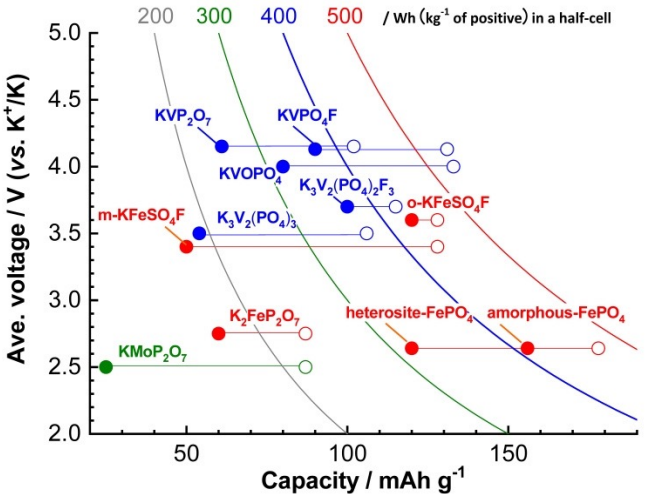

Figure I-21: Overview of polyanionic compounds developed for K-ion batteries cathode materials. The empty circles represent the theoretical performance, while the filled circles represent the reported experimental capacities [151].

The first reported polyanionic material for KIBs was reported in 2012 by Recham *et al.* [114]. It was an iron fluorosulfate ($KFeSO_4F$) obtained by electrochemical oxidation. A few years later, Lander *et al.* showed that this material has two distinct structures: one orthorhombic (Figure I-22a) and one monoclinic (Figure I-22b), and argued that the orthorhombic structure enhances the K^+ mobility due to a less dense structure with larger diffusion channels [115]. This led to an enhancement of the initial discharge capacity reaching 110 mAh/g at the first cycle. Nevertheless, the stability upon cycling is quite low.

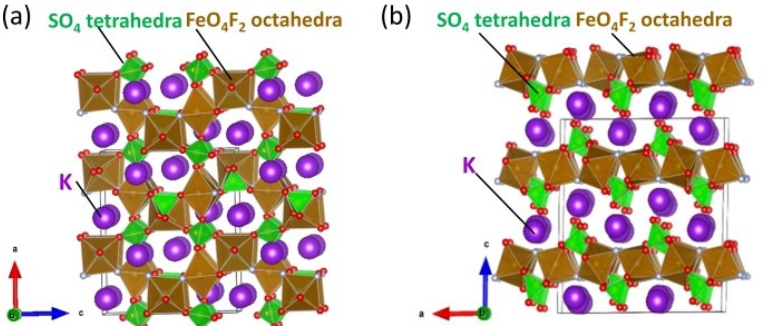

Figure I-22: Polymorphs structure of a) orthorhombic KFeSO4F and b) monoclinic KFeSO4F [151].

Another study shows that the K^+ is reversibly inserted in amorphous $FePO_4$ [152], but as the study of Recham *et al*., this study is more focused on crystal chemistry than on the development of cathode materials for KIBs. Other works focus on developing new cathode materials that emerged a few years later. Among them is the development of NASICON-type $K_3V_2(PO_4)_3$/C that can be used either as the anode, in the potential window of 1-2.5 V, but also as the cathode in 2.5 -4.0 V. This property has been used to make a full symmetric cell by Zhang *et al.*, with a capacity of 70 mAh/g over 500 cycles and working potential of 2.3 V [153]. More recently, Lin *et al.,* reported the electrochemical synthesis of $K_3V_2(PO_4)_2F_3$ as a cathode material for KIB [154]. This synthesis was based on ion exchange of NVPF by potassium, as shown in Figure I-23. The obtained KVPF has shown competitive performance with a voltage of 3.7 V and a reversible capacity of 100 mAh/g. This material was tested in a full cell against graphite and demonstrated good performance.

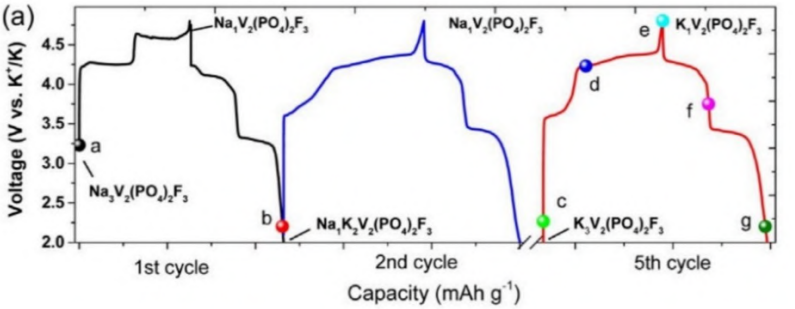

Figure I-23: Charges/discharge curves of the potassiation of Na3V2(PO4)2F3 materials [154].

This work developed a new cathode material based on vanadium and phosphate ($K_3V(PO_4)_2$). It has an increased K/V ratio that enhances the theoretical capacity of this kind of material (chapter 4). In chapter 5, the vanadium of the KVP materials is replaced by iron to make it eco-friendlier and cheaper.

5. The spray drying synthesis and shaping techniques

The performance of the polyanionic compounds both for NIBs of KIBs make them materials of choice for the next generation batteries, but their complex structure and stoichiometry make their synthesis quite hard and challenging. All the materials present in this work have been synthesized by the spray-drying method. In this section, the advantage and issues of this technique, as well as the influencing parameters for the synthesis of our material will be discussed.

Spray-drying is commonly found in food or pharmaceutical industry for powder production. It has recently expanded to synthesize or shape electrode materials for rechargeable batteries. One of its strengths, compared to other synthesis techniques, is the easy upscaling with the conservation of the microstructural properties [153]. This technique is based on the atomization of fluid into small droplets and the dehydration of these droplets with hot gas to obtain a powder. The size, shape, and agglomeration degree can be controlled by playing on the composition of the injected suspension (or solution) and the drying parameters such as pressure, temperature, nozzle type, and injection rate. It is an economical, continuous, and fast process with high versatility and control of the obtained particles. Furthermore, it is also suitable for heat-sensitive products as the exposure time is really short [154].

The schematic functioning of the spray dryer is represented in Figure I-24. A liquid is injected into the drying chamber in the form of a spray. This liquid can be a solution or a suspension or an intermediate suspension into a solution. This spray enters in immediate contact with a hot gas stream (generally air). The solvent of each droplet is evaporated in the drying chamber leading to the formation of dry powder in hot wet gas. This powder is separated from the gas stream into a cyclone, and the dry powder can be recovered. In the case of the use

of another gas than air, the wet gas can be recycled after being dried in a condenser, filter, and reheated. This is illustrated in Figure I-30 a and b. The drying mechanism has three main stages: atomization, evaporation of the solvent, and separation of the dry powder from the gas stream. In this work, a GEA Niro Mobile Minor spray-dryer has been used. Figure I-25 shows a picture and the dimensions of the device used in this thesis.

5.1. General principle

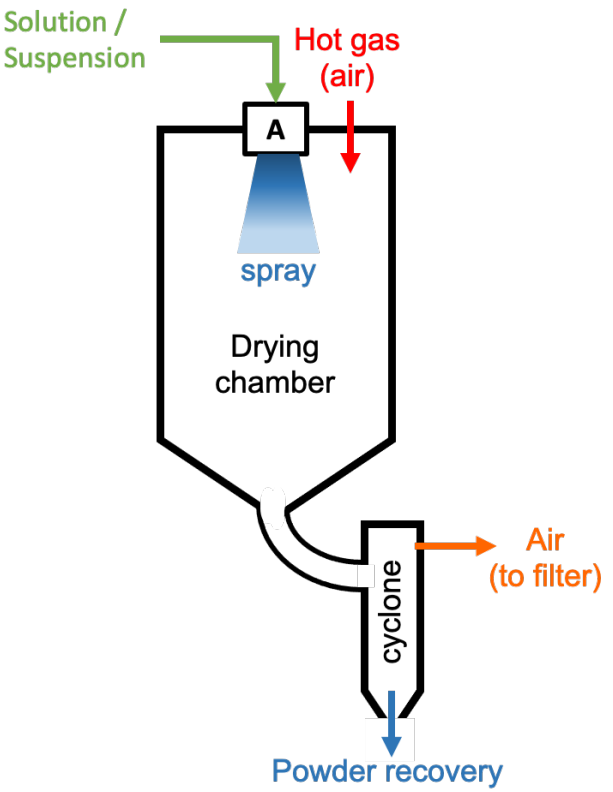

Figure I-24: Schematic representation of a spray-dryer in co-current configuration [153].

Overall spray-dryer size	Drying chamber
Length = 180cm Width = 130cm Height = 192cm	Diameter = 80cm Height of the cylinder = 62cm

Figure I-25: Picture of the GEA Niro Mobile minor spray-dryer used in this work and overall dimension of the equipment.

5.2. The atomization

This step is the transformation of the liquid into an aerosol. This step directly influences the final powder's physical properties (size, morphology, agglomerate…) [155]. The ideal aerosol is made of individual small identical droplets. In this perfect case, the drying time is the same for each drop, leading to the most homogeneous characteristics of the obtained particles. To form an aerosol from a liquid, an atomizer is necessary: it is the instrument that will give the energy to transform the liquid into droplets. Among the different atomizers,

three main technologies exist, the rotary atomizer uses centrifugal force to form droplets from a liquid, the bifluid atomizer, and the pressure atomizer uses a pressured gas to form an aerosol. The difference between these last two is that in the case of bifluid, the two fluid are separated and joined at the outlet of the nozzles, where the pressure atomizer use the same tube for both the liquid and the pressured gas.

5.2.1. Rotary atomizers

This type of atomizer uses centrifuge energy to form droplets from a liquid. It is made of a rotating disk that turns at high speed using compressed air. It is to note that the air used in this case never enters in contact with the fluid. The fluid is injected at the center of the disc, immediately accelerated to high speed, and passes through the channel to be disintegrated into droplets at the nozzle outlet in the drying chamber [154]. The droplets' size depends on the nozzle's peripheral speed (or the rotational speed), the flow of the injected liquid, and the properties of the fluid (viscosity, for example). This type of nozzle can only be used in a co-current configuration, meaning that the liquid and the drying gas are injected in the same way. The main drawback of this nozzle is that the aerosol is formed perpendicularly to the drying chamber leading to more waste as the drops can stick to the surface of the chamber. Figure I-26 shows a rotary nozzle and illustrates its functioning.

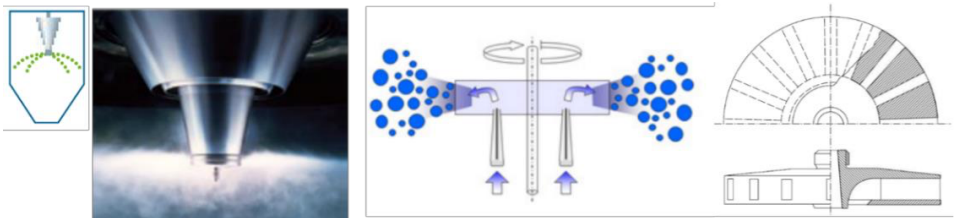

Figure I-26: Rotary nozzles atomizer and illustration of its functioning [156].

5.2.2. Two-fluid nozzle or bifluid nozzle.

The bifluid nozzle uses kinetic energy to form the droplet. The liquid and the drying gas follow two separate trajectories. The aerosol is formed by the contact of the liquid phase with the high speed and pressured gas, so the shear forces exerted by the gas on this liquid. This gas is not the same as the drying gas. Its only duty is to form the droplets. This type of atomizer generates smaller particles than the rotary nozzle and is more suitable for a heat-sensitive compound. The droplet size depends on the pressure injection (up to 7 bars), the size of the nozzle hole, the flow of the injected liquid, and the properties of the liquid. It can be used in the co-current configuration, as explained before, or in the counter-current configuration. In this case, the liquid is injected at the opposite side of the drying gas stream. It is called the fountain mode, and it is used for highly charged suspension with high viscosity, which often leads to larger particle sizes. The residence time in the drying chamber is much longer, so the product spray-dried must not be sensitive to heat. The two-fluid nozzles are illustrated in Figure I-27 showing both the co-current configuration and the fountain mode.

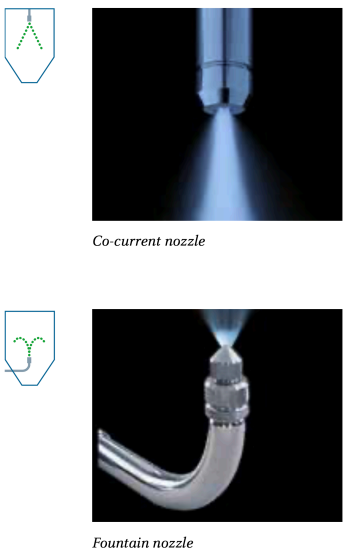

Figure I-27: Two-fluid nozzle in co-current configuration(top) and counter-current configuration (bottom) [157].

5.2.3. Pressure nozzle.

The principle of this nozzle is the same as the bifluid nozzle: it uses kinetic energy to form the droplets. In this case, the liquid is pressurized with compressed gas in the same pipe. The fluid is accelerated due to the high pressure (20-200 bars) and is immediately disintegrated to form droplets at the ejection point of the nozzle. The influencing parameters are the same as for the bifluid nozzle. It requires a bigger drying chamber and is limited to the drying of non-viscous liquid without big particles in it. Furthermore, the installation requires a high-pressure pump and other equipment and is therefore not often used at the lab scale. The main advantage of this injection mode is that the obtained particles have a narrower size distribution.

Figure I-28 shows the particle size distribution obtained under comparable conditions with different injection modes. The Combi-Nozzle® is described as a mix between the pressure nozzle and the two-fluid nozzle. It leads to a smaller particle size with a narrow distribution. The two-fluid nozzle leads to the largest particle size distribution, but the mean diameter is the smallest in co-current configuration. On the contrary, the pressure nozzle has a narrower distribution of size but a larger mean diameter. The rotary nozzle has an intermediate result between these two extremes. Also, the fountain mode or counter-current leads to a larger mean diameter.

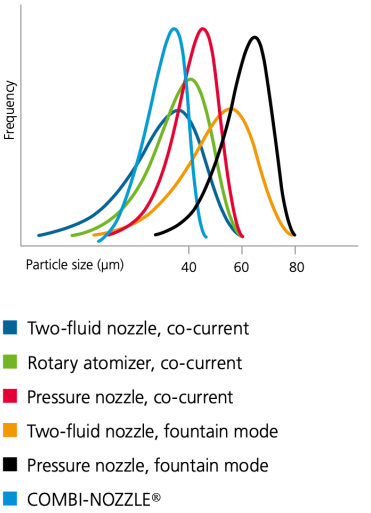

Figure I-28: Particle size distribution with different atomization systems [159].

In this work, we have compared the synthesis of NFPF using a rotary nozzle and bifluid nozzle in chapter 2. The synthesis of KVP and KFP materials is made using the bifluid nozzle. All the syntheses are made in a co-current configuration.

5.3. Drying mechanisms

When the droplets are formed, they will contact the drying gas. The drying mechanism is illustrated in Figure I-29. The first drying step is the increase of concentration of the solid particles inside the droplets due to solvent evaporation and a diminution of the droplet size for the same reason. When the droplet has reached the saturated concentration, a precipitation phenomenon occurs, beginning from the outside, due to the speed of drying that overcomes the gradient force. At this step, the particles are like a core-shell with a wet core made of the solution highly concentrated and the shell made of already precipitated particles. A second step of the drying process begins. The temperature of the particles increases because the evaporation, which consumes the energy, is limited due to the presence of the shell. If the surface is porous, the pressure inside the particles decreases, and the morphology and size are now fixed. If the shell is not porous or not porous enough, the pressure inside the particles increases rapidly, leading

to an inflation of the droplet or, in the worst case, destruction of the shell of the particles[160]. The particles are now dried, and the only remaining solvent is linked chemically to the crystal and is not removable by drying[161–163].

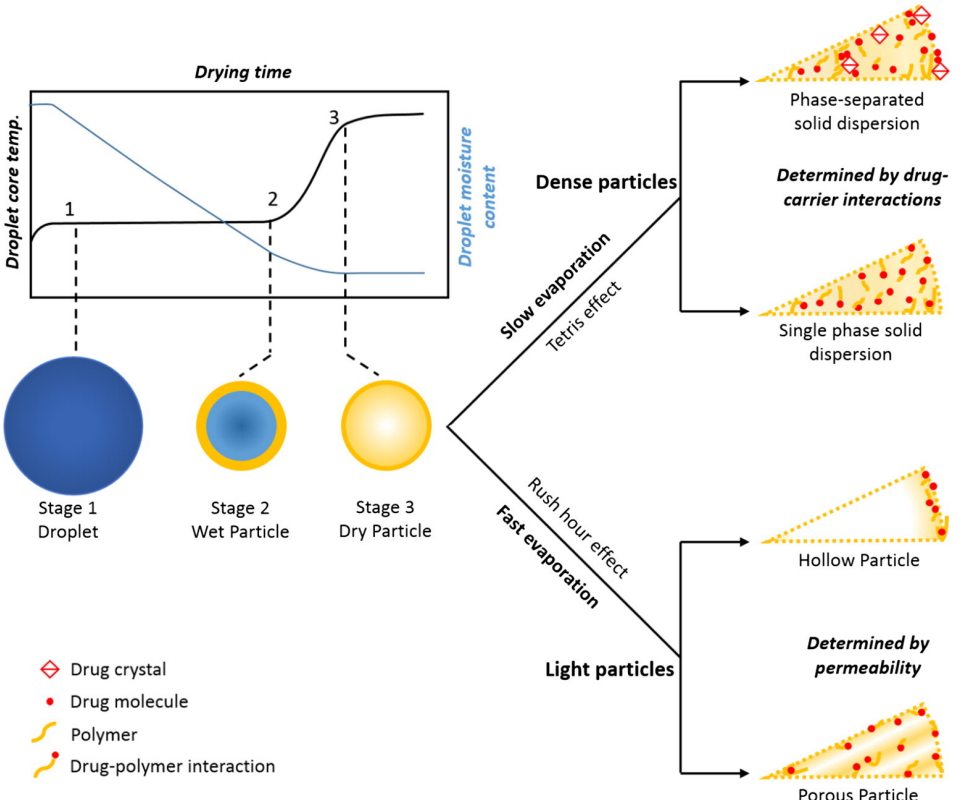

Figure I-29: Drying step during the spray-drying [161].

5.4. Powder recovery

The particles can be recovered at different points, depending on their mass and morphology, as shown in Figure I-30a. For now, the powder is in suspension in the gas stream. The first collection point is at the bottom of the drying chamber and is used to recover particles not carried in the gas flow due to their size and mass. Then the flow of charged gas is conducted to a cyclone (Figure I-30b). The cyclone is a separator of particles that uses centrifugal forces. The powders and the air goes into it tangentially, with equal speed. The particles are exposed to

centrifugal force due to a vortex movement of the flow and push on the walls of the cyclones. This phenomenon induces a reduction in the speed of the particles that are not in the flow of gas anymore. The particles fall into a pot at the base of the cyclone, and the airflow rises along the same axis to continue towards the next recovery. Indeed, if the cyclone is powerful and widely used due to its ease of functioning, it cannot recover all the particles. The recovery in the cyclone depends on the residence time of the gas in the cyclone and the particles' size, weight, shape, and density. The final recovery step is a filter that can recover the nanosized and light particles. The gas is completely discharged of particles after this step.

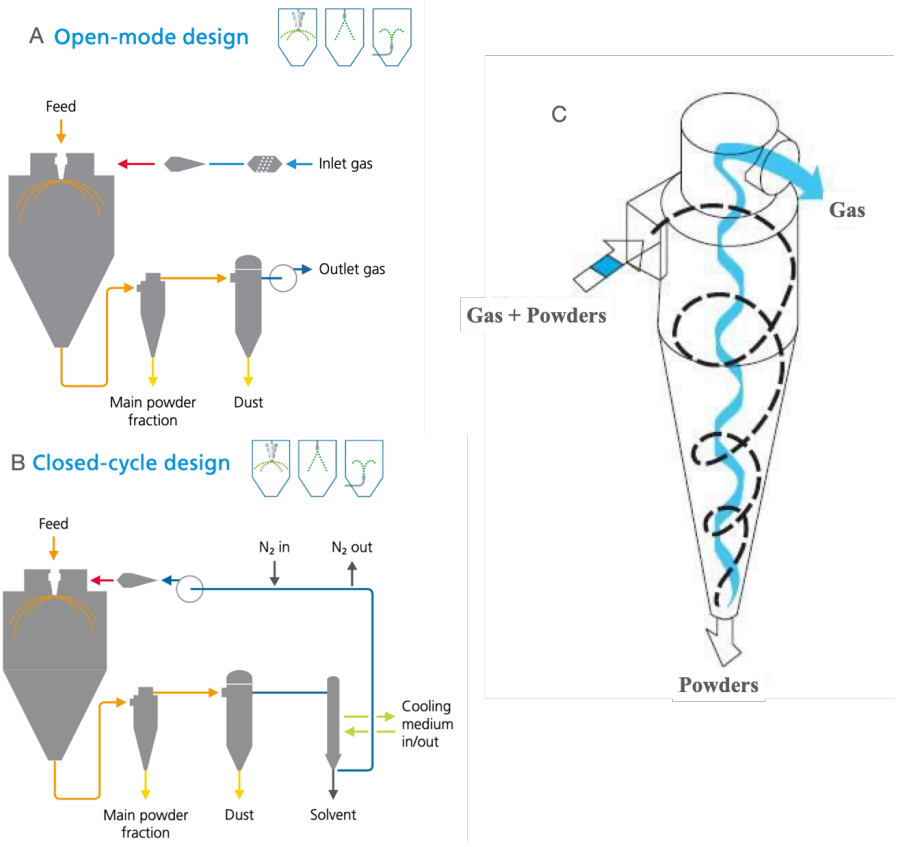

Figure I-30: A) Dry powder recovery in open cycle design, B) in closed-cycle design, C) Schematic representation of a cyclone used to separate particles from gas [157,162].

5.5. Morphology and shape of the particles

Spray-drying is a highly versatile method that can be tuned to obtain different sizes and shapes of particles, as shown in Figure I-31. It is well established that the morphology of the particles has a significant influence on the properties of the materials, including the secondary batteries field [155]. The first parameter that can influence the morphology is, for sure, the injected liquid properties. Indeed, different morphologies will be obtained using a solution or suspension and even with a mixed suspension in a solution. The type of solvent, the presence of additive or structuring agent, and the viscosity of the fluid, all these parameters strongly influence the formation of the droplet and so the final morphology. Regarding the spray-drying, the parameters such as injection flow, air pressure, type of nozzle, and temperature can give a good control to obtain the desired morphology and properties of the powders. All these parameters mainly influence the droplet size. For example, the higher injection pressure leads to smaller droplet size, and the higher viscosity of the injected liquid leads to bigger droplet size. At the formation of the droplet, the particle shape is a sphere cause it is the most stable form. This spherical form can generally be conserved, and it is the most encountered morphology. In the case of the injection of a suspension of the solid particle in a solution of precursor, different morphologies can be obtained, depending on the size of the component. If the component size is almost the same: a well-mixed component can be obtained. If the size is different, encapsulated particles can be obtained. If the solid particle can be removed by thermal or chemical treatment, porous particles are obtained. In the case of the addition of carbon nanotubes, the spherical shape is not recovered, and the obtained morphology looks like a deflated balloon due to the reticulating effect of the CNT [124,165]. Also, this shape is hairy because the CNTs are linked to the surface. To conclude, spray-drying allows the preparation of well-controlled particles with high reproducibility. The morphology can be tuned to respond to the desired properties

of the final product by playing either on the spray-drying parameters or the injected fluid.

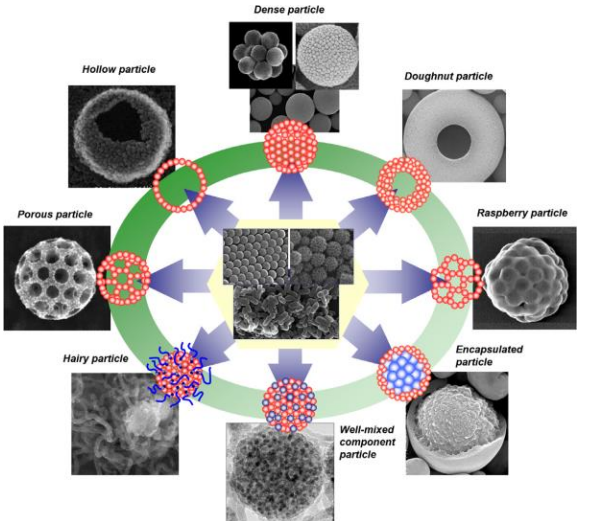

Figure I-31: Different morphology of particles obtained through the spray-drying process [164].

The spray-drying has been used in this work thanks to its versatility and advantages mentioned above, as it allows the simple, continuous, and rapid production of our material. In contrast, conventional solid-state synthesis often uses multistep for the synthesis of polyanionic compounds.

6. Thesis Overview and Aims

This thesis aims to develop new, eco-friendly, cheap, and performant cobalt-free phosphate-based cathode materials for Na-ion and K-ion batteries. Spray-drying technique was mainly used to prepare the materials by taking advantage of its great versatility, to propose an enhancement of the properties of existing materials, and synthesize new cathode materials at a pilot scale. After the general introduction (chapter I), the work carried out in this thesis is mainly divided into two main parts:

The first part (Chapters II and III) concerns the enhancement of the electrochemical performance of Na_2FePO_4F cathode materials in Na-ion and K-ion batteries. The second chapter presents the optimization of the synthesis of NFPF by playing on the spray-drying synthesis parameters and preparing a composite with carbon nanotubes (CNT). Several developments were done to avoid the reduction of iron during the annealing step, to finally obtained pure and well-crystalized material with optimized morphology. The performance of this material has been greatly enhanced, and the theoretical capacity has been obtained in NIB. The performance in KIB is also presented, and a precycling of the material has allowed it to reach more than 110 mAh/g in KIB half cells.

Chapter III focuses on the study of the cycling mechanism of NFPF in both NIB and KIB and the comparison of both reactions mechanism during cycling. *Operando* Mössbauer spectroscopy and *operando* XRD analyses were performed and combined to have more insights on the evolution of the structural properties of the materials during charge/discharge processes.

The second part focuses on the synthesis and development of new cathode materials for K-ion batteries using spray drying method. Indeed, the preparation of three new electrode materials for cathode for K-ion batteries was carried: $K_3V(PO_4)_2$, $K_3Fe(PO_4)_2$, and $K_3Fe_2(PO_4)_3$.

Chapter IV presents the development of $K_3V(PO_4)_2$ materials as a new cathode for KIB. The optimization of the synthesis and, therefore, of the morphology of the materials is discussed. Also, several composite materials were prepared with carbon nanotubes, graphene oxide, or a mix of both. The influence of the carbon addition on the structural and morphological properties of the composite materials was investigated. Finally, the influence on the electrochemical properties is analyzed for each material: the impact on the conductivity of the cathode materials was investigated using electrochemical impedance spectroscopy, and the effect of the energy storage was studied using galvanostatic cycling.

Chapter V presents a preliminary study of both $K_3Fe(PO_4)_2$ and $K_3Fe_2(PO_4)_3$ as new potential active cathode materials for KIB. The development of an easy synthesis process by spray-drying is presented for both materials. For both materials, the influence of complexing agent addition on the synthesis, structure, and morphology, as well as on the electrochemical performance, is deeply analyzed. The strategies used to prepare composite material with CNT are also presented, but the synthesis of the materials needs calcination under air, which complicates the addition of carbon to enhance the conductivity of the phosphate. Also, for KFP_3 materials, several iron precursors were tested and compared to obtain a better electrochemical performance.

Finally, I would like to attract your attention to the annexed chapter, Appendix 1, which concerns an entirely different subject linked to the pandemic that began almost two years ago (at the time of this thesis writing) and is such a big part of my Ph.D. formation. Indeed, using the spray-drying techniques, we have successfully synthesized the reactive materials that extract the SARS-COV2 RNA from the sample before the RT-PCR test, which lead to the production of about 10 million tests for Belgium. Moreover, we will see that this synthesis method may also be useful to stabilize this material as an anode material in LIB.

7. References

[1] World Health Organization, COP26 Special Report on Climate Change and Health. The Health Argument for Climate Action, 2021.

[2] D. Larcher, J.M. Tarascon, Towards greener and more sustainable batteries for electrical energy storage, Nat Chem. 7 (2015) 19–29. https://doi.org/10.1038/nchem.2085.

[3] T. Hosaka, K. Kubota, A.S. Hameed, S. Komaba, Research Development on K-Ion Batteries, Chem Rev. 120 (2020) 6358–6466. https://doi.org/10.1021/acs.chemrev.9b00463.

[4] K. Kubota, M. Dahbi, T. Hosaka, S. Kumakura, S. Komaba, Towards K-Ion and Na-Ion Batteries as "Beyond Li-Ion," Chemical Record. 18 (2018) 459–479. https://doi.org/10.1002/tcr.201700057.

[5] Parlement du conseil europeen, Directive 2006/66/CE du Parlement Européen et du Conseil du 6 septembre 2006 relative aux piles et accumulateurs ainsi qu'aux déchets de piles et d'accumulateurs et abrogeant la directive 91/157/CEE, Journal Officiel de l'Union Européenne. (2006). (accessed June 8, 2022).

[6] C.D. Parker, Applications - Stationary | Energy Storage Systems: Batteries, Encyclopedia of Electrochemical Power Sources. (2009) 53–64. https://doi.org/10.1016/B978-044452745-5.00382-8.

[7] N. Yabuuchi, K. Kubota, M. Dahbi, S. Komaba, Research development on sodium-ion batteries, Chem Rev. 114 (2014) 11636–11682. https://doi.org/10.1021/cr500192f.

[8] K. Xu, Electrolytes and interphases in Li-ion batteries and beyond, Chem Rev. 114 (2014) 11503–11618. https://doi.org/10.1021/cr500003w.

[9] M.R. Palacín, Recent advances in rechargeable battery materials: A chemist's perspective, Chem Soc Rev. 38 (2009) 2565–2575. https://doi.org/10.1039/b820555h.

[10] K. Chayambuka, G. Mulder, D.L. Danilov, P.H.L. Notten, Sodium-Ion Battery Materials and Electrochemical Properties Reviewed, Adv Energy Mater. 8 (2018) 1800079. https://doi.org/10.1002/aenm.201800079.

[11] J.P. Singer, K.P. Birke, Volume strain in lithium batteries, in: Modern Battery Engineering: A Comprehensive Introduction, World Scientific Publishing Co., 2019: pp. 121–140. https://doi.org/10.1142/9789813272163_0006.

[12] W.J. Zhang, Lithium insertion/extraction mechanism in alloy anodes for lithium-ion batteries, J Power Sources. 196 (2011) 877–885. https://doi.org/10.1016/j.jpowsour.2010.08.114.

[13] N. Nitta, F. Wu, J.T. Lee, X. Wang, W. Gu, J. Benson, E. Zhao, A. Magasinski, K. Evanoff, I. Kovalenko, H. Kim, G. Yushin, Nanostructured composites for high energy batteries and supercapacitors, IEEE-NANO

2015 - 15th International Conference on Nanotechnology. (2015) 572–576. https://doi.org/10.1109/NANO.2015.7388669.

[14] N. Eshraghi, L. Berardo, A. Schrijnemakers, V. Delaval, M. Shaibani, M. Majumder, R. Cloots, B. Vertruyen, F. Boschini, A. Mahmoud, Recovery of Nano-Structured Silicon from End-of-Life Photovoltaic Wafers with Value-Added Applications in Lithium-Ion Battery, ACS Sustain Chem Eng. 8 (2020) 5868–5879. https://doi.org/10.1021/acssuschemeng.9b07434.

[15] A. Ponrouch, P.L. Taberna, P. Simon, M.R. Palacín, On the origin of the extra capacity at low potential in materials for Li batteries reacting through conversion reaction, Electrochim Acta. 61 (2012) 13–18. https://doi.org/10.1016/j.electacta.2011.11.029.

[16] W.H. Woodford, W.C. Carter, Y.M. Chiang, Design criteria for electrochemical shock resistant battery electrodes, Energy Environ Sci. 5 (2012) 8014–8024. https://doi.org/10.1039/c2ee21874g.

[17] J.N. Reimers, J.R. Dahn, Electrochemical and In Situ X-Ray Diffraction Studies of Lithium Intercalation in Li x CoO2, J Electrochem Soc. 139 (1992) 2091–2097. https://doi.org/10.1149/1.2221184.

[18] I. Saadoune, C. Delmas, On the Lix Ni0.8 Co0.2 O2 System, J Solid State Chem. 136 (1998) 8–15.

[19] Y. Itou, Y. Ukyo, Performance of LiNiCoO2 materials for advanced lithium-ion batteries, J Power Sources. 146 (2005) 39–44. https://doi.org/10.1016/j.jpowsour.2005.03.091.

[20] T. Ohzuku, Y. Makimura, Layered lithium insertion material of LiCo1/3Ni1/3Mn1/3O2 for lithium-ion batteries, Chem Lett. (2001) 642–643. https://doi.org/10.1246/cl.2001.642.

[21] N. Meethong, H.Y.S. Huang, S.A. Speakman, W.C. Carter, Y.M. Chiang, Strain accommodation during phase transformations in olivine-based cathodes as a materials selection criterion for high-power rechargeable batteries, Adv Funct Mater. 17 (2007) 1115–1123. https://doi.org/10.1002/adfm.200600938.

[22] J.C. Hunter, Preparation of a new crystal form of manganese dioxide: λ-MnO2, J Solid State Chem. 39 (1981) 142–147. https://doi.org/10.1016/0022-4596(81)90323-6.

[23] K. Ariyoshi, Y. Iwakoshi, N. Nakayama, T. Ohzuku, Topotactic Two-Phase Reactions of Li[Ni[sub 1/2]Mn[sub 3/2]]O[sub 4] (P4[sub 3]32) in Nonaqueous Lithium Cells, J Electrochem Soc. 151 (2004) A296. https://doi.org/10.1149/1.1639162.

[24] A. Manthiram, Y. Fu, S. Chung, C. Zu, Y. Su, Rechargeable Lithium − Sulfur Batteries, Chem Rev. 114 (2014) 11751–11787.

[25] T. Ohzuku, Y. Iwakoshi, K. Sawai, Formation of Lithium-Graphite Intercalation Compounds in Nonaqueous Electrolytes and Their Application as a Negative Electrode for a Lithium Ion (Shuttlecock) Cell, J

Electrochem Soc. 140 (1993) 2490–2498. https://doi.org/10.1149/1.2220849.
[26] T. Ohzuku, A. Ueda, N. Yamamoto, Zero-Strain Insertion Material of Li [Li1 / 3Ti5 / 3] O 4 for Rechargeable Lithium Cells, J Electrochem Soc. 142 (1995) 1431–1435. https://doi.org/10.1149/1.2048592.
[27] L.Y. Beaulieu, K.W. Eberman, R.L. Turner, L.J. Krause, J.R. Dahna, Colossal reversible volume changes in lithium alloys, Electrochemical and Solid-State Letters. 4 (2001). https://doi.org/10.1149/1.1388178.
[28] N. Imanishi, A.C. Luntz, P. Bruce, The lithium air battery: Fundamentals, 2014. https://doi.org/10.1007/978-1-4899-8062-5.
[29] N. Nitta, F. Wu, J.T. Lee, G. Yushin, Li-ion battery materials: Present and future, Materials Today. 18 (2015) 252–264. https://doi.org/10.1016/j.mattod.2014.10.040.
[30] N. Nitta, F. Wu, J.T. Lee, G. Yushin, Li-ion battery materials: Present and future, Materials Today. 18 (2015) 252–264. https://doi.org/10.1016/j.mattod.2014.10.040.
[31] K. Mizushima, P.C. Jones, P.J. Wiseman, J.B. Goodenough, LixCoO2 (0<x<-1): A new cathode material for batteries of high energy density, Mater Res Bull. 15 (1980) 783–789. https://doi.org/10.1016/0025-5408(80)90012-4.
[32] M.S. Islam, C.A.J. Fisher, Lithium and sodium battery cathode materials: Computational insights into voltage, diffusion and nanostructural properties, Chem Soc Rev. 43 (2014) 185–204. https://doi.org/10.1039/c3cs60199d.
[33] S. Kim, W. Cho, X. Zhang, Y. Oshima, J.W. Choi, A stable lithium-rich surface structure for lithium-rich layered cathode materials, Nat Commun. 7 (2016) 1–8. https://doi.org/10.1038/ncomms13598.
[34] J. Xu, M. Sun, R. Qiao, S.E. Renfrew, L. Ma, T. Wu, S. Hwang, D. Nordlund, D. Su, K. Amine, J. Lu, B.D. McCloskey, W. Yang, W. Tong, Elucidating anionic oxygen activity in lithium-rich layered oxides, Nat Commun. 9 (2018) 1–10. https://doi.org/10.1038/s41467-018-03403-9.
[35] F. Zheng, C. Yang, X. Xiong, J. Xiong, R. Hu, Y. Chen, M. Liu, Nanoscale Surface Modification of Lithium-Rich Layered-Oxide Composite Cathodes for Suppressing Voltage Fade, Angewandte Chemie - International Edition. 54 (2015) 13058–13062. https://doi.org/10.1002/anie.201506408.
[36] J. Dong H, Y.J. Shin, S.M. Oh, Dissolution of Spinel Oxides and Capacily Losses in 4 V, J Electrochem Soc. 143 (1996) 2204–2211. https://doi.org/10.1149/1.1836981.
[37] M. Aklalouch, J.M. Amarilla, R.M. Rojas, I. Saadoune, J.M. Rojo, Sub-micrometric LiCr0.2Ni0.4Mn1.4O4 spinel as 5 V-cathode material exhibiting huge rate capability at 25 and 55 °C, Electrochem Commun. 12 (2010) 548–552. https://doi.org/10.1016/j.elecom.2010.01.040.
[38] W. Lee, S. Muhammad, C. Sergey, H. Lee, J. Yoon, Y. Kang, W. Yoon, Advances in the Cathode Materials for Lithium Rechargeable Batteries,

Angewandte Chemie International Edition. 59 (2020) 2578–2605. https://doi.org/10.1002/anie.201902359.
[39] C. Wang, J. Hong, Ionic/electronic conducting characteristics of LiFePO4 cathode materials, Electrochemical and Solid-State Letters. 10 (2007) A65. https://doi.org/10.1149/1.2409768.
[40] C. Gong, Z. Xue, S. Wen, Y. Ye, X. Xie, Advanced carbon materials/olivine LiFePO4 composites cathode for lithium ion batteries, J Power Sources. 318 (2016) 93–112. https://doi.org/10.1016/j.jpowsour.2016.04.008.
[41] W. Zhang, H.L. Zhuang, L. Fan, L. Gao, Y. Lu, A "cation-anion regulation" synergistic anode host for dendrite-free lithium metal batteries, Sci Adv. 4 (2018). https://doi.org/10.1126/sciadv.aar4410.
[42] J.J. Arayamparambil, Metal carbodiimides and cyanamides, a new family of electrode materials for Li-ion batteries, 2019.
[43] D. Larcher, J.T.-N. Chemistry, U. 2015, J.M. Tarascon, Towards greener and more sustainable batteries for electrical energy storage, Nat Chem. 7 (2015) 19–29. https://doi.org/10.1038/nchem.2085.
[44] J. Liu, X. Wei, F. Meng, Lithium Titanate-Based Lithium-Ion Batteries, in: Advanced Battery Materials, Wiley, 2019: pp. 87–157. https://doi.org/10.1002/9781119407713.ch2.
[45] H. Yoo, J.I. Lee, H. Kim, J.P. Lee, J. Cho, S. Park, Helical silicon/silicon oxide core-shell anodes grown onto the surface of bulk silicon, Nano Lett. 11 (2011) 4324–4328. https://doi.org/10.1021/nl202417c.
[46] G.G. Amatucci, N. Pereira, Fluoride based electrode materials for advanced energy storage devices, J Fluor Chem. 128 (2007) 243–262. https://doi.org/10.1016/j.jfluchem.2006.11.016.
[47] H.D. Yoo, E. Markevich, G. Salitra, D. Sharon, D. Aurbach, On the challenge of developing advanced technologies for electrochemical energy storage and conversion, Materials Today. 17 (2014) 110–121. https://doi.org/10.1016/j.mattod.2014.02.014.
[48] P.G. Bruce, B. Scrosati, J.-M. Tarascon, Nanomaterials for Rechargeable Lithium Batteries, Angewandte Chemie International Edition. 47 (2008) 2930–2946. https://doi.org/10.1002/anie.200702505.
[49] H.D. Yoo, E. Markevich, G. Salitra, D. Sharon, D. Aurbach, On the challenge of developing advanced technologies for electrochemical energy storage and conversion, Materials Today. 17 (2014) 110–121. https://doi.org/10.1016/j.mattod.2014.02.014.
[50] Björklund, E. Avoiding ageing. (Uppsala University Sweden, 2019). - (accessed June 8, 2022).
[51] P. Verma, P. Maire, P. Novák, A review of the features and analyses of the solid electrolyte interphase in Li-ion batteries, Electrochim Acta. 55 (2010) 6332–6341. https://doi.org/10.1016/j.electacta.2010.05.072.

[52] Y. Matsuda, Behavior of Some Ions in Mixed Organic Electrolytes of High Energy Density Batteries, J Electrochem Soc. 128 (1981) 2552. https://doi.org/10.1149/1.2127289.
[53] J. Lyklema, Principles of interactions in non-aqueous electrolyte solutions, Curr Opin Colloid Interface Sci. 18 (2013) 116–128. https://doi.org/10.1016/j.cocis.2013.02.002.
[54] E.J. Berg, C. Villevieille, D. Streich, S. Trabesinger, P. Novák, Rechargeable Batteries: Grasping for the Limits of Chemistry, J Electrochem Soc. 162 (2015) A2468–A2475. https://doi.org/10.1149/2.0081514jes.
[55] R. van Noorden, The rechargeable revolution: A better battery, Nature. 507 (2014) 26–28. https://doi.org/10.1038/507026a.
[56] A. Eftekhari, Lithium Batteries for Electric Vehicles: From Economy to Research Strategy, ACS Sustain Chem Eng. 7 (2019) 5602–5613. https://doi.org/10.1021/acssuschemeng.8b01494.
[57] J.M. Tarascon, Is lithium the new gold?, Nat Chem. 2 (2010) 510. https://doi.org/10.1038/nchem.680.
[58] Guillaume Pitron, La Guerre des Métaux Rares. La face cachée de la transition énergétique et numérique, Projet. 363 (2018) 90. https://doi.org/10.3917/pro.363.0090.
[59] • Lithium carbonate price 2021 | Statista, (n.d.). https://www.statista.com/statistics/606350/battery-grade-lithium-carbonate-price/ (accessed June 8, 2022).
[60] C.P. Grey, J.M. Tarascon, Sustainability and in situ monitoring in battery development, Nat Mater. 16 (2016) 45–56. https://doi.org/10.1038/nmat4777.
[61] J.J. Braconnier, C. Delmas, C. Fouassier, P. Hagenmuller, Comportement electrochimique des phases NaxCoO2, Mater Res Bull. 15 (1980) 1797–1804. https://doi.org/10.1016/0025-5408(80)90199-3.
[62] A. Eftekhari, Potassium secondary cell based on Prussian blue cathode, J Power Sources. 126 (2004) 221–228. https://doi.org/10.1016/j.jpowsour.2003.08.007.
[63] Y. Zhao, K.R. Adair, X. Sun, Recent developments and insights into the understanding of Na metal anodes for Na-metal batteries, Energy Environ Sci. 11 (2018) 2673–2695. https://doi.org/10.1039/c8ee01373j.
[64] Y. Wang, Y. Wang, Y.X. Wang, X. Feng, W. Chen, X. Ai, H. Yang, Y. Cao, Developments and Perspectives on Emerging High-Energy-Density Sodium-Metal Batteries, Chem. 5 (2019) 2547–2570. https://doi.org/10.1016/j.chempr.2019.05.026.
[65] I.E.N. ADEME, Electrification du parc automobile mondial et criticité du Lithium à l'horizon 2050 - La librairie ADEME, 2018. https://librairie.ademe.fr/mobilite-et-transport/3803-electrification-du-parc-automobile-mondial-et-criticite-du-lithium-a-l-horizon-2050.html (accessed June 8, 2022).

[66] S. Komaba, T. Hasegawa, M. Dahbi, K. Kubota, Potassium intercalation into graphite to realize high-voltage/high-power potassium-ion batteries and potassium-ion capacitors, Electrochem Commun. 60 (2015) 172–175. https://doi.org/10.1016/j.elecom.2015.09.002.

[67] J. Landesfeind, M. Graf, M. Dahbi, K. Kubota, S. Komaba, H. A. Gasteiger, Meeting Abstract of 231st ECS Meeting, Vol. MA2017-01, New Orleans, Louisiana, 2017, in: Meeting Abstract of 231st ECS Meeting, 2017: pp. 211–211.

[68] B.Y.R.D. Shannon, M. H, N.H. Baur, O.H. Gibbs, M. Eu, V. Cu, Revised Effective Ionic Radii and Systematic Studies of Interatomie Distances in Halides and Chalcogenides Central Research and Development Department , Experimental Station , E . L Du Pont de Nemours The effective ionic radii of Shannon & Prewitt, Acta, Acta Crystallogr. A 32 (1976) 751.

[69] Y. Matsuda, H. Nakashima, M. Morita, Y. Takasu, Behavior of Some Ions in Mixed Organic Electrolytes of High Energy Density Batteries, J Electrochem Soc. 128 (1981) 2552–2556. https://doi.org/10.1149/1.2127289.

[70] T. Hasegawa, M. Dahbi, K. Kubota, K. Miyamoto, T. Nakano, K. Yamagiwa, S. Komaba, T. Chafik, Study of electrochemical alkali insertion into carbonaceous materials, in: Proceedings of 2014 International Renewable and Sustainable Energy Conference, IRSEC 2014, Institute of Electrical and Electronics Engineers Inc., 2014: pp. 642–646. https://doi.org/10.1109/IRSEC.2014.7059852.

[71] C. Zhang, H. Zhao, Y. Lei, Recent Research Progress of Anode Materials for Potassium-ion Batteries, ENERGY & ENVIRONMENTAL MATERIALS. 3 (2020) 105–120. https://doi.org/10.1002/eem2.12059.

[72] J.Y. Hwang, S.T. Myung, Y.K. Sun, Sodium-ion batteries: Present and future, Chem Soc Rev. 46 (2017) 3529–3614. https://doi.org/10.1039/c6cs00776g.

[73] J.M. Tarascon, M. Armand, Issues and challenges facing rechargeable lithium batteries., Nature. 414 (2001) 359–67. https://doi.org/10.1038/35104644.

[74] Z. Jian, W. Luo, X. Ji, Carbon Electrodes for K-Ion Batteries, J Am Chem Soc. 137 (2015) 11566–11569. https://doi.org/10.1021/jacs.5b06809.

[75] H. Kim, J. Hong, Y.U. Park, J. Kim, I. Hwang, K. Kang, Sodium storage behavior in natural graphite using ether-based electrolyte systems, Adv Funct Mater. 25 (2015) 534–541. https://doi.org/10.1002/adfm.201402984.

[76] B. Jache, P. Adelhelm, Use of Graphite as a Highly Reversible Electrode with Superior Cycle Life for Sodium-Ion Batteries by Making Use of Co-Intercalation Phenomena, Angewandte Chemie. 126 (2014) 10333–10337. https://doi.org/10.1002/ange.201403734.

[77] J.R. Dahn, T. Zheng, Y. Liu, J.S. Xue, Mechanisms for lithium insertion in carbonaceous materials, Science (1979). 270 (1995) 590–593. https://doi.org/10.1126/science.270.5236.590.

[78] S. Zhang, A.A. Teck, Z. Guo, Z. Xu, M. Titirici, Carbon Composite Anodes with Tunable Microstructures for Potassium-Ion Batteries, Batter Supercaps. 4 (2021) 663–670. https://doi.org/10.1002/batt.202000306.
[79] B. Zhang, C.M. Ghimbeu, C. Laberty, C. Vix-Guterl, J.-M. Tarascon, Correlation Between Microstructure and Na Storage Behavior in Hard Carbon, Adv Energy Mater. 6 (2016) 1501588. https://doi.org/10.1002/aenm.201501588.
[80] J.M. Stratford, P.K. Allan, O. Pecher, P.A. Chater, C.P. Grey, Mechanistic insights into sodium storage in hard carbon anodes using local structure probes, Chemical Communications. 52 (2016) 12430–12433. https://doi.org/10.1039/c6cc06990h.
[81] C. Bommier, T.W. Surta, M. Dolgos, X. Ji, New Mechanistic Insights on Na-Ion Storage in Nongraphitizable Carbon, Nano Lett. 15 (2015) 5888–5892. https://doi.org/10.1021/acs.nanolett.5b01969.
[82] S. Komaba, W. Murata, T. Ishikawa, N. Yabuuchi, T. Ozeki, T. Nakayama, A. Ogata, K. Gotoh, K. Fujiwara, Electrochemical Na Insertion and Solid Electrolyte Interphase for Hard-Carbon Electrodes and Application to Na-Ion Batteries, Adv Funct Mater. 21 (2011) 3859–3867. https://doi.org/10.1002/adfm.201100854.
[83] D.A. Stevens, J.R. Dahn, The Mechanisms of Lithium and Sodium Insertion in Carbon Materials, J Electrochem Soc. 148 (2001) A803. https://doi.org/10.1149/1.1379565.
[84] S. Komaba, W. Murata, T. Ishikawa, N. Yabuuchi, T. Ozeki, T. Nakayama, A. Ogata, K. Gotoh, K. Fujiwara, Electrochemical Na Insertion and Solid Electrolyte Interphase for Hard-Carbon Electrodes and Application to Na-Ion Batteries, Adv Funct Mater. 21 (2011) 3859–3867. https://doi.org/10.1002/adfm.201100854.
[85] A. Kano, T. Okano, N. Hojo, S. Ito, M. Fujimoto, K. Nakura, New Carbon Materials with Large Closed Pore Volume for the Anode of High Energy Na-Ion Batteries, ECS Meeting Abstracts. MA2016-02 (2016) 668–668. https://doi.org/10.1149/ma2016-02/5/668.
[86] H. Morito, T. Yamada, T. Ikeda, H. Yamane, Na-Si binary phase diagram and solution growth of silicon crystals, J Alloys Compd. 480 (2009) 723–726. https://doi.org/10.1016/j.jallcom.2009.02.036.
[87] J. Witte, H.G. Schnering, W. Klemm, Das Verhalten der Alkalimetalle zu Halbmetallen. XI. Die Kristallstruktur von NaSi und NaGe, Zeitschrift F□r Anorganische Und Allgemeine Chemie. 327 (1964) 260–273. https://doi.org/10.1002/zaac.19643270319.
[88] Z. Li, J. Ding, D. Mitlin, Tin and Tin Compounds for Sodium Ion Battery Anodes: Phase Transformations and Performance, Acc Chem Res. 48 (2015) 1657–1665. https://doi.org/10.1021/acs.accounts.5b00114.
[89] H. Kim, H. Ji, J. Wang, G. Ceder, Next-Generation Cathode Materials for Non-aqueous Potassium-Ion Batteries, Trends Chem. 1 (2019) 682–692. https://doi.org/10.1016/j.trechm.2019.04.007.

[90] Y. Hironaka, K. Kubota, S. Komaba, P2- and P3-KxCoO2 as an electrochemical potassium intercalation host, Chemical Communications. 53 (2017) 3693–3696. https://doi.org/10.1039/c7cc00806f.
[91] C. Vaalma, D. Buchholz, S. Passerini, Non-Aqueous Potassium-Ion Batteries: A Review, Curr Opin Electrochem. (2018). https://doi.org/10.1016/j.coelec.2018.03.031.
[92] X. Wang, X. Xu, C. Niu, J. Meng, M. Huang, X. Liu, Z. Liu, L. Mai, Earth Abundant Fe/Mn-Based Layered Oxide Interconnected Nanowires for Advanced K-Ion Full Batteries, Nano Lett. 17 (2017) 544–550. https://doi.org/10.1021/acs.nanolett.6b04611.
[93] X. Ma, H. Chen, G. Ceder, Electrochemical Properties of Monoclinic NaMnO2, J Electrochem Soc. 158 (2011) A1307. https://doi.org/10.1149/2.035112jes.
[94] N. Yabuuchi, R. Hara, M. Kajiyama, K. Kubota, T. Ishigaki, A. Hoshikawa, S. Komaba, New O2/P2-type Li-Excess Layered Manganese Oxides as Promising Multi-Functional Electrode Materials for Rechargeable Li/Na Batteries, Adv Energy Mater. 4 (2014) 1301453. https://doi.org/10.1002/aenm.201301453.
[95] B. Ammundsen, J. Paulsen, Novel Lithium-Ion Cathode Materials Based on Layered Manganese Oxides, Advanced Materials. 13 (2001) 943–956. https://doi.org/10.1002/1521-4095(200107)
[96] A.J. Perez, D. Batuk, M. Saubanère, G. Rousse, D. Foix, E. McCalla, E.J. Berg, R. Dugas, K.H.W. van den Bos, M.L. Doublet, D. Gonbeau, A.M. Abakumov, G. van Tendeloo, J.M. Tarascon, Strong oxygen participation in the redox governing the structural and electrochemical properties of Na-rich layered oxide Na2IrO3, Chemistry of Materials. 28 (2016) 8278–8288. https://doi.org/10.1021/acs.chemmater.6b03338.
[97] R. Malini, U. Uma, T. Sheela, M. Ganesan, N.G. Renganathan, Conversion reactions: A new pathway to realise energy in lithium-ion battery - Review, Ionics (Kiel). 15 (2009) 301–307. https://doi.org/10.1007/s11581-008-0236-x.
[98] Y. Chen, W. Luo, M. Carter, L. Zhou, J. Dai, K. Fu, S. Lacey, T. Li, J. Wan, X. Han, Y. Bao, L. Hu, Organic electrode for non-aqueous potassium-ion batteries, Nano Energy. 18 (2015) 205–211. https://doi.org/10.1016/j.nanoen.2015.10.015.
[99] Z. Jian, Y. Liang, I.A.R. Pérez, Y. Yao, X. Ji, Poly(anthraquinonyl sulfide) cathode for potassium-ion batteries, Electrochem Commun. 71 (2016) 5–8. https://doi.org/10.1016/j.elecom.2016.07.011.
[100] F. Xu, H. Wang, J. Lin, X. Luo, S.A. Cao, H. Yang, Poly(anthraquinonyl imide) as a high capacity organic cathode material for Na-ion batteries, J Mater Chem A Mater. 4 (2016) 11491–11497. https://doi.org/10.1039/c6ta03956a.
[101] A. Aqil, C. Jérôme, F. Boschini, A. Mahmoud, Enhancing Performances of Polydopamine as Cathode for Lithium- and Potassium-Ion Batteries by

Simple Grafting of Sulfonate Groups, Batter Supercaps. 4 (2021) 374–379. https://doi.org/10.1002/batt.202000242.
[102] Y. Lu, L. Wang, J. Cheng, J.B. Goodenough, Prussian blue: A new framework of electrode materials for sodium batteries, Chemical Communications. 48 (2012) 6544–6546. https://doi.org/10.1039/c2cc31777j.
[103] B. Huang, Y. Shao, Y. Liu, Z. Lu, X. Lu, S. Liao, Improving Potassium-Ion Batteries by Optimizing the Composition of Prussian Blue Cathode, ACS Appl Energy Mater. 2 (2019) 6528–6535. https://doi.org/10.1021/acsaem.9b01097.
[104] D. Baster, Ł. Kondracki, E. Oveisi, S. Trabesinger, H.H. Girault, Prussian Blue Analogue-Sodium-Vanadium Hexacyanoferrate as a Cathode Material for Na-Ion Batteries, ACS Appl Energy Mater. (2021). https://doi.org/10.1021/acsaem.1c01832.
[105] R. Chen, Y. Huang, M. Xie, Q. Zhang, X. Zhang, L. Li, F. Wu, Preparation of Prussian Blue Submicron Particles with a Pore Structure by Two-Step Optimization for Na-Ion Battery Cathodes, ACS Appl Mater Interfaces. 8 (2016) 16078–16086. https://doi.org/10.1021/acsami.6b04151.
[106] Y. You, X.L. Wu, Y.X. Yin, Y.G. Guo, High-quality Prussian blue crystals as superior cathode materials for room-temperature sodium-ion batteries, Energy Environ Sci. 7 (2014) 1643–1647. https://doi.org/10.1039/c3ee44004d.
[107] L. Wang, J. Song, R. Qiao, L.A. Wray, M.A. Hossain, Y. de Chuang, W. Yang, Y. Lu, D. Evans, J.J. Lee, S. Vail, X. Zhao, M. Nishijima, S. Kakimoto, J.B. Goodenough, Rhombohedral Prussian white as cathode for rechargeable sodium-ion batteries, J Am Chem Soc. 137 (2015) 2548–2554. https://doi.org/10.1021/ja510347s.
[108] Y. You, X. Yu, Y. Yin, K.W. Nam, Y.G. Guo, Sodium iron hexacyanoferrate with high Na content as a Na-rich cathode material for Na-ion batteries, Nano Res. 8 (2015) 117–128. https://doi.org/10.1007/s12274-014-0588-7.
[109] J. Song, L. Wang, Y. Lu, J. Liu, B. Guo, P. Xiao, J.J. Lee, X.Q. Yang, G. Henkelman, J.B. Goodenough, Removal of interstitial H2O in hexacyanometallates for a superior cathode of a sodium-ion battery, J Am Chem Soc. 137 (2015) 2658–2664. https://doi.org/10.1021/ja512383b.
[110] D. Su, A. McDonagh, S. Qiao, G. Wang, High-Capacity Aqueous Potassium-Ion Batteries for Large-Scale Energy Storage, Advanced Materials. 29 (2017) 1604007. https://doi.org/10.1002/adma.201604007.
[111] L. Xue, Y. Li, H. Gao, W. Zhou, X. Lü, W. Kaveevivitchai, A. Manthiram, J.B. Goodenough, Low-Cost High-Energy Potassium Cathode, J Am Chem Soc. 139 (2017) 2164–2167. https://doi.org/10.1021/jacs.6b12598.
[112] X. Bie, K. Kubota, T. Hosaka, K. Chihara, S. Komaba, A novel K-ion battery: hexacyanoferrate(ii)/graphite cell, J Mater Chem A Mater. 5 (2017) 4325–4330. https://doi.org/10.1039/c7ta00220c.

[113] J.B.; K.N. Padhi, A.K.; Goodenough, A.K.Pahdi, Journal of Electrochemical Society. 144 (1997) 1188.
[114] N. Recham, G. Rousse, M.T. Sougrati, J.N. Chotard, C. Frayret, S. Mariyappan, B.C. Melot, J.C. Jumas, J.M. Tarascon, Preparation and characterization of a stable FeSO4F-based framework for alkali ion insertion electrodes, Chemistry of Materials. 24 (2012) 4363–4370. https://doi.org/10.1021/cm302428w.
[115] L. Lander, G. Rousse, A.M. Abakumov, M. Sougrati, G. van Tendeloo, J.M. Tarascon, Structural, electrochemical and magnetic properties of a novel KFeSO4F polymorph, J Mater Chem A Mater. 3 (2015) 19754–19764. https://doi.org/10.1039/c5ta05548b.
[116] M. Gnanavel, O.I. Lebedev, P. Bazin, B. Raveau, V. Pralong, Reversible transformation from amorphouse Na3Fe3(SO4)2(OH)6 to crystallized NaFe3(SO4)2(OH)6 Jarosite-type hydroxysulfate, Solid State Ion. 278 (2015) 38–42. https://doi.org/10.1016/j.ssi.2015.05.013.
[117] W.B. Park, S.C. Han, C. Park, S.U. Hong, U. Han, S.P. Singh, Y.H. Jung, D. Ahn, K.-S. Sohn, M. Pyo, KVP_2O_7 as a Robust High-Energy Cathode for Potassium-Ion Batteries: Pinpointed by a Full Screening of the Inorganic Registry under Specific Search Conditions, Adv Energy Mater. 8 (2018) 1703099. https://doi.org/10.1002/aenm.201703099.
[118] H. Kim, R.A. Shakoor, C. Park, S.Y. Lim, J.-S. Kim, Y.N. Jo, W. Cho, K. Miyasaka, R. Kahraman, Y. Jung, J.W. Choi, $Na_2FeP_2O_7$ as a Promising Iron-Based Pyrophosphate Cathode for Sodium Rechargeable Batteries: A Combined Experimental and Theoretical Study, Adv Funct Mater. 23 (2013) 1147–1155. https://doi.org/10.1002/adfm.201201589.
[119] P. Barpanda, T. Ye, S.I. Nishimura, S.C. Chung, Y. Yamada, M. Okubo, H. Zhou, A. Yamada, Sodium iron pyrophosphate: A novel 3.0 v iron-based cathode for sodium-ion batteries, Electrochem Commun. 24 (2012) 116–119. https://doi.org/10.1016/j.elecom.2012.08.028.
[120] T. Honma, T. Togashi, N. Ito, T. Komatsu, Fabrication of Na2FeP2O7 glass-ceramics for sodium ion battery, Journal of the Ceramic Society of Japan. 120 (2012) 344–346. https://doi.org/10.2109/jcersj2.120.344.
[121] K. Trabelsi, J. Bodart, K. Karoui, F. Boschini, A. ben Rhaiem, A. Mahmoud, Electrochemical mechanism and effects of Fe doping and grinding process on the microstructural and electrochemical properties of Na2Co1-xFexSiO4 cathode material for sodium-ion batteries, Electrochim Acta. 391 (2021) 138935. https://doi.org/10.1016/j.electacta.2021.138935.
[122] Y. Liu, Y. Zhou, J. Zhang, Y. Xia, T. Chen, S. Zhang, Monoclinic phase Na3Fe2(PO4)3: Synthesis, structure, and electrochemical performance as cathode material in sodium-ion batteries, ACS Sustain Chem Eng. 5 (2017) 1306–1314. https://doi.org/10.1021/acssuschemeng.6b01536.
[123] Q. Liu, H. Wang, C. Jiang, Y. Tang, Multi-ion strategies towards emerging rechargeable batteries with high performance, Energy Storage Mater. 23 (2019) 566–586. https://doi.org/10.1016/j.ensm.2019.03.028.

[124] N. Eshraghi, S. Caes, A. Mahmoud, R. Cloots, B. Vertruyen, F. Boschini, Sodium vanadium (III) fluorophosphate/carbon nanotubes composite (NVPF/CNT) prepared by spray-drying: good electrochemical performance thanks to well-dispersed CNT network within NVPF particles, Electrochim Acta. 228 (2017) 319–324. https://doi.org/10.1016/j.electacta.2017.01.026.
[125] J. Bodart, N. Eshraghi, T. Carabin, B. Vertruyen, R. Cloots, F. Boschini, A. Mahmoud, Spray-dried K3V(PO4)2/C composites as novel cathode materials for K-ion batteries with superior electrochemical performance, J Power Sources. 480 (2020). https://doi.org/10.1016/j.jpowsour.2020.229057.
[126] F. Lalère, V. Seznec, M. Courty, R. David, New insights into the effect of a washingin water on thepropertiesof Na3V2(PO4)2F3-yOy (0 y 2) materials as positive electrodes for Na-ion batteries, J Mater. 2 (2015). http://pubs.rsc.org/en/content/articlehtml/2015/ta/c5ta03528g.
[127] M. Bianchini, N. Brisset, F. Fauth, F. Weill, E. Elkaim, E. Suard, C. Masquelier, L. Croguennec, Na3V2(PO4)2F3 revisited: A high-resolution diffraction study, Chemistry of Materials. 26 (2014) 4238–4247. https://doi.org/10.1021/cm501644g.
[128] H. Xiong, Y. Liu, H. Shao, Y. Yang, Understanding the electrochemical mechanism of high sodium selective material Na3V2(PO4)2F3 in Li+/Na+ dual-ion batteries, Electrochim Acta. 292 (2018) 234–246. https://doi.org/10.1016/j.electacta.2018.09.173.
[129] C. Zhu, C. Wu, C.C. Chen, P. Kopold, P.A. van Aken, J. Maier, Y. Yu, A High Power-High Energy Na3V2(PO4)2F3 Sodium Cathode: Investigation of Transport Parameters, Rational Design and Realization, Chemistry of Materials. 29 (2017) 5207–5215. https://doi.org/10.1021/acs.chemmater.7b00927.
[130] T. Broux, T. Bamine, L. Simonelli, L. Stievano, F. Fauth, M. Ménétrier, D. Carlier, C. Masquelier, L. Croguennec, VIV Disproportionation Upon Sodium Extraction from Na3V2(PO4)2F3 Observed by Operando X-ray Absorption Spectroscopy and Solid-State NMR, Journal of Physical Chemistry C. 121 (2017) 4103–4111. https://doi.org/10.1021/acs.jpcc.6b11413.
[131] R. Malik, A. Abdellahi, G. Ceder, A Critical Review of the Li Insertion Mechanisms in LiFePO 4 Electrodes , J Electrochem Soc. 160 (2013) A3179–A3197. https://doi.org/10.1149/2.029305jes.
[132] P. Serras, V. Palomares, T. Rojo, High-Voltage Cathodes for Na-Ion Batteries: Sodium– Vanadium Fluorophosphates, in: Alkali-Ion Batteries, InTech, 2016. https://doi.org/10.5772/62317.
[133] P. Barpanda, L. Lander, S. Nishimura, A. Yamada, Polyanionic Insertion Materials for Sodium-Ion Batteries, Adv Energy Mater. 8 (2018) 1703055. https://doi.org/10.1002/aenm.201703055.
[134] W. Song, X. Ji, Z. Wu, Y. Yang, Z. Zhou, F. Li, Q. Chen, C.E. Banks, Exploration of ion migration mechanism and diffusion capability for Na

3V2(PO4)2F3 cathode utilized in rechargeable sodium-ion batteries, J Power Sources. 256 (2014) 258–263. https://doi.org/10.1016/j.jpowsour.2014.01.025.

[135] M. Xu, C.J. Cheng, Q.Q. Sun, S.J. Bao, Y. bin Niu, H. He, Y. Li, J. Song, A 3D porous interconnected NaVPO4F/C network: Preparation and performance for Na-ion batteries, RSC Adv. 5 (2015) 40065–40069. https://doi.org/10.1039/c5ra05161d.

[136] Y. Zhong, Z. Wu, Y. Tang, W. Xiang, X. Guo, B. Zhong, Micro-nano structure Na2MnPO4F/C as cathode material with excellent sodium storage properties, Mater Lett. 145 (2015) 269–272. https://doi.org/10.1016/j.matlet.2015.01.110.

[137] K. Kubota, K. Yokoh, N. Yabuuchi, S. Komaba, Na2CoPO4F as a high-voltage electrode material for na-ion batteries, Electrochemistry. 82 (2014) 909–911. https://doi.org/10.5796/electrochemistry.82.909.

[138] B.L. Ellis, W.R.M. Makahnouk, Y. Makimura, K. Toghill, L.F. Nazar, A multifunctional 3.5V iron-based phosphate cathode for rechargeable batteries, Nat Mater. 6 (2007) 749–753. https://doi.org/10.1038/nmat2007.

[139] B.L. Ellis, W.R. Michael Makahnouk, W.N. Rowan-Weetaluktuk, D.H. Ryan, L.F. Nazar, Crystal structure and electrochemical properties of A2MPO 4F fluorophosphates (A = Na, Li; M = Fe, Mn, Co, Ni), Chemistry of Materials. 22 (2010) 1059–1070. https://doi.org/10.1021/cm902023h.

[140] R. Tripathi, S.M. Wood, M.S. Islam, L.F. Nazar, Na-ion mobility in layered Na2FePO4F and olivine Na[Fe,Mn]PO4, Energy Environ Sci. 6 (2013) 2257–2264. https://doi.org/10.1039/c3ee40914g.

[141] Linda Faye Nazar (Inventor), Michael Makahnouk (Inventor), Brian Ellis (Inventor), Kathryn Toghill (Inventor), Yoshinari. Makimura (Inventor), Mixed lithium/sodium iron fluorophosphate cathode materials for lithium-ion batteries. - Research Portal | Lancaster University, US20080153002A1, 2014. https://www.research.lancs.ac.uk/portal/en/publications/mixed-lithiumsodium-iron-fluorophosphate-cathode-materials-for-lithiumion-batteries(2814871a-b2d5-4b75-8824-301215d929f0).html (accessed June 8, 2022).

[142] M. Brisbois, S. Caes, M.T. Sougrati, B. Vertruyen, A. Schrijnemakers, R. Cloots, N. Eshraghi, R.P. Hermann, A. Mahmoud, F. Boschini, Na2FePO4F/multi-walled carbon nanotubes for lithium-ion batteries: Operando Mössbauer study of spray-dried composites, Solar Energy Materials and Solar Cells. 148 (2016) 67–72. https://doi.org/10.1016/j.solmat.2015.09.005.

[143] M. Brisbois, N. Krins, R.P. Hermann, A. Schrijnemakers, R. Cloots, B. Vertruyen, F. Boschini, Spray-drying synthesis of Na2FePO4F/carbon powders for lithium-ion batteries, Mater Lett. 130 (2014) 263–266. https://doi.org/10.1016/j.matlet.2014.05.121.

[144] H. Hu, Y. Wang, Y. Huang, H. bo Shu, X. you Wang, Na2FePO4F/C composite synthesized via a simple solid state route for lithium-ion

batteries, J Cent South Univ. 26 (2019) 1521–1529. https://doi.org/10.1007/s11771-019-4108-5.
[145] D. Cui, S. Chen, C. Han, C. Ai, L. Yuan, Carbothermal reduction synthesis of carbon coated Na2FePO4F for lithium ion batteries, J Power Sources. 301 (2016) 87–92. https://doi.org/10.1016/j.jpowsour.2015.09.123.
[146] A. Mahmoud, S. Caes, M. Brisbois, R.P. Hermann, L. Berardo, A. Schrijnemakers, C. Malherbe, G. Eppe, R. Cloots, B. Vertruyen, F. Boschini, Spray-drying as a tool to disperse conductive carbon inside Na2FePO4F particles by addition of carbon black or carbon nanotubes to the precursor solution, Journal of Solid State Electrochemistry. 22 (2018) 103–112. https://doi.org/10.1007/s10008-017-3717-x.
[147] W. Ko, J.K. Yoo, H. Park, Y. Lee, H. Kim, Y. Oh, S.T. Myung, J. Kim, Development of Na2FePO4F/Conducting-Polymer composite as an exceptionally high performance cathode material for Na-ion batteries, J Power Sources. 432 (2019) 1–7. https://doi.org/10.1016/j.jpowsour.2019.05.066.
[148] J. Yan, X. Liu, B. Li, Nano-assembled Na2FePO4F/carbon nanotube multi-layered cathodes for Na-ion batteries, Electrochem Commun. 56 (2015) 46–50. https://doi.org/10.1016/j.elecom.2015.04.009.
[149] J.S. Ko, V.V.T. Doan-Nguyen, H.S. Kim, X. Petrissans, R.H. Deblock, C.S. Choi, J.W. Long, B.S. Dunn, High-rate capability of Na2FePO4F nanoparticles by enhancing surface carbon functionality for Na-ion batteries, J Mater Chem A Mater. 5 (2017) 18707–18715. https://doi.org/10.1039/c7ta05680j.
[150] L. Sharma, A. Bhatia, L. Assaud, S. Franger, P. Barpanda, Ultra-rapid combustion synthesis of Na2FePO4F fluorophosphate host for Li-ion and Na-ion insertion, Ionics (Kiel). 24 (2018) 2187–2192. https://doi.org/10.1007/s11581-017-2376-3.
[151] T. Hosaka, T. Shimamura, K. Kubota, S. Komaba, Polyanionic Compounds for Potassium-Ion Batteries, Chemical Record. 19 (2019) 735–745. https://doi.org/10.1002/tcr.201800143.
[152] V. Mathew, S. Kim, J. Kang, J. Gim, J. Song, J.P. Baboo, W. Park, D. Ahn, J. Han, L. Gu, Y. Wang, Y.S. Hu, Y.K. Sun, J. Kim, Amorphous iron phosphate: Potential host for various charge carrier ions, NPG Asia Mater. 6 (2014) e138–e138. https://doi.org/10.1038/am.2014.98.
[153] L. Zhang, B. Zhang, C. Wang, Y. Dou, Q. Zhang, Y. Liu, H. Gao, M. Al-Mamun, W.K. Pang, Z. Guo, S.X. Dou, H.K. Liu, Constructing the best symmetric full K-ion battery with the NASICON-type K 3 V 2 (PO 4) 3, Nano Energy. 60 (2019) 432–439. https://doi.org/10.1016/j.nanoen.2019.03.085.
[154] X. Lin, J. Huang, H. Tan, J. Huang, B. Zhang, K3V2(PO4)2F3 as a robust cathode for potassium-ion batteries, Energy Storage Mater. 16 (2019) 97–101. https://doi.org/10.1016/j.ensm.2018.04.026.

[155] B. Vertruyen, N. Eshraghi, C. Piffet, J. Bodart, A. Mahmoud, F. Boschini, Spray-drying of electrode materials for lithium- and sodium-ion batteries, Materials. 11 (2018). https://doi.org/10.3390/ma11071076.
[156] W.A. Stein, Spray Drying. An Introduction to Principles, Operational Practice and Applications. Von K. Masters. Aus d. Reihe: Chemical and Process Engineering Series. Intertext Publishing Ltd., Leonard Hill Books, London 1972. 1. Aufl., 668 S., zahlr. Abb. u. Tab., L, Chemie Ingenieur Technik. 45 (1973) 906–907. https://doi.org/10.1002/cite.330451311.
[157] A.B.D. Nandiyanto, K. Okuyama, Progress in developing spray-drying methods for the production of controlled morphology particles: From the nanometer to submicrometer size ranges, Advanced Powder Technology. 22 (2011) 1–19. https://doi.org/10.1016/j.apt.2010.09.011.
[158] C. Piffet, Spray-drying synthesis of Ti-based materials for Li / Na-ion batteries : development of Li 4 Ti 5 O 12 flexible electrodes and in-situ characterizations of Na 2 Ti 3 O 7, University of Liege, 2021.
[159] GEA, Spray Drying for Small Scale Solutions, (n.d.). https://www.gea.com/assets/Spray Drying for Small Scale Solutions-171168.pdf (accessed June 8, 2022).
[160] P. Seydel, J. Blömer, J. Bertling, Modeling Particle Formation at Spray Drying Using Population Balances, Drying Technology. 24 (2006) 137–146. https://doi.org/10.1080/07373930600558912.
[161] A. Singh, G. van den Mooter, Spray drying formulation of amorphous solid dispersions, Adv Drug Deliv Rev. 100 (2016) 27–50. https://doi.org/10.1016/j.addr.2015.12.010.
[162] M. Mezhericher, A. Levy, I. Borde, Spray drying modelling based on advanced droplet drying kinetics, Chemical Engineering and Processing: Process Intensification. 49 (2010) 1205–1213. https://doi.org/10.1016/j.cep.2010.09.002.
[163] Handbook of Industrial Drying, CRC Press, 2006. https://doi.org/10.1201/9781420017618.
[164] F. GOMEZ, K. SALEH, Mise en forme des poudres - Séchage par atomisation. Principes, Opérations Unitaires. Génie de La Réaction Chimique. (2012). https://doi.org/10.51257/a-v1-j2256.
[165] A. Mahmoud, S. Caes, M. Brisbois, R.P. Hermann, L. Berardo, A. Schrijnemakers, C. Malherbe, G. Eppe, R. Cloots, B. Vertruyen, F. Boschini, Spray-drying as a tool to disperse conductive carbon inside Na2FePO4F particles by addition of carbon black or carbon nanotubes to the precursor solution, Journal of Solid State Electrochemistry. (2017). https://doi.org/10.1007/s10008-017-3717-x.
[166] A.B.D. Nandiyanto, K. Okuyama, Progress in developing spray-drying methods for the production of controlled morphology particles: From the nanometer to submicrometer size ranges, Advanced Powder Technology. 22 (2011) 1–19. https://doi.org/10.1016/j.apt.2010.09.011.

Chapter II

Na_2FePO_4F/CNT composite as advanced cathode material for Na-ion and K-ion batteries: Optimization of morphology and composition of spray-dried particles toward better electrochemical performance.

Abstract

In this chapter, we report an optimized and easily scalable spray-drying process for the synthesis of Na_2FePO_4F/Carbon nanotubes composite with controlled morphology and good electrochemical performance. The synthesis conditions have been optimized to avoid the formation of Fe-based impurities (Fe(0), Fe_3C, Fe_2O_3). Particular attention has been given to the spray-drying process to optimize both the morphology and composition of the composite material. Several synthesis parameters were modified and adjusted including changing the injection nozzle and the drying atmosphere. The structural and morphological properties of the materials were investigated combining X-ray diffraction, scanning electron microscopy, surface area analysis, and ^{57}Fe Mössbauer spectroscopy characterization techniques. The electrochemical properties were first evaluated in sodium-ion batteries showing excellent performance with an initial discharge specific capacity of 123 mAh/g at C/15 (99% of the theoretical capacity). Also, NFPF-15CNT demonstrated promising electrochemical performance as cathode material for K-ion with a good specific capacity of 80 mAh/g at C/15. The electrochemical desodiation revealed to be the key strategy behind the outstanding performance of $NaKFePO_4F$/CNT cathode material in K-ion batteries with a stable capacity of 114 mAh/g at C/15 which is one of the highest reported capacity as cathode for K-ion batteries.

1. Introduction

The environmental problem that our century is enduring has led to extensive efforts to develop new eco-friendly and efficient energy storage and conversion technologies to ensure the energy transition. Among these, electrochemical storage based on Li-ion technology is expected to be one major solution to energy storage [1] Nevertheless, the demand for large-scale battery systems, to store the energy from wind turbines or solar panels, is rapidly growing. Lithium-ion technology suffers from the uneven distribution and low abundance of lithium in the earth's crust resulting in raising the cost of the technology. The abundance of material is the fundamental factor to consider for the development of electrode materials for large-scale applications. $LiFePO_4$ is considered one of the most promising eco-friendly cathode materials to develop larger-scale production of lithium technology [2]. However, the limited resource of lithium strongly increases the material cost and inhibits the possibility of the development of this technology for large-scale applications.

Sodium is the second lightest and smallest alkali metal after lithium and is widely distributed and highly abundant in the earth's crust. This indicates that finding suitable high-performance electrode materials will place sodium-ion batteries (SIBs) among the promising candidates for the large-scale development of green energy storage technologies [3]. However, the poor diffusion kinetic of Na^+-ions and the volume expansion of the host material upon cycling limit the practical applications of the Na-ion batteries (NIB) technology. Different cathode materials have been reported in the effort to find high-performance electrode materials including metal oxides [4,5], polyanionic systems[6,7], Prussian blue [8,9], and metal fluoride [10]. One of the promising cathode material families is the polyanionic materials and more precisely phosphate compounds. Among these, fluorinated iron-based phosphate, Na_2FePO_4F (NFPF) is reported as one of the

most promising candidates thanks to its strong crystal structure with facile 2D Na^+ pathways and low volume change as well as a relatively high theoretical capacity of 124 mAh/g [11,12]. The presence of fluorine with a strong ionicity leads to the increase of the operating voltage (3 V) and thus the energy density of the material (375 Wh/kg) [11,13]. NFPF material was presented for the first time by Ellis *et al.,* in 2007 and proved to be electrochemically active [14]. It crystallizes in the orthorhombic crystal lattice with Pbcn space group. The FeO_4Fe octahedra are bridged by F^- ions and form dioctahedral units. These units are connected by PO_4^{3-} anions and form the layered structure promoting good Na^+ diffusions. This framework offers great structural stability during cycling as confirmed by NMR study [15]. The challenge linked to this material lies in its poor intrinsic electronic conductivity due to both: the phosphate group and the fluorine ionicity that disturbed the electron localization [11,13].

Despite this drawback, the eco-friendliness and the promising electrochemical performance of NFPF have attracted the interest of the scientific community. Table II-1 presents a non-exhaustive list of investigated synthesis processes and strategies to enhance the electrochemical performance of NFPF material in Na-ion batteries. There are mainly three synthesis processes that have been studied: solid state [11–13,16–20], hydrothermal/solvothermal[21–24], and sol gel [25-28]. More exotic synthesis processes were also reported such as soft templating [29], electrospinning [30], or ultrasonic spray pyrolysis [31]. All these works present pioneering strategies to enhance the electrochemical performance of the material. Particle size reduction and carbon encapsulation are considered effective and simpler approaches to increase both the ionic and electronic conductivity of the NFPF material. Kawabe *et al.*, [11] reported a carbon-coated NFPF solid-state method inspired by a similar method used for $LiFePO_4$ by adding ascorbic acid as a carbon source. The developed NFPF cathode material delivered an initial discharge capacity of 110 mAh/g at C/20. This approach of adding carbon precursors that are reduced during the heat treatment steps to form

conductive carbons seems to be efficient for enhancing electrochemical performance. Indeed, several carbon precursors were tested such as sucrose, citric acid, ascorbic acid, and biocarbon from yeast. Other methods rely on the addition of carbon after the synthesis of the NFPF material such as conductive polymer, mesoporous carbon, graphene nanosheet, and carbon nanotube. Ko *et al.,* [17] present NFPF composite with a coating of poly(3,4-ethylene dioxythiophene) (PEDOT) as a conductive polymer. The prepared material exhibits a discharge capacity of 123.1 mAh/g at C/5 and 76 mAh/g at a high C-rate of 10 C showing one of the best electrochemical performances for this material reported in the literature but with a complicated, multi-step, and expensive synthesis method. Particle nanosizing by grinding or by controlling the particle size evolution during the synthesis was also presented in recent works [16,22,29,30]. Different morphologies have been tested to enhance the electrochemical performance like a hollow sphere [23], nanorod [22], nanofibers [30]. Recent works also presented the combination of both nanosizing and carbon composite formation. For example, Xun *et al.,* reported a one-step synthesis of NFPF nanorods with a ball mixing addition of carbon nanotubes (CNT) and graphene oxide (GO) [22]. They obtained a specific capacity of 118 mAh/g at C/10 and 67.5 mAh/g at a 10 C rate with a capacity retention of 80% after 1200 cycles.

Table II-1: A non-exhaustive list of investigated synthesis processes and strategies to enhance the electrochemical performance of NFPF material in Na-ion batteries.

Synthesis Process	Reported discharge Capacity	Strategy to enhance the electrochemical performance	Reference
Solid-state	110 mAh/g at C/20	Carbon coating with ascorbic acid	[11]
Solid-state	108.6 mAh/g at C/10	Nanosizing with polyfurfuryl alcohol as size reducing agent + carbon coating from glucose reduction	[12]
Solid-state	100-110 mAh/g at C/10	Coating with ascorbic acid and partial substitution of iron with Mn	[13]
Multistep Solid-state	110 mAh/g at C/10	Polyol coating + Nanosizing	[16]
Multistep Solid-state	123.1 mAh/g at C/5	Coating with conductive polymer PEDOT	[17]
Multistep Solid-state	115 mAh/g at C/10	Metal-organic framework + mesoporous carbon network	[18]
Ball milling combined with solid-state	114 mAh/g at C/10	Mesoporous composite	[19]
Solid-state	117 mAh/g at C/10	Green carbon coating with ascorbic acid	[20]
Solvothermal	114.3 mAh/g at C/10	Carbon coating with glucose	[21]
Hydrothermal	118 mAh/g at C/10	Nanoshaping into nanorod and carbon composite by ball mixing with CNT and GN	[22]
Solvothermal	120.1 mAh/g at C/10	Double shelled hollow microsphere composite with carbon	[23]
Hydrothermal	80 mAh/g at C/10	Crystalline transformation to alpha-NFPF	[24]
Sol-gel	100 mAh/g at C/10	Carbon composite by reduction of citric acid or ascorbic acid or urea during synthesis	[25]
Sol-gel	114.3 mAh/g at C/10	Biocarbon nanocomposite hollow sphere from yeast cell	[26]
Ultra-rapid combustion	70 mAh/g at C/10	Carbon composite from citric acid	[27]
Sol-gel	115.5 mAh/g at C/10	Porous sponge-like morphology and composite with carbon from oxalic acid	[28]
Soft templating	116 mAh/g at C/10	Nanosizing by high energy ball milling	[29]
Electrospinning	117.8 mAh/g at C/10	Nanosizing and composite structuration with carbon fibers	[30]

Ultrasonic spray pyrolysis	89 mAh/g at C/10	Carbon coating by sucrose reduction + hollow sphere structuration	[31]
Spray-drying assisted solid-state	**123.8 mAh/g at C/15**	**Carbon nanotubes network inside particles**	**This work**

In previous works, we presented the synthesis protocol of NFPF by spray-drying method [32–34] This technique is easily up-scalable and offers a high homogeneity of the precursors. This synthesis method leads to the formation of spherical particles using the rotary nozzle (particle size around 10 µm). The dense structure of the spheres and limitation of ion diffusion in these large particles in the previous work [33–35] showed limitations of the electronic conductivity of the pristine material. Two strategies could overcome these limitations. The first one consists of grinding the particles and the second one is the carbon addition during synthesis. Our previous works evidenced that the grinding leads to the oxidation of iron in the structure [35]. It also evidenced the effect of carbon addition (carbon nanotubes or carbon black) to NFPF on structural, morphological, and electrochemical properties in lithium-ion batteries [33–35]. This work aims to enhance the electrochemical performance of NFPF cathode material for Na-ion batteries using different and innovative strategies. Particular attention is paid to the control of the morphology of the NFPF particles to reduce the size of the obtained particles after spray drying. The use of an alternative injection mode will be discussed. This work also presents the effect of the drying gas on the structural and electrochemical properties of the materials with special attention to avoid the partial oxidation of the iron during each step of the synthesis process. Finally, the optimized NFPF is used as cathode material in K-ion batteries for the first time. The structural and morphological properties were systematically investigated by combining X-ray diffraction, Mössbauer spectroscopy, scanning electron microscopy, and BET measurement. The electrochemical performance of the materials were investigated using galvanostatic cycling, impedance spectroscopy, and cyclic voltammetry.

2. Experimental

2.1. Materials synthesis

NFPF and NFPF_xCNT powders were prepared by spray-drying method followed by calcination under a controlled atmosphere. 100 mmol of Fe^0 (99.9%, abcr GmbH) is attacked in 100 mL of milliQ water (18.2 MΩ/cm) by 200 mmol of acetic acid at 90°C under argon. 75 mmol of citric acid (Alfa Aesar) is directly added to complex and to stabilize Fe^{2+}. After 24 h, 100 mmol of $NH_4H_2PO_4$ (Sigma Aldrich), 100 mmol of NaF(Sigma Aldrich), and 100 mmol of NaOH (Sigma Aldrich) were added to the solution with 900 mL of milliQ water (18.2 MΩ/cm). The solution was then homogenized under argon at room temperature by magnetic stirring for one hour. In the case of the NFPF_xCNT composite powders, 5 to 15wt% of carbon nanotube (1.07 to 3.23g) (AQ30X Nanocyl) were added at the same time as the other precursors. The solution/suspension (with CNT) is then spray-dried in a Niro mobile minor spray dryer at an inlet temperature of 150°C and outlet temperature of about 90°C with 25 mL/min feed rate and 3 bars of air pressure using a rotating or a bi-fluid injector. The obtained powders were then heat-treated at 600°C under Ar flow for different durations with a heating rate of 150°C/h.

2.2. Structural and morphological characterization of NFPF and NFPF_xCNT

The crystallographic structure of powders was studied by the X-ray powder diffraction (XRD) technique using a Bruker D8 diffractometer (Cu K_α radiation). The diffraction data were recorded in the 2Theta range of 10-60° with a step size of 0.02. The morphology of the obtained materials was investigated with scanning electron microscopy (XL30 FEG-ESEM, FEI). Measurements of specific surface

area and texture properties, including analysis of porosity for all the samples (NFPF and NFPF_xCNT), were determined through measuring nitrogen (N_2) adsorption-desorption isotherms with a Micromeritics ASAP 2020 Plus system. Samples were degassed at 150°C for 6 h before analysis.

^{57}Fe transmission Mössbauer spectroscopy spectra were recorded at room temperature with a constant-acceleration spectrometer with a ^{57}Co(Rh) source. The Mössbauer spectral absorbers were prepared with 40 mg/cm^2 of materials mixed with boron nitride. The spectrometer was calibrated at room temperature with the magnetically split sextet spectrum of a high-purity α-Fe foil as the reference absorber. The measurements were carried out in the [± 4 mm/s] and [± 12 mm/s] velocity ranges. Fitting the experimental data, the spectral parameters such as isomer shift (δ), quadrupole splitting (Δ), linewidth (Γ), and relative resonance areas of the different spectral components were determined. The validity of fits was judged based on minimizing the number of parameters and χ^2 values.

2.3. Electrochemical characterization

The electrochemical measurements were performed at room temperature in CR2032 coin cell configuration. The positive electrode was prepared by mixing the active material, carbon black as a conductive agent, and polyvinylidene fluoride (PVDF) as a binder with a ratio of 7:2:1. In the case of the composite NFPF/CNT with 15% of CNT, the amount of carbon black was adjusted to obtain 20wt% of carbon in the electrode. The electrode was mixed in N-methyl-2-pyrrolidone (NMP) with zirconia balls (5mm of diameter) for 1 h using a planetary mill (Retsch PM400/2, 150 rpm, alternate rotation mode). The slurry was then tape cast on aluminum foil by doctor blade method and then dried at 110°C for 12 h under vacuum. The electrodes were then cut to obtain an electrode disc of 15 mm in diameter with about 1 mg/cm^2. The coin cells were

assembled in an argon-filled glove box using a Whatman® filter separator and 1 M $NaPF_6$ dissolved in propylene carbonate as an electrolyte. Sodium foil was used as the counter and the reference electrode. K-ion button cells were assembled with the same protocol as for sodium, the electrolytes used were 0.8 M KPF_6 in different solvents like propylene carbonate or ethylene carbonate and propylene carbonate 1:1 volume ratio, with our without 10wt% fluoroethylene carbonate as a stabilizing agent leading to these three compositions: i) 0.8 M KPF_6 in PC with 10wt.% of FEC, ii) 0.8 M KPF_6 in EC:PC (1:1 v:v) and iii) 0.8 M KPF_6 in EC:PC (1:1 v:v) with 10wt.% of FEC. Metallic potassium was used as a counter and reference electrode. Galvanostatic cycling tests were carried out in the voltage ranges of 2.2-4.5 V and 2-4.3 V *vs.* Na^+/Na and 2-4.2 V *vs.* K^+/K at different cycling rates using a Neware BTS4000 potentiostat. Electrochemical impedance spectroscopy (EIS) with 5 mV amplitude in the frequency range from 1 MHz to 10 mHz and cyclic voltammetry between 1 and 5 V *vs.* Na^+/Na at a speed rate of 0.05 to 1 mV/s were measured using a VMP3 Bio-logic potentiostat. The obtained EIS data were fitted with Aftermath software from Pine Research Instrumentation. All electrochemical tests were carried out at room temperature.

3. Results and discussion

3.1. Influence of the nozzle type on microstructure.

Spray drying is a highly versatile process and can be adapted to tune the particle's size and morphology. The size of spray-dried particles is influenced by feedstock properties, spray drying geometry, spraying conditions, and drying conditions. Our previous works show that electrode materials (phosphates, oxides, titanate…) with a particle size of 5-20 µm were obtained using a conventional rotary nozzle by spray drying method [33–36]. Two injections are compared in this work: the rotary and bi-fluid nozzles. In the spray drying process, all injection modes result in the formation of droplets from a feedstock (solution or suspension). For the rotary nozzle, these droplets are formed due to centrifugal force and the particle size is inversely proportional to the rotation velocity. In the case of the bi-fluid nozzle, this is the mixing of two fluid (solution and gas) that forms the droplet, the droplet size can be greatly reduced by an increase of the gas injection pressure.

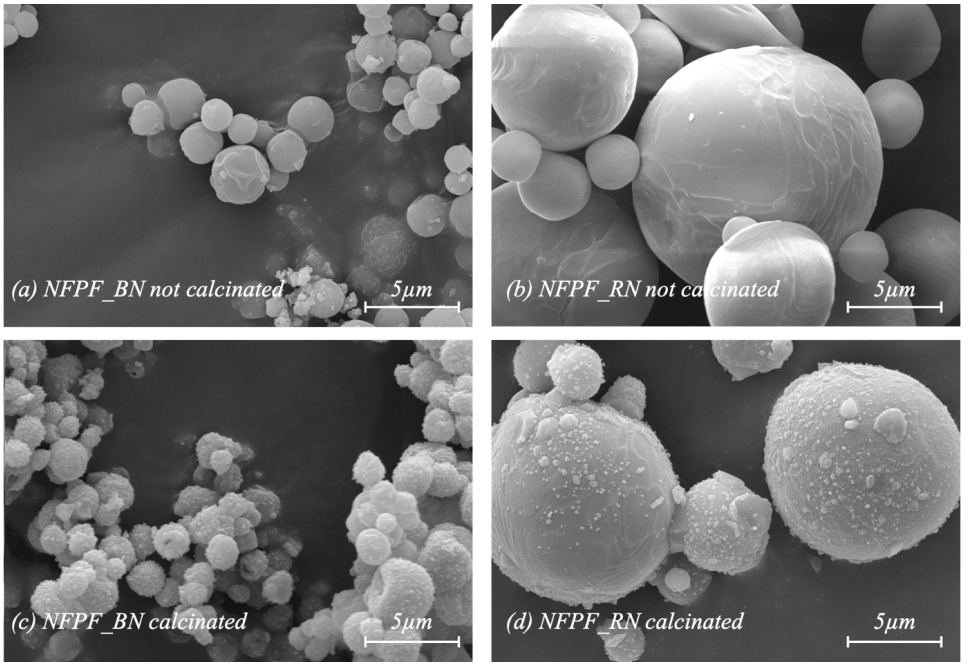

Figure II-1: SEM micrographs of spray-dried precursors of NFPF materials obtained before and after calcination at 600°C for 12h under Ar flow: left) bi-fluid nozzle (BN) and right) rotary nozzle (RN).

Figure II-1 compares the scanning electron micrographs of NFPF materials prepared using two nozzle modes, rotary nozzle (NFPF_RN) and bi-fluid nozzle (NFPF_BN) before and after heat treatment. Both nozzle modes lead to the formation of spherical particles when applying the same pressure of injection. However, a clear difference in particle size is observed with about 8-10 µm (for NFPF_RN) and 1.5 µm to 3 µm for NFPF_BN. The smaller particle size would result in a better electrode active material-electrolyte contact and promote shorter electron diffusion pathways leading to enhanced electrochemical performances.

Previous works have shown that the crystalline NFPF phase is obtained at 600°C for 12 h by spray drying method with the rotary nozzle (NFPF_RN). The influence of the reduction of particle size on the duration and temperature of crystallization

was investigated by X-ray diffraction at varied heat treatment durations. Figure II-2 illustrates the XRD patterns of obtained NFPF_BN powders at different heat treatment durations ranging from 1 h to 12 h at 600°C. First of all, the temperature of crystallization has to remain at 600°C despite the diminution of the size of the primary particles. In Figure II-2, the sample after 2 h presents a better crystallinity, but it has not been registered on the same sample and this difference cannot be explained in another way. However, a heat treatment duration of 1 h is inadequate to fully crystallize the NFPF material.

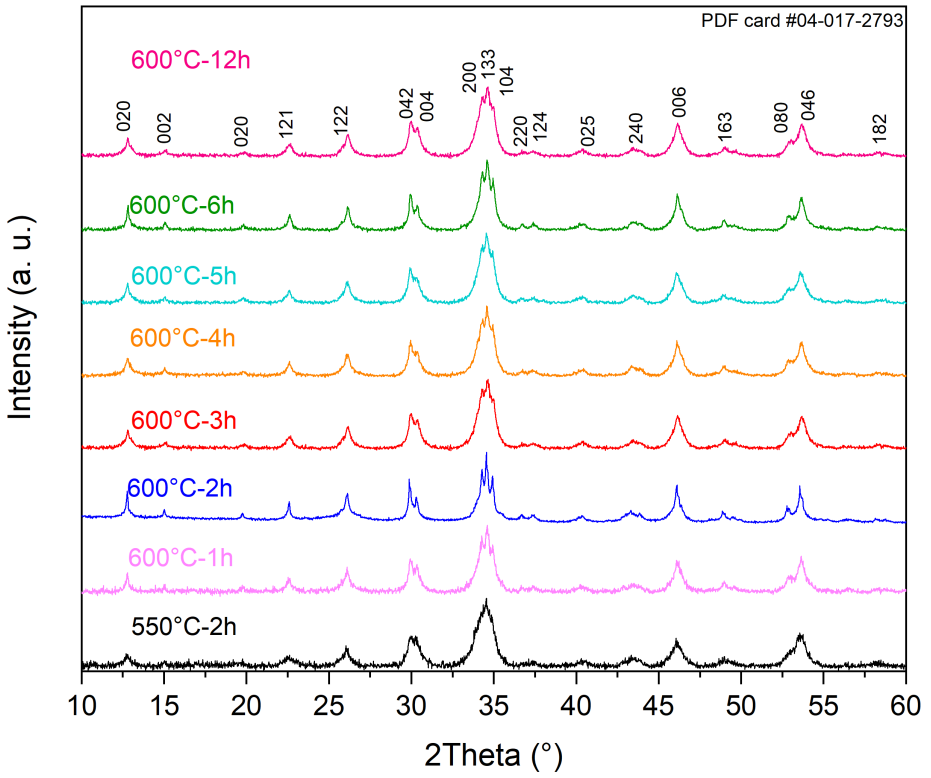

Figure II-2: XRD patterns of NFPF_BN powders obtained by spray drying at different temperatures of 550°C and 600°C for a duration ranging from 1 h to 12 h under argon.

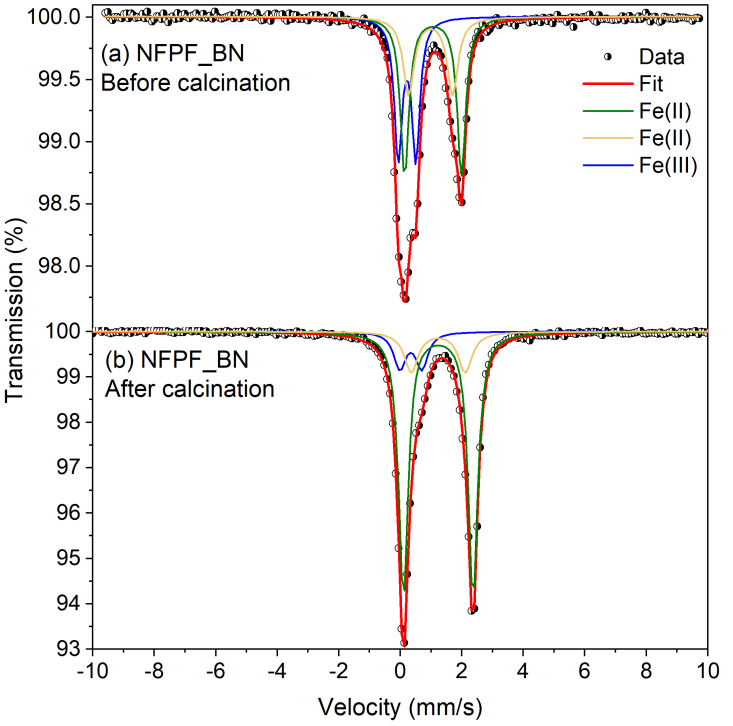

Figure II-3: ^{57}Fe Mössbauer spectra recorded at room temperature of NFPF material obtained by spray-drying (a) before and (b) after calcination at 600°C (under Ar flow) for 2 hours.

Table II-2: ^{57}Fe Mössbauer hyperfine parameters for NFPF prepared by spray drying with a bi-fluid nozzle before and after calcination at 600°C for 2 hours.

Samples		δ (mm/s)	ΔEq (mm/s)	Γ (mm/s)	Area (%)
NFPF_BN	Fe(II)	1.23 (1)	1.78(4)	0.52(4)	26
Before calcination	Fe(II)	1.23(2)	2.30(6)	0.42(3)	41
	Fe(III)	0.27 (4)	0.71(9)	0.38(8)	33
NFPF_BN	Fe(II)	1.23 (3)	2.266(6)	0.369(1)	72
After calcination	Fe(II)	1.23(2)	1.754(2)	0.526(7)	16
	Fe(III)	0.34(1)	0.719(3)	0.467(1)	12

The room temperature ^{57}Fe Mössbauer spectra of NFPF_BN before and after calcination at 600°C for 2 h under argon are presented in Figure II-3, and their corresponding Mössbauer hyperfine parameters are summarized in Table II-2. The spectrum before the calcination consists of an asymmetric doublet. This confirms the presence of only paramagnetic iron at room temperature, which indicates that no magnetic iron is found in the sample like Fe_2O_3 or alpha-Fe^0. A good fit has been obtained using three components: two components correspond to Fe(II) (26% and 41% surface area) with a close isomer shift but a slightly different quadrupole splitting showing two different local environments. The third component corresponds to Fe(III) which indicates that partial oxidation of the iron precursors during the spray drying step occurred due to the use of hot air as drying gas. In addition, the high value of full width at half maximum (FWMH) confirms the amorphous state of the material. After calcination, the ^{57}Fe Mössbauer spectrum consists of a sharp asymmetric doublet. A good fit has been obtained using three components corresponding to two Fe(II) sites and one Fe(III) site. The total area of the Fe(II) site is 88 % showing a great carbothermal reduction during the calcination step. These two sites have the same isomer shift with a slightly different quadrupole splitting, corresponding to octahedral sites in the NFPF structure [33–35]. The presence of Fe(III) site in the NFPF material is not harmful to the electrochemical performance as it was shown in our previous work using *in situ* Mössbauer studies [33] that this Fe(III), corresponding to oxidized NFPF, is completely reduced to Fe(II) after the first discharge (sodiation process). Also, the change of nozzle has another influence on the impurities found in the NFPF samples. Indeed, the use of the rotary nozzle leads to the presence of γ-Fe_2O_3 impurities in the NFPF_RN sample which is no more the case in the NFPF_BN sample [33–35].

A galvanostatic charge-discharge cycling test was used to evaluate the electrochemical performance of the NFPF material as cathode material for Na-ion batteries. The obtained electrochemical performance at different current densities

within the voltage range of 2.2-4.5 V *vs.* Na^+/Na for NFPF_BN and NFPF_RN were compared. The charge-discharge profiles are presented in Figure II-4. The NFPF_RN sample in Na-ion cell delivered discharge capacities of 17, 13, 7, and 6 mAh/g at cycling rates of C/15, C/10, C/5, and 1C respectively. The capacity of 17 mAh/g at C/15 corresponds to only 14% of the theoretical capacity (124 mAh/g), which decreases with the increase of the C-rate. The plateau can only be seen in the discharge profile at C/15 at around 3 V which is consistent with the results reported in the literature and is not visible in the other C-rates[11]. The NFPF_BN-based cathode in Na-ion cell delivered discharge capacities of 55, 35, 21, and 10 mAh/g at cycling rates of C/15, C/10, C/5, and 1C respectively. The discharge capacity at C/15 of 55 mAh/g represents 44% of the theoretical capacity. In comparison, NFPF_BN delivered higher capacities compared to NFPF_RN at all C-rates. The charges-discharge profiles are similar at current densities of C/5, C/10, and C/15. The two plateaus are observed at C/15 at 3 and 2.8 V in the discharge curve. A polarization phenomenon is observed at all C-rates and the insertion/disinsertion plateau is no more visible at 1C current densities. The comparison of the NFPF_BN and NFPF_RN demonstrates that the decrease of the particle size leads to improved electrochemical performance thanks to the smaller ionic and electronic pathway during the insertion/disinsertion of sodium ions. However, both samples show a huge polarization phenomenon with a decrease of the insertion potential leading to a decrease of the performance during cycling. This is the consequence of the low electrical conductivity of the NFPF material and low electrode/electrolyte contact area, leading to an insufficient electron diffusion during Na-insertion/deinsertion into/from NFPF material. The advantage of the spray-drying technique is its versatility which enables the formation of carbon-based composite electrode materials in one step to enhance the electrical conductivity. Indeed, the addition of CNT in the solution of the precursors leads to the formation of a carbon network inside the cathode materials particles [32]. As it is stated that the bi-fluid nozzle allows the preparation of

a smaller particle size with enhanced electrochemical performance, the composite materials will be prepared with this nozzle to maximize the electronic conductivity and reduce the ion diffusion lengths in particles.

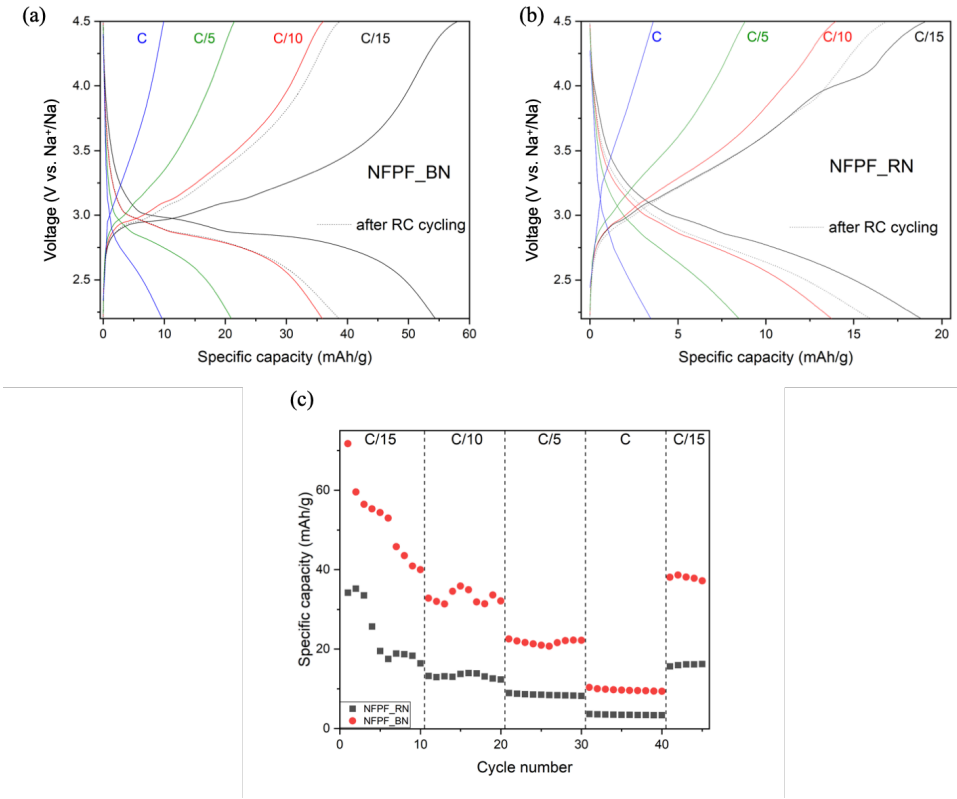

Figure II-4: Charge/discharge curves of the first cycle of NFPF prepared by (a) a bi-fluid nozzle, (b) a rotary nozzle, and (c) Evolution of discharge capacity vs. cycle number of both materials cycled at C/15, C/10, C/5, 1C rates (2.2-4.5 V vs. Na^+/Na) at room temperature.

Figure II-5 illustrates the XRD patterns of NFPF with different carbon nanotubes (CNTs) ratios of 0, 5, 10 and 15% (NFPF_xCNT, with x= 5, 10, 15wt%) after heat treatment. The addition of both 5% and 10% has a quite low influence on the structural properties of the NFPF as illustrated by XRD analysis. Indeed, each peak in the diffractograms can be indexed in the NFPF (Pbcn space group)

structure. The crystallite size remains small of about 6 to 8 nm as calculated by Scherrer formula: CS = 0.9 λ/(β.cos(θ)), where λ is the wavelength, β is the full width at half maximum of the peak, and θ is the Bragg angle of diffraction. The addition of 15% of CNTs leads mainly to the formation of Fe^0. Indeed, the most intense peak at about 45° (2Theta) corresponds to the Fe^0. The crystallite size of the NFPF remains small of about 9 nm.

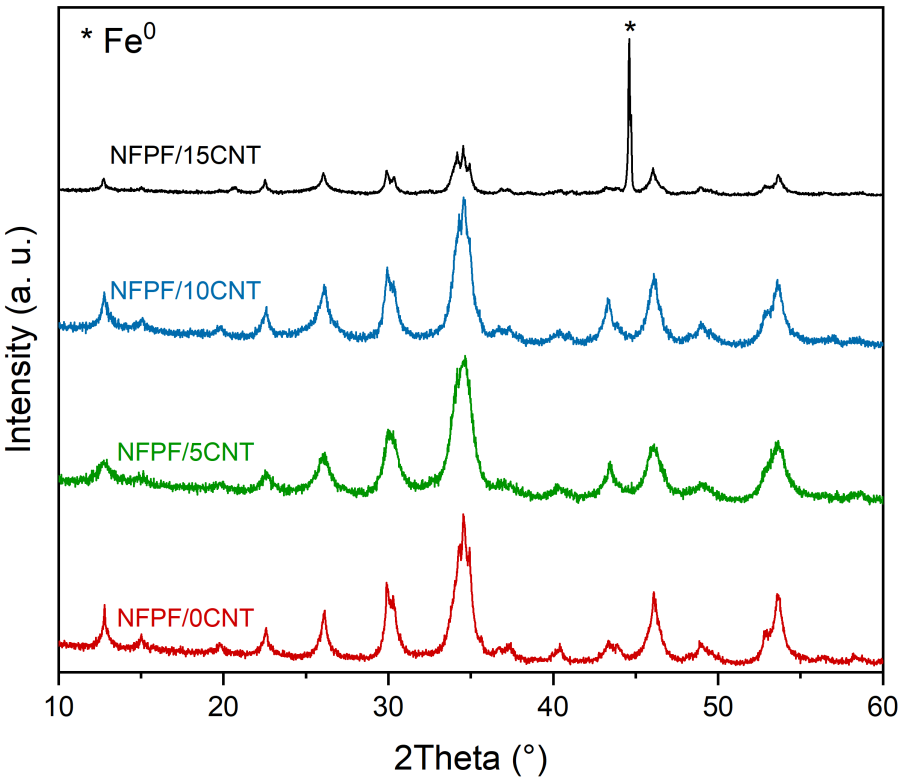

Figure II-5: XRD patterns of NFPF_BN materials obtained by spray drying at 600°C for 2 h without CNT (red) with 5wt% of CNT (green), with 10wt% of CNT (blue) and 15wt% of CNT (black).

To deeply investigate the influence of the addition of CNT on NFPF materials, ^{57}Fe Mössbauer analysis was performed. The Mössbauer spectra are presented in

Figure II-6 and fitted parameters are summarized in Table II-3. The obtained results evidenced the presence of Fe^0 in NFPF_10CNT and NFPF_5CNT materials. Indeed, the ^{57}Fe Mössbauer spectrum of NFPF_10CNT has mainly a doublet form with a small intensity sextet component. This spectrum was fitted using 4 components: 2 sites of Fe(II) and one site of Fe(III) that can be attributed to the octahedral environment of Fe site in NFPF. The last component is magnetically ordered at room temperature with an isomer shift of 0.12 mm/s that is consistent with the presence of Fe^0. The concentration of the Fe^0 impurity is about 7%. The same conclusion can be done for NFPF_5CNT with a percentage of Fe^0 of 9%. As the Fe^0 was not visible through XRD analysis, it means that it has an amorphous structure or that it is mainly nanoparticles. Regarding the NFPF_15CNT, the ^{57}Fe Mössbauer analysis shows a presence of sextet with a high concentration (30%) corresponding to Fe^0. The NFPF_15CNT spectrum was fitted also with 4 components: 2 Fe(II) sites, one Fe(III) site in NFPF, and the Fe^0. The addition of CNTs leads to a higher carbothermal reduction of the iron.

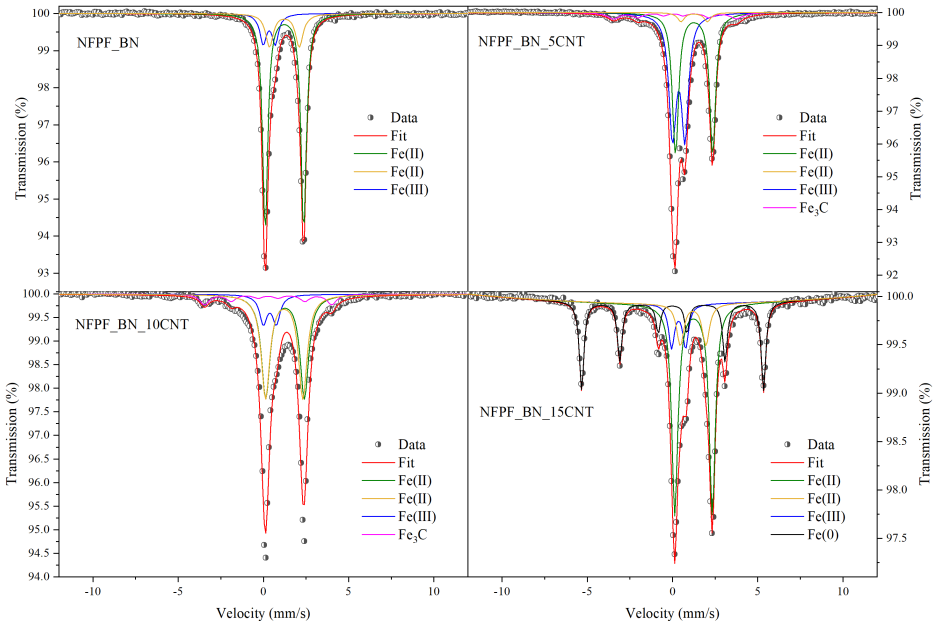

Figure II-6: ^{57}Fe Mössbauer spectra recorded at room temperature of NFPF_BN, NFPF-5CNT, NFPF_10CNT, and NFPF_15CNT prepared by spray drying method after calcination at 600°C for 2 h.

Table II-3: Hyperfine Mössbauer parameters for NFPF_BN, NFPF_5CNT, NFPF_10CNT, and NFPF_15CNT prepared by spray drying method with a bi-fluid nozzle after calcination at 600°C for 2 h.

		∂ (mm/s)	ΔEq (mm/s)	Γ (mm/s)	Field	Area (%)
NFPF_BN	Fe(II)-NFPF	1.23(3)	2.26(6)	0.36(9)	-	72(1)
	Fe(II)-NFPF	1.23(2)	1.75(4)	0.52(7)	-	16(1)
	Fe(III)-NFPF	0.34(1)	0.71(9)	0.46(7)	-	12(1)
NFPF _5CNT	Fe_3C	0.10(1)	0.092(1)	0.559(5))	22.4(3)	6(1)
	Fe(II)-NFPF	1.26(1)	2,18(3)	0.424(4)	-	45(1)
	Fe(II)-NFPF	1.26(1)	1.556(3)	0.471(4)	-	3(1)
	Fe(III)-NFPF	0.36(1)	0.725(4)	0.509(4)	-	45(1)
NFPF_10CNT	Fe_3C	0.27(2)	0.01(5)	0.66	23.1(2)	9(1)
	Fe(II)-NFPF	1.218(1)	2.19(2)	0.62	-	41(1)
	Fe(II)-NFPF	1.268(1)	2.27(2)	0.62	-	41(1)
	Fe(III)-NFPF	0.377(1)	0.76(2)	0.54	-	10(1)
NFPF_15CNT	Fe(0)	0.001(5)	0.00	32(2)	33.12(4)	31(1)
	Fe(II)-NFPF	1.235(5)	2.19(1)	0.43(2)	-	49(1)
	Fe(II)-NFPF	1.203(3)	1.50(5)	0.48(2)	-	11(1)
	Fe(III)-NFPF	0.36(2)	0.82(4)	0.41(2)	-	10(1)

The effect of carbon nanotubes addition on the morphological features of NFPF material was investigated by scanning electron microscopy. Figure II-7 displays the SEM images of the NFPF_xCNT (with x=0, 5, 10, 15 wt.% of CNT) materials prepared by the bi-fluid nozzle. NFPF_xCNT materials consisted of collapsed particles with an average diameter from 1.5 to 5 µm, the average particle size increases with the increase of the percentage of CNT, which is in good agreement with literature that explained this particular morphology result from the formation of a viscoelastic shell during the drying step [35,38]. This microstructure is attractive for an electrode material as the major limitation of fluorophosphate compounds is their low electronic conductivity. Indeed, the homogeneous network of CNTs should ensure and increase the electronic conductivity and circumvent the kinetic limitations during cycling [38–40]. Also, the specific surface area of the powders, measured by BET technique, greatly increases with the increase of the amount of carbon nanotube (Table II-4). As it can be seen, the surface area of NFPF_BN is low (less than 2 m^2/g), with the addition of 5wt% of CNT, the BET values are already 8 times higher. This value increases even more with the addition of 10% or 15wt% of CNT. In this last case, the specific surface area reaches 100 m^2/g. This high surface area facilitates the percolation of electrolyte and ensures improved contact with the cathode material.

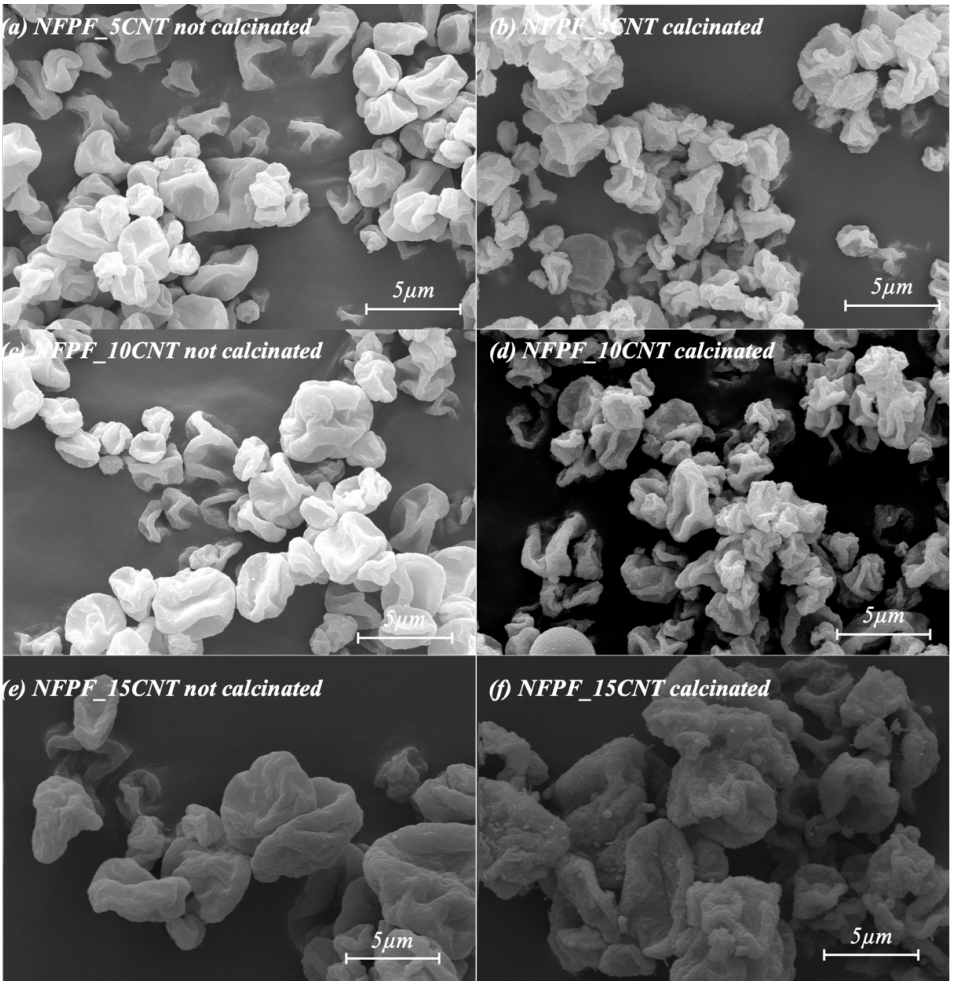

Figure II-7: Scanning electron micrographs of (a)-(b)NFPF_5CNT, (c)-(d) NFPF_10CNT,(e)-(f) NFPF_15CNT before (left) and after (right) calcination at 600°C for 2h under argon.

Table II-4: Specific surface area of NFPF_xCNT samples measured by BET.

Sample	Specific surface area (m^2/g)
NFPF_BN	1.75
NFPF_5CNT	13.83
NFPF_10CNT	75.85
NFPF_15CNT	100.09

The evolution of the charge/discharge curves recorded at different C-rates of C/15, C/10, C/5, and C are presented in Figure II-8a, b, and c for NFPF_5CNT, NFPF_10CNT, and NFPF_15CNT, respectively. All the first charge curves for different electrodes (NFPF_XCNT) illustrate a similar voltage profile. The difference between each sample can be observed at the first discharge. Indeed, for NFPF_5CNT, the discharge plateau is almost not visible while with 10 and 15wt% of CNT, the two discharge plateaus are observed. From the C/10 rate, the plateaus are only visible for NFPF_15CNT. In addition, the sample with only 5wt% of CNT demonstrates really low capacity at C/15, C/10, C/5, and 1C rate. Figure II-8d presents the evolution of the capacity with cycle number at different cycle rates of NFPF_xCNT (with x=0, 5, 10, and 15wt%). As shown the presence of CNT greatly influences the electrochemical performance of the NFPF material. The initial discharge capacity at C/15 of NFPF_xCNT with 0, 5, 10, and 15wt% of CNT are 71, 66, 79, and 94 mAh/g, respectively. The addition of only 5wt% of CNT leads to slightly higher specific capacity in the first cycle at C/15 rates. After three cycles, the capacity fades in both cases but NFPF_5CNT shows a slower decrease and the capacity obtained is slightly higher than NFPF_BN. At the 5th cycle and the capacity of NFPF_5CNT is 57 mAh/g and only 42 mAh/g for NFPF_BN. The addition of 5wt% of CNT leads to the increase of the specific at each cycling rate compared to NFPF_BN. The addition of 10wt% leads even to higher capacity at C/15 rate of 72 mAh/g but the difference is no more visible with the increase of the cycling rate to C/5 or C and also at C/15 after cycling at high speed. This concludes that 10wt% is not sufficient to improve the electrochemical performance. A clear difference is observed for 15wt% of CNT with improved specific capacity at all cycling rates. Discharge capacities of 94, 79, 55, 30, and 72 mAh/g are delivered at C/15, C/10, C/5, C, and then at C/15 respectively. Nevertheless, 75% of the theoretical capacity was delivered at the first cycle at C/15 which decreases to 56% after the rate capability test. This low specific

capacity is caused by the presence of Fe^0 impurity. To solve this issue, we studied different synthesis parameters to obtain a pure phase with 15wt% of CNT.

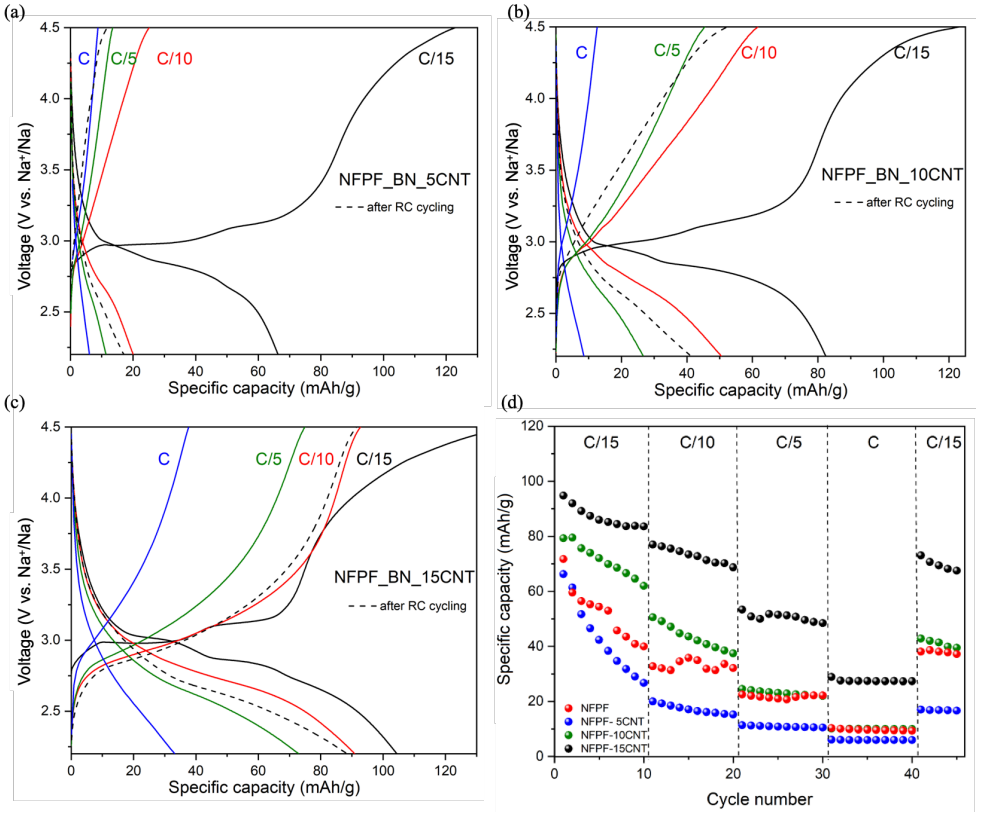

Figure II-8:Charge/discharge curves of the first cycles at C/15, C/10, C/5, 1C of a) NFPF_5CNT, b) NFPF_10CNT and c) NFPF_15CNT materials. d) Evolution of discharge capacity vs. cycle number of NFPF, NFPF_5CNT, NFPF_10CNT, and NFPF_15CNT materials cycled at C/15, C/10, C/5, 1C rates (2.2-4.5 V vs. Na^+/Na) at room temperature.

3.2. Influence of the synthesis process on the purity and electrochemical performance of the material.

To avoid the partial oxidation of Fe(II) in NFPF material, an ATEX spray-dryer (O_2 < 50 ppm) with argon as drying inert gas was used. The spray-dried powder was transferred to an argon-filled glovebox to avoid contact with Air. In addition, degassed water was used in the preparation of the precursors' solution as described in the synthesis protocol of NFPF material.

Figure II-9 illustrates the ^{57}Fe Mössbauer spectra of the NFPF_BN_ATEX powders and the corresponding fitted parameters are presented in Table II-5. The first sample studies the precursors just after spray drying under Ar. The Mössbauer spectrum has a symmetric doublet shape. The fit of the spectrum reveals the presence of only Fe(II) sites. As expected, the change of drying gas prevents the partial oxidation of iron during the drying step. After calcination (NFPF_BN_ATEX) (Figure II-9b), the Mössbauer spectrum consists of an asymmetric doublet that can be fitted using only three components corresponding to 2 Fe(II) sites and one Fe(III) site. This result shows the same tendency as the previous experiment and it does not prevent oxidation. The major difference is that the amount of Fe(III) present in the sample after annealing is divided by a factor 2.

The Mössbauer spectrum of NFPF_15CNT_ATEX is presented in Figure II-9. Good quality fits of the data were obtained using a distribution of doublets (66 Fe-at%) with average isomer shift and quadrupole splitting values typical of Fe(II) in Na_2FePO_4F [33], another doublet (27 Fe-at%), typical of Fe(III), which is associated to some oxidized NFPF material and a sextet (6 Fe-at%) with an isomer shift, $\delta = 0.01$ mm/s, and magnetic hyperfine field $B_{hf} = \mu_0 H_{hf} = 33$ T, which is attributed to Fe^0. Even if the use of ATEX conditions does not prevent the

formation of Fe^0, it greatly reduces the amount of this impurity. Indeed, only 6 Fe-at% is detected after synthesis under Ar whereas more than 30 Fe-at% was found in the NFPF_15CNT sample prepared in Air. In addition, the amount of Fe(III) corresponding to oxidized NFPF materials has been dramatically increased denoting the benefits of preparation under a controlled atmosphere. The NFPF_15CNT_ATEX powder has over a quarter of its iron content as Fe(III) where NFPF_15CNT has only 11 Fe-at%. Even if the Fe(III) is completely reduced after the first discharge, this high proportion of Fe(III) is harmful for its possible application. As the reduction of Fe(III) occurs, it also consumes Na-ion which makes it unsuitable for full battery application, or a pre-cycling against sodium should be performed to prevent depletion of Na.

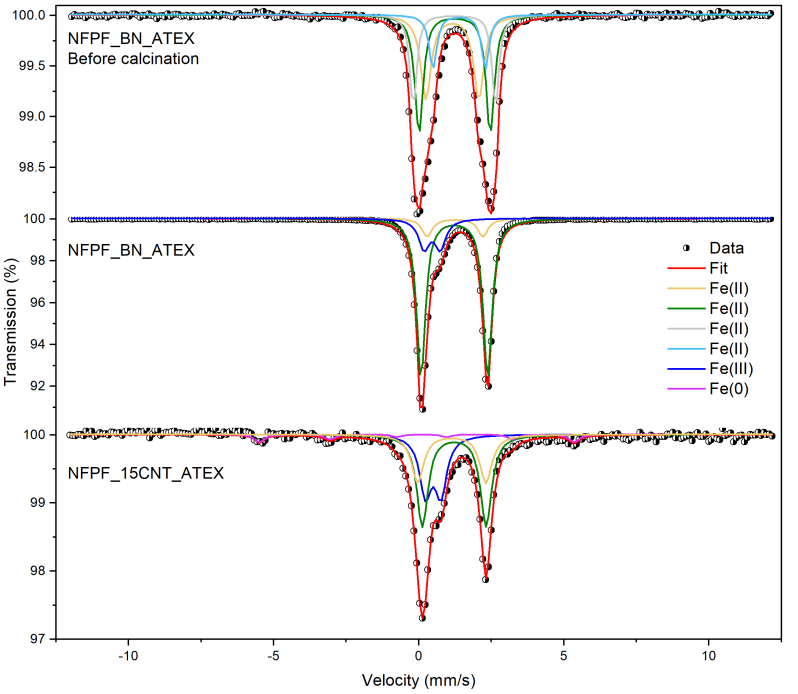

Figure II-9: ^{57}Fe Mössbauer spectra recorded at room temperature of NFPF_BN_ATEX before calcination, NFPF_BN_ATEX, and NFPF_15CNT_ATEX after calcination at 600°C for 2 h under argon.

Table II-5: Fitted Mössbauer parameters of NFPF_BN_ATEX before calcination, NFPF_BN_ATEX calcinated NFPF_15CNT_ATEX after calcination at 600°C for 2 h under argon.

		∂ (mm/s)	ΔE_q(mm/s)	Γ (mm/s)	B_{hf}(T)	Area (%)
NFPF-ATEX-before calcination	Fe(II)-NFPF	1.16(1)	1.82(3)	0.43(3)	-	30(1)
	Fe(II)-NFPF	1.24(1)	2.45(2)	0.32(2)	-	34(1)
	Fe(II)-NFPF	1.23(1)	2.83(2)	0.26(2)	-	22(1)
	Fe(II)-NFPF	1.39(2)	1.80(3)	0.30(4)	-	14(1)
NFPF-ATEX-after calcination	Fe(II)-NFPF	1.25(1)	1.92(1)	0.41(1)	-	10
	Fe(II)-NFPF	1.23(1)	2.30(1)	0.34(1)	-	73
	Fe(III)-NFPF	0.46(1)	0.56(1)	0.45(1)	-	17
NFPF-15CNT-ATEX-after calcination	Fe(II)-NFPF	1.22(1)	2.20(2)	0.47(1)	-	42
	Fe(II)-NFPF	1.14(2)	2.35(3)	0.49(1)	-	24
	Fe(III)-NFPF	0.50(1)	0.53(2)	0.49(1)	-	27
	Fe(0)	0.01	0.16(9)	0.42(1)	33.7(3)	6

The rate capability test presented in Figure II-10 gives the evolution of discharge capacity on cycling at increasing rates from C/15 to 1C of NFPF_BN_ATEX and NFPF_15CNT_ATEX. NFPF_BN_ATEX shows no improvement in capacity retention despite the lower percentage of Fe(III) contained in the NFPF material. Nevertheless, the lower amount of Fe(III) has the advantage of consuming less sodium during the first discharge, which is necessary for further developments in full cell configuration. The significant reduction of Fe^0 content in the NFPF_15CNT_ATEX composite material induced an increase of specific capacity mainly at low cycling rate. Indeed, a discharge capacity of 104 mAh/g is delivered at the first cycles at C/15. These results tend to denote that a composite material without any Fe^0 impurities should lead to much better performance even if the NFPF is partially oxidized. To reduce the amount of Fe^0 and Fe_3C, a

combination of both approaches has been tested. The NFPF_15CNT_NF was obtained by an acidic attack in degassed water by avoiding the presence of the oxygen but using spray drying with air as drying gas. This approach should prevent the reduction of NFPF caused by the carbothermal reaction during calcination.

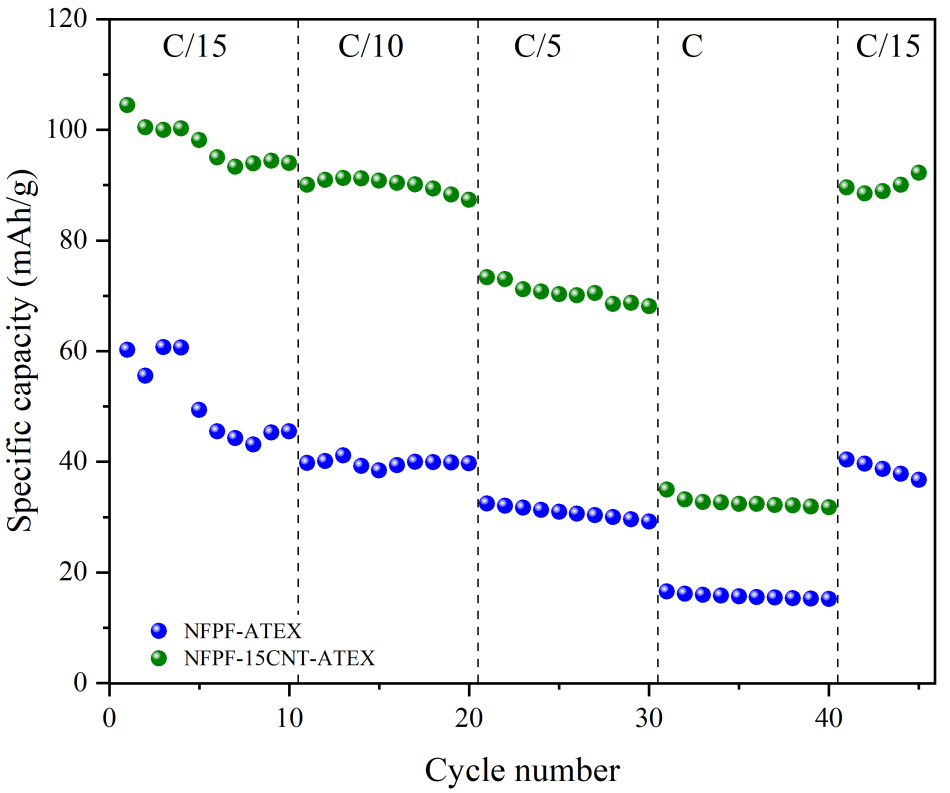

Figure II-10:Evolution of discharge capacity vs. cycle number of NFPF_BN_ATEX and NFPF_15CNT_ATEX materials cycled at C/15, C/10, C/5, 1C rates (2.2-4.5 V vs. Na^+/Na) at room temperature.

The Mössbauer analysis of NFPF_15CNT_NF sample is presented in Figure II-11 and the associated fitted parameters are presented in Table II-6. The spectrum has an asymmetric doublet shape. This spectrum can be fit using: two doublets (75 Fe-at%) with average isomer shift and quadrupole splitting typical of Fe(II)

and one doublet (25 Fe-at%) with parameters corresponding to Fe(III) in NFPF. No other iron species with magnetic ordering or other oxidation states like Fe^0 are detected. Also, no other impurities like γ-Fe_2O_3 are found. These results were confirmed by XRD analysis (see Figure II-12) as all peaks can be indexed in the NFPF crystal lattice with no impurity present in the powder. The crystallite size determined by Scherrer formula is about 27 nm. The SEM analysis reveals the same typical morphology for NFPF_15CNT composite materials.

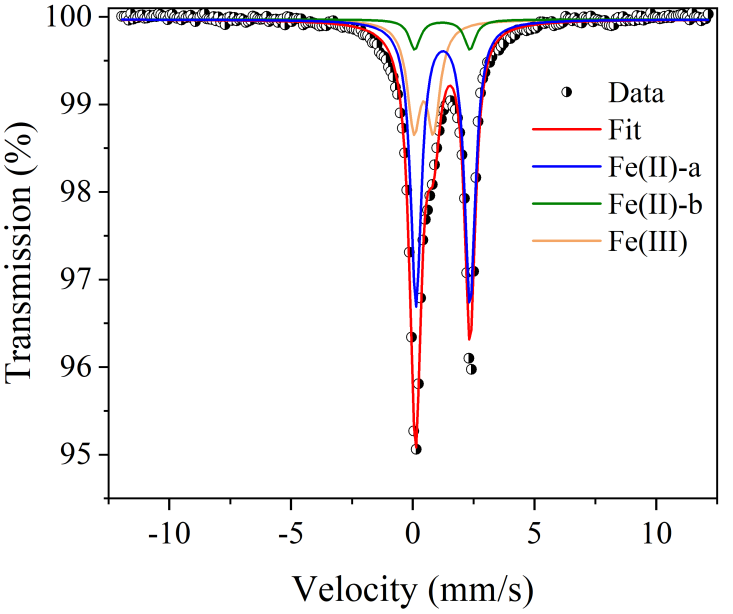

Figure II-11: ^{57}Fe Mössbauer spectra recorded at room temperature of NFPF_15CNT_NF prepared with degas water and air spray-dryer after calcination at 600°C 2 h under argon.

Table II-6: Fitted Mössbauer parameters for NFPF_15CNT_NF made with degas water and air spray-dryer.

		∂ (mm/s)	ΔEq (mm/s)	Γ (mm/s)	Area (%)
NFPF-15CNT-degas water-annealed	Fe(II)-NFPF	1.237(2)	2.218(4)	0.540(3)	65(1)
	Fe(II)-NFPF	1.21(2)	2.27(4)	0.543(3)	7(1)
	Fe(III)-NFPF	0.446(6)	0.80(1)	0.659(4)	28(1)

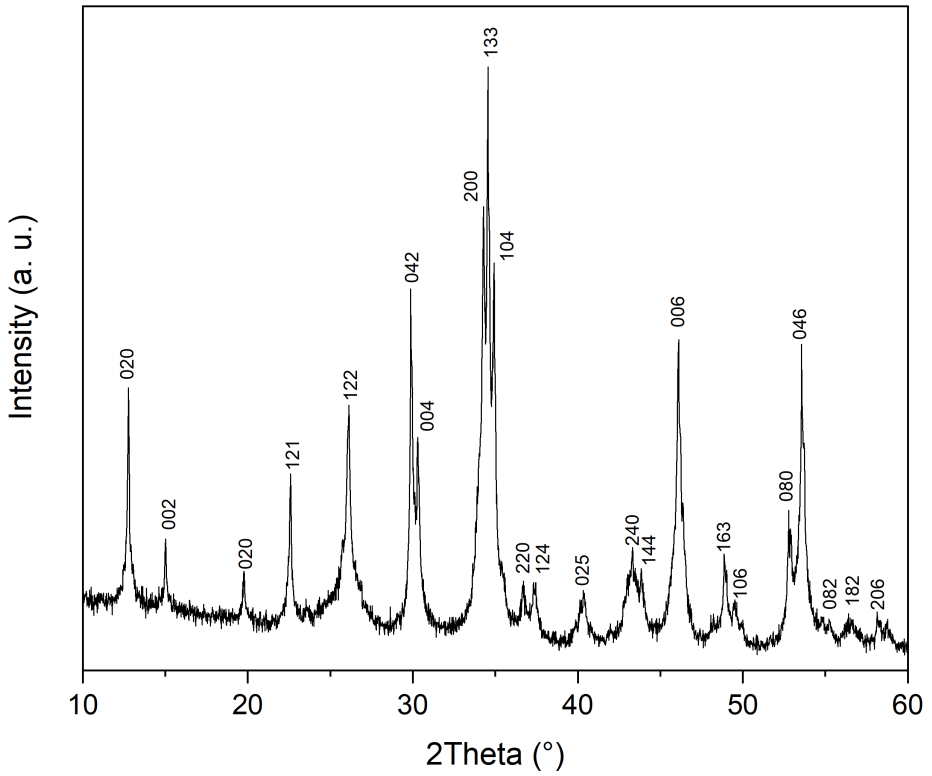

Figure II-12: XRD patterns of NFPF_15CNT_NF prepared with degassed water and spray drying under airflow, after calcination at 600°C 2 h.

This material was cycled in Na-half cells at room temperature at different cycling rates from C/15 to 1C in the voltage range of 2.2-4.5 V. The evolution of the discharge capacity as a function of the cycling rate is presented in Figure II-13a and the associated charge-discharge profiles are illustrated in Figure II-13b. The initial discharge capacity at C/15 is 123 mAh/g which corresponds to 99% of the theoretical capacity. Discharge capacities of 123, 111, 86, and 56 mAh/g are obtained at C/15, C/10, C/5, and 1C cycling rates, respectively. Also, after the rate capability test, the electrode delivers a discharge capacity of 110 mAh/g at C/15.

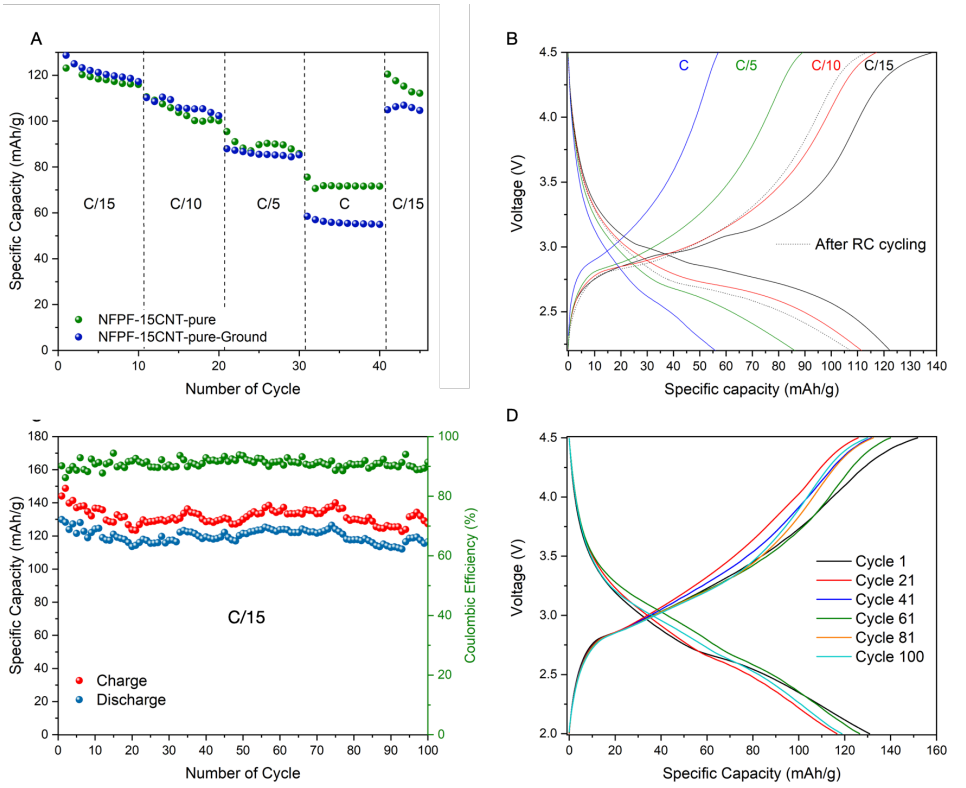

Figure II-13: (a) Evolution of charge and discharge capacity vs. cycle number of NFPF_15CNT_NF and NFPF_15CNT_NF_ground materials cycled at C/15, C/10, C/5, 1C rates at room temperature. The voltage window explored was 2.2-4.5 V vs. Na^+/Na. (b) Charge/discharge curves of the first cycles at C/15, C/10, C/5, 1C of NFPF_15CNT_NF materials. (c) Evolution of charge and discharge capacity vs. cycle number of the pure NFPF_15CNT_NF materials cycled at C/15 rates at room temperature and coulombic efficiency at each cycle. (d) Charge/discharge curves of 1^{st}, 21^{st}, 41^{st}, 61^{st}, 81^{st}, and 100^{th} cycles at C/15 of NFPF_15CNT_NF materials.

As the obtained particles still exhibit a large size, a powder grinding was performed to prove the efficiency of the carbon addition to improve electrochemical performance. If the carbon is well dispersed inside and the surface

of the particles, there should be no difference after a grinding step because the electronic conductivity is sufficient, and the diminution of size will not enhance an already optimized conductivity. The powder was ground in anhydrous isopropanol for 60 min with zirconia balls of 5 mm in diameter. This sample is compared in Figure II-13a (in blue). The grinding step is now useless and even harmful to the capacity retention at high cycling rates as lower capacities are obtained after the grinding process. No difference in specific capacity is observed at low cycling rates which proves that the well-distributed carbon network inside and at the surface of the NFPF particle is sufficient to ensure the good electrochemical performance of the material. The charge-discharge profile in Figure II-13b demonstrates the presence of 2 distinct discharge plateaus at C/15 and C/10 around 2.75 to 3 V which is consistent with literature [11,13]. However, only one plateau is observable at C/5 and no plateau at 1C.

A long cycling term test for 100 cycles was performed and shows relatively high irreversibility at the first cycle which can be explained by the degradation of electrolyte at high voltage. After this, the material presents 91% of the capacity retention after 100 cycles. The corresponding charge-discharge profiles are illustrated in Figure II-13d. A similar charge-discharge profile is observed as before with the presence of 2 discharge plateaus at the first cycle. The fluctuation is associated with variations of the temperature during the long cycling test. Despite the good capacity retention, our material is characterized by poor coulombic efficiency lower than 90%.

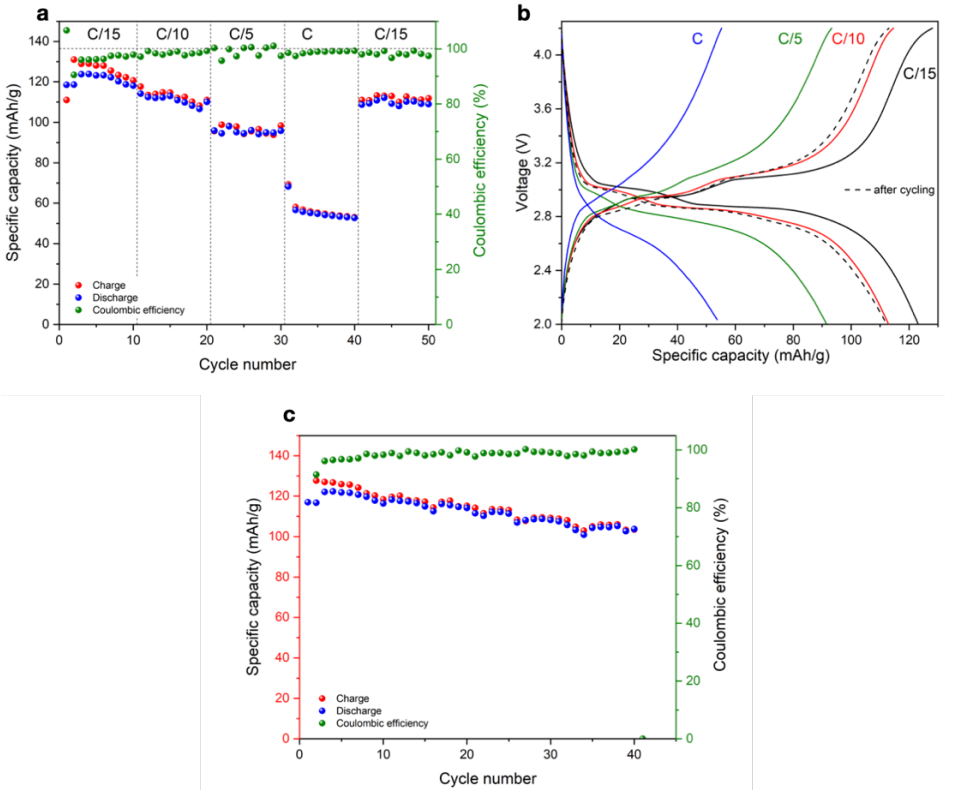

Figure II-14: (a) Evolution of charge and discharge capacity vs. cycle number of NFPF_15CNT_NF cycled at C/15, C/10, C/5, 1C rates at room temperature. The voltage window explored was 2–4.2 V. (b) Charge/discharge curves at C/15, C/10, C/5, 1C of NFPF_15CNT_NF pure materials in Na half cells. (c) Evolution of charge and discharge capacity vs. cycle number of the NFPF_15CNT_NF materials cycled at C/15 rates at room temperature.

A degradation phenomenon seems to occur from 4.3 V which can explain the poor coulombic efficiency during the cycling in the voltage range of 2-4.5 V. To confirm the hypothesis of partial electrolyte degradation at high voltage during cycling leading to poor coulombic efficiency (<90%), galvanostatic cycling tests were performed in the voltage window of 2-4.2 V (Figure II-14) The difference in capacity retention is not significant as the theoretical capacity is achieved at low cycling rate using the new potential window. However, the difference of capacity

of charge and discharge is now almost negligible. A coulombic efficiency of more than 98.5% is obtained at each cycling rate. Besides, the theoretical capacity at C/15 is still obtained during the first cycles and after increasing the rate of cycling during the rate capability test, more than 92% of the initial capacity is still recovered. Regarding the cycling performance, the capacity is still fading at high cycling rates to reach a loss of 5% of the initial discharge capacity after 50 cycles. The reduction of voltage windows does not reduce the obtained values of specific capacity of our material but greatly enhances the coulombic efficiency of the material during cycling.

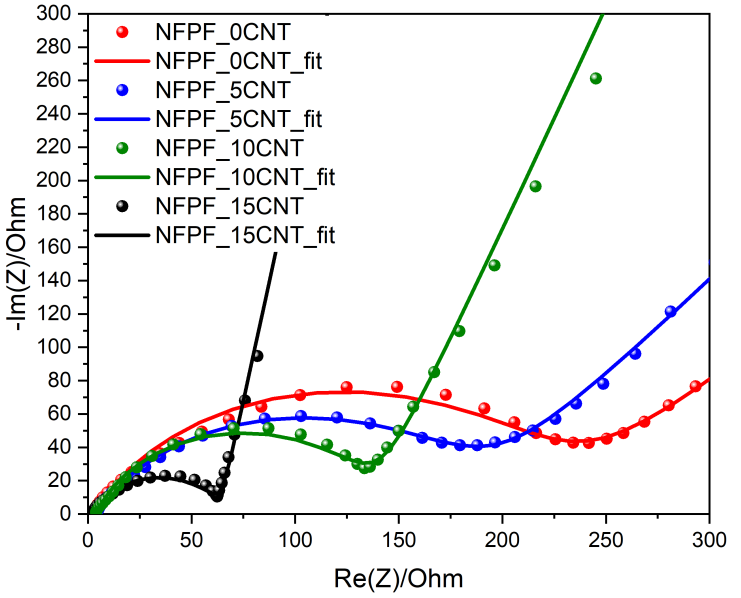

Figure II-15: Nyquist plots of NFPF_0CNT, NFPF_5CNT, NFPF_10CNT, and NFPF_15CNT_NF with their corresponding fitted curves.

Table II-7: Calculated resistances by fitting using the equivalent circuit for both electrolyte resistance (R_e) and charge transfer resistance (R_{CT}) of NFPF_xCNT electrode materials.

Electrode	Re (Ω)	RCT (Ω)
NFPF_0CNT	2.379±0.5	227.3±21
NFPF_5CNT	3.557±0.5	189±17
NFPF_10CNT	3.63±0.5	141±10
NFPF_15CNT_NF	2.095±0.2	63.59±4

Electrochemical impedance spectroscopy (EIS) measurements were performed to analyze the influence of carbon addition on the electrochemical performance of NFPF materials. The Nyquist plots of NFPF and NFPF_xCNT electrodes recorded at open-circuit voltage are presented in Figure II-15. The data were fitted and resistances were extracted by the Aftermath Electrochemical studio software developed by Pine Research instrumentation and using $R_e(R_{CT}. Q)/Q$ as the equivalent circuit where R_e (intercept of the curve on the x-axis in the high-frequency region), the resistance of charge transfer (R_{CT}) and Q is a constant phase element (CPE) replacing the double-layer capacitance. The obtained parameters are summarized in Table II-7. All impedance spectra are similar and formed by a semicircle at high frequencies and a line at low frequencies.

First, all electrodes show a similar and low electrolyte resistance (R_e=±3 Ω). This is expected as the same electrolyte was used for all electrodes. Regarding the R_{CT}, different resistances were obtained for the different electrodes. R_{CT} greatly depends on the percentage of the added CNTs in the composite electrode materials, the high CNT ratio leads to lower resistance. The NFPF_BN material exhibits a R_{CT} that is 4 times higher than for NFPF_15CNT_NF. However, the resistance diminution is not linear, indeed, for the addition of 5 and 10% of CNT a diminution of about 40 Ω while the addition of 15wt% of CNT reduces by more than 2 times the R_{CT} compared to the composite with 10wt% of CNT. In conclusion, the EIS measurements confirm a high electronic conductivity of the NCPF_xCNT materials which leads to better electrochemical performance.

3.3. Na_2FePO_4F-15CNT cycled against potassium

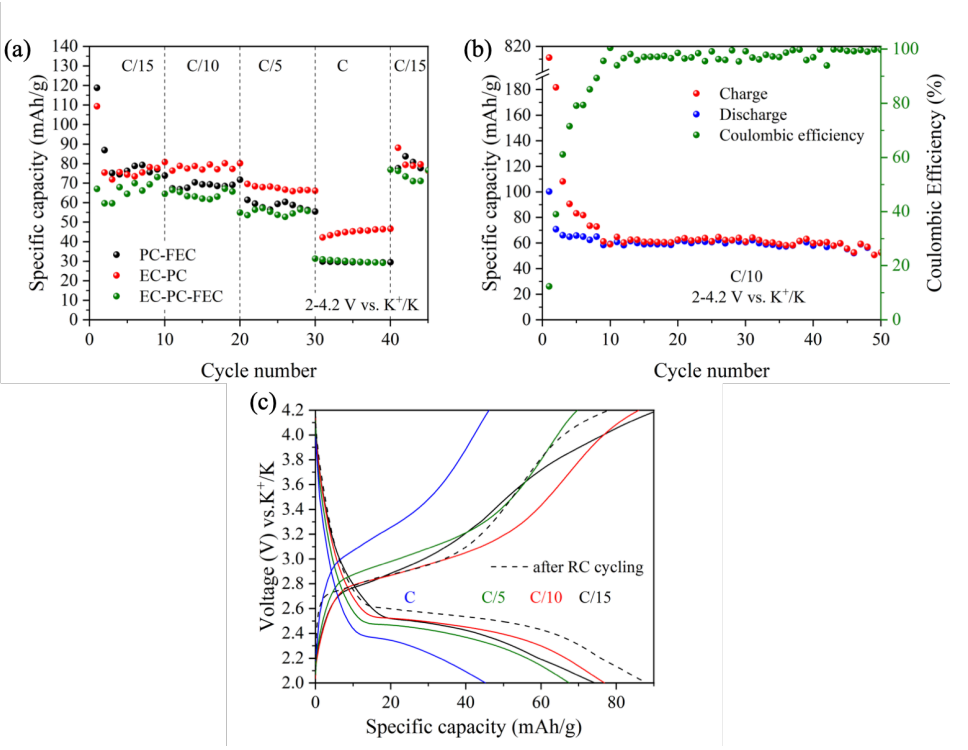

Figure II-16: NFPF_15CNT_NF in K-half cell (room temperature): (a) Evolution of discharge capacity vs. cycle number for cycling at C/15, C/10, C/5, and C rates, with different electrolytes: 0.8 M KPF_6 in PC with 10 wt% of FEC (black circles), 0.8 M KPF_6 in EC and PC (1:1) (red circles), and 0.8 M KPF_6 in EC and PC (1:1) with 10 wt% of FEC (green circles). (b) Evolution of discharge capacity vs. cycle number over 50 cycles at C/10 (red circles), with 0.8 M KPF_6 in EC and PC (1:1). (c) Charge/discharge curves extracted from the rate capability experiment at C/15, C/10, C/5, and 1C rates using 0.8 M KPF_6 in EC and PC.

Figure II-16 presents preliminary cycling tests that were performed on K half-cells in order to assess whether the NFPF phase is able to act as a cathode material for

K-ion batteries (KIBs). Figure II-16a illustrates the rate performance at different current densities for NFPF_15CNT_NF in K half-cells in the voltage window of 2-4.2 V. Three different electrolyte compositions were evaluated: (i) 0.8 M KPF_6 in PC with 10wt% of FEC (PC-FEC), (ii) 0.8 M KPF_6 in EC:PC (1:1 v:v) (EC-PC) and (iii) 0.8 M KPF_6 in EC:PC (1:1 v:v) with 10 wt% of FEC (EC-PC-FEC).

The first cycles at C/15 show that the PC-FEC and EC-PC electrolytes lead to a strong decrease of the specific capacity from 120 to 75 mAh/g, suggesting a secondary reaction. In the case of the EC-PC-FEC electrolyte, the capacity is about 70 mAh/g from the beginning. Using the additive-free 0.8 M KPF_6 in EC:PC electrolyte leads to higher capacity retentions during further cycles in the rate capability tests. The cells using this electrolyte exhibit discharge capacities of 75, 82, 68, 45, and 80 mAh/g at C/15, C/10, C/5, 1C, and C/15 after high C-rate measurements, respectively (red circles in Figure II-16a). This represents 71% of the theoretical capacity of $NaKFePO_4F$ (115 mAh/g). The lower capacity retention observed at higher cycling rates is expected for such materials and is associated with kinetic limitations. The specific capacity of 79 mAh/g (69% of theoretical capacity) observed after the rate capability testing suggests stable structure and insertion properties of the material after going through a kinetically limiting cycling procedure. The obtained capacity using the other two electrolytes is similar except at the highest rate (1C), where the capacity obtained with the EC-PC electrolyte is almost two times higher than the others. A cycling test was performed at C/10 rate for 50 cycles (Figure II-16b). This slower rate should favor the adaptation of the structure to the bigger K^+ ion. After a strong irreversibility in the first cycle, the observed reversible capacity is about 70 mAh/g for the second cycle, decreases slightly over the next 10 cycles and stabilizes at 60 mAh/g, with a good coulombic efficiency. Figure II-16c shows the charge and discharge curves obtained at different C-rates; only one plateau can be observed at each cycling rate.

To enhance the electrochemical performance of NFPF_15CNT_NF as cathode material for KIBs, NFPF_15CNT_NF electrodes were first fully charged in Na half-cells to ensure the removal of one Na ion following the protocol described in the experimental section. These precharged electrodes were then tested in K half-cells, using 0.8 M KPF_6 in EC:PC (1:1 v:v) as electrolyte. Figure II-17 shows the results for three cells, in order to estimate the reproducibility of the observed electrochemical behavior. After the first few cycles suffering from irreversibility (probably enhanced due to the transfer of the electrode from the Na half-cell to the K half-cell), the specific capacity stabilizes at higher values than in the non-pre-charged cells, with 114, 104, 88, 60, and 105 mAh/g at C/15, C/10, C/5, 1C, and back to C/15, respectively. The formation cycle to prepare $NaFePO_4F$ electrochemically allows to reach over 99% of the theoretical capacity at C/15. However, the charge/discharge profiles in Figure II-17 reveal the presence of an additional plateau at 3 V in the first charge (C/15), suggesting that Na ions are still extracted during the first cycle in K half-cell. After a few cycles, only one plateau is visible. A similar behavior was observed by Lin *et al*. in 2019, when replacing progressively the Na^+ ions by K^+ ions in $Na_3V_2(PO_4)_2F_3$ [41]. These authors obtained a decent capacity of 100 mAh/g at 3.4 V, positioning this work among the best performance reported for a KIB cathode. The reversible capacity of 114 mAh/g at 3 V obtained here for NFPF cathode material confirms the huge interest of using Na^+ or Li^+ analog materials for the development of high capacity cathode materials for KIBs [41].

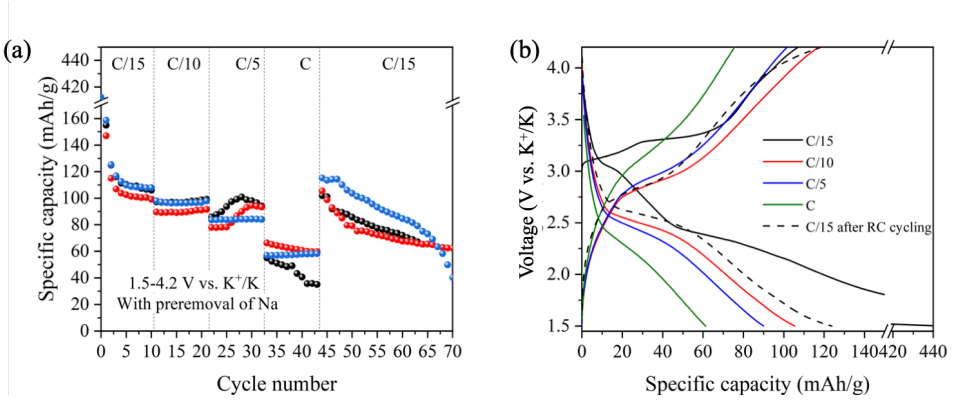

Figure II-17: Pre-charged NFPF_15CNT_NF in K-half cell (room temperature): (a) Evolution of discharge capacity vs. cycle number for 3 similarly-prepared electrodes with 0.8 M KPF_6 in EC:PC (1:1) as electrolyte and C/15, C/10, C/5, 1C rates. (b) Charge/discharge curves extracted from the rate capability test of precycled NFPF_15CNT_NF in K half-cells at C/15, C/10, C/5, and 1C rates.

The comparison between the behaviors when cycling *vs.* Na and *vs.* K was further studied by cyclic voltammetry (CV). Figure II-18a presents the cyclic voltammograms *vs.* Na for scan rates between 0.05 mV/s and 1 mV/s. In agreement with the cycling curves, two peaks of oxidation (A: 3 V, B: 3.2 V) and two peaks of reduction (C: 2.75 V and D: 3 V) are observed at all scan rates. The maximum current intensity of the redox peaks is plotted in Figure II-18b versus the square root of the scan rate. The observed linearity for both the oxidation and reduction peaks indicates that the diffusion process is limited by the diffusion of the sodium ions in the electrode material [42–44].

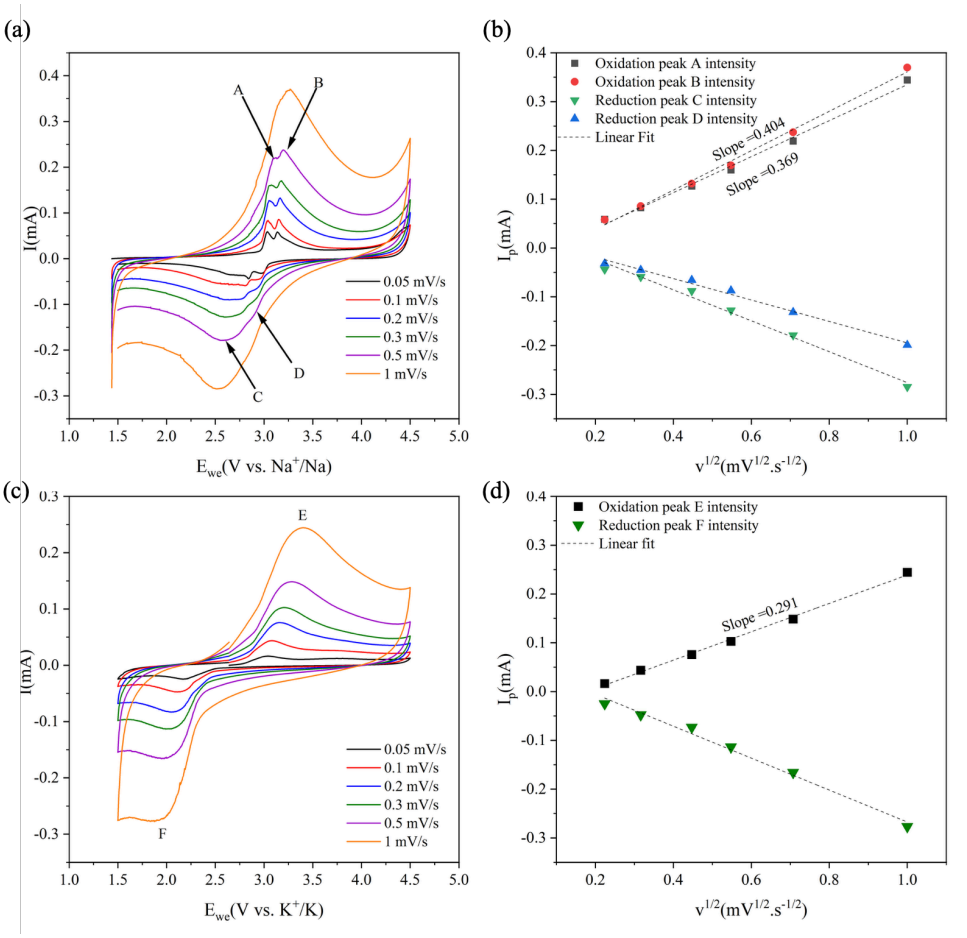

Figure II-18: (a,b) Cyclic voltammograms at scan rates between 0.05 and 1 mV/s and evolution of the peak current versus the square root of the scan rate for NFPF_15CNT_NF in Na-half cell. (c,d) Cyclic voltammograms at scan rates between 0.05 and 1 mV/s and evolution of the peak current versus the square root of the scan rate in K-ion half-cell after a precharge in Na-half cell.

Figure II-18c presents the results of a similar cyclic voltammetry experiment performed *vs.* K with a pre-charged electrode. By comparison with the corresponding results against Na, only one peak can be observed in oxidation and in reduction. There is also a displacement of the voltage peak depending on the scan rate: at 0.05 mV/s the oxidation peak (E) appears at 3.04 V, and at a higher

scan rate (1 mV/s) the maximum intensity of the oxidation peak shifts to 3.40 V. The same phenomenon is observed for the reduction peak (F) shifting from 2.16 V at 0.05 mV/s to 1.89 V at 1 mV/s. Figure II-18d shows that the maximum current intensity is linearly dependent on the square root of the scan rate. This linearity indicates that the diffusion process is limited by the potassium ion movement in the electrode material.

This linear relationship observed for both Na^+ and K^+ is described by Randles-Sevcik equation [43–45]:

$$I_p = (2.69E^{+5})\, n^{3/2}\, S\, (D_A{}^+)^{1/2}\, C_A{}^+\, v^{1/2}$$

where I_p is the peak intensity current, n is the number of electrons, S is the effective surface area, $D_A{}^+$ is the diffusion coefficient of sodium/potassium ions and $C_A{}^+$ is the maximum concentration of A^+ ions (either Na^+ or K^+) in the electrode during the electrochemical analysis. Since the number of electrons and the surface area are the same, the two parameters that can influence the slope are the diffusion coefficient and the concentration of the alkali ions. The slope for the evolution of the oxidation peaks is 0.29 for the K half-cell and 0.40 for the Na half-cell, revealing a difference between the two experiments. Assuming that the concentrations of the alkali ions are similar, this difference in slope can be attributed to a slightly more difficult diffusion of the K^+ ions in the NFPF structure, since the ionic radius of the K^+ is 1.33 Å where Na^+ radius is only 0.97 Å [46]. The decrease of the diffusion coefficient by only 25% proves the electrochemical activity and potential applications of the NFPF phase as a cathode material for KIBs.

4. Conclusions

The use of the bifluid nozzle greatly reduces the particle size of the NFPF materials made by spray-drying. This reduction of size enhanced the performance compared to the rotary nozzle synthesis but is insufficient to compensate the poor electronic conductivity of the material. The addition of carbon nanotubes to make composite leads to the formation of metallic iron and iron carbide during the annealing step. This drawback can be prevented by tuning the acidic attack of the Fe and the atmosphere during the spray drying step. A too low percentage of Fe^{3+} after the spray-drying lead to a huge amount of Fe^{0} and a too high level of Fe^{3+} leads to oxidation of the NFPF before cycling or in the worst case the presence of Fe_2O_3 impurity. The pure phase was successfully obtained by using degas water during the acidic attack and by spray-drying with hot airflow.

The NFPF_15CNT_NF exhibits the best electrochemical performance with a specific capacity of 123 mAh/g at C/15 which corresponds to 99% of the theoretical capacity. The discharge capacity retention is 91% after 100 cycles. The addition of CNT and the reduction of size induced by the use of a bifluid nozzle shows that the grinding can be avoided even if particles of about 3 µm are obtained due to a homogeneous distribution of carbon inside the NFPF particles. The best performance is obtained on the voltage window of 2.0-4.2 V with a coulombic efficiency of more than 99% and a specific capacity of 123 mAh/g.

For the first time, cycling tests were performed to investigate the electrochemical performance of NFPF/CNT as cathode material for K-ion batteries. A discharge capacity of 80 mAh/g is obtained, which represents 71% of the theoretical capacity of $NaKFePO_4F$ with 0.8 M KPF_6 in EC:PC as the best-tested electrolyte. Initial cycles present irreversibility that can be associated with the replacement of sodium with potassium in the crystal lattice. The pre-cycling of the material in a Na half-cell to remove Na before cycling in K half-cells led to improved

performance with a specific capacity of 114 mAh/g at C/15, i.e., 99% of the theoretical capacity. These results highlight the potential of NFPF_15CNT_NF prepared by spray-drying as a promising cathode material for both NIBs and KIBs.

5. References

[1] B. Dunn, H. Kamath, J.-M. Tarascon, Electrical Energy Storage for the Grid: A Battery of Choices, Science (1979). 334 (2011) 928–935. https://doi.org/10.1126/science.1212741.

[2] J.B.; K.N. Padhi, A.K.; Goodenough, A.K.Pahdi, Journal of Electrochemical Society. 144 (1997) 1188.

[3] N. Yabuuchi, K. Kubota, M. Dahbi, S. Komaba, Research development on sodium-ion batteries, Chemical Reviews. 114 (2014) 11636–11682. https://doi.org/10.1021/cr500192f.

[4] X. Ma, H. Chen, G. Ceder, Electrochemical Properties of Monoclinic NaMnO2, Journal of The Electrochemical Society. 158 (2011) A1307. https://doi.org/10.1149/2.035112jes.

[5] N. Yabuuchi, R. Hara, M. Kajiyama, K. Kubota, T. Ishigaki, A. Hoshikawa, S. Komaba, New O2/P2-type Li-excess layered manganese oxides as promising multi-functional electrode materials for rechargeable Li/Na batteries, Advanced Energy Materials. 4 (2014). https://doi.org/10.1002/aenm.201301453.

[6] K. Zaghib, J. Trottier, P. Hovington, F. Brochu, A. Guerfi, A. Mauger, C.M. Julien, Characterization of Na-based phosphate as electrode materials for electrochemical cells, Journal of Power Sources. 196 (2011) 9612–9617. https://doi.org/10.1016/j.jpowsour.2011.06.061.

[7] N. Recham, G. Rousse, M.T. Sougrati, J.N. Chotard, C. Frayret, S. Mariyappan, B.C. Melot, J.C. Jumas, J.M. Tarascon, Preparation and characterization of a stable FeSO4F-based framework for alkali ion insertion electrodes, Chemistry of Materials. 24 (2012) 4363–4370. https://doi.org/10.1021/cm302428w.

[8] R. Chen, Y. Huang, M. Xie, Q. Zhang, X. Zhang, L. Li, F. Wu, Preparation of Prussian Blue Submicron Particles with a Pore Structure by Two-Step Optimization for Na-Ion Battery Cathodes, ACS Applied Materials and Interfaces. 8 (2016) 16078–16086. https://doi.org/10.1021/acsami.6b04151.

[9] D. Baster, Ł. Kondracki, E. Oveisi, S. Trabesinger, H.H. Girault, Prussian Blue Analogue-Sodium-Vanadium Hexacyanoferrate as a Cathode Material for Na-Ion Batteries, ACS Applied Energy Materials. (2021). https://doi.org/10.1021/acsaem.1c01832.

[10] G. Ali, S.H. Oh, S.Y. Kim, J.Y. Kim, B.W. Cho, K.Y. Chung, An open-framework iron fluoride and reduced graphene oxide nanocomposite as a high-capacity cathode material for Na-ion batteries, Journal of Materials Chemistry A. 3 (2015) 10258–10266. https://doi.org/10.1039/c5ta00643k.

[11] Y. Kawabe, N. Yabuuchi, M. Kajiyama, N. Fukuhara, T. Inamasu, R. Okuyama, I. Nakai, S. Komaba, Synthesis and electrode performance of carbon coated Na 2FePO4F for rechargeable Na batteries, Electrochemistry Communications. 13 (2011) 1225–1228. https://doi.org/10.1016/j.elecom.2011.08.038.

[12] H. Hu, Y. Bai, C. Miao, Z. Luo, X. Wang, Polyfurfuryl alcohol assisted synthesis of Na2FePO4F/C nanocomposites as cathode material of sodium ion batteries, Journal of Electroanalytical Chemistry. 867 (2020) 114187. https://doi.org/10.1016/j.jelechem.2020.114187.

[13] Y. Kawabe, N. Yabuuchi, M. Kajiyama, N. Fukuhara, T. Inamasu, R. Okuyama, I. Nakai, S. Komaba, A comparison of crystal structures and electrode performance between Na 2FePO 4F and Na 2Fe 0.5Mn 0.5PO 4F synthesized by solid-state method for rechargeable na-ion batteries, Electrochemistry. 80 (2012) 80–84. https://doi.org/10.5796/electrochemistry.80.80.

[14] B.L. Ellis, W.R.M. Makahnouk, Y. Makimura, K. Toghill, L.F. Nazar, A multifunctional 3.5V iron-based phosphate cathode for rechargeable batteries, Nature Materials. 6 (2007) 749–753. https://doi.org/10.1038/nmat2007.

[15] D.L. Smiley, D. Carlier, G.R. Goward, Combining density functional theory and 23Na NMR to characterize Na2FePO4F as a potential sodium ion battery cathode, Solid State Nuclear Magnetic Resonance. 103 (2019) 1–8. https://doi.org/10.1016/j.ssnmr.2019.07.001.

[16] J.S. Ko, V.V.T. Doan-Nguyen, H.S. Kim, X. Petrissans, R.H. Deblock, C.S. Choi, J.W. Long, B.S. Dunn, High-rate capability of Na2FePO4F nanoparticles by enhancing surface carbon functionality for Na-ion batteries, Journal of Materials Chemistry A. 5 (2017) 18707–18715. https://doi.org/10.1039/c7ta05680j.

[17] W. Ko, J.K. Yoo, H. Park, Y. Lee, H. Kim, Y. Oh, S.T. Myung, J. Kim, Development of Na2FePO4F/Conducting-Polymer composite as an exceptionally high performance cathode material for Na-ion batteries, Journal of Power Sources. 432 (2019) 1–7. https://doi.org/10.1016/j.jpowsour.2019.05.066.

[18] H. Li, T. Wang, X. Wang, G. Li, J. Shen, J. Chai, MOF-derived Al-doped Na2FePO4F/mesoporous carbon nanonetwork composites as high-performance cathode material for sodium-ion batteries, Electrochimica Acta. 373 (2021) 137905. https://doi.org/10.1016/j.electacta.2021.137905.

[19] J. Zhang, X. Zhou, Y. Wang, J. Qian, F. Zhong, X. Feng, W. Chen, X. Ai, H. Yang, Y. Cao, Highly Electrochemically-Reversible Mesoporous Na2FePO4F/C as Cathode Material for High-Performance Sodium-Ion Batteries, Small. 15 (2019) 1–7. https://doi.org/10.1002/smll.201903723.

[20] X. Deng, W. Shi, J. Sunarso, M. Liu, Z. Shao, A Green Route to a Na2FePO4F-Based Cathode for Sodium Ion Batteries of High Rate and Long Cycling Life, ACS Applied Materials and Interfaces. 9 (2017) 16280–16287. https://doi.org/10.1021/acsami.7b03933.

[21] R. Ling, S. Cai, S. Shen, X. Hu, D. Xie, F. Zhang, X. Sun, N. Yu, F. Wang, Synthesis of carbon coated Na2FePO4F as cathode materials for high-performance sodium ion batteries, Journal of Alloys and Compounds. 704 (2017) 631–640. https://doi.org/10.1016/j.jallcom.2017.02.075.

[22] J. Xun, Y. Zhang, B. Zhang, H. Xu, L. Xu, Facile Synthesis of High Electrochemical Performance Na2FePO4F@CNT&GN Cathode Material as Sodium Ion Batteries, ACS Applied Energy Materials. 3 (2020) 6232–6239. https://doi.org/10.1021/acsaem.0c00323.

[23] R. Ling, S. Cai, D. Xie, W. Shen, X. Hu, Y. Li, S. Hua, Y. Jiang, X. Sun, Double-shelled hollow Na2FePO4F/C spheres cathode for high-performance sodium-ion batteries, Journal of Materials Science. 53 (2018) 2735–2747. https://doi.org/10.1007/s10853-017-1738-6.

[24] M.A. Kirsanova, A.S. Akmaev, D.A. Aksyonov, S. v. Ryazantsev, V.A. Nikitina, D.S. Filimonov, M. Avdeev, A.M. Abakumov, Monoclinic α-Na2FePO4F with Strong Antisite Disorder and Enhanced Na+Diffusion, Inorganic Chemistry. 59 (2020) 16225–16237. https://doi.org/10.1021/acs.inorgchem.0c01961.

[25] L. Sharma, P.K. Nayak, E. de La Llave, H. Chen, S. Adams, D. Aurbach, P. Barpanda, Electrochemical and Diffusional Investigation of Na2FeIIPO4F Fluorophosphate Sodium Insertion Material Obtained from FeIII Precursor, ACS Applied Materials and Interfaces. 9 (2017) 34961–34969. https://doi.org/10.1021/acsami.7b10637.

[26] H. Li, T. Wang, X. Wang, G. Li, J. Shen, J. Chai, Na2FePO4F/Biocarbon Nanocomposite Hollow Microspheres Derived from Biological Cell Template as High-Performance Cathode Material for Sodium-Ion Batteries, Chemistry - A European Journal. 27 (2021) 9022–9030. https://doi.org/10.1002/chem.202100096.

[27] L. Sharma, A. Bhatia, L. Assaud, S. Franger, P. Barpanda, Ultra-rapid combustion synthesis of Na2FePO4F fluorophosphate host for Li-ion and Na-ion insertion, Ionics (Kiel). 24 (2018) 2187–2192. https://doi.org/10.1007/s11581-017-2376-3.

[28] S. Hua, S. Cai, R. Ling, Y. Li, Y. Jiang, D. Xie, S. Jiang, Y. Lin, K. Shen, Synthesis of porous sponge-like Na2FePO4F/C as high-rate and long cycle-life cathode material for sodium ion batteries, Inorganic Chemistry Communications. 95 (2018) 90–94. https://doi.org/10.1016/j.inoche.2018.07.011.

[29] M. Law, V. Ramar, P. Balaya, Synthesis, characterisation and enhanced electrochemical performance of nanostructured Na2FePO4F for sodium batteries, RSC Advances. 5 (2015) 50155–50164. https://doi.org/10.1039/c5ra07583a.

[30] F. Wang, N. Zhang, X. Zhao, L. Wang, J. Zhang, T. Wang, F. Liu, Y. Liu, L.Z. Fan, Realizing a High-Performance Na-Storage Cathode by Tailoring Ultrasmall Na2FePO4F Nanoparticles with Facilitated Reaction Kinetics, Advanced Science. 6 (2019). https://doi.org/10.1002/advs.201900649.

[31] A. Langrock, Y. Xu, Y. Liu, S. Ehrman, A. Manivannan, C. Wang, Carbon coated hollow Na 2FePO 4F spheres for Na-ion battery cathodes, Journal of Power Sources. 223 (2013) 62–67. https://doi.org/10.1016/j.jpowsour.2012.09.059.

[32] A. Mahmoud, S. Caes, M. Brisbois, R.P. Hermann, L. Berardo, A. Schrijnemakers, C. Malherbe, G. Eppe, R. Cloots, B. Vertruyen, F. Boschini, Spray-drying as a tool to disperse conductive carbon inside Na2FePO4F particles by addition of carbon black or carbon nanotubes to the precursor solution, Journal of Solid State Electrochemistry. 22 (2018) 103–112. https://doi.org/10.1007/s10008-017-3717-x.

[33] M. Brisbois, S. Caes, M.T. Sougrati, B. Vertruyen, A. Schrijnemakers, R. Cloots, N. Eshraghi, R.P. Hermann, A. Mahmoud, F. Boschini, Na2FePO4F/multi-walled carbon nanotubes for lithium-ion batteries: Operando Mössbauer study of spray-dried composites, Solar Energy Materials and Solar Cells. 148 (2016) 67–72. https://doi.org/10.1016/j.solmat.2015.09.005.

[34] M. Brisbois, N. Krins, R.P. Hermann, A. Schrijnemakers, R. Cloots, B. Vertruyen, F. Boschini, Spray-drying synthesis of Na2FePO4F/carbon powders for lithium-ion batteries, Materials Letters. 130 (2014) 263–266. https://doi.org/10.1016/j.matlet.2014.05.121.

[35] A. Mahmoud, S. Caes, M. Brisbois, R.P. Hermann, L. Berardo, A. Schrijnemakers, C. Malherbe, G. Eppe, R. Cloots, B. Vertruyen, F. Boschini, Spray-drying as a tool to disperse conductive carbon inside Na2FePO4F particles by addition of carbon black or carbon nanotubes to the precursor solution, Journal of Solid State Electrochemistry. (2017). https://doi.org/10.1007/s10008-017-3717-x.

[36] B. Vertruyen, N. Eshraghi, C. Piffet, J. Bodart, A. Mahmoud, F. Boschini, Spray-drying of electrode materials for lithium- and sodium-ion batteries, Materials. 11 (2018) 1076. https://doi.org/10.3390/ma11071076.

[37] Q. Li, Z. Liu, F. Zheng, R. Liu, J. Lee, G.L. Xu, G. Zhong, X. Hou, R. Fu, Z. Chen, K. Amine, J. Mi, S. Wu, C.P. Grey, Y. Yang, Identifying the Structural Evolution of the Sodium Ion Battery Na2FePO4F Cathode, Angewandte Chemie - International Edition. 57 (2018) 11918–11923. https://doi.org/10.1002/anie.201805555.

[38] N. Eshraghi, S. Caes, A. Mahmoud, R. Cloots, B. Vertruyen, F. Boschini, Sodium vanadium (III) fluorophosphate/carbon nanotubes composite (NVPF/CNT) prepared by spray-drying: good electrochemical performance thanks to well-dispersed CNT network within NVPF particles, Electrochimica Acta. 228 (2017) 319–324. https://doi.org/10.1016/j.electacta.2017.01.026.

[39] P.R. Kumar, Y.H. Jung, C.H. Lim, D.K. Kim, Na3V2O2x(PO4)2F3-2x: A stable and high-voltage cathode material for aqueous sodium-ion batteries with high energy density, Journal of Materials Chemistry A. 3 (2015) 6271–6275. https://doi.org/10.1039/c5ta00980d.

[40] J. Bodart, N. Eshraghi, T. Carabin, B. Vertruyen, R. Cloots, F. Boschini, A. Mahmoud, Spray-dried K3V(PO4)2/C composites as novel cathode materials for K-ion batteries with superior electrochemical performance, Journal of Power Sources. 480 (2020). https://doi.org/10.1016/j.jpowsour.2020.229057.

[41] X. Lin, J. Huang, H. Tan, J. Huang, B. Zhang, K3V2(PO4)2F3 as a robust cathode for potassium-ion batteries, Energy Storage Materials. 16 (2019) 97–101. https://doi.org/10.1016/j.ensm.2018.04.026.

[42] C. Zhu, C. Wu, C. Chen, P. Kopold, P.A. van Aken, J. Maier, A High Power − High Energy Na 3 V 2 (PO 4) 2 F 3 Sodium Cathode : Investigation of Transport Parameters , Rational Design and Realization, 2 (2017) 1–14. https://doi.org/10.1021/acs.chemmater.7b00927.

[43] K. Wang, R. Cai, T. Yuan, X. Yu, R. Ran, Z. Shao, Process investigation, electrochemical characterization and optimization of LiFePO4/C composite from mechanical activation using sucrose as carbon source, Electrochimica Acta. 54 (2009) 2861–2868. https://doi.org/10.1016/j.electacta.2008.11.012.

[44] W.L. Liu, J.P. Tu, Y.Q. Qiao, J.P. Zhou, S.J. Shi, X.L. Wang, C.D. Gu, Optimized performances of core-shell structured LiFePO4/C nanocomposite, Journal of Power Sources. 196 (2011) 7728–7735. https://doi.org/10.1016/j.jpowsour.2011.05.046.

[45] C. Zhu, C. Wu, C.C. Chen, P. Kopold, P.A. van Aken, J. Maier, Y. Yu, A High Power-High Energy Na3V2(PO4)2F3 Sodium Cathode: Investigation of Transport Parameters, Rational Design and Realization, Chemistry of Materials. 29 (2017) 5207–5215. https://doi.org/10.1021/acs.chemmater.7b00927.

[46] K. Kubota, M. Dahbi, T. Hosaka, S. Kumakura, S. Komaba, Towards K-Ion and Na-Ion Batteries as "Beyond Li-Ion," Chemical Record. 18 (2018) 459–479. https://doi.org/10.1002/tcr.201700057.

Chapter III

Insights into Na_2FePO_4F electrochemical reaction mechanism: A combination of *operando* ^{57}Fe Mössbauer spectroscopy and *operando* X-ray diffraction to further understand Na-, and K- insertion/extraction processes during cycling.

Abstract:

In the previous chapter, Na_2FePO_4F/Carbon nanotubes (NFPF-15CNT) material was optimized through its synthesis and shaping by spray-drying. NFPF was used as cathode material for both Na-ion and K-ion batteries. In this chapter, insights into the cycling mechanism of NFPF cathode material are presented. This chapter summarizes the electrochemical reaction mechanism of NFPF-15CNT material during cycling analyzed by combining *operando* X-ray diffraction (with Cobalt anticathode) and *operando* ^{57}Fe Mössbauer spectroscopy techniques. The obtained data sets are analyzed using a statistical approach using Principal Component Analysis and Multivariate Curve Resolution-Alternating least square . This method allows the extraction of the main varying features of the materials during electrochemical cycling. This method determines first the number of the mathematical components that allows the descriptions of all the experimental data. Then, Multivariate Curve Resolution is used to the construction of the spectral components that describe the best the electrochemical reactions and thus could improve the understanding of the cycling mechanism of NFPF In Na-ion batteries and K-ion batteries. Using these techniques, the cycling mechanism in Na-ion batteries has been determined as a double biphasic reaction with a clear intermediate $Na_{1.5}FePO_4F$ phase. For the cycling in K-ion batteries, although the amorphization of the materials has limited the data obtained by X-ray diffraction, ^{57}Fe Mössbauer proves the variation of the iron oxidation state. In this case there is no evidence of an intermediate formation as for Na-ion batteries.

1. Introduction:

Understanding the electrochemical reaction mechanism of the electrode materials for rechargeable batteries reveals now to be an essential step in designing advanced electrodes and to enhance their electrochemical performance [1–8]. Among the different advanced characterization techniques used to deeply investigate the electrode material behavior during cycling, Mössbauer spectroscopy is a particularly powerful characterization technique to follow the oxidation state and the local environment of the iron [9–11]. Indeed, Mössbauer spectroscopy is a nuclear technique, which allows one to study the electronic properties via the nuclear probe. This makes it a suitable and convenient method for the analysis of the Na_2FePO_4F material mechanism during charge and discharge processes [7]. When the cathode materials are well crystalized, X-ray diffraction (XRD) technique allows an accurate monitoring of the structural evolution and change during cycling [8]. *Operando* analysis requires a special electrochemical cell to be fully compatible with the conditions of the testing method (Mössbauer or XRD) to obtain reliable results. This cell (See Figure III-1) is sealed and from top to bottom, we find in the center, beryllium foil that is protected by a thin aluminum foil to avoid oxidation on which our electrode is deposited, then a separator is placed with electrolyte. Finally, the metallic counter electrode is placed on a cylindrical plunger that maintained the pressure with a spring. In transmission geometry Mössbauer spectroscopy measurements, this plunger is hollow, and a second beryllium window closes the system. In the case of XRD analysis, the cylinder is full because the measurement is performed in reflection geometry.

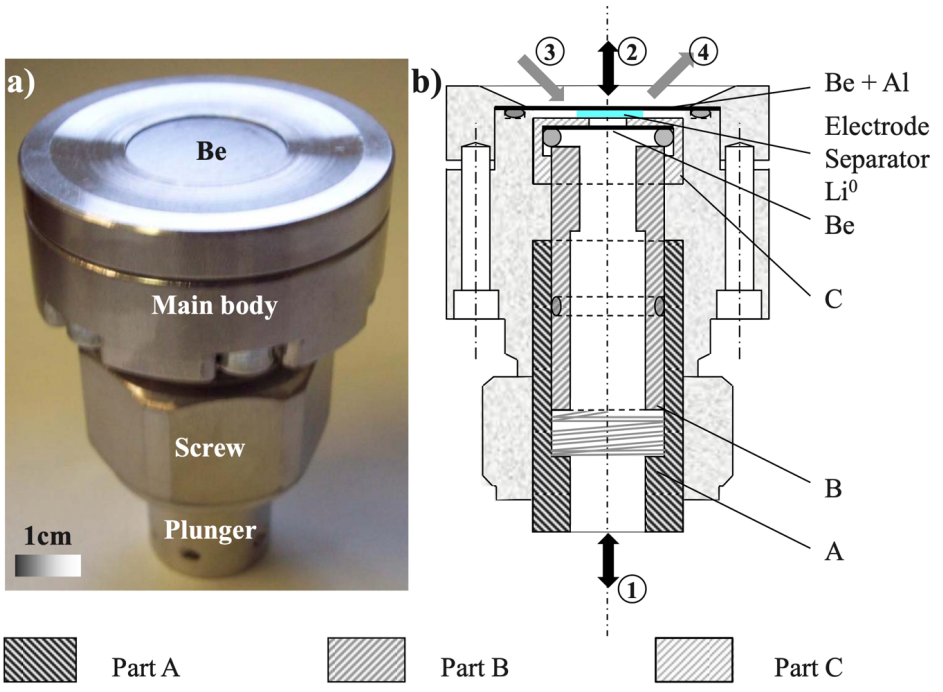

Figure III-1: Electrochemical cell for operando measurement. a) Photo and (b) detailed schematic of the cell with the incoming (1) and outcoming (2) paths of the γ-beams in transmission (for Mössbauer spectroscopy) and (3) incoming and (4) outcoming path of the X-ray beams in reflection geometry (X-ray diffractometry). Reproduced from [12]

Such measurements provide a large experimental dataset that contains tens of spectra or patterns. A successful technique can rely on chemometrics to manage such complex datasets without missing crucial information in a fair amount of time. A variety of multivariate tools, aiming at the decomposition of a data matrix into a linear model of dyads (the bilinear model), have been developed in this interdisciplinary field between analytical chemistry and statistics, which owes its origin to the rise of the use of computer and automated data acquisition in the 1970s [13,14]. The most popular techniques are Principal Component Analysis (PCA), Independent Component Analysis (ICA), and Multivariate

Curve Resolution (MCR), all of which aim to resolve complex mixtures into pure-component contributions using little information. By computing orthogonal components aligned to the directions that explain the majority of the variance in the data matrix, the first of these approaches, PCA, provides a completely blind abstract decomposition of a matrix of experimental data [14]. However, PCA does not generate matrices with chemical or physical meanings. Contrarily, MCR seeks to decompose the data matrix into a product of two matrices with physical or chemical meanings and achieves this decomposition by imposing particular restrictions [15,16]. MCR has the significant advantage of producing "pure" spectral components and concentration profiles which can be analyzed as real spectra/patterns and compared with raw data, even though this strategy makes the solution of MCR dependent upon the chosen constraints. Due to this benefit, MCR has become the method of choice for the analysis of large data sets. Since its initial application in 1971, a wide variety of algorithms have been created in a variety of research fields, all of which share the presumption that the data should be bilinear or multilinear [16]. Today, Multivariate Curve Resolution by Alternating Least Squares (MCR-ALS), which Tauler first presented in 1995 [17] and which is easily implementable using Matlab® Graphical User Interface [18], is without a doubt the most well-liked and adaptable MCR technique [14]. This technique has already been used in the battery field to handle such a large dataset. The first report used was made by Rodriguez *et al.* in 2007 which use MCR-ALS to extract the main information from an *in situ* X-ray diffraction analysis of $(CF_x)_n$ batteries [19]. In the case of Mössbauer spectroscopy, several reports have been carried out and prove its successful use [5,20,21].

Previous studies have already been reported on the investigation of the cycling mechanism of NFPF cathode material for Li-ion and Na-ion batteries. The first work on the study of a potential mechanism of the NFPF material was reported by Ellis *et al.,* [22]. Indeed, the authors suggested the formation of an intermediate phase with a composition of $Na_{1.5}FePO_4F$ through a “quasi-solid-solution”

mechanism, however, this mechanism was not established in a battery by electrochemical cycling but by chemical oxidation of NFPF with $NOBF_4$. At this time, the electrochemical performance was evaluated in Li-ion cell. Brisbois *et al*. in 2016, performed *operando* ^{57}Fe Mössbauer spectroscopy to analyze the evolution of the oxidation state and local environment of iron in NFPF cathode material in Li-ion batteries [7]. In this study, a systematic spectrum by spectrum analysis was performed and the intermediate state was not evidenced. For Na-ion batteries, Li *et al*. in 2018 [23], and Smiley *et al*. in 2016 [24], reported an *ex situ* nuclear magnetic resonance (NMR) study of the evolution of Na site in NFPF material combined with DFT calculation. The obtained results established an intermediate phase with one of the two Na sites being inert during electrochemical cycling, Li et *al.,* are the first to report a double biphasic reaction without any solid-solution mechanism based on sodium environments evolution since nuclear magnetic resonance (NMR) is not suitable for the investigation of the oxidation state and local environment of the iron.

In this work, we mainly focused on the evolution of the iron local environment and oxidation state in NFPF material to deeply investigate the reaction mechanism to complement the previously obtained results. Our study will also be based on the evolution of the structural properties of the NFPF materials followed by *operando* XRD. Finally, we will give a first insight into the mechanism of NFPF in K-ion using the same *operando* techniques (XRD and Mössbauer) and compare it with the mechanism in NIB.

2. Experimental:

Materials synthesis is explained in the previous chapter (II 2.1). The sample used is the NFPF with 15wt% of CNT.

2.1. Structural characterization

Operando ^{57}Fe transmission Mössbauer spectroscopy spectra were recorded at room temperature with a constant-acceleration spectrometer with a ^{57}Co(Rh) source. The spectrometer was calibrated at room temperature with the magnetically split sextet spectrum of a high-purity α-Fe foil as the reference absorber. The measurements were carried out in the [± 4 mm/s] velocity ranges. Each spectrum is recorded for 4 h. The sample was in a specifically designed *in situ* cell with two Be windows (the amount of Fe contamination is negligible), allowing experiments in the transmission mode. The cell was assembled in an argon-filled glove box with a mix of powders of NFPF-15CNT (with a controlled ratio of active material 60% and total carbon 40%, including CNT and addition of carbon black) as the positive electrode, a Whatman quartz fiber separator, and sodium or potassium disc as the counter electrode. The electrolyte used was $NaPF_6$ 1 M +10wt% FEC in PC for the sodium cell and KPF_6 0.8 M in EC:PC for the potassium cell. The cycling rate is C/40 assuming a full theoretical charge or discharge in 40 h in the voltage window of 2.0 V-4.2 V.

Operando X-ray diffraction analysis was performed using a Malvern PANalytical Empyrean M with Co K_α radiation. The diffraction data were recorded in the 2Theta range of 14-45° with a step size of 0.02. The step time is adjusted to obtain a recording time of 1 h for each diffractogram. The cell used is presented in Figure III-1 and is mounted in the same conditions as for Mössbauer spectroscopy analysis. The cycling rate is C/20 assuming a full theoretical charge or discharge in 20 h between 2.0 V and 4.2 V.

2.2. Data analysis

The complete *operando* Mössbauer spectroscopy and XRD data were analyzed by combining Principal Component Analysis (PCA) and Multivariate Curve Resolution by Alternating Least Square (MCR-ALS). The MCR-ALS analysis was carried out with the following constraints: non-negativity of the concentration of the components and closure (sum of the concentrations of the component equal to 100%). The components deriving from the analysis of the Mössbauer spectra were fitted with appropriate combinations of Lorentzian lines. The hyperfine parameters such as isomer shift (δ), quadrupole splitting (ΔEq), linewidth (Γ), hyperfine field (H) and relative resonance areas of the different spectral components were determined using the Fullham program. The validity of fits was judged based on minimizing the number of parameters and χ^2 values. The component derived from XRD experiments were analyzed using TOPAS software [25] to extract lattice parameters.

3. Results and discussions:

3.1. Pristine compound analysis

The initial state (pristine) of the materials has been first analyzed to establish the basement of the *operando* experiments. Figure III-2 shows the ^{57}Fe Mössbauer spectrum of the NFPF-15CNT material, and Table III-1 presents the corresponding hyperfine parameters. The spectrum is mainly composed of an asymmetric doublet and a sextet with low intensity. The spectrum can be fitted using 5 contributions. Two contributions correspond to Fe(II) (66% and 7% of surface area) with close isomer shifts of 1.18 mm/s and 1.23 mm/s and different quadrupole splitting of 2.19 mm/s and 1.61 mm/s showing two local environments of iron that correspond to the octahedral sites in NFPF [7,26,27]. The third contribution is characterized by an isomer shift of 0.33 mm/s and quadrupole splitting of 0.74 mm/s and can be attributed to Fe(III) in oxidized NFPF. The two minor last contributions are magnetic and correspond to Fe_3C and Fe(0) with 4% and 3% of surface area respectively. Figure III-3 presents the XRD pattern of the pristine material registered in the *operando* cell at OCV. As it can be seen, a huge bump is observed between 15 and 35° 2Theta which corresponds to added carbon (40%) and experimental conditions. Despite that, the main diffraction peaks are attributed to the NFPF material. The other peaks which are not attributed to the NFPF material correspond to the e-cell. This has been determined by measuring an empty e-cell with all the constituents except the cathode material. This means that despite the impurities detected by the Mössbauer spectrum (Fe_3C and metallic Fe), the XRD analysis cannot evidence the presence of secondary phases and thus these contaminations should not interfere with the *operando* XRD analysis. Based on the full scale (+/- 12 mm/s) the total amount of impurities is about 7%. The main intense peaks are out of the range +/- 4 mm/s to be used in the *operando*

experiment in order to reduce the needed time to collect reasonable quality Mössbauer spectra in a short time (4 h) by spectrum compared to more than 24 h in the case of the pristine material (see Figure III-2). Therefore, the peaks located between -4 and 4 mm/s are less resolved on the *operando* dataset.

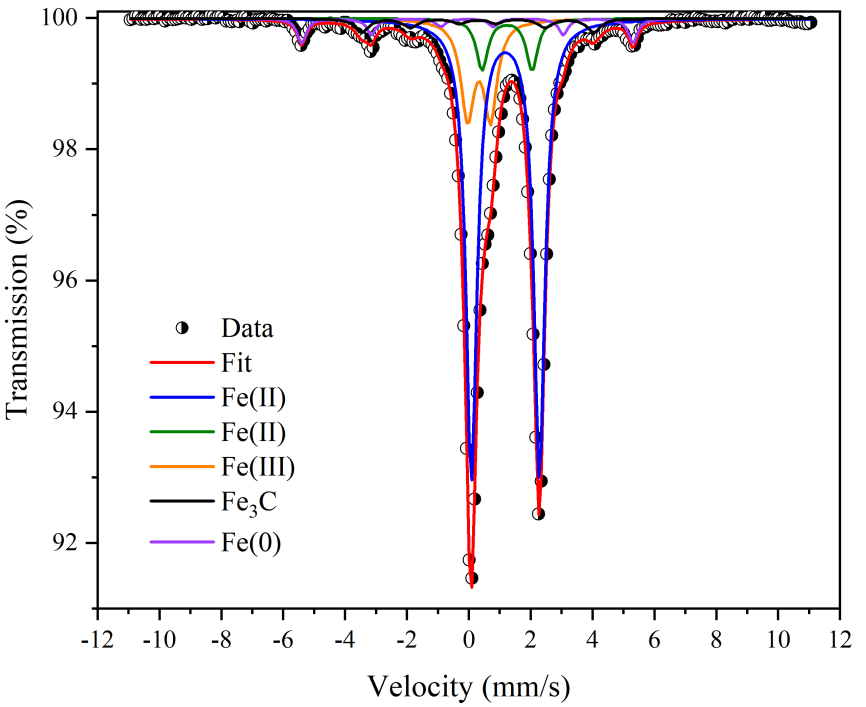

Figure III-2: Room temperature ^{57}Fe Mössbauer spectrum of pristine Na_2FePO_4F-15CNT

Table III-1: ^{57}Fe Mössbauer hyperfine parameters of the pristine Na_2FePO_4F-15CNT material

Pristine		δ (mm/s)	ΔEq (mm/s)	Γ (mm/s)	Field (Tesla)	Area (%)
	Fe(II)	1.184(6)	2.19(2)	0.43(3)	-	68(1)
	Fe(II)	1.23(4)	1.6(1)	0.43(3)	-	8(1)
	Fe(III)	0.33(3)	0.75(6)	0.50(8)	-	16(1)
	Fe_3C	0.3(1)	0	0.50(9)	23.2(1)	4(1)
	Fe(0)	0.05(1)	0	0.36*	33.2(1)	3(1)

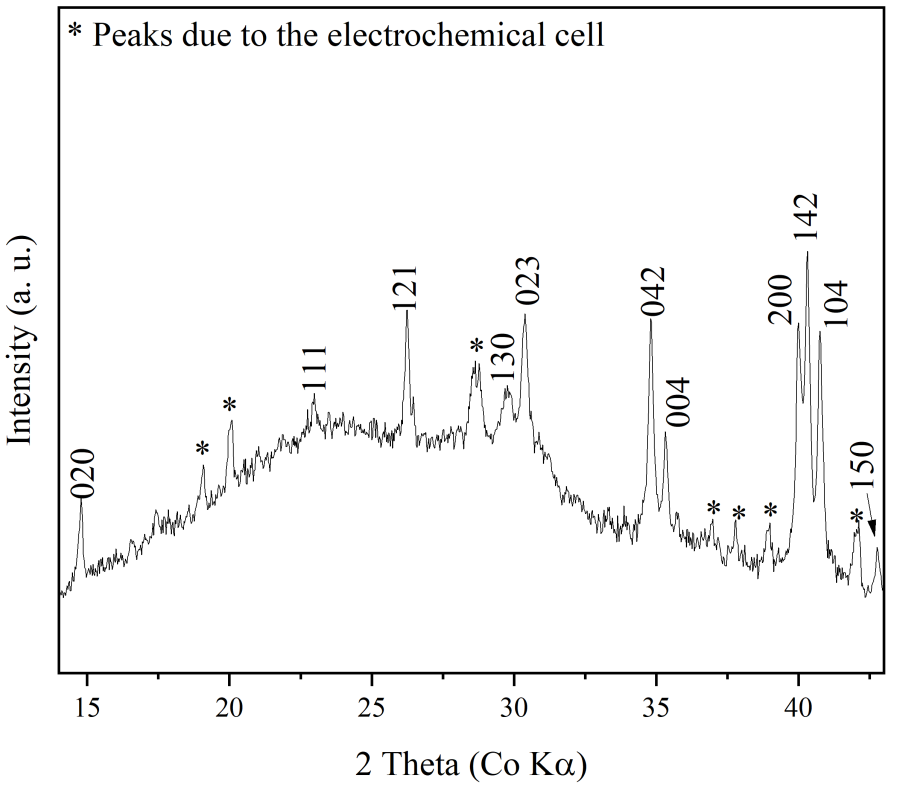

Figure III-3: XRD pattern of pristine Na_2FePO_4F-15CNT in operando electrochemical cell at OCV.

3.2. Operando Mössbauer Spectroscopy of NFPF cathode material vs. Na.

Evolution of *operando* ^{57}Fe Mössbauer spectra recorded during the first desodiation up to 4.2 V, sodiation down to 2.0 V, and subsequent desodiation up to 4.2 V of Na_2FePO_4F/CNT and corresponding voltage profile is presented in Figure III-4. The evolution of the Mössbauer spectra - i.e. the diminution of the intensity of the doublets corresponding to the Fe(II) and the simultaneous apparition of a doublet with an isomer shift of around 0.5 mm/s that corresponds to Fe(III) which- indicates the oxidation of the Fe(II) to Fe(III) during the first

charge. The reverse phenomenon is observed during the discharge. At the end of the second charge, the obtained spectrum is similar to the end of the first charge. This already shows that the process is completely reversible. It can be noticed that the first galvanostatic charge-discharge curves contain two distinct plateaus, each of which typically denotes a two-phase transformation process, during the sodium extraction and insertion processes.

To deeply analyze and investigate the phenomena occurring during the charge and discharge processes, the PCA analysis was performed and reveals that the entire *operando* dataset can be reproduced by 3 orthogonal vectors. This excludes biphasic reactions and also a solid solution mechanism hypothesis. Indeed, in the case of the biphasic reactions, only two components would have been found and in the case of solid solution, the number of distinct components would have been equal to the number of the registered spectra. The MCR-ALS should then reconstruct three spectral components. The concentration profile obtained after the MCR-ALS analysis is presented in Figure III-5 with the corresponding cycling curve at the bottom. The concentration profile reveals that the first component (OCV) is dominant at the initial state and then diminishes rapidly in favor of the intermediate component. This intermediate component has its highest concentration in the middle of the charge corresponding to the change of the plateau in the electrochemical curve. Then, the concentration of this intermediate component decreases, and a third component appears with a highest concentration at the end of the charge. The following discharge shows a similar reverse profile to recover the pristine component at the end of discharge showing the good reversibility during cycling of the NFPF-15CNT cathode material. The concentration at the end of discharge of the OCV component is slightly higher than at the initial state in line with a slightly oxidized pristine material.

The three components obtained by MCR-ALS analysis are fitted conventionally. The obtained fits are presented in Figure III-6 and Table III-2 summarizes the corresponding hyperfine parameters.

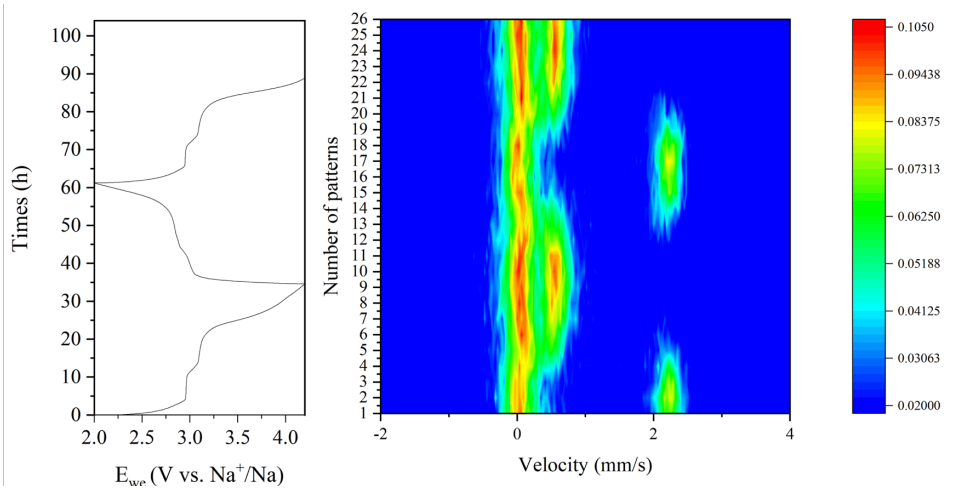

Figure III-4: Evolution of the operando ^{57}Fe Mössbauer spectra with the corresponding electrochemical cycling curve vs. Na^+/Na on left. The intensity color scale is given on the right.

The initial Mössbauer spectrum component has a similar shape to the pristine material and can be fitted using three doublets: two Fe(II) (62% and 19% of surface area) and one Fe(III) (12% of surface area) the hyperfine parameters of the two Fe(II) are similar to the ones obtained in the pristine materials with almost the same isomer shift for both Fe(II) sites: 1.21 and 1.28 mm/s but a slightly different quadrupole splitting of 2.25 mm/s and 1.97 mm/s respectively. The Fe(III) is also similar to the one in the pristine material. The observed impurities contributions in the pristine materials are also added to the fitting model of all the spectral components. The second spectral component is fitted also using three constituents but this times two Fe(III) and only one Fe(II). The new Fe(III) doublet has hyperfine parameters that are different compared to the Fe(III) observed in the pristine material. Indeed, the isomer shift is slightly higher (0.43 mm/s compared to 0.33 mm/s) and the quadrupole splitting is two times lower (0.34 compared to

0.75 mm/s) suggesting that the local iron environment is more symmetric in the oxidized state. Also, the Fe(II) contribution is slightly different from the previous one with an isomer shift a bit lower (1.19 mm/s) and a quadrupole splitting (1.97 mm/s) in the middle of the two previous ones for the pristine component. It is interesting to note that the concentration ratio of Fe(II) to Fe(III) in this second component is almost 50:50. This component is a mixed valence component with half of Fe(II) and half Fe(III). The third spectral component is a symmetric doublet that was fitted using three doublets corresponding to Fe(III) (δ=0.39 mm/s and ΔEq=0.54 mm/s) with 77% of surface area, a second contribution similar to the Fe(III) found in the pristine material and a third doublet corresponding to non-oxidized Fe(II) (δ=1.22 mm/s and ΔEq=2.25 mm/s) also similar to the one found in the pristine component with 12% of surface area confirming that Fe(II) is still found in this cathode material at the end of charge.

It is interesting to note that the amount of Fe(II) is slightly higher at the end of discharge than in its initial state. Indeed, the relative concentration of the pristine component at the initial state is about 85% while at the end of discharge it is almost 95%. This means that the oxidized iron Fe(III) in the initial pristine material is partially recovered after a first cycle. This phenomenon was already evidenced in LIB by Brisbois *et al.* [7].

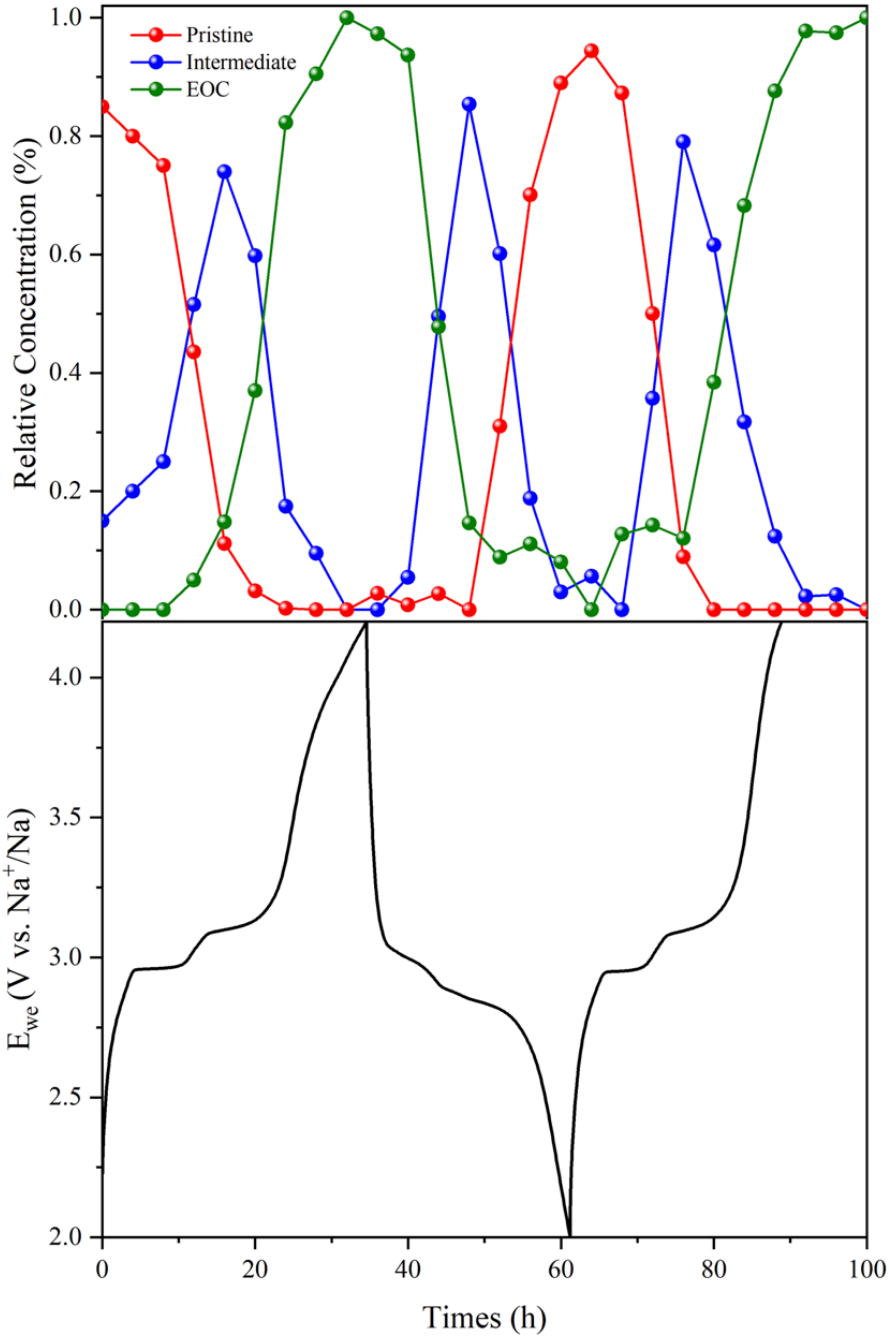

Figure III-5: Concentration profile of the components from ^{57}Fe Mössbauer MCR-ALS and the corresponding electrochemical curve vs. Na^+/Na.

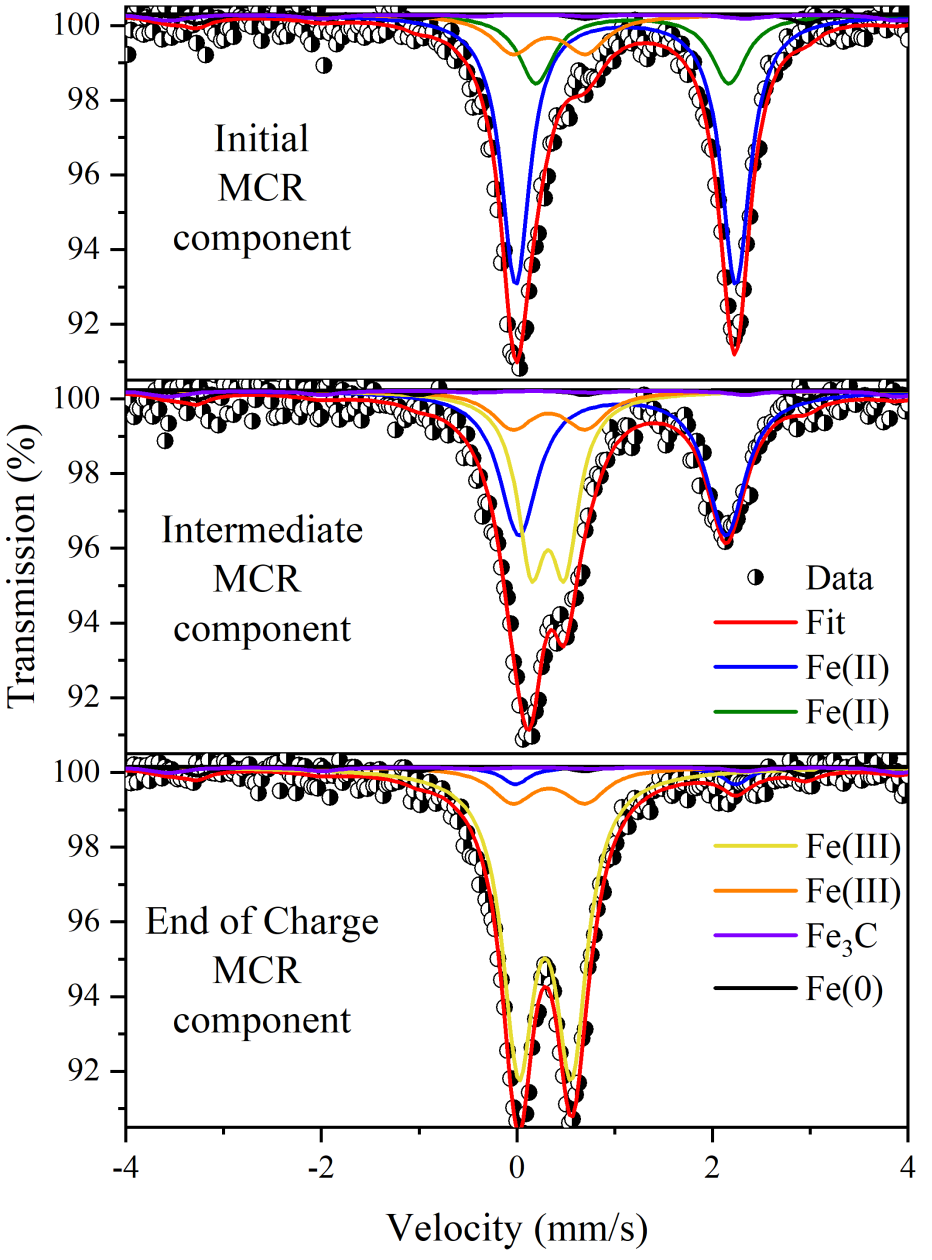

Figure III-6: Mössbauer fit of components obtained via MCR-ALS for initial component (pristine), intermediate component, and end of charge component in the top, center, and bottom respectively for NFPF vs. Na^+/Na cycling.

Table III-2: ^{57}Fe Mössbauer hyperfine parameters of the MCR-ALS components for NFPF vs. Na^+/Na cycling.

Na-ion		∂ (mm/s)	ΔEq (mm/s)	Γ (mm/s)	Field (Tesla)	Area (%)
Initial MCR component	Fe(II)	1.223(4)	2.251(6)	0.356(9)	-	62(1)
	Fe(II)	1.29(4)	1.97(5)	0.43*	-	19(1)
	Fe(III)	0.33(3)	0.75(6)	0.50(8)	-	12(1)
	Fe_3C	0.3*	0*	0.50*	23.2*	4*
	Fe(0)	0.05*	0*	0.36*	33.2*	3*
Intermediate MCR component	Fe(III)	0.430(5)	0.343(8)	0.34(1)	-	36(1)
	Fe(II)	1.191(6)	2.12(1)	0.48(2)	-	45(1)
	Fe(III)	0.33(3)	0.75(6)	0.50(8)	-	12(1)
	Fe_3C	0.3*	0*	0.50*	23.2*	4*
	Fe(0)	0.05*	0*	0.36*	33.2*	3*
End-of-charge MCR component	Fe(III)	0.398(2)	0.543(4)	0.389(6)	-	77(1)
	Fe(II)	1.22(4)	2.251(6)	0.35*	-	4(1)
	Fe(III)	0.33(3)	0.75(6)	0.50(8)	-	12(1)
	Fe_3C	0.3*	0*	0.50*	23.2*	4*
	Fe(0)	0.05*	0*	0.36*	33.2*	3*

3.3. Operando X-ray diffraction of NFPF in Na-ion batteries

To follow the structural evolution of NFPF during cycling, an *operando* XRD analysis was performed in *vs.* Na. The evolution of the diffractograms is presented in Figure III-7 as well as the corresponding electrochemical curve. The initial XRD pattern fully corresponds to the pristine material. As the pristine diffraction peaks disappear; a small peak appears around 36° at about the middle of the charge then disappear and a higher intensity peak appears around 36.5°. The same reverse phenomenon is observed during the discharge. To fully handle this dataset, we have performed a PCA and then MCR-ALS analysis in the same way. This analysis also leads to three spectral components. The evolution of their concentration is presented in Figure III-8 and looks very similar to that obtained in *operando* Mössbauer analysis. In total agreement with Mössbauer data, the initial predominant state is rapidly decreasing when the intensity of an intermediate component is increasing. Then this second component is decreasing with the appearance of a third component that becomes predominant at the end of discharge.

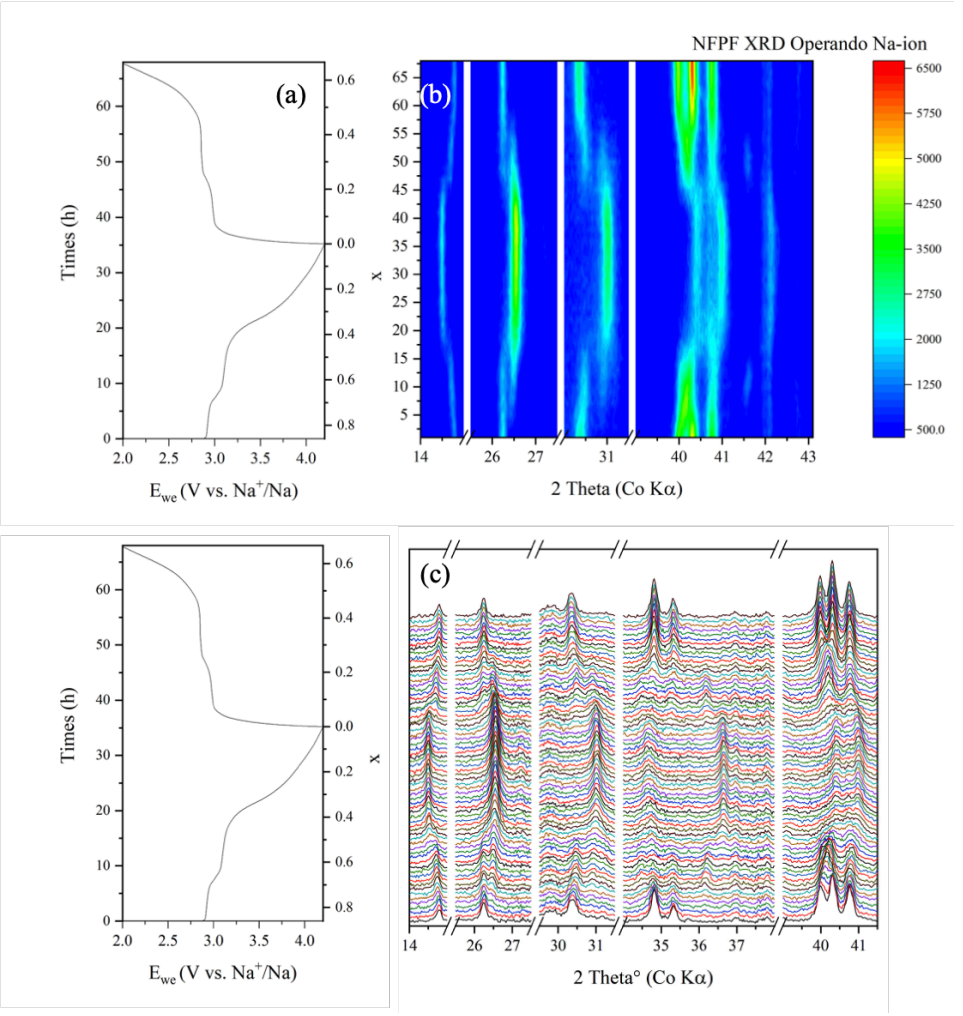

Figure III-7: The evolution of the operando X-ray diffraction patterns of the Na_2FePO_4F-15CNT during the first charge and discharge against Na^+/Na, (a) corresponding electrochemical curves, (b) topographic view with corresponding intensity color scale, (c) 2D view evolution of the XRD patterns.

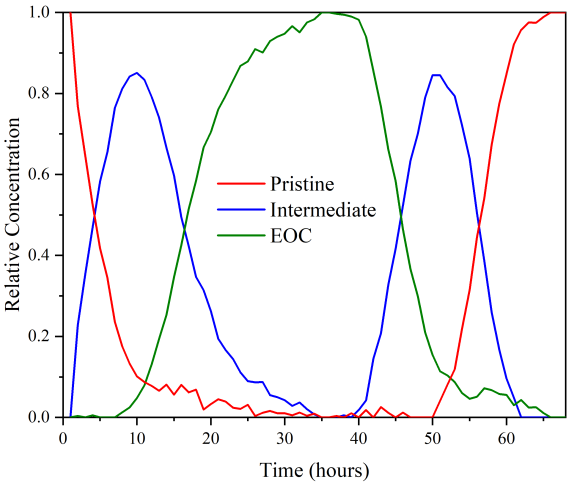

Figure III-8: Concentration profile of XRD MCR-ALS components during the first cycle of Na_2FePO_4F vs. Na.

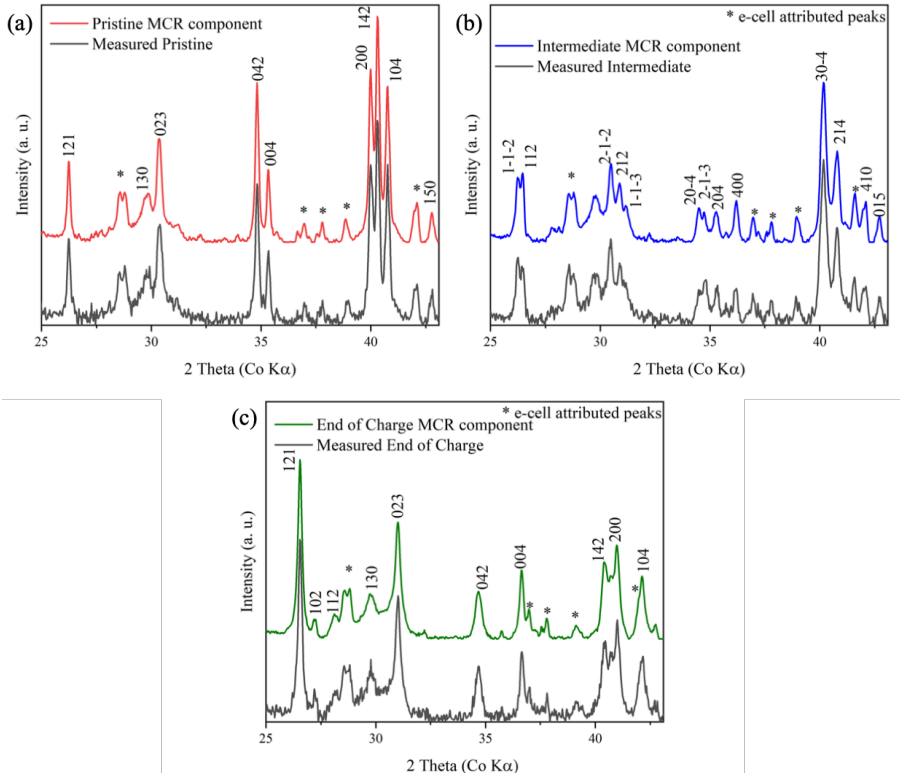

Figure III-9: XRD components obtained via MCR-ALS and their corresponding ex situ measured diffractograms for (a) Pristine in red, (b) Intermediate in blue, and (c) End of Charge in green for NFPF cycling against Na^+/Na.

The obtained component patterns are presented in Figure III-9. In order to confirm the physical meaning of these component patterns, an experimental diffractogram has been associated with all three components. For the pristine component, the profile is identical to the measured initial diffractogram at OCV in the e-cell. As for the pristine material, all diffraction peaks can be indexed in the Pbcn space group (NFPF). Starting from the published structural models for the different phases [22,28], approximate cell parameters, for the powder studied here, were extracted by progressive modification of the cell parameters to achieve the best visual match between the experimental and calculated peak positions in the diffractograms (using TOPAS software). The obtained cell parameters are: a=5.222 Å, b=13.854 Å, and c=11.772 Å leading to a cell volume of 851.65 $Å^3$. The third component peaks can be indexed in the Pbcn space group (Na_1FePO_4F) corresponding to the fully charged electrode material with the calculated cell parameters of a=5.112 Å, b= 14.121 Å, and c= 11.375 Å thus a volume of cell= 821.12 $Å^3$. Finally, the second component cannot be indexed in Pbcn space group, which is consistent with the results reported in the literature obtained by DFT calculations that indicate that this intermediate phase crystallizes in a monoclinic crystal system of $P2_1/c$ space group [22,23,29]. The calculated cell parameters are a=11.513 Å, b=5.200 Å, c=13.907 Å, and β=91.36° leading to a cell volume of 832.58 $Å^3$. The volume decreases progressively from 851 Å at the initial pristine component to 832 Å at the intermediate state component and finally reached 821 Å at the EOC component. The volume cell decreases simultaneously with the decrease of concentration of Na amount in the material.

All these results prove the double biphasic electrochemical mechanism of NFPF in NIBs. Indeed, the components are sufficiently different to confirm two biphasic components. According to the amount of Fe(II) and Fe(III) in the three components, the intermediate state of $Na_{1.5}FePO_4F$ is also found, leading to:

$$Na_2FePO_4F \xleftrightarrow{Dis/charge} Na_{1.5}FePO_4F \xleftrightarrow{Dis/charge} Na_1FePO_4F$$

To conclude this part, the proposed mechanism passing through an intermediate state has been evidenced by MCR-ALS analysis of *operando* XRD and *operando* Mössbauer spectroscopy analysis. The mechanism is a clear double biphasic reaction. The identified intermediate state has a mixed valence Fe(III)/Fe(II) confirming the extraction of only half of the sodium. The NFPF-15CNT cathode material also exhibits excellent reversibility during cycling.

3.4. Operando Mössbauer Spectroscopy of NFPF in vs. K.

The evolution of *operando* ^{57}Fe Mössbauer spectra during the first charge, first discharge, and second discharge in K-ion batteries between 1.5 V and 4.2 V is presented in Figure III-10 with the corresponding voltage profiles. First of all, the quality of the data is lower than in the case of the Na-ion, due to a higher absorption of 14.4 keV radiation by potassium (note that the thinnest potassium foil that can be hand made in glovebox is still few millimeters thick). This issue makes the data analysis and interpretation more difficult.

At the beginning of the charge, there are two main peaks of intensity at open-circuit voltage. The first charge has the only objective to remove Na from the material. Gradually during the first charge, the doublet situated around 2 mm/s disappears and a new one appears around 0.5 mm/s. This new doublet appears to be at its max intensity after a full charge. The reverse observations can be done during the first discharge but the concentration of the new Mössbauer spectra is not fully recovered meaning that some irreversibility may occur and that the K^+ ions cannot intercalate as well as in the case of Na^+ ions.

The great advantage of the PCA and MCR-ALS analysis is even more convincing when the dataset has a low resolution. Indeed, as these techniques use all data sets at the same time, the spectral component resolution will be higher than the individual spectrum [14].

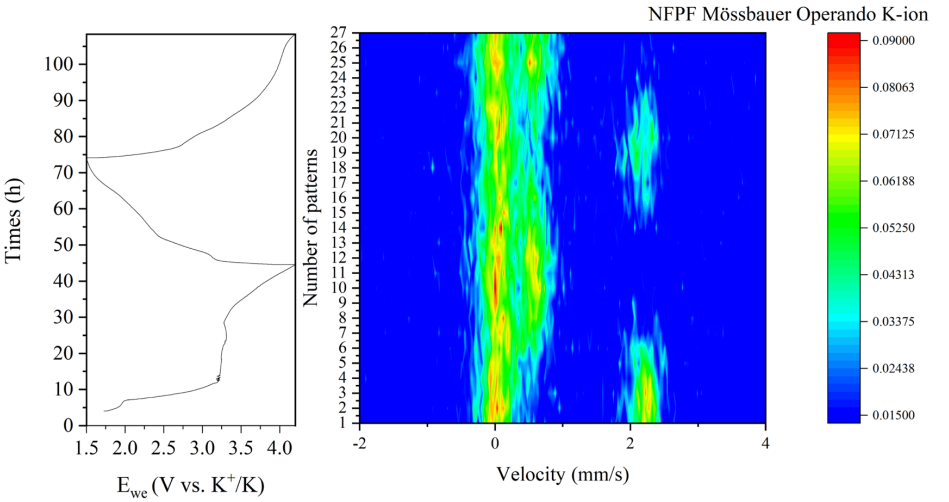

Figure III-10: Evolution of operando ^{57}Fe Mössbauer spectra with corresponding electrochemical cycling curve vs. K^+/K on left.

In this case, the PCA analysis concludes that all the datasets can be reproduced by 2 orthogonal vectors. The MCR-ALS should reconstruct two spectral components still inducing a biphasic mechanism but not a double biphasic mechanism. The concentration profile obtained after the MCR-ALS analysis is presented in Figure III-11 with the corresponding voltage profile. The concentration profile shows as expected that a first component is predominant at the OCV and beginning of the charge, its concentration gradually decreases to reach 50% at about the middle of the charge desodiation plateau. In this case, the material has not been precycled and the first charge corresponds to the desodiation process. The first component continue to decrease and finally reached 0% at the end of the charge. During the decrease of the first component, the second spectral component has a reverse slope of concentration to reach a maximum at the end of the charge. During the first discharge corresponding to the potassiation process of the NFPF-15CNT material, the second component concentration decreases and the first component increases at the same time. Contrary to the cycling in NIB, at the

end of the discharge, the first component concentration is only 70% and about 30% of the second component is still present. Meaning that the insertion of the potassium is not complete and that some oxidized Fe(III) is still present at the end of the discharge. This is likely due to a low kinetic for potassium intercalation. After the second charge, the second component has a concentration of 100% similar to the first charge.

The two components obtained by MCR-ALS are fitted and the results are presented in Figure III-12. Table III-3 presented the associated hyperfine parameters. The initial component is a doublet with the main peak around 1 mm/s. This spectrum can be fitted using three doublets. The two first doublets are associated with Fe(II) (29% and 52% of the surface area) with similar isomer shifts (δ_1=1.22 mm/s and δ_2=1.25 mm/s) but slightly different quadrupole splitting (ΔEq_1=2.33 mm/s and ΔEq_2=1.96 mm/s) as for the pristine material. The third constituent is associated with Fe(III) and represents 12% of the surface area and is similar to the one in pristine component. Finally, the two sextets corresponding to Fe_3C and Fe(0) are also added to the fit even though the low quality of the *operando* data doesn't allow clear observation of any magnetic constituent in the spectrum.

The second MCR spectral component is an asymmetric doublet that can be fitted with three main contributions. In this case, there is two Fe(III) contributions ((δ_1=0.41 mm/s and δ_2=0.33 mm/s (ΔEq_1=0.55 mm/s and ΔEq_2=0.75 mm/s) and one Fe(II) contribution. The hyperfine parameters are close to the ones found for the third component of the *operando* Mössbauer spectroscopy in NIB. This means that iron is in the same state at the EOC in both NIB and KIB. The two Fe(III) doublet represents 81% (69% for the first doublet and 12% for the second) of the surface area and the Fe(II) doublet represents 12%. The later has a lower isomer shift than other Fe(II) of 1.08 mm/s but a similar quadrupole splitting of 2.35 mm/s to the first doublet of the initial component in KIB.

This result confirms the incomplete insertion of potassium in the NFPF material in this case. Indeed, the concentration profile proves that some oxidized material is still present at the end of the discharge but also the second component still has about 12% of Fe(II) meaning that at the end of charge the material is not fully oxidized and that a part of the sodium is not correctly extracted. These observations are different from the one obtained in NIB where the reversibility was clearly established and the oxidation at the end of charge was considered as complete as the Fe(II) doublet was only representing 4% of the surface area. This may be explained by interference in the electrolyte between K^+ and Na^+ ions leading to lower performance of the material or by a problem in the cell mounting that has led to lower electrochemical performance.

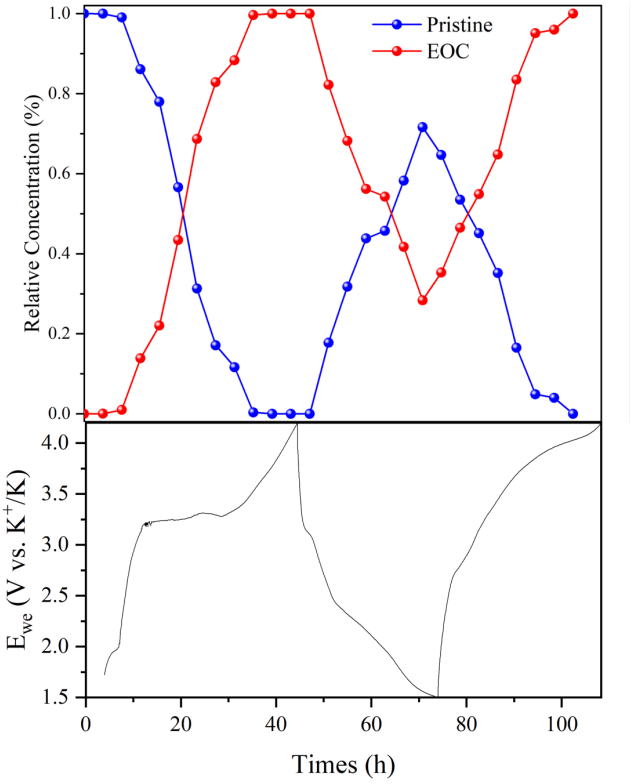

Figure III-11: Concentration profile of ^{57}Fe Mössbauer MCR-ALS components and corresponding electrochemical curve vs. K^+/K.

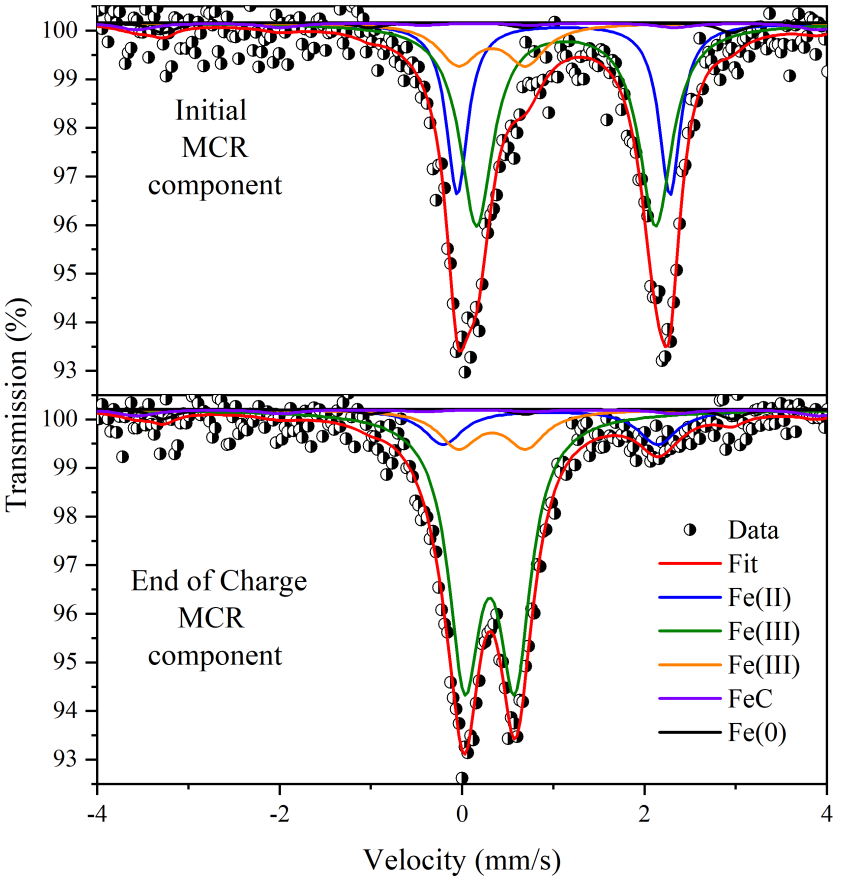

Figure III-12: Fittings of MCR Mössbauer components for initial component (pristine), and end of charge component in the top and bottom respectively for NFPF vs. K^+/K.

Table III-3: ^{57}Fe Mössbauer hyperfine parameters of the MCR-ALS components for NFPF *vs.* K^+/K cycling.

K-ion		δ (mm/s)	ΔEq (mm/s)	*Γ* (mm/s)	Field (Tesla)	Area (%)
Initial MCR component	Fe(II)	1.223(4)	2.33(2)	0.28(3)	-	29(1)
	Fe(II)	1.252(5)	1.96(3)	0.44(2)	-	52(1)
	Fe(III)	0.33(3)	0.75(6)	0.50(8)	-	12(1)
	Fe_3C	0.3*	0*	0.50*	23.2*	4*
	Fe(0)	0.05*	0*	0.36*	33.2*	3*
End of Charge MCR Component	Fe(III)	0.414(4)	0.551(6)	0.42(1)	-	69(1)
	Fe(II)	1.08(3)	2.35(6)	0.5(1)	-	12(1)
	Fe(III)	0.33(3)	0.75(6)	0.50(8)	-	12(1)
	Fe_3C	0.3*	0*	0.50*	23.2*	4*
	Fe(0)	0.05*	0*	0.36*	33.2*	3*

3.5. *Operando X-ray diffraction of NFPF in Na-ion batteries*

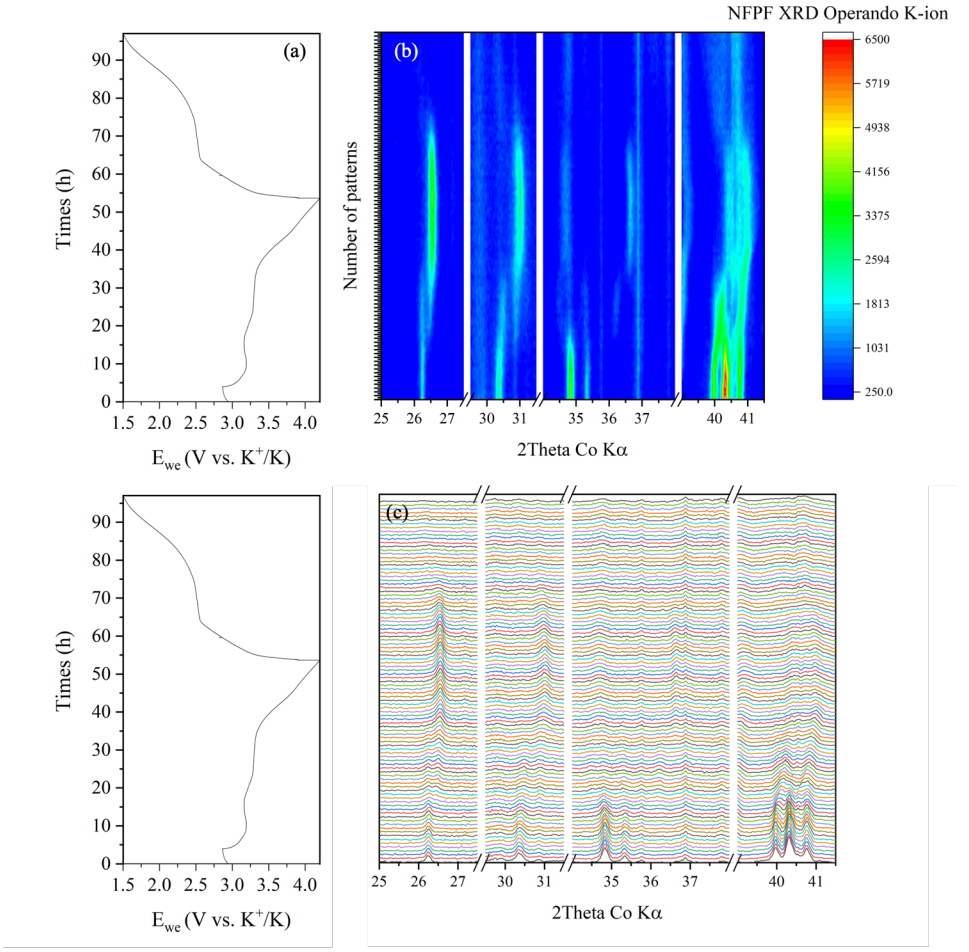

Figure III-13: Operando X-ray diffraction of the Na_2FePO_4F cycling against K^+/K, (a) corresponding electrochemical curves, (b) topographic view with corresponding intensity color scale, (c) 2D view evolution of the XRD patterns.

The evolution of the X-ray diffractograms recorded during the first charge-discharge NFPF cathode material in KIB is presented in Figure III-13 with its associated voltage profile. The initial XRD pattern corresponds as expected to

the pristine material. At the end of the first charge, only a few peaks can be detected at around 26.5°, 31°, and 41° that are located at higher 2Theta values. Also, the peaks around 37° are split in two at the end of charge. The three peaks around 41° merged and displace to the right and only two are visible at the EOC. These observations can be explained by the formation of the desodiated Na_1FePO_4F phase. Despite, the lower intensity these observations are similar to the one done in *operando* XRD *vs.* Na^+/Na, this is expected as the first charge in both only results in the removal of the Na from the material. During the discharge, the peaks seem to return to their initial position but with a clear decrease in intensity indicating partial amorphization of the electrode material during the first discharge.

The PCA analysis has provided that three orthogonal vectors are sufficient to analyze all the dataset of the two first cycles. MCR-ALS analysis reconstructed the three components diffractograms. The concentration profile and the associated voltage profiles are presented in Figure III-14.

In this case regarding only the first charge, a similar profile is observed with an intermediate that doesn't reach as high intensity as in NIB but that is present and its low intensity can be explained by the lower quality of the data due to the amorphization of the electrode material. At the end of the first charge, the initial pristine component fully disappears, and the 100% concentration is attributed to the third component. After this point, the potassiation of the material begins to occur with the first discharge and simultaneously the third component disappears with the appearance of the intermediate component that increases in concentration. After the full discharge, the next cycle shows poor reversibility with almost no change in the concentration profile of the intermediate component and an increase of the EOC component. This proves that the reversibility is not achieved in this cell but also that better data are required to deeply understand the change induced by the replacement of Na by K in the NFPF material. Indeed, we

expected 4 components to be determined by PCA and MCR-ALS analysis the three first ones are already discussed but the fourth component should have been attributed to $NaKFePO_4$ at the end of the first discharge. The MCR diffractograms are presented in Figure III-15. As expected the first component corresponds to the pristine material, the third component is associated with the desodiated Na_1FePO_4F and the intermediate component cannot be associated with any known phase and no conclusive information can be extracted from this third component. Also, the intensity is erroneously high compared to the other component as the patterns are normalized.

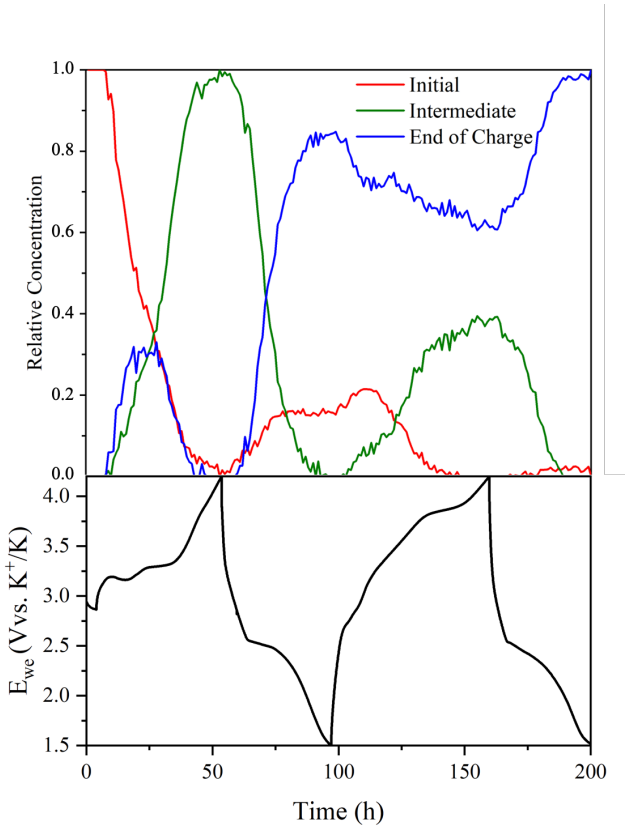

Figure III-14: Concentration profile of XRD MCR-ALS components during the first cycle of Na_2FePO_4F vs. K^+/K.

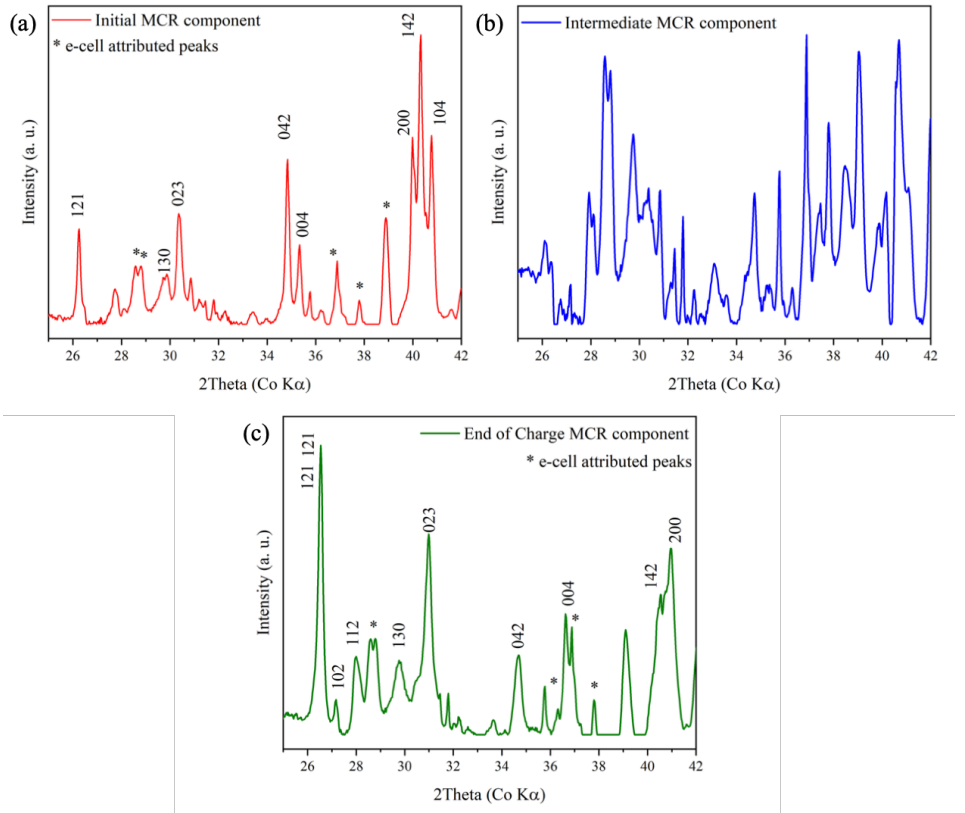

Figure III-15: XRD components obtained via MCR-ALS and (a) for the initial state in red,(b) for intermediate in blue, and (c) for End of Charge in green for NFPF vs. K^+/K.

4. Conclusion

The *operando* ^{57}Fe Mössbauer spectroscopy combined with *operando* X-ray diffraction has been successfully used to analyze the electrochemical mechanism of NFPF *vs.* Na^+/Na batteries during cycling. The double biphasic mechanism has been clearly established by using PCA and MCR-ALS chemometric tools. The intermediate state $Na_{1.5}FePO_4F$ appears directly when charging refuting the idea of a quasi-solid-solution mechanism. Regarding the cycling mechanism of the same materials in K-ions mat *vs.* K^+/K, our preliminary results show that the EOC component is similar to that of NIB, and that the iron oxidation state follows a reversible variation along cycling. Some clear differences have been evidenced and in particular, the lower reversibility that is observed in the case of K-ion batteries, but also the absence of an intermediate during the first potassiation. To get more insights, a better quality dataset should be obtained and one way to enhance the quality of the cycling is to perform a precycling preparation as presented at the end of chapter 2 because it leads to enhanced electrochemical performance.

5. References

[1] C.P. Grey, J.M. Tarascon, Sustainability and in situ monitoring in battery development, Nature Materials. 16 (2016) 45–56. https://doi.org/10.1038/nmat4777.

[2] F. Orsini, A. du Pasquier, B. Beaudoin, J.M. Tarascon, M. Trentin, N. Langenhuizen, E. de Beer, P. Notten, In situ Scanning Electron Microscopy (SEM) observation of interfaces within plastic lithium batteries, Journal of Power Sources. 76 (1998) 19–29. https://doi.org/10.1016/S0378-7753(98)00128-1.

[3] J.N. Reimers, J.R. Dahn, Electrochemical and In Situ X-Ray Diffraction Studies of Lithium Intercalation in Li x CoO2, Journal of The Electrochemical Society. 139 (1992) 2091–2097. https://doi.org/10.1149/1.2221184.

[4] T. Broux, T. Bamine, L. Simonelli, L. Stievano, F. Fauth, M. Ménétrier, D. Carlier, C. Masquelier, L. Croguennec, VIV Disproportionation Upon Sodium Extraction from Na3V2(PO4)2F3 Observed by Operando X-ray Absorption Spectroscopy and Solid-State NMR, Journal of Physical Chemistry C. 121 (2017) 4103–4111. https://doi.org/10.1021/acs.jpcc.6b11413.

[5] A. Darwiche, M. Fehse, A. Mahmoud, C. la Fontaine, B. Fraisse, R. Hermann, M.-L. Doublet, L. Monconduit, M. Sougrati, M. ben Yahia, L. Stievano, The Electrochemical Sodiation of Sb Investigated by Operando X-ray Absorption and 121Sb Mössbauer Spectroscopy: What Does One Really Learn?, Batteries. 4 (2018) 25. https://doi.org/10.3390/BATTERIES4020025.

[6] M. Bianchini, F. Fauth, N. Brisset, F. Weill, E. Suard, C. Masquelier, L. Croguennec, Comprehensive Investigation of the Na 3 V 2 (PO 4) 2 F 3 – NaV 2 (PO 4) 2 F 3 System by Operando High Resolution Synchrotron X-ray Diffraction, Chemistry of Materials. 27 (2015) 3009–3020. https://doi.org/10.1021/acs.chemmater.5b00361.

[7] M. Brisbois, S. Caes, M.T. Sougrati, B. Vertruyen, A. Schrijnemakers, R. Cloots, N. Eshraghi, R.P. Hermann, A. Mahmoud, F. Boschini, Na2FePO4F/multi-walled carbon nanotubes for lithium-ion batteries: Operando Mössbauer study of spray-dried composites, Solar Energy Materials and Solar Cells. 148 (2016) 67–72. https://doi.org/10.1016/j.solmat.2015.09.005.

[8] M. Bianchini, F. Fauth, N. Brisset, F. Weill, E. Suard, C. Masquelier, L. Croguennec, L. de Réactivité, D. Chimie, U. de Picardie, J. Verne, F.-A. Cedex, S. Table, N.V.P.O. F, A comprehensive investigation of the by operando high resolution synchrotron X-ray diffraction SI, 2 (n.d.).

[9] D. Beltran-porter, R. Olazcuaga, L. Fournès, F. Ménil, F.G. Le, Etude magnétique et par résonance Mössbauer de l ' orthophosphate Na 3Fe2 (PO4) 3 α et d ' une phase vitreuse dérivée, Revue de Physique Appliquée, Société Française de Physique. 15(6) (1980) 1155–1160.

[10] M. Fehse, D. Bessas, A. Mahmoud, A. Diatta, R.P. Hermann, L. Stievano, M.T. Sougrati, The Fe4+/3+ Redox Mechanism in NaFeO2: A Simultaneous Operando Nuclear Resonance and X-ray Scattering Study, Batteries and Supercaps. 3 (2020) 1341–1349. https://doi.org/10.1002/batt.202000157.

[11] I.K. Lee, I.B. Shim, C.S. Kim, Phase transition studies of sodium deintercalated Na2-xFePO 4F (0≤x≤1) by Mössbauer spectroscopy, Journal of Applied Physics. 109 (2011) 2009–2012. https://doi.org/10.1063/1.3561798.

[12] J.B. Leriche, S. Hamelet, J. Shu, M. Morcrette, C. Masquelier, G. Ouvrard, M. Zerrouki, P. Soudan, S. Belin, E. Elkaïm, F. Baudelet, An Electrochemical Cell for Operando Study of Lithium Batteries Using Synchrotron Radiation, Journal of The Electrochemical Society. 157 (2010) A606. https://doi.org/10.1149/1.3355977.

[13] N. Kumar, A. Bansal, G.S. Sarma, R.K. Rawal, Chemometrics tools used in analytical chemistry: An overview, Talanta. 123 (2014) 186–199. https://doi.org/10.1016/j.talanta.2014.02.003.

[14] M. Fehse, A. Iadecola, M.T. Sougrati, P. Conti, M. Giorgetti, L. Stievano, Applying chemometrics to study battery materials: Towards the comprehensive analysis of complex operando datasets, Energy Storage Materials. 18 (2019) 328–337. https://doi.org/10.1016/j.ensm.2019.02.002.

[15] A. de Juan, J. Jaumot, R. Tauler, Multivariate Curve Resolution (MCR). Solving the mixture analysis problem, Analytical Methods. 6 (2014) 4964–4976. https://doi.org/10.1039/c4ay00571f.

[16] C. Ruckebusch, L. Blanchet, Multivariate curve resolution: A review of advanced and tailored applications and challenges, Analytica Chimica Acta. 765 (2013) 28–36. https://doi.org/10.1016/j.aca.2012.12.028.

[17] R. Tauler, Multivariate curve resolution applied to second order data, Chemometrics and Intelligent Laboratory Systems. 30 (1995) 133–146. https://doi.org/10.1016/0169-7439(95)00047-X.

[18] J. Jaumot, A. de Juan, R. Tauler, MCR-ALS GUI 2.0: New features and applications, Chemometrics and Intelligent Laboratory Systems. 140 (2015) 1–12. https://doi.org/10.1016/j.chemolab.2014.10.003.

[19] M.A. Rodriguez, M.R. Keenan, G. Nagasubramanian, In situ X-ray diffraction analysis of (CFx)n batteries: Signal extraction by multivariate analysis, Journal of Applied Crystallography. 40 (2007) 1097–1104. https://doi.org/10.1107/S0021889807042045.

[20] M. Fehse, D. Bessas, A. Darwiche, A. Mahmoud, G. Rahamim, C. la Fontaine, R.P. Hermann, D. Zitoun, L. Monconduit, L. Stievano, M.T.

Sougrati, The Electrochemical Sodiation of FeSb2: New Insights from Operando 57Fe Synchrotron Mössbauer and X-Ray Absorption Spectroscopy, Batteries and Supercaps. 2 (2019) 66–73. https://doi.org/10.1002/batt.201800075.

[21] M. Fehse, M.T. Sougrati, A. Darwiche, V. Gabaudan, C. la Fontaine, L. Monconduit, L. Stievano, Elucidating the origin of superior electrochemical cycling performance: New insights on sodiation-desodiation mechanism of SnSb from: Operando spectroscopy, Journal of Materials Chemistry A. 6 (2018) 8724–8734. https://doi.org/10.1039/c8ta02248h.

[22] B.L. Ellis, W.R.M. Makahnouk, Y. Makimura, K. Toghill, L.F. Nazar, A multifunctional 3.5V iron-based phosphate cathode for rechargeable batteries, Nature Materials. 6 (2007) 749–753. https://doi.org/10.1038/nmat2007.

[23] Q. Li, Z. Liu, F. Zheng, R. Liu, J. Lee, G. Xu, G. Zhong, X. Hou, R. Fu, Z. Chen, K. Amine, J. Mi, S. Wu, C.P. Grey, Y. Yang, Identifying the Structural Evolution of the Sodium Ion Battery Na 2 FePO 4 F Cathode , Angewandte Chemie. 130 (2018) 12094–12099. https://doi.org/10.1002/ange.201805555.

[24] D.L. Smiley, G.R. Goward, Ex Situ 23Na Solid-State NMR Reveals the Local Na-Ion Distribution in Carbon-Coated Na2FePO4F during Electrochemical Cycling, Chemistry of Materials. 28 (2016) 7645–7656. https://doi.org/10.1021/acs.chemmater.6b02539.

[25] R.W. Cheary, A. Coelho, Fundamental parameters approach to x-ray line-profile fitting, Journal of Applied Crystallography. 25 (1992) 109–121. https://doi.org/10.1107/S0021889891010804.

[26] M. Brisbois, N. Krins, R.P. Hermann, A. Schrijnemakers, R. Cloots, B. Vertruyen, F. Boschini, Spray-drying synthesis of Na2FePO4F/carbon powders for lithium-ion batteries, Materials Letters. 130 (2014) 263–266. https://doi.org/10.1016/j.matlet.2014.05.121.

[27] A. Mahmoud, S. Caes, M. Brisbois, R.P. Hermann, L. Berardo, A. Schrijnemakers, C. Malherbe, G. Eppe, R. Cloots, B. Vertruyen, F. Boschini, Spray-drying as a tool to disperse conductive carbon inside Na2FePO4F particles by addition of carbon black or carbon nanotubes to the precursor solution, Journal of Solid State Electrochemistry. 22 (2018) 103–112. https://doi.org/10.1007/s10008-017-3717-x.

[28] Q. Li, Z. Liu, F. Zheng, R. Liu, J. Lee, G.L. Xu, G. Zhong, X. Hou, R. Fu, Z. Chen, K. Amine, J. Mi, S. Wu, C.P. Grey, Y. Yang, Identifying the Structural Evolution of the Sodium Ion Battery Na2FePO4F Cathode, Angewandte Chemie - International Edition. 57 (2018) 11918–11923. https://doi.org/10.1002/anie.201805555.

[29] X. Deng, W. Shi, J. Sunarso, M. Liu, Z. Shao, A Green Route to a Na2FePO4F-Based Cathode for Sodium Ion Batteries of High Rate and Long Cycling Life, ACS Applied Materials and Interfaces. 9 (2017) 16280–16287. https://doi.org/10.1021/acsami.7b03933.

Chapter IV

Spray-dried $K_3V(PO_4)_2$/C composites as novel cathode materials for K-ion batteries with superior electrochemical performance

ABSTRACT:

Intensive efforts are needed to find an alternative to replace Li-ion batteries. Among the potential candidates, K-ions batteries have received a lot of interest thanks to the low reduction potential and low cost of potassium due to the high abundance and broad distribution of potassium sources. In this regard, the development of high performance cathode materials has raised some challenges. Phosphate-based materials are considered as the most promising cathode materials for KIBs owing to their high structural stability upon cycling, high ionic conductivity and high insertion potential. Here, $K_3V(PO_4)_2$ and $K_3V(PO_4)_2$/C composites are reported as new cathode materials for KIBs with a high theoretical capacity (150 mAh/g) and a high working potential (3.5-4 V). The pristine $K_3V(PO_4)_2$ and $K_3V(PO_4)_2$/C composite materials are obtained by spray-drying process. The influence of grinding process on the structural, morphological and the electrochemical properties is investigated. The composite with carbon nanotubes (KVP/20CNT) demonstrates the best reversible capacity of 101 mAh/g at C/40 using 0.8 M KPF_6 in PC +10wt% FEC as electrolyte. Different characterization techniques are combined to investigate the structural and morphological properties of the materials such as X-ray driffraction, scanning electron microscopy, transmission electron microscopy and Laser granulometry.

1. Introduction

Our planet faces major sustainability challenges, demanding innovative research in various disciplines which include, among others, the field of energy storage technologies. Indeed, large-scale energy storage systems with long cycle life, high efficiency, low cost and excellent safety characteristics are urgently required to ensure the rapid shift from fossil-fuel-powered to clean energy sources.

Li-ion batteries (LIBs), which display the highest energy density compared to other technologies, have conquered the electronics field and are regarded as the best technology for powering mobile devices and electric vehicles. However, Li-ion batteries face many difficulties and limitations: in addition to safety concerns, the relative abundance of lithium is limited to 20 ppm in the Earth's crust and lithium resources are unevenly distributed leading to high extraction cost [1,2]. These issues are raising doubts regarding the security of supply and cost of lithium in the future. For these reasons, intensive efforts are ongoing to find alternatives to replace Li-ion battery technology. Sodium, as one of the most abundant elements in the earth crust with only slightly higher reduction potential compared to lithium (+0.3 V *vs.* Li), is an obvious candidate and research on Na-ion batteries (NIBs) has been a very active field for years [2]. Along with NIBs, potassium-ion batteries (KIBs) have recently been receiving a lot of interest: geographically well distributed, 880 times more abundant and 90% cheaper than lithium[2–4], potassium offers a reduction potential similar to lithium so that, for an equivalent specific capacity, KIBs should deliver higher energy density than NIBs. Besides, graphite (the commercial anode for LIBs since 1990) presents good performance for KIBs [2,5,6]. Thus, KIBs theoretically combine the advantages of LIBs and NIBs and are currently considered as strong candidates to replace LIBs for many applications including transportation and stationary applications [1,2,4].

In order to fulfill the promise of KIBs with high energy densities, the key issue is now the development of long life, high voltage and high capacity cathode materials. Breakthroughs in materials design/processing are essential, by addressing the synthesis of new nanostructured composite positive electrode materials. Only a few cathode materials have been reported to date for KIBs and mainly four classes of electrode material families have attracted the attention of researchers in the recent years: i) organic compounds [7], ii) layered oxides [8], iii) Prussian blue analogues (PBAs) [9] or Prussian white analogues (PWAs) [10], and iv) polyanionic materials [5]. Among these materials, polyanionic materials are of high interest due to their high structural stability upon cycling, high insertion potential and good ionic conductivity. Only a few polyanionic materials such as $KFeSO_4F$, $K_3V_2(PO_4)_3/C$ and $K_3V_2(PO_4)_2F_3/C$ [5] have been investigated so far and the reported results suggest that the diffusion coefficient of K^+ ions is higher than those of Li^+ and Na^+ ions [11]. The crystallographic structure of polyanionic materials is characterized by a highly covalent three-dimensional framework generating large interstitial spaces and providing three-dimensional tunnels for fast ion diffusion. This is combined with a high theoretical specific capacity due to the multiple oxidation states of vanadium and iron ions, leading to good structural stability upon cycling [12-14]. However, their poor electronic conductivity needs to be addressed to remedy the low discharge/charge capacity and poor cycling performance especially at high cycling rates [15].

Table IV-1: A non-exhaustive list of recently investigated polyanionic compounds as cathode materials for K-ion batteries

Materials	Structure	Theoretical capacity (mAh/g)	Reported capacity (mAh/g)	Discharge potential V *vs.* K^+/K	Ref
Amorphous $FePO_4$	-	178	156	2.64	[16]
$Fe_2(MoO_4)_3$	Monoclinic anti-NASICON type ($P2_1$)	91 ($1e^-$/Fe)	78	2.6	[17]
$K_2[(VO)_2(HPO_4)_2(C_2O_4)]$	Triclinic $P\bar{1}$	109 ($1e^-$/V)	81	3.5-4.1	[18]
$K_{3-x}Rb_xV_2(PO_4)_3$/C	NASICON-type structure tetragonal ($P4_2/mnm$)	97	55.70	3.75	[19]
$K_3V_2(PO_4)_2F_3$	NASICON-type structure tetragonal ($P4_2/mnm$)	115 ($1e^-$/V)	100	3.7	[20]
$K_3V_2(PO_4)_3$/C	NASICON-type structure tetragonal ($P4_2/mnm$)	106 ($1e^-$/V)	90	3.7	[21]
			54	3.6-3.9	[22]
$KFePO_4$/C	Triphylite-type structure Orthorhombic ($Pnma$)	141	25	3	[23]
$KFeSO_4F$	Layered Monoclinic ($C2/c$)	128	50 (*vs.* Li)	3.5 (*vs.* Li)	[24]
			100	4	[25]
$KMnPO_4$/C	Triphylite-type structure Orthorhombic ($Pnma$)	141	30	3	[23]
$KMoP_2O_7$	$KAlP_2O_7$-type monoclinic ($P2_1/c$)	87	25	2.9	[26]
$KTi_2(PO_4)_3$/C	NASICON-type structure tetragonal ($P4_2/mnm$)	128	80	1.6	[22]
$KTiP_2O_7$	$KAlP_2O_7$-type monoclinic ($P2_1/c$)	102	9.2	2.5	[26]
$KVOPO_4$	$KTiOPO_4$-type structure ($Pna2_1$)	133	54	4	[27]
			115	4	[18]
			84	4	[28]
KVP_2O_7	$KAlP_2O_7$-type monoclinic ($P2_1/c$)	102	61	4.2	[26]
$KVPO_4F$	$KTiOPO_4$-type structure ($Pna2_1$)	131	92	4	[28]
			111 (*vs.* Li)	4.2 (*vs.* Li)	[29]
			125 (*vs.* Li)	4.05 (*vs.* Li)	[30]
			105	4.3	[31]
			80	3.5-4	[32]
$K_3V(PO_4)_2$/C	**Monoclinic ($P2_1/c$)**	**150 ($2e^-$/V)**	**101**	**3.5**	**This Work**

Table IV-1 presents a non-exhaustive list of polyanionic compounds, mostly phosphates and pyrophosphates, recently investigated as cathode materials for K-ion batteries. The redox metal couples Ti^{3+}/Ti^{4+}, Fe^{2+}/Fe^{3+} and $V^{3+/}V^{4+}/V^{5+}$ are characterized by working potentials of 1.5-2.5 V, 2.5-3.5 V and 3.5-4.5 V, respectively. These working potentials can be enhanced with the incorporation of fluorides in the structure [23]. The highest energy density is thus expected for vanadium-based compounds. However, most of the compounds in Table IV-1 are characterized by a relatively low theoretical capacity. One way to increase the theoretical capacity is to investigate candidates with lower molar mass or with a transition metal with multiple oxidation states (like vanadium). In this work, we propose $K_3V(PO_4)_2$ (KVP) as cathode material. Compared to $K_3V_2(PO_4)_3$ which has a theoretical capacity of 106 mAh/g for the extraction of one potassium for one vanadium, KVP has a higher K/V ratio leading to a higher theoretical specific capacity of 150 mAh/g for the extraction of two potassium for one vanadium. As such, KVP combines a high working potential of 3.5-4.0 V and a high theoretical capacity. KVP was first synthesized by Benhamada *et al*. in 1991 and the crystallographic structure was reported as monoclinic type in $P2_1/c$ space group [33], but it has never been investigated as a possible cathode material for K-ion batteries. The monoclinic structure is shown in Figure IV-1. The potassium ions are positioned within the network formed by slightly distorted VO_6 octahedra sharing corners with phosphate tetrahedra.

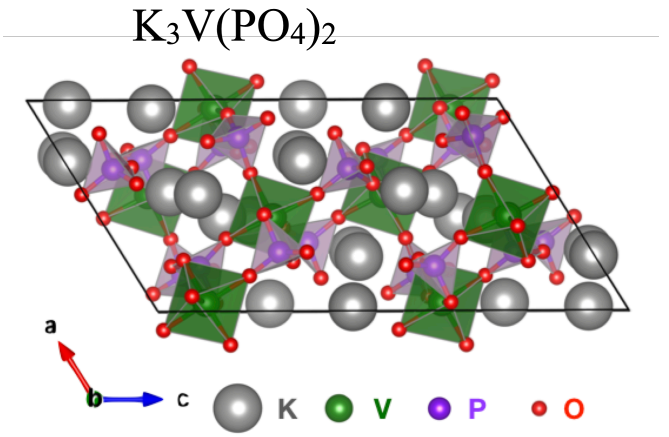

Figure IV-1: Representation of the monoclinic crystalline structure of potassium vanadium phosphate, $K_3V(PO_4)_2$ ($P2_1/c$ space group) with VO_6 octahedra (in green), PO_4 tetrahedra (in violet), oxygen atoms (as red spheres) and potassium atoms (as grey spheres).

In the present work, $K_3V(PO_4)_2$ and $K_3V(PO_4)_2$/C cathode materials were prepared using spray-drying route. This synthesis method is easy, inexpensive and suitable for obtaining complex multi-component powders with a high degree of homogeneity required for very good electrochemical properties [34]. To synthesize the pure $K_3V(PO_4)_2$ material, different temperatures and durations for the heat treatment were tested. To ensure adequate electronic conductivity especially when the electrode was cycled at high rate, the precursors were mixed with different carbon allotropes (graphene oxide (GO) and carbon nanotubes (CNT)) during the material synthesis, leading to carbon/active material composite blends at the nanometric level for $K_3V(PO_4)_2$/C composite cathodes. The good mixture of the electrode material and carbon would increase the electronic conductivity and induce a positive impact on the electrochemical properties as it has already been shown for Na-ion batteries [13,15]. The particle size and morphology of the electrode materials have also significant influence on the electrochemical properties [13,15]; thus, the prepared materials were then subjected to ball-milling to decrease the particle size and enhance K^+ ion diffusion

in the electrode during charge/discharge process. The thermal behavior and decomposition of the spray-dried precursor were analyzed using Thermogravimetric analysis technique. The structural and morphological properties of the prepared materials were systematically investigated by combining X-ray diffraction (XRD), Scanning electron microscopy (SEM), Transmission Electron microscopy (TEM), Brunauer-Emmett-Teller surface measurement (BET) and laser granulometry characterization techniques. The electrochemical performances were evaluated in half-cells by galvanostatic techniques and electrochemical impedance spectroscopy.

2. Experimental Section

2.1. Materials and chemicals

V_2O_5 powder (98% purity) was purchased from Sigma Aldrich. $NH_4H_2PO_4$ (99% purity) and KOH (99.95% purity) were purchased from Acros Organics. Ascorbic acid (99% purity) and citric acid (99.5% purity) were obtained from Alfa Aesar and used as received. The suspension of carbon nanotubes (Aquacyl AQ0302-nanocyl 3 wt% in water, NC7000 multiwall carbon nanotubes waterborne dispersion) was purchased from Nanocyl and the graphene oxide suspension (0.4 wt% in water) was obtained from Graphenea.

2.2. Synthesis of $K_3V(PO_4)_2$ (KVP) and $K_3V(PO_4)_2$/C (KVP/C) materials.

$K_3V(PO_4)_2$ and $K_3V(PO_4)_2$/C materials were prepared by the spray-drying method. Firstly, V_2O_5, $NH_4H_2PO_4$, citric acid ($C_6H_8O_7$) and ascorbic acid ($C_6H_8O_6$) in molar ratio 0.5/2/1/1 were dissolved and stirred in milliQ water (18.2 MΩ/cm) at 80°C under argon atmosphere for 1 hour to obtain a 0.1 M solution of precursors. Then, KOH was added to the solution in stoichiometric ratio followed by 1 hour stirring at 80°C. In the case of composite materials with carbon (KVP/C), suspensions were prepared with 20wt% (*vs.* total mass of KVP) of either CNT or GO (for KVP/20CNT and KVP/20rGO) or a mix of 10wt% of CNT + 10wt% of GO (for KVP/10CNT+10rGO) added to the KVP precursor solution. After cooling down to room temperature, the solution or suspensions were injected in a semi industrial spray-dryer (GEA-Niro Mobile Minor) using a bi-fluid nozzle injection mode. Spray-drying was carried out under an air pressure of 3 bars with a 25 ml/min feed rate, an inlet temperature of 240°C and an outlet temperature of 120 ± 1°C. The collected powders were immediately stored at 60°C to minimize the contact with humidity. The effect of the heat treatment temperature and

duration on crystalline phase formation was investigated to determine the optimized conditions to obtain pure materials. The spray-dried powders were submitted to heat treatment at different temperatures and durations under argon atmosphere with a heating rate of 150°C/h. The powders (2.5 g) were then placed with 0.5 mm diameter zirconia balls (50 g) and 25 ml isopropanol in zirconia grinding jars and were ground at 375 rpm during different durations from 30 to 120 minutes (by steps of 30 min) using a planetary mill (Retsch PM400/2, alternate rotation mode) followed by drying at 70°C for 24 h.

2.3. Thermal, structural and morphological characterizations

In order to optimize the synthesis process of the KVP material, the thermal behavior of the spray-dried KVP powder was analyzed by thermogravimetric analysis (TGA) using a Q100 system from TA instruments. About 10 mg of each sample was placed in an alumina crucible and heated under argon from room temperature to 800°C at a heating rate of 20 K/min to yield the onset decomposition temperature.

X-ray diffraction (XRD) was carried out to identify the obtained phases over the 2Theta range from 9° to 50° with a Bruker D8 Twin-Twin powder diffractometer using Cu Kα radiation. The cell parameters were refined with TOPAS software [35], using the $P2_1/c$ space group and atomic positions proposed by Benhamada *et al*.[33]. Crystallite size (CS) was evaluated using the Scherrer formula $CS = 0.9\,\lambda / (\beta \cos\theta)$,where λ is the wavelength, β is the full width at half maximum of the (123) peak and θ is the Bragg angle of diffraction.

The microstructures of the KVP and KVP/C materials were examined using a scanning electron microscope FEG-SEM (XL 30, FEI) operated at 15 kV and a transmission electron microscope TECNAI G2 TWIN (FEI) operating at 200 kV. Measurements of specific surface area and texture properties, including analysis of porosity for all the samples (KVP and KVP/C), were determined through

measuring nitrogen (N_2) adsorption–desorption isotherms with a Micromeritics ASAP 2020 Plus system. Samples were degassed at 150°C for 6 h prior to analysis.

The evolution of the particle size distribution of the powders during ball-milling was followed by laser granulometry using a Mastersizer 2000 Malvern system.

2.4. Electrochemical characterizations

Electrochemical measurements of KVP and KVP/C as cathode materials for K-ion batteries were conducted in two-electrode coin cells. The composite electrodes were prepared by mixing 70wt% of KVP powder as active material with 20wt% carbon black as electronic conductor and 10wt% polyvinylidene fluoride (PVDF) as binder dissolved in n-methyl pyrrolidinone (NMP). In the case of KVP/C samples, the carbon content was first measured with a carbon analyzer (Multi EA 4000, Analytik Jena) at 1200°C with an oxygen flow in order to determine the exact quantity of CNT and/or rGO in the composite material. The quantity of KVP and carbon was then adapted to reach the ratio 70/20/10 (KVP/C/PVDF). Each suspension was mixed in a 50 ml volume jar with 5 mm diameter zirconia balls at 250 rpm during 1 h. The resulting slurry was then coated on a 25 µm thick aluminum foil as current collector by the Doctor blade method followed by drying at 110°C under vacuum for 12 h. Electrodes were cut into 15 mm diameter discs with active mass loading of approximately 1-2 mg. Coin cells were assembled in an argon-filled glove box using a glass microfiber paper (Whatman GF/A) as separator, 0.8 M KPF6 +10wt% of fluoroethylene carbonate (FEC) dissolved in propylene carbonate (PC) as electrolyte, and potassium foil as the counter and reference electrodes. All cells were tested within a fixed voltage window, between 2.0-4.5 V *vs.* K^+/K, under galvanostatic conditions at different current density rates: C/40-1C (1C corresponds to the extraction/insertion current of 1 K/KVP in 1 h). All electrochemical tests were

carried out at room temperature using a Neware BTS4000 Electrochemical Test System.

Electrochemical Impedance Spectroscopy (EIS) experiments were performed in 3 electrodes Swagelok-type cells, the electrodes were prepared as mentioned before for working electrode, metallic potassium was used both as counter and reference electrode. The electrolyte and separators were the same as for cycling experiments. The EIS analyses were performed at room temperature at open circuit voltage (OCV) (E_{OCV}= ~2.9 V) in the frequency range from 1 MHz to 10 mHz with 5 mV amplitude using a VMP3 Bio-Logic potentiostat. EIS data were analyzed by a non-linear least-square (NLLSQ) fit software developed by B.A. Boukamp [36]. The equivalent circuit used to fit the data was $Re+(R_{CT}.Q)/Q$ where Re is the electrolyte resistance, R_{CT} is the charge transfer resistance and Q is a constant phase element (CPE) replacing the double layer capacity.

The cyclic voltammetry tests were performed in two-electrode coin cells (with the same electrode preparation method as explained before) at different scan rates from 0.1 to 0.5 mV/s. The tests were realized using a VMP3 Bio-Logic potentiostat.

3. Results and discussion

3.1. Synthesis and characterization of KVP

Thermogravimetric analysis (TGA) and differential scanning calorimetry (DSC) are widely used characterization techniques to evaluate the thermal behavior and the effects of heat treatment on the material degradation and crystallization [37]. Here, we used TGA/DSC analyses to optimize the synthesis conditions (temperature of formation) of the KVP material, by following the variation of the sample mass when heating up the spray-dried powder from room temperature to 800°C under argon.

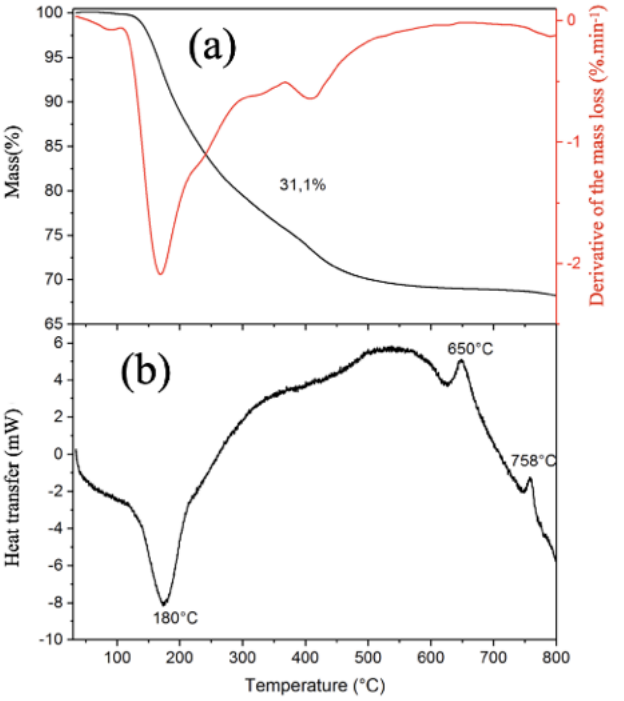

Figure IV-2: (a) TGA profile and its derivative curve, (b) DSC curve of the spray-dried precursor of the KVP powder.

The TGA and derivative thermogravimetric (DTG) curves are presented in Figure IV-2a. The data show a continuous mass loss between 25°C and 600°C. The powder undergoes a mass loss (0.31wt%) up to 100°C (corresponding to a small peak observed in the DTG curve) which is due to the elimination of the water in the powder. Then, two significant weight losses are detected at 180°C and 400°C associated with the degradation of the precursors used for the preparation of the material. Indeed, the degradation of $NH_4H_2PO_4$ and potassium citrate/ascorbate have been reported to start at 160°C and at 225°C, respectively [38,39]. The complete degradation of the precursors occurs at 600°C leading to a total mass loss of 31%. At 600°C, the TGA curve stabilizes with no further decrease denoting the formation of KVP. Consequently, 600°C is the lowest temperature to synthesize the KVP phase.

The DSC profile obtained in the temperature range of 25 to 800°C under the dynamic atmosphere of argon is shown in Figure IV-2b.

The DSC curve displays mainly 3 peaks at 180, 650 and 758°C corresponding to the endothermic/exothermic processes during the heat treatment. The endothermic peak observed at 180°C corresponds to the degradation of $NH_4H_2PO_4$ precursor, in good agreement with TGA results. The two exothermic peaks detected at 650°C and 758°C are related to the crystallization and/or degradation of KVP.

3.2. Crystal structure of synthesized KVP

The spray-dried KVP powder was subjected to different heat treatments at 550, 600, 650, 700 and 750°C during 1, 8 and 16 h under argon, in order to investigate the KVP formation in relation with the key temperatures detected by TGA/DSC analyses. The X-ray diffraction patterns of the KVP samples are shown in Figure IV-3a.

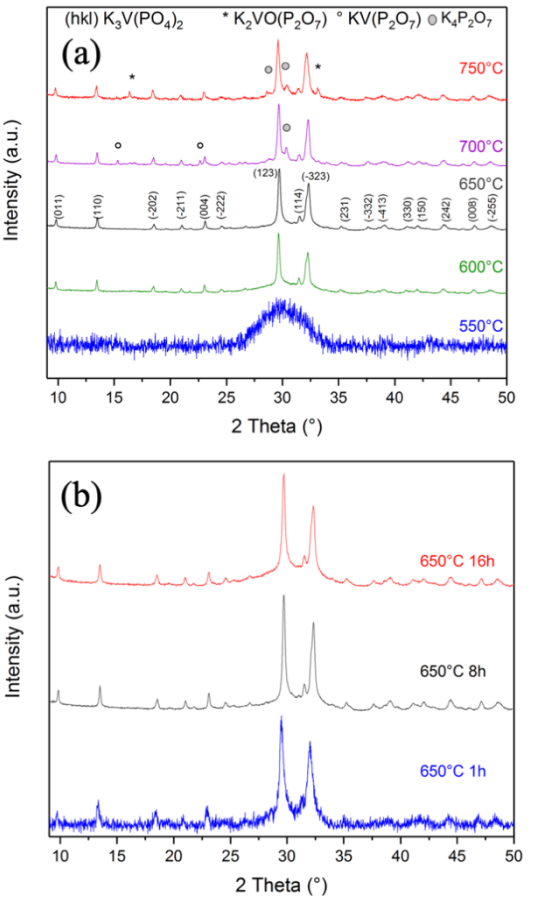

Figure IV-3: (a) XRD patterns of $K_3V(PO_4)_2$ samples prepared at different pyrolysis temperatures during 8 h under argon and (b) at different durations at 650°C under argon.

The XRD pattern of the sample prepared at 550°C during 8 h displays an amorphous phase which confirms that 550°C is not sufficient to obtain pure crystallized KVP. On the contrary, temperatures of 600°C or 650°C are high enough to obtain the pure and crystalline KVP material. All the XRD peaks of the powder prepared at 650°C during 8 h can be indexed in the monoclinic structure with space group $P2_1/c$ (04-011-3486-PDF) proposed by Benhamada *et al*. [33]. The cell parameters were refined to values of a=9.573±0.002 Å, b= 11.146±0.002

Å, c=18.129±0.004 Å and β=121.75±0.02°, in good agreement (i.e., difference below 0.5%) with the originally reported values. The atomic positions and occupation factors were not refined since the structure model includes 28 independent atoms, all on general positions, so that a reliable refinement was not possible for our datasets obtained with a laboratory powder diffractometer. However, the atomic positions and occupation factors taken from the published structure [33] provide a decent fit with the experimental data (see Figure IV-4). This confirms that 650°C is high enough to obtain the KVP-material with high purity and good crystallinity. The KVP material was pyrolyzed at 650°C (highest temperature) in order to maximize the crystallinity of the material. Further increase of the pyrolysis temperature from 650 to 700°C or 750°C leads to the degradation of KVP and the formation of pyrophosphates as secondary phase. The evolution of the XRD patterns of KVP prepared at 650 °C with the pyrolysis time is illustrated in Figure IV-3b. The XRD patterns display lower crystallinity after 1 h of pyrolysis as compared to 8 and 16 h. The increase of the pyrolysis duration from 8 to 16 h has no obvious effect on the KVP structure and shows the good thermal stability of the synthesized KVP samples. To summarize, the optimal conditions to obtain high purity and well crystalized KVP powder are 650°C during 8 h. These conditions were applied to KVP and KVP/C powders studied in terms of microstructure and electrochemical properties.

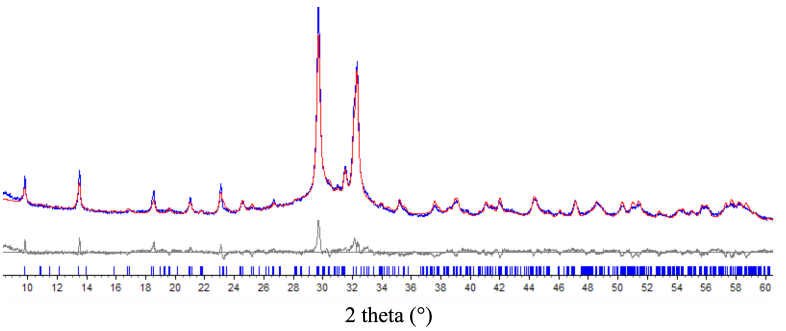

Figure IV-4: Refinement of the cell parameters of the KVP powder prepared at 650°C during 8 h, based on the structural model proposed by Benhamada et al. [33], [PDF 04-011-3486 in ICDD database]. Experimental data in blue, calculated pattern in red, difference curve in grey, blue ticks show authorized hkl positions in the $P2_1/c$ space group.

3.3. Morphological characterization of KVP

The SEM micrographs of the spray-dried KVP powders before and after pyrolysis at 650°C during 8 h under argon atmosphere are presented in Figure IV-5a and 5b. Before pyrolysis, the spray-dried particles are constituted of a homogeneous mixture of precursor nanoparticles forming dense spherical particles with a smooth surface and an average particle size of 2 µm.

After pyrolysis, the particles remain spherical with the same size but with a rough surface. The surface roughness is mainly due to the decomposition of precursors at the surface in favor of formation of the crystalized phase (in good agreement with XRD result). The BET technique was used to measure the specific surface area of the heat-treated material. The KVP powder exhibits a small specific surface area of 1.7 m^2/g due to the large size and low porosity of spherical particles.

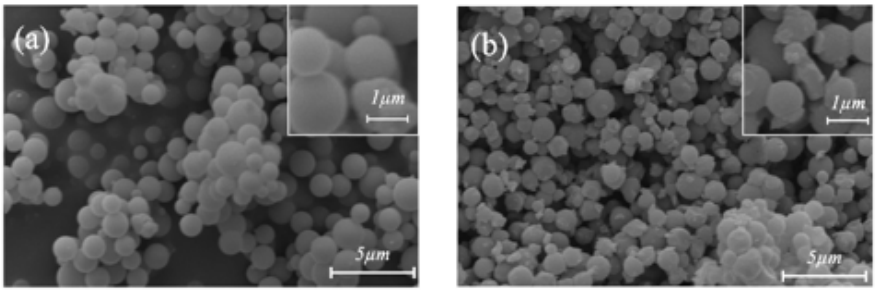

Figure IV-5: (a) SEM micrographs of $K_3V(PO_4)_2$ prepared by spray-drying method before and (b) after pyrolysis at 650°C during 8 h.

3.4. Electrochemical performance of KVP microparticles

In this section, electrochemical performance of spray-dried KVP was assessed by galvanostatic charge-discharge cycling in half-cell configuration in the voltage range 2-4.5 V *vs.* K^+/K^0. Indeed, the spray-dried KVP is evaluated as a candidate material for cathode in KIBs, since phosphate-based materials demonstrate high

mobility of the K^+ ions during the extraction/intercalation process in 3D open-framework structures [23]. Figure IV-6a presents the charge/discharge voltage profiles of the first 3 cycles of KVP electrode at C/40. During charge, the voltage profile between 2 and 3.5 V has a steep slope with no clear plateau followed by a pseudo plateau between 3.5 and 4 V, and finally a continuous increase in voltage with K^+ ion extraction is observed. Reversible phenomena are observed during the discharge process. A comparable reaction mechanism was reported for $KVPO_4F$ material when used as cathode material for K-ion battery [31]. The cell delivers low initial charge and discharge capacities of 45 and 30 mAh/g corresponding to 30% and 20% of the theoretical capacity (150 mAh/g), respectively. Then, the capacity decays after the first cycle which is accompanied by the decrease of the operating voltage due to polarization. Figure IV-6b presents the evolution of the discharge and charge capacity *vs.* cycle number at C/40 rate for KVP cathode. The discharge capacities decrease during the first 4 cycles and reach around 25 mAh/g, then stabilizes for the 20 subsequent cycles. This low electrochemical performance is associated with the low specific surface area of the microspheres and a low intrinsic electronic conductivity of the KVP phase. To improve the electrochemical performances of the material, it is therefore necessary to increase the electronic conductivity of the KVP particles and/or reduce the particle size [13,15].

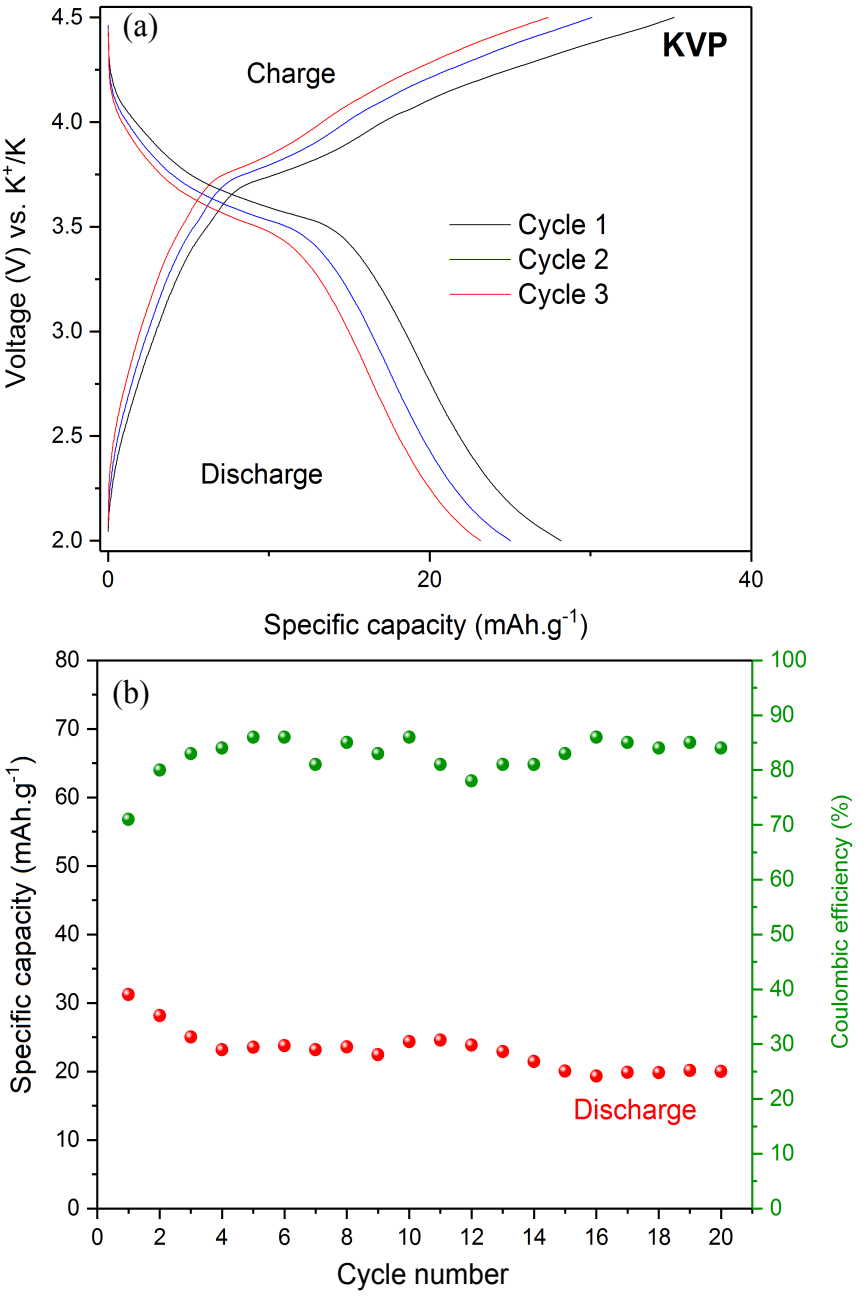

Figure IV-6: (a) Discharge/charge voltage profiles of the first 3 cycles. (b) Cycling stability of KVP at C/40 in the voltage window of 2-4.5 V vs. K^+/K. Data collected at room temperature.

3.5. Effect of the addition of conductive carbon on the structural, microstructural and electrochemical properties of KVP/C composite

In order to enhance the electrochemical performance of the KVP material, two solutions were considered. The first one is to grind the materials to decrease the size of the particles and thereby to reduce the electron diffusion path during the charge/discharge process. Another solution is to incorporate conductive carbon in the structure to prepare composite materials. This carbon addition should enhance the electrochemical performance by helping to solve the issue of the low electronic conductivity of the phosphate-based material. The addition of carbon to the precursor solution was chosen as the first approach to study in this work since spray-drying process is highly compatible to fabrication of multicomponent mixtures. Three KVP/C composite materials were prepared by addition of 20wt% of CNT (KVP/20CNT), 20wt% of GO (KVP/20rGO) and 10wt% of CNT + 10wt% of GO (KVP/10CNT+10rGO) to the KVP precursor solution. The GO is reduced during the heat treatment leading to reduced graphene oxide (rGO). The XRD patterns of KVP, KVP/20CNT, KVP/20rGO and KVP/10CNT+10rGO are shown in Figure IV-7a.

All the peaks can be indexed in the monoclinic structure with space group $P2_1/c$ with no crystalline impurity in the synthesized KVP/C composite materials. Carbon addition does not affect the purity of the KVP phase, however, small differences in XRD pattern upon carbon addition are observed. A broad bump appears between 25° and 35° in the background of the XRD pattern and the diffraction peaks become broader. The bump between 25° and 35° can be attributed to the carbon [40-42]. The broader peak shape of the KVP reflections is attributed to a smaller crystallite size. Table IV-2 presents the crystallite size of KVP and KVP/C materials as calculated using the Scherrer formula. The crystallites size decreases with carbon addition from 39 nm for KVP to 31 nm

for KVP/20rGO, 26 nm for KVP/10CNT and 23 nm for KVP/10CNT+10rGO. This phenomenon has already been observed and suggests difference in crystallite growth mechanism for KVP material with the presence of the carbon nanotubes and graphene oxide [43]. Two possible reasons are a higher number of nucleation sites and the geometric constraints due to the rigidity of carbon [13,44,45].

Table IV-2: Crystallite size of KVP, KVP/20CNT, KVP/20rGO and KVP/10CNT+10rGO samples before and after grinding.

Samples	Average crystallite size (nm)	
	before grinding	after grinding
KVP	39±3	13 ±4
KVP/20CNT	26±1	16 ±6
KVP/20rGO	31±2	30±2
KVP/10CNT+10rGO	23±1	19 ±8

The effect of carbon addition on the microstructure of KVP was studied by combining scanning electron microscopy (SEM) and transmission electron microscopy (TEM). Figure IV-7b, c, d, e present the SEM micrographs of KVP, KVP/20CNT, KVP/20rGO and KVP/10CNT+10rGO powders respectively and Figure IV-7f, g, h, i present the corresponding TEM images. The addition of CNT leads to the formation of collapsed particles with flattened morphology characterized by high particle size of 2.5 µm. The addition of carbon nanotubes and their high mechanical strength leads to the buckling of the particles. The first step during the drying process by spray-drying is the formation of a viscoelastic shell due to the aggregation induced by the solvent flow [46]. During the drying of the droplets multiple depressions are formed leading to wrinkled shape. With the reduction of volume these wrinkles overlap leading to highly deformed shapes [15]. The CNT are well dispersed at the surface and inside of the KVP particles, forming a strong CNT network as shown in Figure IV-7g. In comparison with KVP (Figure IV-7b), KVP/20rGO and KVP/10CNT+10rGO show particles with semi-spherical shape and slight deformation at the surface of the secondary particles (Figure IV-7e, 7f). The quasi-spherical shape of the

particles was not deteriorated due to the good dispersion of the graphene layer at the surface of the KVP materials. As observed in TEM images (Figure IV-7h, 7i), KVP was successfully covered by reduced graphene oxide flakes for KVP/20rGO and rGO and CNT for KVP/10CNT+10rGO. It turns out that, for all KVP/C materials, carbon is uniformly distributed amongst and at the surface of the KVP particles for the CNT (Figure IV-7g and 7i) and surrounding the surface of the particles for the rGO (Figure IV-7h, 7i and Figure IV-8).

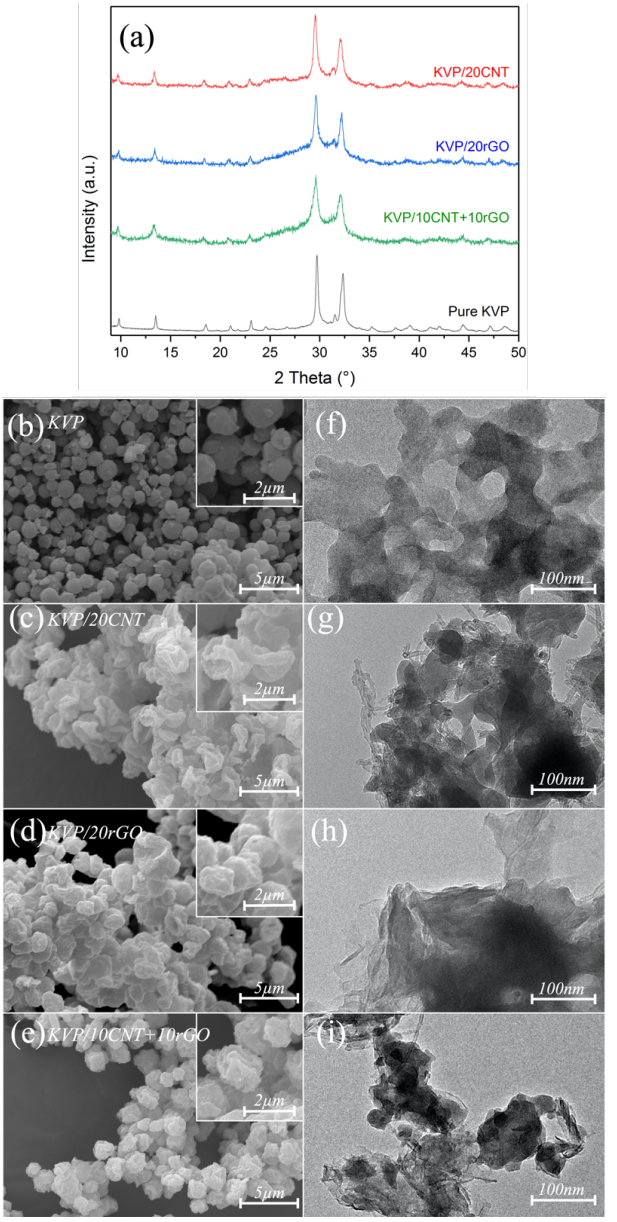

Figure IV-7: (a) XRD patterns of pure KVP, KVP/20CNT, KVP/20rGO and KVP/10CNT+10rGO samples prepared by spray-drying method and pyrolyzed at 650°C during 8h under argon. SEM micrographs of (b) KVP, (c) KVP/20CNT, (d) KVP/20rGO and (e) KVP/10CNT+10rGO prepared by spray-drying with carbon allotropes added in solution and pyrolyzed at 650°C during 8 h under argon (higher magnification in the inset). TEM micrographs of (f) KVP, (g) KVP/20CNT, (h) KVP/20rGO and (i) KVP/10CNT+10rGO prepared by spray-drying and pyrolyzed at 650°C during 8 h under argon.

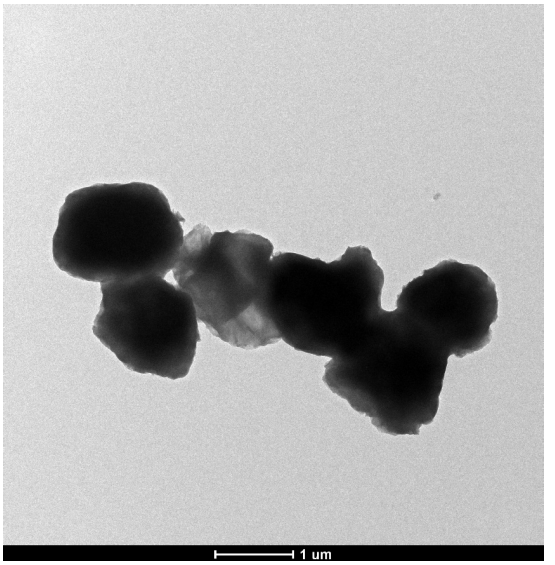

Figure IV-8: TEM micrographs of KVP/20rGO prepared by spray-drying and pyrolyzed at 650°C during 8 h under argon.

Table IV-3: Specific surface area measured by BET method for KVP and KVP/C samples.

Samples	Specific surface area (m^2/g)
KVP	1.8
KVP/20CNT	36.8
KVP/20rGO	6.6
KVP/10CNT+10rGO	11.2

The specific surface area increased hugely with addition of 20wt% CNT to 36.8 m^2/g as compared to 1.8 m^2/g in pristine KVP (Table IV-3). This is attributed to a combination of the large specific surface area of the CNT themselves with the increase of specific surface area of KVP reflected in the smaller crystallite size detected by XRD. The electron microscopy results show that the CNTs are well deagglomerated and well dispersed at the surfaces of the KVP particles (Figure IV-7c, 7g). This increase in specific surface area is favorable for K^+ ions diffusion by the increase of the active surface of the material that contributes in the electrochemical reaction. In the case of the GO addition, the specific surface of 6.6 m^2/g is only moderately higher than the carbon free KVP, probably because the rGO sheets wrap around the KVP particles. This should increase the

conductivity at the surface of the particle and also improve the electrochemical performance due to the easier movement of electrons. In the case of the mixed composite, we obtain a value of 11.2 m^2/g intermediate between KVP/20CNT and KVP/20rGO. These results suggest that the most promising electrochemical performance should be displayed by KVP/10CNT+10rGO thanks to combining the positive effects of the two carbon allotropes in terms of surface area and electronic conductivity.

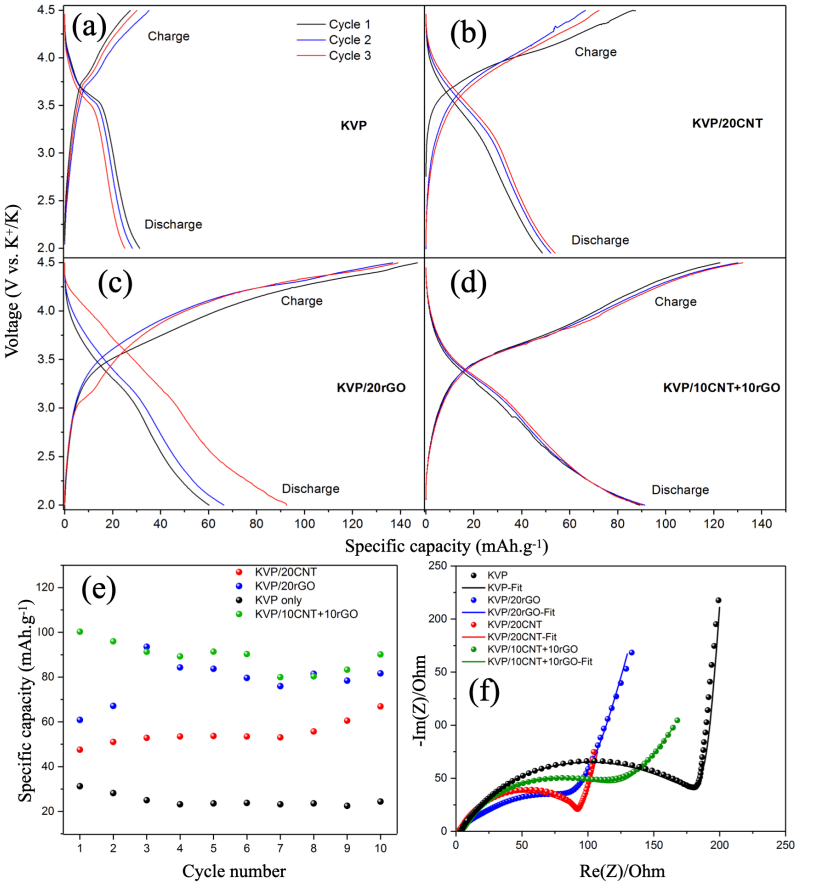

Figure IV-9: Charge/discharge curves of the first 3 cycles of (a) KVP, (b) KVP/20CNT, (c) KVP/20rGO and (d) KVP/10CNT+10rGO and (e) Cycling performance of KVP and KVP/C electrodes at room temperature at C/40. The voltage window explored was 2.0-4.5 V, (f) Nyquist plots of KVP, KVP/20CNT, KVP/20GO and KVP/10CNT+10GO and their corresponding fitted curve.

The effect of the carbon addition on the electrochemical properties of KVP and KVP/C cathode materials for K-ion batteries were studied by galvanostatic measurements at C/40 in the voltage range of 2-4.5 V. Figure IV-9a-d present the charge/discharge profiles of KVP and KVP/C in the first 3 cycles. The cycling performance for 10 cycles is presented in Figure IV-9e, indicating clearly that the addition of conductive carbon improves the electrochemical performance of KVP/C cathodes and allowed to enhance the discharge capacities in comparison with the KVP material. Indeed, KVP/20CNT, KVP/20rGO and KVP/10CNT+10rGO present higher initial discharge capacities compared to 30 mAh/g for KVP with delivering 45, 60 and 101 mAh/g, respectively. This result is due to the uniform distribution of KVP particles in the carbon matrix (CNT and rGO) and high surface area of KVP/C materials that reduce the electronic diffusion lengths during the charge/discharge process and increase the electrochemical performance. It is also important to indicate that the type of carbon allotrope plays a key role in enhancing the electrochemical properties in KVP/C.

This is in good agreement with previous results reported in the literature [13,15], highlighting the interest of the carbon addition to the phosphate-based electrode materials for rechargeable batteries. KVP/10CNT+10rGO demonstrates the highest capacity over 10 cycles which is associated with lower polarization between the charge and discharge curves during cycling. This is due to the combined positive effect of the CNT and rGO on electronic conductivity. This is also due to the open framework of the KVP structure that permits a rapid transport of K^+ ions and leads to a high ionic conductivity [23].

This observation confirms that improvement in electron transport is achieved by carbon addition during the spray-drying preparation of the KVP/C composite material. Electrochemical impedance spectroscopy (EIS) tests were performed to investigate the influence of carbon addition on electrochemical performance of KVP material [47,48]. The Nyquist plots of KVP and KVP/C electrodes recorded

at OCV before galvanostatic cycling are presented in Figure IV-9f. The equivalent circuit model used for the analysis of the impedance spectra is presented in the Figure IV-10. EIS data were analyzed by the non-linear least-square (NLLSQ) fit software developed by B.A. Boukamp [36]. All electrodes show similar impedance spectra formed by a semicircle at high frequency and a line at low frequency. $R_e(R_{CT}Q)Q$ equivalent circuit was used to analyze the different spectra and extract the resistance of the electrolyte R_e (intercept of the curve on the $R_e(Z)$ axis in the high frequency region) and the resistance of charge transfer R_{CT}. The different values are summarized in Table IV-4.

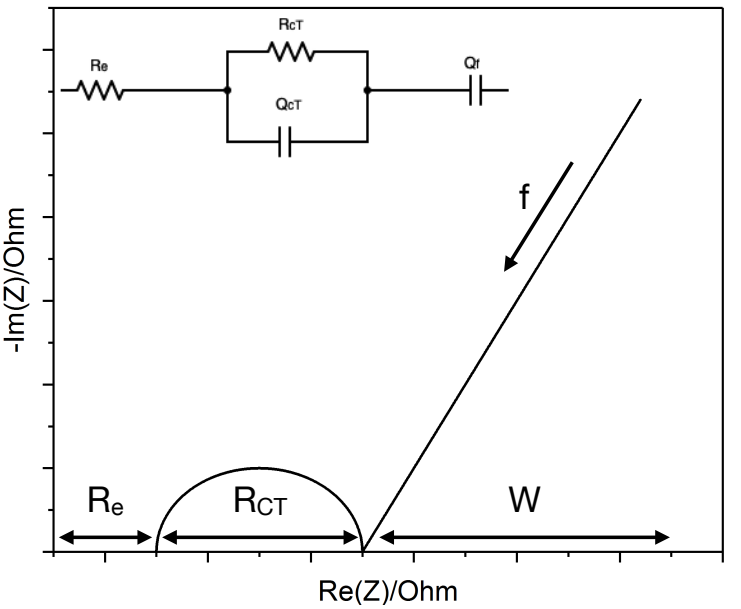

Figure IV-10 : Equivalent circuit model used to analyze the impedance spectra and Nyquist plot.

The different elements are explained in the experimental section.

Table IV-4: Calculated resistances by fitting using equivalent circuit for both electrolyte resistance R_e and charge transfer resistance R_{CT} of KVP and KVP/C electrodes materials

Samples	R_e (Ω)	R_{CT}(Ω)
KVP	3.7±2	187.6 ±5
KVP/20CNT	3.1±2	92.9±8
KVP/20rGO	2.5±3	99.3±10
KVP/10CNT+10rGO	5.5±3	113.8±26
KVP/20rGO - Ground	5.6±3	189.2±19

The resistance of the electrolyte is relatively low and in the same range for all electrodes (R_e= ± 3.5 Ω) because the same electrolyte was used in the cell configuration. Regarding the charge transfer resistance, it can be observed that R_{CT} is different for all electrodes which is due to the addition of the different carbon allotropes during the synthesis of the KVP/C materials. Indeed, the R_{CT} of pristine KVP electrode is almost two times higher than of KVP/20CNT composite electrode. Similar results are observed with the two other composite electrodes (KVP/20rGO and KVP/10CNT+10rGO) illustrating resistance values that are clearly lower than the R_{CT} of KVP electrode. In summary, the EIS results suggest that the addition of carbon allotrope enhances the electronic conductivity which improved charge transfer reaction kinetics and leads to better cycling performance for KVP/C electrode materials with lower charge transfer resistance and optimized electrode-electrolyte interface in terms of ionic conduction.

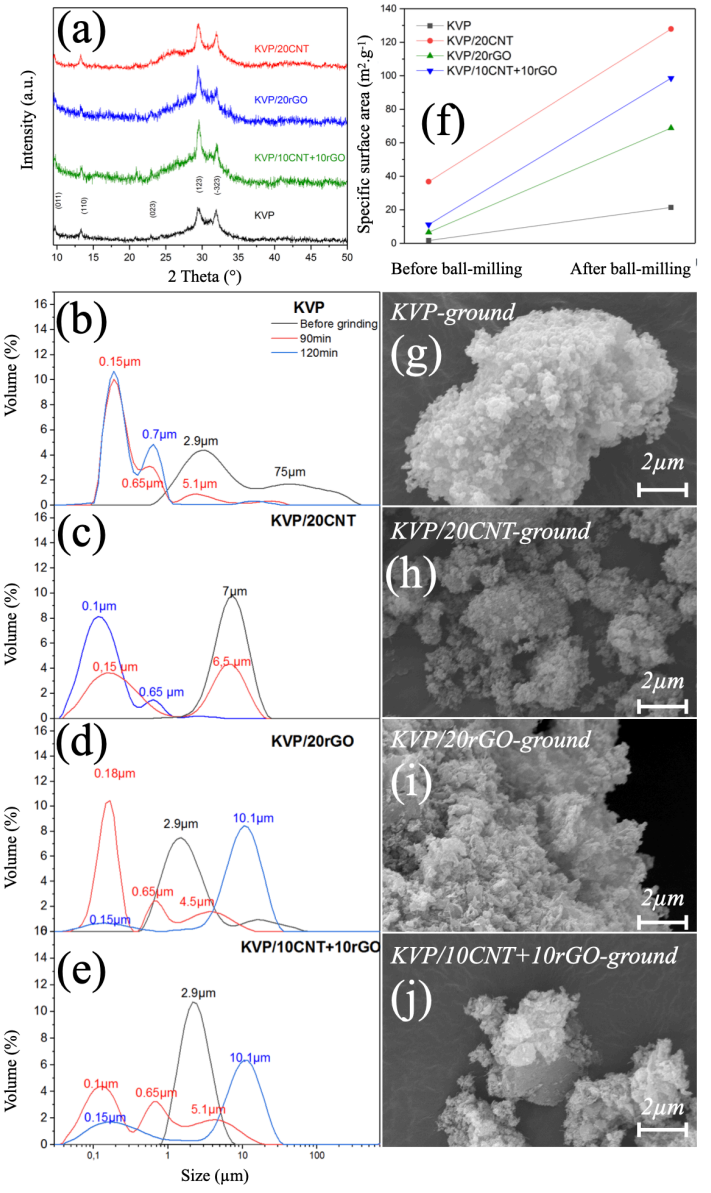

Figure IV-11: (a) XRD patterns of KVP, KVP/20CNT, KVP/20rGO and KVP/10CNT+10rGO prepared by spray-drying with carbon allotropes, pyrolyzed at 650°C for 8 h under argon, after grinding in isopropanol. Particle-size distribution during ball-milling process of (b) KVP, (c) KVP/20CNT, (d) KVP/20rGO and (e) KVP/10CNT+10rGO. (f) Evolution of the specific surface area of the KVP and KVP/C sample before and after ball-milling. SEM micrographs of (g) KVP, (h) KVP/20CNT, (i) KVP/20rGO and (j) KVP/10CNT+10rGO prepared by spray-drying with addition of carbon, after grinding in isopropanol.

3.6. Influence of a ball milling process on the structural and microstructural properties of KVP and KVP/C

With the aim to further enhance the electrochemical performance of the KVP and KVP/C materials, the powders were ground to decrease their particle size to about 100 nm and thus increase the surface area. The XRD patterns of the ground materials are indexed as pure KVP phase and reveal no crystallized impurity peaks (see Figure IV-11a). However, peaks become broader and the peak area decreases after the milling process due to the amorphization. The decrease in average crystallite size after ball-milling process for KVP, KVP/20CNT and KVP/10CNT+10rGO is shown in Table IV-2 that is expected to be favorable for the electrochemical applications because in general, smaller crystallite size enhance the discharge/charge process during electrochemical cycling [13]. The crystallite size of KVP/20rGO is an exception and remains unchanged which suggests that the graphene layer formed on the surface of the KVP particles inhibited the decrease of the crystallite size by being itself broken during grinding.

It is known that smaller and homogeneous active material particles are suitable for battery applications. In this section, the effect of the milling time on the particle size in KVP and KVP/C powders is investigated. The evolution of particle size with time was probed by laser granulometry. Figure IV-11b-e present the particle-size distribution and SEM images of KVP and KVP/C after ball milling during 90 and 120 min (Figure IV-11g-j). The powders have initially particles larger than 2.9 µm for KVP, KVP/20rGO and KVP/10CNT+10rGO and 6.5 µm for KVP/20CNT. A clear shift of the particle-size distribution toward lower values is observed after ball milling. The primary particle size for the ball-milled samples is reduced to about 100 nm after 90 min for KVP, KVP/20rGO and KVP/10CNT+10rGO. However, after 120 min the particles agglomerate and the apparent size increases to 2.9 µm for KVP/20rGO and KVP/10CNT+10rGO while

the size distribution does not change much for KVP. After ball-milling during 90 min the compact rigid particles were crushed and transformed into small particles with pronounced reduction of the particle size; the boundaries between different particles are more distinguishable which leads to maximizing the surface area and formation of nano-sized powder particles. It is clear that KVP/20CNT required longer time of ball-milling (120 min) to decrease the particle size to 100 nm, which is due to the higher mechanical strength imparted by the homogeneous distribution of the carbon nanotubes inside and at the surface of KVP particles, which makes the milling process harder.

Figure IV-11c shows that after 90min of grinding the KVP/20CNT sample has a particle-size distribution with two major peaks at 0.15 µm and 6.5 µm of equivalent volume proportion. After 120 min the KVP/20CNT sample is mainly composed of 100 nm particles. Relatively symmetric and narrow distribution curves were obtained for KVP, KVP/20rGO and KVP/20CNT after ball-milling which confirms a more homogeneous particle size distribution after grinding. A poly-dispersed distribution is obtained for KVP/10CNT+10rGO indicating inhomogeneous particle size distribution since the sample contains both large and small particles which could be due to the presence of two carbon types which leads to flattened 2D CNT/GO giving higher size. This result was confirmed by SEM micrographs (Figure IV-11g-j). The composite materials with rGO (KVP/20rGO and KVP/10CNT+10rGO) are constituted by two sorts of particles; small particles with rough sand irregular surface and shape and the second sort with higher particle size made of blocks with regular flat surface.

The grinding process has a strong influence on the specific surface of the samples as shown in Figure IV-11f. All ground samples demonstrated a significant increase in the specific surface area. The KVP/20CNT sample shows the highest specific surface area of 127.9 m^2/g, thanks to the presence of CNT and the marked decrease in the particle size. The carbon-free KVP sample shows the lowest specific surface area (21.4 m^2/g) amongst the ground samples, which is still 10 times higher than

before grinding. The KVP/20rGO sample revealed also a tenfold increase of the specific surface after grinding (68.8 m^2/g) and the mixed composite shows a specific surface area value between KVP/20CNT and KVP/20rGO with 98.5 m^2/g.

3.7. Influence of the ball milling process on the electrochemical properties of KVP and KVP/C

The KVP material should deliver higher specific capacities after grinding thanks to smaller and homogeneous particle size of KVP. Galvanostatic tests were performed with a cycling rate of C/40 for the positive electrodes prepared from ground KVP and KVP/C within the voltage range 2.0-4.5 V as shown in Figure IV-12a. The ground KVP, KVP/20rGO, KVP/20CNT and KVP/10CNT+10rGO delivered reversible capacities of around 60, 50, 101 and 60 mAh/g, respectively. KVP and KVP/20CNT exhibited higher discharge capacities after grinding thanks to the decrease of their particle size and the increase of the specific surface area. However, the electrochemical performance of KVP/20rGO and KVP/10CNT+10rGO were lower than before grinding. Figure IV-12b presents rate performance and Figure IV-12c-f presents the galvanostatic charge–discharge voltage curves of the ground KVP and KVP/C positive electrodes obtained at various current densities from C/20 to 1C. The initial discharge capacities delivered by KVP, KVP/20rGO, KVP/20CNT and KVP/10CNT+10rGO are 53, 21, 73 and 64 mAh/g, respectively. Similar to the result obtained at C/40, the sample with reduced graphene oxide after ball-milling shows the lowest capacity. In the case of KVP/20rGO the graphene layer breaks during the milling process resulting in heterogeneous carbon mixing with the KVP material; sluggish K^+ ion diffusion and high charge-transfer resistance leading to low discharge capacities at different current densities. This effect has been evidenced by EIS analysis. The Nyquist plots of KVP/20rGO before and after grinding from 1 MHz to 10 mHz are displayed in Figure IV-13a. We can clearly see that the grinding step has deteriorated the rGO layer thus leading to a huge increase in the transfer charge

resistance. The RCT almost doubled from 99 Ω before grinding to 189 Ω after grinding, which is almost the same value compared to the pristine KVP electrode (Table IV-4). This result confirms that rGO layer on KVP particles was destroyed during the grinding step, which leads to inferior electrochemical performance of the KVP/GO composite material.

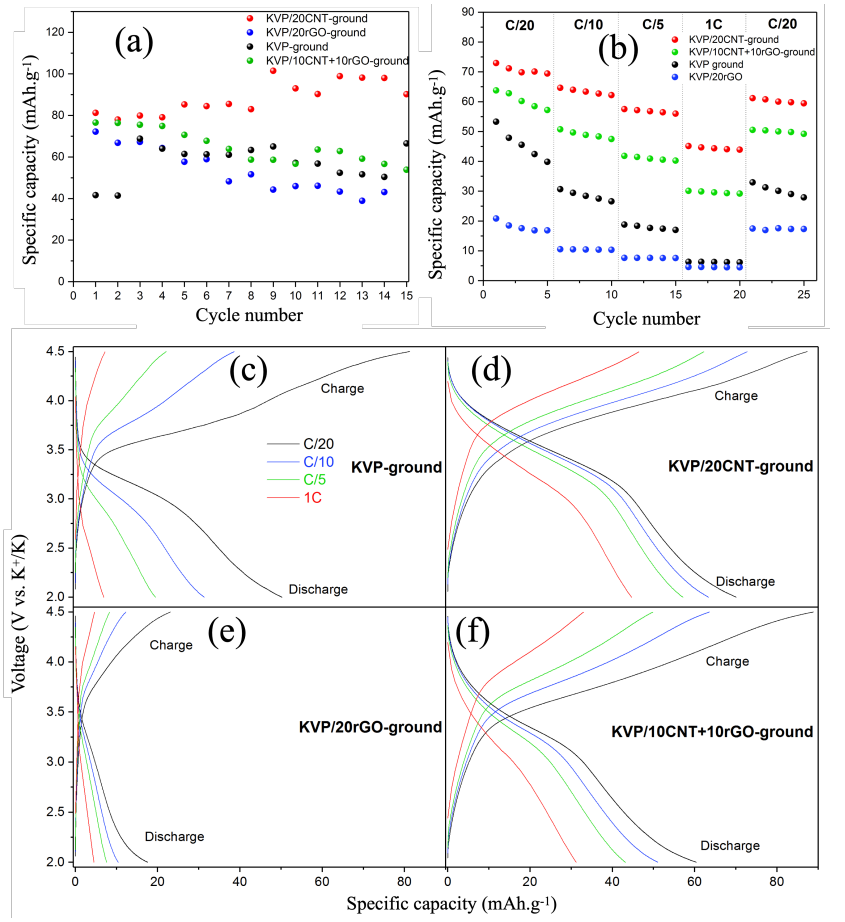

Figure IV-12: (a) Evolution of charge and discharge capacity vs. cycle number of the ground KVP, KVP/20CNT, KVP/20rGO and KVP/10CNT+10rGO materials at room temperature at C/40. The voltage window explored was 2.0-4.5 V. (b) Evolution of charge and discharge capacity vs. cycle number of the ground KVP, KVP/20CNT, KVP/20rGO and KVP/10CNT+10rGO materials cycled at C/20, C/10, C/5, 1C rates at room temperature. Charge/discharge curves of the first 3 cycles of (c) KVP, (d) KVP/20CNT, (e) KVP/20rGO and (f) KVP/10CNT+10rGO.

As the current density increases, the discharge capacity of the four electrodes decreases due to polarization and kinetic limitations (Figure IV-13b). The original delivered capacity of all samples is however restored when the cycling rate is reduced back to C/20, confirming the high structural stability of the KVP during the cycling even at high C-rate (1C). This result indicates that the capacity decay with increasing current density is induced by kinetic limitation. Indeed, the discharge capacity of KVP electrode decreases much faster than that of the other electrodes due to its low electronic conductivity resulting in the rapid decrease of the discharge and charge voltage plateaus with increase of the current density. The ground KVP/20CNT material exhibits the best discharge capacities and rate capability compared to ground KVP, KVP/10CNT+10rGO and KVP/20rGO. The ground KVP/20CNT electrode exhibits the best electrochemical performance which is due to the homogeneous particle-size distribution with small particles of about 100 nm.

This induced an increase of the specific surface area (127.9 m^2/g) as confirmed by BET measurements. Consequently, first the contact between the particle's surface and the electrolyte is increased which creates more active surface material and leads to fast ion diffusion pathways. Secondly the conductive carbon nanotube network facilitates rapid electron transport during charge/discharge process which leads to improved electrochemical performance during cycling. Figure IV-13b presents the cycling performance of ground KVP/20CNT electrode at a cycling rate of C/10 over 70 cycles. The initial specific discharge capacity was 80 mAh/g with a capacity retention of 82% and a corresponding coulombic efficiency of 96%. The galvanostatic results clearly showed that the ground KVP/20CNT positive electrode material exhibited good cyclability.

Cyclic voltammetry (CV) can be used to study the kinetics of the electrochemical reactions in the electrode material and the diffusion of K^+ ions. The CV tests were performed at different scan rates (0.1 to 0.5 mV/s) for KVP, KVP-ground, KVP/20CNT and KVP/20CNT-ground (Figure IV-13c). For pure KVP, no redox

peaks are observed which is in agreement with the poor electrochemical performance obtained for this cathode material. For the KVP-ground and KVP/CNT, low intensity oxidation and reduction peaks are observed. When the addition of carbon and the grinding of the material are combined, intense redox peaks are observed. This result confirms the superior performance achieved for the KVP/20CNT-ground sample. To study and compare the reaction kinetics of these materials, we plotted the current of the redox peaks versus the square root of the scan rate ($v^{1/2}$), these parameters have a linear relationship (Figure IV-13d). This indicates that the diffusion process is controlled by insertion/disinsertion of potassium for each electrode material. This relationship can be described by Randles-Sevcik equation [49-51]:

$$I_p = (2.69E+5)\, n^{3/2}\, A\, (D_{K+})^{½}\, C_{K+}\, v^{½}$$

where I_p is the peak current, n is the number of electrons, A is the effective surface area, D_{K+} is the diffusion coefficient of potassium ion and C_{K+} is the maximum concentration of K^+ ion in the electrode during electrochemical analysis.

Table IV-5: Slope of the linear fit curve from the graph of the evolution of current peaks intensity versus the square root of the scan rate.

Samples	Ox(Ω)	Red(Ω)
KVP-Ground	0.00101	/
KVP/20CNT	0.00098	-0.00056
KVP/20CNT-Ground	0.00202	-0.0051

The slope of the curves is reported in Table IV-5. As it can be observed the slope of oxidation current for both KVP-ground and KVP/20CNT electrodes are similar, contrary to the slope of the oxidation current in KVP/20CNT-ground electrode which is twice higher. As the number of electrons and the concentration are equivalent for these electrode materials, and that the diffusion of K^+ takes place through the same crystallographic structure for each sample (similar for each electrode), the difference between the current values is mainly related to the effective surface area between electrode and electrolyte. For KVP-ground and

KVP-20CNT, as almost the same slope is obtained for the evolution of I_p current, we can assume that the effect of the grinding of KVP and the presence of CNT in the spherical particles lead to almost the same active surface area between electrode and electrolyte. In the case of KVP/20CNT-ground, the grinding step and the addition of CNT have a cumulative effect on the increase of active surface area since the slope is twice higher for cathodic current and even ten times higher for the anodic current. This increase of active surface area is the main reason behind the superior electrochemical performance confirmed by the galvanostatic cycling results.

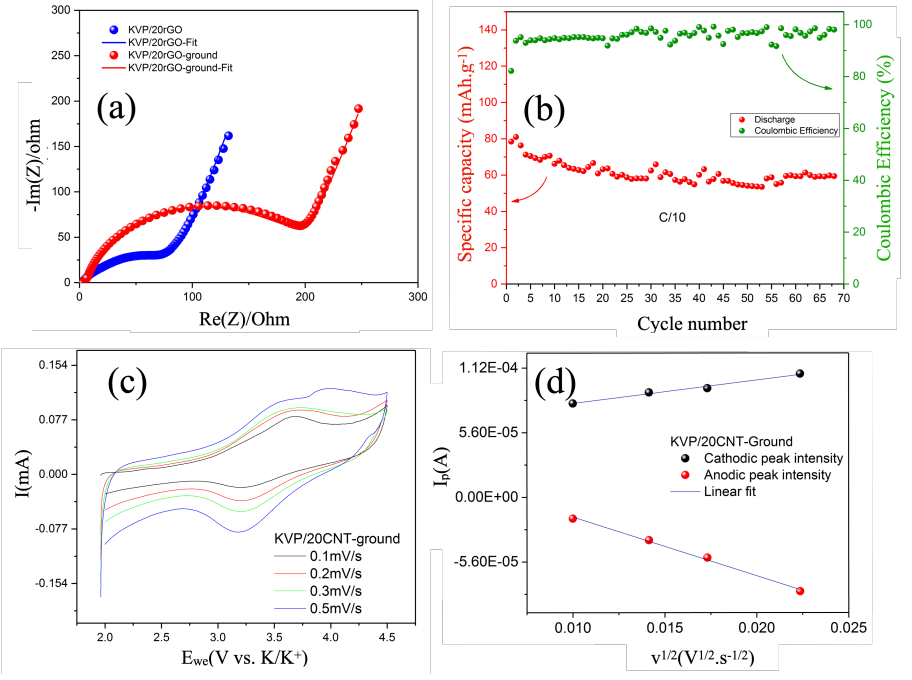

Figure IV-13: (a) Nyquist plot for impedance measurements of KVP/20rGO and KVP/20rGO-ground electrodes materials at Open Circuit Voltage (OCV). (b) Evolution of discharge capacity and the coulombic efficiency vs. cycle number of the grinded KVP/20CNT material cycled at C/10 rate at room temperature, the explored voltage window was 2.0–4.5 V. (c) Cyclic voltammogram of KVP/20CNT-ground recorded at scan rate between 0.1 and 0.5 mV/s. (d) Evolution of the peak current versus the square root of the scan rate for KVP/20CNT-ground.

4. Conclusions

$K_3V(PO_4)_2$ (KVP) and $K_3V(PO_4)_2$/C (KVP/C) pure materials have been successfully prepared by spray-drying followed by a heat treatment at 650°C during 8 h under argon atmosphere. The as-obtained KVP compound exhibits low electrochemical performance due to low electronic conductivity associated to the anionic structure and also due to the large particle size and low specific surface of the spherical KVP particles, which limit the K^+ ions insertion reaction kinetics during cycling.

The *in situ* addition of conductive carbon during spray-drying synthesis of KVP/C composite particles results in a large improvement of the specific capacity and enhanced capacity retention upon cycling. Indeed, the specific capacity obtained for KVP/20CNT and KVP/20rGO are doubled and tripled at C/40 compared to the original KVP electrode material. Grinding of the KVP and KVP/C particles induces an amorphization of the phase with significant reduction of the particle size and a homogeneous particle size distribution except for KVP/20rGO. The grinding step was actually found to be harmful for the two composites with rGO because the graphene layers that surround the KVP particles are broken. On the contrary, the KVP/20CNT composite electrode shows excellent electrochemical performance after ball-milling leading to high discharge capacity (101 mAh/g at C/40) and excellent capacity retention even at higher C-rates (C/20 to 1C).

5. References

[1] N. Yabuuchi, K. Kubota, M. Dahbi, S. Komaba, Research development on sodium-ion batteries, Chem. Rev. 114 (2014) 11636–11682. https://doi.org/10.1021/cr500192f.

[2] K. Kubota, M. Dahbi, T. Hosaka, S. Kumakura, S. Komaba, Towards K-Ion and Na-Ion Batteries as "Beyond Li-Ion," Chem. Rec. 18 (2018) 459–479. https://doi.org/10.1002/tcr.201700057.

[3] X. Wu, D.P. Leonard, X. Ji, Emerging Non-Aqueous Potassium-Ion Batteries: Challenges and Opportunities, Chem. Mater. 29 (2017) 5031–5042. https://doi.org/10.1021/acs.chemmater.7b01764.

[4] H. Kim, J.C. Kim, M. Bianchini, D.H. Seo, J. Rodriguez-Garcia, G. Ceder, Recent Progress and Perspective in Electrode Materials for K-Ion Batteries, Adv. Energy Mater. 8 (2018) 1–19. https://doi.org/10.1002/aenm.201702384.

[5] S. Komaba, T. Hasegawa, M. Dahbi, K. Kubota, Potassium intercalation into graphite to realize high-voltage/high-power potassium-ion batteries and potassium-ion capacitors, Electrochem. Commun. 60 (2015) 172–175. https://doi.org/10.1016/j.elecom.2015.09.002.

[6] X. Bie, K. Kubota, T. Hosaka, K. Chihara, S. Komaba, A novel K-ion battery: hexacyanoferrate(ii)/graphite cell, J. Mater. Chem. A. 5 (2017) 4325–4330. https://doi.org/10.1039/c7ta00220c.

[7] Y. Chen, W. Luo, M. Carter, L. Zhou, J. Dai, K. Fu, S. Lacey, T. Li, J. Wan, X. Han, Y. Bao, L. Hu, Organic electrode for non-aqueous potassium-ion batteries, Nano Energy. 18 (2015) 205–211. https://doi.org/10.1016/j.nanoen.2015.10.015.

[8] Y. Hironaka, K. Kubota, S. Komaba, P2- and P3-KxCoO2 as an electrochemical potassium intercalation host, Chem. Commun. 53 (2017) 3693–3696. https://doi.org/10.1039/c7cc00806f.

[9] B. Huang, Y. Shao, Y. Liu, Z. Lu, X. Lu, S. Liao, Improving Potassium-Ion Batteries by Optimizing the Composition of Prussian Blue Cathode, ACS Appl. Energy Mater. 2 (2019) 6528–6535. https://doi.org/10.1021/acsaem.9b01097.

[10] G. He, L.F. Nazar, Crystallite Size Control of Prussian White Analogues for Nonaqueous Potassium-Ion Batteries, ACS Energy Lett. 2 (2017) 1122–1127. https://doi.org/10.1021/acsenergylett.7b00179.

[11] X. Wang, X. Xu, C. Niu, J. Meng, M. Huang, X. Liu, Z. Liu, L. Mai, Earth Abundant Fe/Mn-Based Layered Oxide Interconnected Nanowires for Advanced K-Ion Full Batteries, Nano Lett. 17 (2017) 544–550. https://doi.org/10.1021/acs.nanolett.6b04611.

[12] T. Jungers, A. Mahmoud, C. Malherbe, F. Boschini, B. Vertruyen, Sodium iron sulfate alluaudite solid solution for Na-ion batteries: Moving towards stoichiometric Na2Fe2(SO4)3, J. Mater. Chem. A. 7 (2019) 8226–8233. https://doi.org/10.1039/c9ta00116f.

[13] N. Eshraghi, S. Caes, A. Mahmoud, R. Cloots, B. Vertruyen, F. Boschini, Sodium vanadium (III) fluorophosphate/carbon nanotubes composite (NVPF/CNT) prepared by spray-drying: good electrochemical performance thanks to well-dispersed CNT network within NVPF particles, Electrochim. Acta. 228 (2017) 319–324. https://doi.org/10.1016/j.electacta.2017.01.026.

[14] M. Brisbois, S. Caes, M.T. Sougrati, B. Vertruyen, A. Schrijnemakers, R. Cloots, N. Eshraghi, R.P. Hermann, A. Mahmoud, F. Boschini, Na2FePO4F/multi-walled carbon nanotubes for lithium-ion batteries: Operando Mössbauer study of spray-dried composites, Sol. Energy Mater. Sol. Cells. 148 (2016) 67–72. https://doi.org/10.1016/j.solmat.2015.09.005.

[15] A. Mahmoud, S. Caes, M. Brisbois, R.P. Hermann, L. Berardo, A. Schrijnemakers, C. Malherbe, G. Eppe, R. Cloots, B. Vertruyen, F. Boschini, Spray-drying as a tool to disperse conductive carbon inside Na2FePO4F particles by addition of carbon black or carbon nanotubes to the precursor solution, J. Solid State Electrochem. (2017). https://doi.org/10.1007/s10008-017-3717-x.

[16] V. Mathew, S. Kim, J. Kang, J. Gim, J. Song, J.P. Baboo, W. Park, D. Ahn, J. Han, L. Gu, Y. Wang, Y.S. Hu, Y.K. Sun, J. Kim, Amorphous iron phosphate: Potential host for various charge carrier ions, NPG Asia Mater. 6 (2014). https://doi.org/10.1038/am.2014.98.

[17] B. Senthilkumar, R.K. Selvan, P. Barpanda, Potassium-ion intercalation in anti-NASICON-type iron molybdate Fe2(MoO4)3, Electrochem. Commun. 110 (2020) 106617. https://doi.org/10.1016/j.elecom.2019.106617.

[18] J. Liao, Q. Hu, J. Mu, X. He, S. Wang, C. Chen, A vanadium-based metal-organic phosphate framework material K 2 [(VO) 2 (HPO 4) 2 (C 2 O 4)] as a cathode for potassium-ion batteries, Chem. Commun. 55 (2019) 659–662. https://doi.org/10.1039/c8cc08734b.

[19] S. Zheng, S. Cheng, S. Xiao, L. Hu, Z. Chen, B. Huang, Q. Liu, J. Yang, Q. Chen, Partial replacement of K by Rb to improve electrochemical performance of K3V2(PO4)3 cathode material for potassium-ion batteries, J. Alloys Compd. 815 (2020) 152379. https://doi.org/10.1016/j.jallcom.2019.152379.

[20] X. Lin, J. Huang, H. Tan, J. Huang, B. Zhang, K3V2(PO4)2F3as a robust cathode for potassium-ion batteries, Energy Storage Mater. 16 (2019) 97–101. https://doi.org/10.1016/j.ensm.2018.04.026.

[21] L. Zhang, B. Zhang, C. Wang, Y. Dou, Q. Zhang, Y. Liu, H. Gao, M. Al-Mamun, W.K. Pang, Z. Guo, S.X. Dou, H.K. Liu, Constructing the best symmetric full K-ion battery with the NASICON-type K 3 V 2 (PO 4) 3, Nano Energy. 60 (2019) 432–439. https://doi.org/10.1016/j.nanoen.2019.03.085.

[22] J. Han, Y. Niu, S.J. Bao, Y.N. Yu, S.Y. Lu, M. Xu, Nanocubic KTi2(PO4)3 electrodes for potassium-ion batteries, Chem. Commun. 52 (2016) 11661–11664. https://doi.org/10.1039/c6cc06177j.

[23] T. Hosaka, T. Shimamura, K. Kubota, S. Komaba, Polyanionic Compounds for Potassium-Ion Batteries, Chem. Rec. 19 (2019) 735–745. https://doi.org/10.1002/tcr.201800143.

[24] L. Lander, G. Rousse, A.M. Abakumov, M. Sougrati, G. Van Tendeloo, J.M. Tarascon, Structural, electrochemical and magnetic properties of a novel KFeSO4F polymorph, J. Mater. Chem. A. 3 (2015) 19754–19764. https://doi.org/10.1039/c5ta05548b.

[25] N. Recham, G. Rousse, M.T. Sougrati, J.N. Chotard, C. Frayret, S. Mariyappan, B.C. Melot, J.C. Jumas, J.M. Tarascon, Preparation and characterization of a stable FeSO4F-based framework for alkali ion insertion electrodes, Chem. Mater. 24 (2012) 4363–4370. https://doi.org/10.1021/cm302428w.

[26] W.B. Park, S.C. Han, C. Park, S.U. Hong, U. Han, S.P. Singh, Y.H. Jung, D. Ahn, K.S. Sohn, M. Pyo, KVP2O7 as a Robust High-Energy Cathode for Potassium-Ion Batteries: Pinpointed by a Full Screening of the Inorganic Registry under Specific Search Conditions, Adv. Energy Mater. 8 (2018) 1–12. https://doi.org/10.1002/aenm.201703099.

[27] N.S. Katorova, S.S. Fedotov, D.P. Rupasov, N.D. Luchinin, B. Delattre, Y.M. Chiang, A.M. Abakumov, K.J. Stevenson, Effect of Concentrated Diglyme-Based Electrolytes on the Electrochemical Performance of Potassium-Ion Batteries, ACS Appl. Energy Mater. 2 (2019) 6051–6059. https://doi.org/10.1021/acsaem.9b01173.

[28] K. Chihara, A. Katogi, K. Kubota, S. Komaba, KVPO4F and KVOPO4 toward 4 volt-class potassium-ion batteries, Chem. Commun. 53 (2017) 5208–5211. https://doi.org/10.1039/c6cc10280h.

[29] S.S. Fedotov, N.R. Khasanova, A.S. Samarin, O.A. Drozhzhin, D. Batuk, O.M. Karakulina, J. Hadermann, A.M. Abakumov, E. V. Antipov, AVPO4F (A = Li, K): A 4 v Cathode Material for High-Power Rechargeable Batteries, Chem. Mater. 28 (2016) 411–415. https://doi.org/10.1021/acs.chemmater.5b04065.

[30] N. Goubard-Bretesché, E. Kemnitz, N. Pinna, A general low-temperature synthesis route to polyanionic vanadium phosphate fluoride cathode materials: AVPO 4 F (A = Li, Na, K) and Na 3 V 2 (PO 4) 2 F 3 , Mater. Chem. Front. 3 (2019) 2164–2174. https://doi.org/10.1039/c9qm00325h.

[31] H. Kim, D.H. Seo, M. Bianchini, R.J. Clément, H. Kim, J.C. Kim, Y. Tian, T. Shi, W.S. Yoon, G. Ceder, A New Strategy for High-Voltage Cathodes for K-Ion Batteries: Stoichiometric KVPO4F, Adv. Energy Mater. 8 (2018) 1–12. https://doi.org/10.1002/aenm.201801591.

[32] V.A. Nikitina, S.M. Kuzovchikov, S.S. Fedotov, N.R. Khasanova, A.M. Abakumov, E. V. Antipov, Effect of the electrode/electrolyte interface structure on the potassium-ion diffusional and charge transfer rates: towards a high voltage potassium-ion battery, Electrochim. Acta. 258 (2017) 814–824. https://doi.org/10.1016/j.electacta.2017.11.131.

[33] L. Benhamada, A. Grandin, M.M. Borel, A. Leclaire, B. Raveau, A new vanadium III potassium phosphate with a cage structure: K6V2P4O16, J. Solid State Chem. 91 (1991) 264–270. https://doi.org/10.1016/0022-4596(91)90080-2.

[34] X. Wang, C. Niu, J. Meng, P. Hu, X. Xu, X. Wei, L. Zhou, K. Zhao, W. Luo, M. Yan, L. Mai, Novel K3V2(PO4)3/C Bundled Nanowires as Superior Sodium-Ion Battery Electrode with Ultrahigh Cycling Stability, Adv. Energy Mater. 5 (2015) 1–8. https://doi.org/10.1002/aenm.201500716.

[35] R.W. Cheary, A. Coelho, Fundamental parameters approach to x-ray line-profile fitting, J. Appl. Crystallogr. 25 (1992) 109–121. https://doi.org/10.1107/S0021889891010804.

[36] Bernard A. Boukamp, A package For Impedance/Admittance Data Analysis, Solid State Ionics. 18&19 (1986) 136–140. https://doi.org/10.1017/CBO9781107415324.004.

[37] A. Mahmoud, I. Saadoune, S. Difi, M.T. Sougrati, P.E. Lippens, J.M. Amarilla, Study of the structural and thermal stability of Li0.3Co 2/3Ni1/6Mn1/6O2, Electrochim. Acta. 135 (2014) 536–542. https://doi.org/10.1016/j.electacta.2014.05.058.

[38] R.S. Viswanath, P.J. Miller, High temperature phase transition in NH4H2PO4, Solid State Commun. 32 (1979) 703–706. https://doi.org/10.1016/0038-1098(79)90733-6.

[39] A. Marcilla, A. Gómez-Siurana, M. Beltrán, I. Martínez-Castellanos, I. Blasco, D. Berenguer, TGA-FTIR study of the pyrolysis of sodium citrate and its effect on the pyrolysis of tobacco and tobacco/SBA-15 mixtures under N2 and air atmospheres, J. Sci. Food Agric. 98 (2018) 5916–5931. https://doi.org/10.1002/jsfa.9121.

[40] T. Kavinkumar, S. Manivannan, Synthesis, Characterization and Gas Sensing Properties of Graphene Oxide-Multiwalled Carbon Nanotube Composite, J. Mater. Sci. Technol. 32 (2016) 626–632. https://doi.org/10.1016/j.jmst.2016.03.017.

[41] H.H. Huang, K.K.H. De Silva, G.R.A. Kumara, M. Yoshimura, Structural Evolution of Hydrothermally Derived Reduced Graphene Oxide, Sci. Rep. 8 (2018) 2–10. https://doi.org/10.1038/s41598-018-25194-1.

[42] X. Qiao, S. Liao, C. You, R. Chen, Phosphorus and nitrogen dual doped and simultaneously reduced graphene oxide with high surface area as efficient metal-free electrocatalyst for oxygen reduction, Catalysts. 5 (2015) 981–991. https://doi.org/10.3390/catal5020981.

[43] F. Cheng, Z. Tao, J. Liang, J. Chen, Template-directed materials for rechargeable lithium-ion batteries, Chem. Mater. 20 (2008) 667–681. https://doi.org/10.1021/cm702091q.

[44] C. Karegeya, A. Mahmoud, R. Cloots, B. Vertruyen, F. Boschini, Hydrothermal synthesis in presence of carbon black: Particle-size reduction of iron hydroxyl phosphate hydrate for Li-ion battery, Electrochim. Acta. 250 (2017) 49–58. https://doi.org/10.1016/j.electacta.2017.08.006.

[45] A. Mahmoud, S. Caes, M. Brisbois, R.P. Hermann, L. Berardo, A. Schrijnemakers, C. Malherbe, G. Eppe, R. Cloots, B. Vertruyen, F. Boschini, Spray-drying as a tool to disperse conductive carbon inside Na2FePO4F particles by addition of carbon black or carbon nanotubes to the precursor solution, J. Solid State Electrochem. 22 (2018) 103–112. https://doi.org/10.1007/s10008-017-3717-x.

[46] P. Seydel, J. Blömer, J. Bertling, Modeling particle formation at spray drying using population balances, Dry. Technol. 24 (2006) 137–146. https://doi.org/10.1080/07373930600558912.

[47] C. Karegeya, A. Mahmoud, R. Cloots, B. Vertruyen, F. Boschini, Hydrothermal synthesis in presence of carbon black: Particle-size reduction of iron hydroxyl phosphate hydrate for Li-ion battery, Electrochim. Acta. 250 (2017) 49–58. https://doi.org/10.1016/j.electacta.2017.08.006.

[48] A. Mahmoud, M. Chamas, P.E. Lippens, Electrochemical impedance study of the solid electrolyte interphase in MnSn2 based anode for Li-ion batteries, Electrochim. Acta. 184 (2015) 387–391. https://doi.org/10.1016/j.electacta.2015.10.078.

[49] C. Zhu, C. Wu, C. Chen, P. Kopold, P.A. Van Aken, J. Maier, A High Power − High Energy Na 3 V 2 (PO 4) 2 F 3 Sodium Cathode : Investigation of Transport Parameters , Rational Design and Realization, 2 (2017) 1–14. https://doi.org/10.1021/acs.chemmater.7b00927.

[50] K. Wang, R. Cai, T. Yuan, X. Yu, R. Ran, Z. Shao, Process investigation, electrochemical characterization and optimization of LiFePO4/C composite from mechanical activation using sucrose as carbon source, Electrochim. Acta. 54 (2009) 2861–2868. https://doi.org/10.1016/j.electacta.2008.11.012.

[51] W.L. Liu, J.P. Tu, Y.Q. Qiao, J.P. Zhou, S.J. Shi, X.L. Wang, C.D. Gu, Optimized performances of core-shell structured LiFePO4/C nanocomposite, J. Power Sources. 196 (2011) 7728–7735. https://doi.org/10.1016/j.jpowsour.2011.05.046.

Chapter V

Development of low critical raw material cathode materials for K-ion batteries

Abstract:

Polyanionic compounds have proven their promise as efficient battery materials thanks to their structural and thermal stability and outstanding electrochemical performance. As previously mentioned, phosphate-based compounds are the most promising materials in this category. In the previous chapter, we presented the synthesis of $K_3V(PO_4)_2$ compound and its electrochemical performance as new active cathode material for K-ion batteries. Despite its promising performance, another concern has been raised: developing new materials that avoid the use of lithium is one issue, but developing materials based on either toxic or expensive transition metals is also not ideal. In this regard, using vanadium should be reconsidered due to its criticality (price and toxicity). In this chapter, we are aiming to investigate the substitution of vanadium by iron to prepare new eco-friendly and low-critical raw material cathode materials. A simple replacement of V by Fe leads to the $K_3Fe(PO_4)_2$ material. In addition, we will investigate another material with different stoichiometry, namely $K_3Fe_2(PO_4)_3$ to maximize the theoretical capacity and thus the energy density. In this chapter, we present a preliminary study of both cathode materials for K-ion batteries mainly focused on the optimization of their synthesis to enhance the electrochemical performance. Both materials are obtained successfully after spray-drying and calcination at 600°C for 10 h. The materials cannot be obtained under argon preventing us from forming composite materials with carbon. Different strategies have been tried to improve the electrochemical performance such as: diminution of particle size, change of iron precursors, and addition of *ex situ* carbon nanotubes. These strategies allowed us to obtain good initial discharge capacities of 70 mAh/g for KFP_2 and 100 mAh/g for KFP_3.

1. Introduction

Currently, there are only four known compounds that belong to the pseudo-ternary systems K_2O-Fe_2O_3-P_2O_5, which are phosphates $K_3Fe_2(PO_4)_3$ [1], $K_3Fe(PO_4)_2$ [2], $K_3Fe_5(PO_4)_6$ [3] and the oxy-phosphates $K_{11}Fe_{15}(PO_4)_{18}O$ [4]. Those compounds have been synthesized using the solid-state reaction [1] or flux method [2–4]. Here, we propose an aqueous method to synthesize two of these compounds using spray-drying technique.

$K_3Fe(PO_4)_2$ has been reported for the first time by Lajmi *et al.,* in 2008 [2]. It crystallizes in the monoclinic system with space group $P2_1/n$ (a = 9.598(3) Å, b = 11.086(2) Å, c = 15.462(3) Å, β = 90.30(2)°). Figure V-1 presents the crystal lattice of this compound. It consists of isolated FeO_6 octahedra connected to each other by the phosphate tetrahedra units by sharing corners and edges. The structure can be simply described using $[Fe_2P_4O_{17}]$ chains. Each Fe octahedron is connected to five phosphate tetrahedra sharing apices with four of them and one edge with the last one. These chains are connected via common corners, each tetrahedron of a first chain is associated with one octahedron of the neighboring chains. This led to the formation of the three-dimensional skeleton and the appearance of crossing tunnels where the K-ions are located. This means that there is a possibility for movement of these ions in the 3D frameworks and as a result illustrate the potential for electrochemical reactivity. Although this material has never been reported as cathode for batteries, it has a theoretical capacity of 74 mAh/g as cathode material for K-ion batteries.

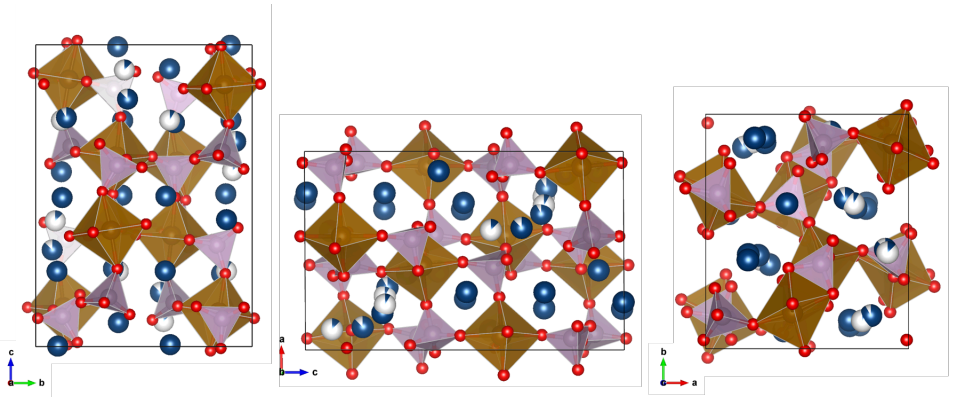

Figure V-1: Crystal structure of $K_3Fe(PO_4)_2$ projection along a axis(left), b axis (middle), and c axis (right).

The second compound that attracted our attention that we explore in this chapter is $K_3Fe_2(PO_4)_3$ (KFP_3), Indeed, this material has the advantage of having 2 iron atoms per formula leading to a higher theoretical capacity of 104 mAh/g as cathode material for K-ion batteries. KFP_3 has been first reported in 1983 by Pintard-Screpel and D'Yvoire, as a monocrystal prepared using a grinding-assisted solid-state method [1]. The 3D structure of the crystal lattice is presented in Figure V-2a. This compound also crystallizes in a monoclinic system with a space group C2/c (a =16.303 (2) Å, b=9.463(1) Å, c= 16.691(2) Å, β = 118.39(1)°). KFP_3 structure is constituted of PO_4 tetrahedra, FeO_6 octahedra, and FeO_5 polyhedra. This skeleton can be described as a succession of planes made of the polyhedra FeO_5 sharing apex with PO_4 tetrahedra. These blocks are connected to each other by FeO_6 octahedra. PO_4 tetrahedra and FeO_6 octahedra create layers with a high density of oxygen and potassium ions are intercalated between those layers.

The rigid structure made by the atoms of P, Fe and O have then an interstitial space that can be described as a three-dimensional channel network where potassium ions are located and can move during the electrochemical reaction. Figure V-2b presents two possible displacement channels of the potassium ion inside the structure.

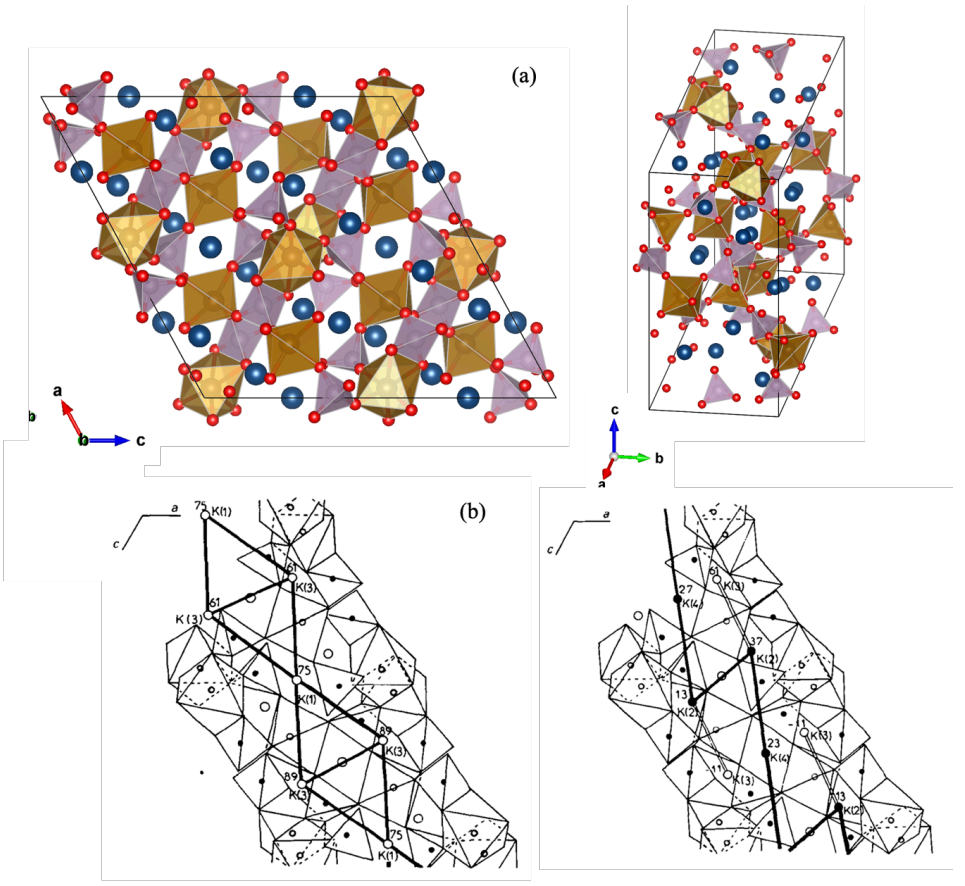

Figure V-2: (a) Crystal structure of $K_3Fe_2(PO_4)_3$ (projection along b axis on left). (b) Possible displacement of the K^+ ions inside the KFP_3 structure projection on (010) reproduced from [1].

Even if these compounds have, for now, never been reported in the literature as active electrode material for rechargeable batteries, the good electrochemical performance of their equivalents with Na or Li as electrode material for Li-ion and Na-ion batteries has already been reported [5–8]. For example, $Li_3Fe_2(PO_4)_3$ has a NASICON (sodium (Na) Super Ionic CONductor) type structure, and $Li_{3+x}Fe_2(PO_4)_3$ demonstrates excellent electrochemical performance in the voltage window 2.0 V-3.5 V for $0<x<1.8$ with a specific capacity of about 115 mAh/g at C/10 and thus an energy density of more than 320 Wh/kg in Li-ion batteries [5]. In Na-ion batteries, similar result has been obtained for the Na equivalent by

delivering a specific capacity of 100 mAh/g and excellent stability upon cycling with more than 60 mAh/g after 1100 cycles at high current density [6]. In the case of KFP_2 no analogy with Na has been found but a similar compound $Na_3V(PO_4)_2$ has already been reported by Kim *et al.,* in 2018 that delivers a capacity of 90 mAh/g at C/5 (99% of the theoretical capacity) [9]. All the previous studies prove the interest in investigating these compounds as cathode for K-ion batteries. For all the materials, the same approach is followed: first start with a discharge process to insert extra Na or Li in the material, this is due to the initial oxidation state of the iron in the compounds which is in Fe^{3+} state. In fact, there are two possibilities: first possibility is to start by a charge that leads to the oxidation of Fe^{3+} to Fe^{4+} [8], however, this is not facilitated using a conventional electrolyte, or second approach to start by a discharge process and insert additional alkali-ion inside the structure which leads to reduction of Fe^{3+} to Fe^{2+}. This second approach has been chosen and explored in our work. The limitations of phosphate-based compounds as electrode materials have been already explained in previous chapters. Indeed, they exhibit poor conductivity, thus the same strategies reported in the previous chapters were used to enhance the performance of the investigated materials in this chapter i.e. diminution of particle size and addition of conductive carbon. The thermal behavior and decomposition of the spray-dried precursors were analyzed using TGA/DSC technique. The structural and morphological properties of the prepared materials were systematically investigated by combining XRD, ^{57}Fe Mössbauer spectroscopy, SEM, BET, and laser granulometry characterization techniques. The electrochemical performances were evaluated in half-cells by galvanostatic techniques and cyclic voltammetry.

2. Experimental

2.1. Synthesis of $K_3Fe(PO_4)_2$ and $K_3Fe_2(PO_4)_3$ materials

$K_3Fe(PO_4)_2$ (KFP_2) and $K_3Fe_2(PO_4)_3$ (KFP_3) materials were prepared by spray–drying process.

For KFP_2, iron(III) citrate, ammonium dihydrogen phosphate, (without and with citric acid, and ascorbic acid) in molar ratio 1/3/1/1 were dissolved in milliQ water (18.2 $M\Omega.cm^{-1}$) at room temperature by magnetic stirring. The stoichiometric amount of potassium hydroxide is then added, and the solution is heated to 90°C for 1 h. The influence of the addition of the complexing agents (citric acid and ascorbic acid) has been investigated. The same strategy is used for the synthesis of KFP_3 using the stoichiometric amounts of the same precursors used for KFP_2. In addition, different iron precursors have been used for the synthesis of KFP_3. In this case, iron (III) citrate has been used instead of iron (III) nitrate or iron (III) acetylacetonate respecting the same ratio and following the same synthesis protocol.

In both compositions, after cooling down to room temperature, the obtained solutions are injected in a semi-industrial spray-dryer (GEA-Niro Mobile Minor) using a bi-fluid nozzle injection mode. Spray drying was carried out under an air pressure of 1 bar with a 25 ml/min feed rate, an inlet temperature of 170°C, and an outlet temperature of 100 ± 1°C. The collected powder was then heat treated to obtain the crystallized compound. The spray-dried powders were submitted to heat treatment at different temperatures and durations under argon or air atmosphere with a heating rate of 150°C/h. The obtained powders have been ball-milled at 375 rpm using a planetary mill (Retsch PM400/2, alternate rotation mode) with zirconia grinding jars containing 0.5 mm diameter zirconia balls

(50 g of balls for 2 g of powders) and 25 ml isopropanol during different durations from 30 to 90 minutes (intervals of 30 min) followed by drying at 70°C for 24 h.

2.2. Thermal, structural, and morphological characterizations

To optimize the synthesis process of the KFP_3 material, the thermal behavior of the spray-dried KFP_3 powders was analyzed by thermogravimetric analysis (TGA) using a Q100 system from TA instruments. About 10 mg of each sample was placed in an alumina crucible and heated under argon from room temperature to 1000°C at a heating rate of 20 K/min to yield the onset decomposition temperature.

X-ray diffraction (XRD) was carried out to identify and verify the purity of the obtained phases over the 2Theta range from 9° to 50° with a Bruker D8 Twin-Twin powder diffractometer using Cu Kα radiation. ^{57}Fe transmission Mössbauer spectra were recorded at room temperature in the ± 4 mm/s and ± 12 mm/s velocity range with a constant-acceleration spectrometer and a $^{57}Co(Rh)$ source. The Mössbauer absorbers were prepared with 40 mg/cm^2 of KFP_3 mixed with boron nitride. The spectrometer was calibrated at room temperature with the magnetically split sextet spectrum of a high-purity α-Fe foil as the reference for isomer shifts. The spectral parameters such as isomer shift (δ), quadrupole splitting (ΔE_q), hyperfine field, linewidth (Γ), and relative resonance areas (A) of the different spectral components were determined with Lorentzian curves using the Fullham program. The validity of fits was judged based on minimizing the number of parameters and χ^2 values.

The microstructures of the KFP_x materials were examined using a scanning electron microscope FEG-SEM (XL 30, FEI) operated at 15 kV. Specific surface area and texture properties, including analysis of porosity for all the samples (KFP_x), were determined by measuring nitrogen (N_2) adsorption-desorption

isotherms with a Micromeritics ASAP 2020 Plus system. Samples were degassed at 150°C for 6 h before analysis.

The evolution of the particle size distribution of the powders during ball-milling was followed by laser granulometry using a Mastersizer 2000 Malvern system.

2.3. Electrochemical characterizations

KFP_x powders were tested as cathode materials for K-ions batteries in two-electrode coin cells. The electrodes were prepared by mixing KFP_x powders as active materials with carbon black as an electronic conductor, carbon nanotube suspension in n-methyl pyrrolidinone (NMP) to enhance the electronic conductivity, and polyvinylidene fluoride (PVDF) as the binder in weight ratio 6/1/2/1 in NMP. The resulting slurry is mixed in 50 mL zirconia jars with 10 zirconia balls (5 mm) at 200 rpm for 1 h. The slurry is then tape-casted on a 25 µm thick aluminum foil as the current collector by Doctor blade method and then dried at 110°C under vacuum for 12 h. Electrodes were cut into 15 mm diameter discs with active mass loading of approximately 1-2 mg. Coin cells were assembled in an argon-filled glove box using a glass microfiber paper (Whatman GF/A) as separator, 0.8 M KPF_6 +10wt% of fluoroethylene carbonate (FEC) dissolved in propylene carbonate (PC) as the electrolyte, and potassium foil as the counter and reference electrodes. All cells were tested within a fixed voltage window, between 1.0 and 4.5 V *vs.* K^+/K, under galvanostatic conditions at different current density rates: C/40-1C (1C corresponds to the extraction/insertion current of 1 K/KFP_x in 1 h). All electrochemical tests were carried out at room temperature using a Neware BTS4000 Electrochemical Test System. The cyclic voltammetry tests were performed in two-electrode coin cells (with the same electrode preparation method as explained before) at scan rates of 0.1 mV/s. The test was conducted using a VMP3 Bio-Logic potentiostat.

3. Results and discussions:

3.1. Synthesis and characterization of $K_3Fe(PO_4)_2$

The obtained powders after the spray drying and calcination steps were characterized by X-ray diffraction technique to analyze the composition and crystallinity. Two different compositions are prepared during the synthesis of spray-dried KFP_2. The first one has no complexing agent (KFP_2) and the other one has citric acid and ascorbic acid mixed in the precursors' powders (KFP_2a). The calcination of these two powders has been performed at 600°C for 10 h with a heating ramp of 150°C/h under air. To transform the acid additive into conductive carbon, heat treatment under argon was performed by applying the same calcination parameters. XRD patterns of the obtained powders are illustrated in Figure V-3.

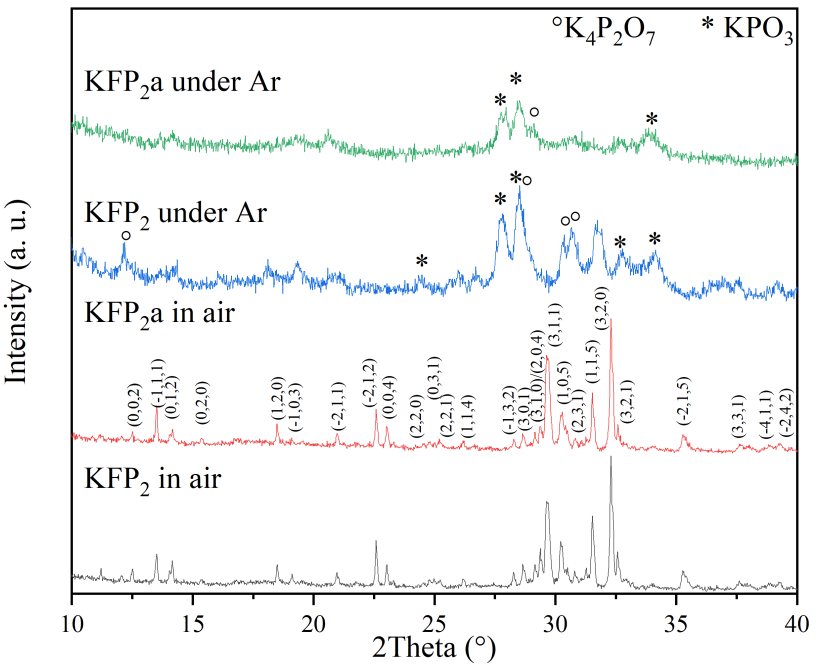

Figure V-3: XRD patterns of spray-dried $K_3Fe(PO_4)_2$ after calcination at 600°C for 10 h under argon or in air.

The calcination of both KFP_2 and KFP_2a under air at 600°C for 10 h leads to the formation of the pure and crystalline $K_3Fe(PO_4)_2$ phase. It means that the complexing agents are not essential to stabilize the solution before the spray drying step and to obtain the targeted material. There is no noticeable difference between the two diffractograms as the complexing agents are completely transformed into CO_2 in the calcination step. Regarding the heat treatment under argon, a significant amorphous phase was detected for KFP_2 phase, as well as for KFP_2a with lower crystallinity. Unfortunately, the crystalline phase mainly corresponds to KPO_3 and $K_4P_2O_7$. There is no peak that can be attributed to an iron-containing phase. This result suggests that the formation of crystalline and pure KFP_2 material requires calcination under an oxygen atmosphere meaning that the addition of carbon in the precursors solution before spray drying will not lead to the formation of the desired composite material (calcination under argon) or will be eliminated during the annealing step (calcination under oxygen). However, we should highlight that this is the first time that this phase is obtained with a simple method (spray drying), and the only reported method up until now, is a flux method [2].

Knowing that the main drawback of phosphate compounds is related to their poor electronic conductivity, the synthesis of composite material has been tried by spray drying with addition of carbon nanotubes (CNT) in the precursors' solution. The obtained spray-dried powders have been annealed in different conditions. For each sample, the calcination at 600°C under air was conducted for only 60 min to avoid a complete degradation of the CNT, as well as a heat treatment carried out under argon at 600°C for 10 h. The XRD patterns of the calcined powders are presented in Figure V-4.

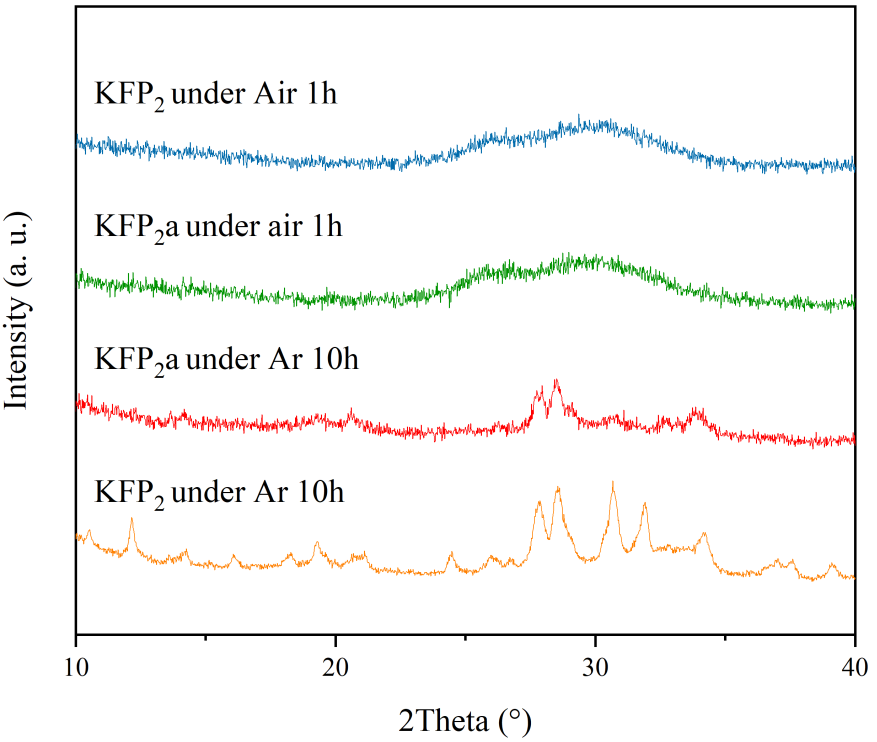

Figure V-4: XRD patterns of KFP_2/CNT with or without complexing agent samples obtained after calcination under air at 600°C for 1 h or under argon at 600°C for 10 h.

As evidenced in Figure V-4, the treatment for 1 h at 600°C is insufficient to crystallize the powders as no peak is observed except a bump between 25° and 35° 2Theta that can be attributed to the carbon. Regarding the heat treatment under argon, the obtained phase cannot be attributed to the KFP_2 phase and the XRD peaks are mainly attributed to iron pyrophosphate $Fe_2(P_2O_7)$ meaning that the iron is reduced by the carbothermal reaction from Fe^{3+} to Fe^{2+}. This confirms the previous observation that the KFP_2 phase can only be obtained under oxygen containing atmosphere with a long heat treatment (10 h). Additionally, this result confirms that the KFP_2/Carbon composite material was not obtained. Thus, the prepared KFP_2 powder under air at 600°C 10 h with high purity and good

crystallinity is further investigated by scanning electron microscopy (See Figure V-5).

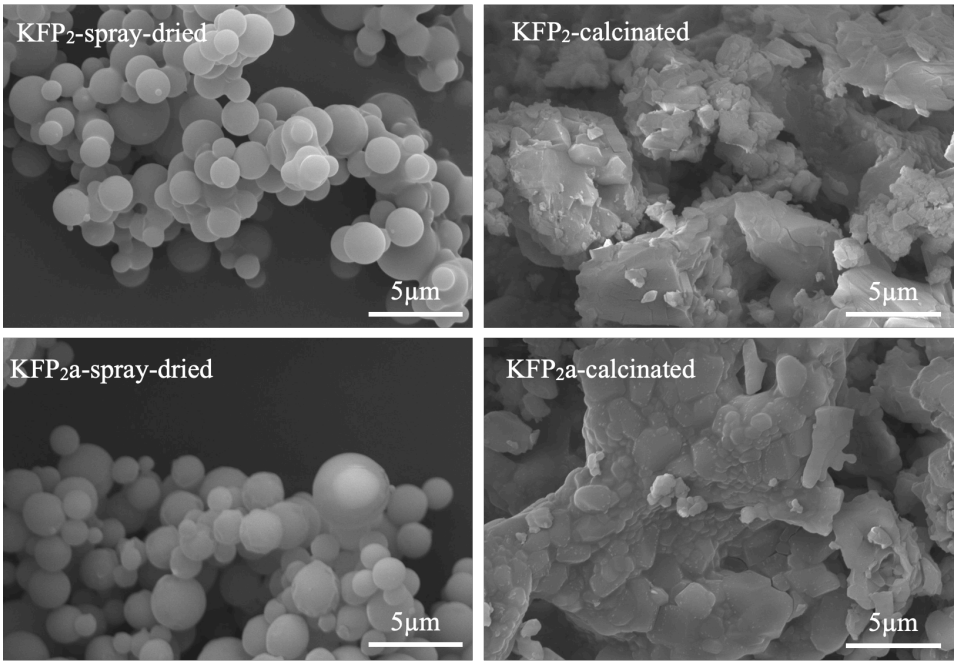

Figure V-5: Scanning electron micrographs of KFP_2 and KFP_2a before and after calcination at 600°C-10 h under air.

After the spray drying step, spherical particles were obtained which is a common shape of spray-dried powders. No difference is observed between the two samples with or without complexing agents. After the calcination step of 600°C for 10 h under air, the spherical morphology is completely modified. The primary particles are no more distinguishable and only large agglomerates are formed after the calcination. This result may be explained by a partial fusion of the sample at this temperature that induces the noticed modification in the morphology. To solve this issue, a grinding step of 90 min is performed for both samples, the evolution of the particle size distribution after the grinding was analyzed by laser granulometry particle size analyzer and the corresponding curves registered before and after the grinding process are presented in Figure V-6.

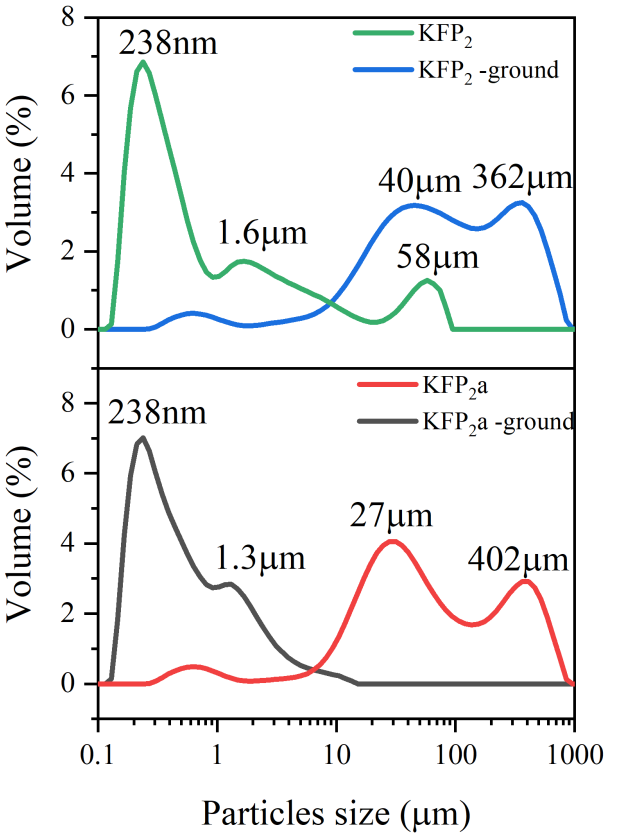

Figure V-6: Comparison of particle size of KFP_2 powders with or without complexing agent before and after grinding.

Before grinding, both materials present a huge average particle size (D_{50}) of about 130 µm. Indeed, KFP_2 and KFP_2a powders have a broad and multimodal particle size distribution from 10 to 1000 µm that is not influenced by the addition of the complexing agent. After grinding, the particle size is greatly reduced, and the average particle size is now 0.4 µm. Nevertheless, the particle size distribution is not narrow and monomodal. In this case, the addition of complexing agents has a small influence as the average particle size with complexing agents after grinding is lower. This may be explained by the decomposition of the complexing agent during the calcination which creates more porosity and leads to a more friable powder. The high reduction of particle size after the grinding process leads to an increase in the specific surface area which allows better contact with the

electrolyte in the battery. All these features are very suitable to enhance the electrochemical performance, especially at high current densities. Indeed, the reduction in particle size leads to a faster K^+ ions transport thanks to a shorter diffusion pathways.

To check the influence of different preparations of KFP_2 powders, without and with complexing agents and ground powders, a series of electrochemical characterizations were performed. The electrodes were tested by galvanostatic cycling at C/10 in the voltage window of 1.5-4.0 V *vs.* K^+/K for K-ion batteries. The evolution of the discharge capacity with cycle number of these KFP_2 powders is presented in Figure V-7.

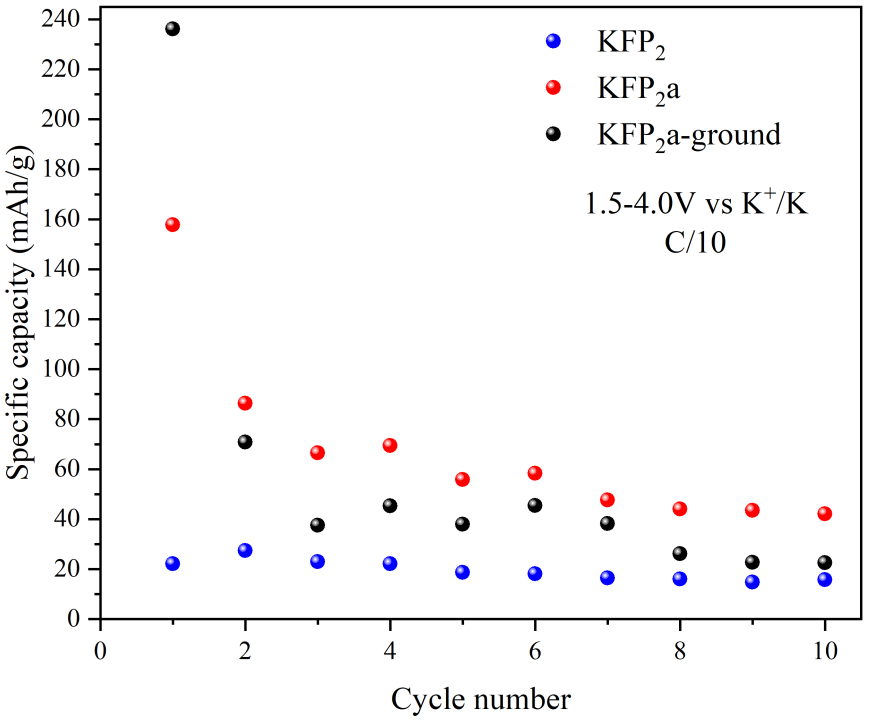

Figure V-7: Evolution of the specific capacity with cycle number at C/10 in the voltage window of 1.5-4.0 V vs. K^+/K for of KFP_2 cathode material for K-ion batteries.

As shown in Figure V-7, a significant difference is observed when the complexing agents are added during the synthesis. The specific capacity of powders in the presence of acids is almost three times (70 mAh/g, almost the theoretical capacity: 74 mAh/g) higher than those without acids (20 mAh/g).

A rather surprising result is the absence of marked enhancement between the ground and unground powders. As seen in the previous chapter, electrochemical performance improvement was expected after grinding. However, the ground powder has lower electrochemical performance. This can be related to the high irreversibility occurring during the first cycle. The irreversibility of the unground powder is much lower. This irreversibility may be due to electrolyte degradation or secondary reactions taking place in the cell. The improvement of the electronic conductivity of this cathode material would lead to the enhancement of its electrochemical performance. However, the low theoretical capacity of the KFP_2 material (74 mAh/g) does not make it a candidate of choice for commercial batteries. To conclude this section, the $K_3Fe(PO_4)_2$ phase is obtained for the first time by spray drying followed by calcination and additionally its application as cathode material for K-ion batteries is tested and presented for the first time.

In the next section, we mainly focus on $K_3Fe_2(PO_4)_3$ cathode material which has a higher theoretical capacity of (104 mAh/g) thanks to the presence of two iron atoms allowing the insertion/extraction of 2 K^+ while keeping the advantages of being an eco-friendly and low-cost electrode material.

3.2. Synthesis and characterization of $K_3Fe_2(PO_4)_3$

The synthesis protocol of this compound is the same as for KFP_2. A precursor solution with iron citrate, potassium hydroxide, ammonium dihydrogen phosphate, ascorbic acid, and citric acid in 2/3/3/1/1 molar ratio is made in milliQ water. Similar to KFP_2, two samples have been prepared with or without complexing agents for KFP_3. The same spray drying parameters were used.

Thermogravimetric analysis has been used to evaluate the thermal behavior and the effects of heat treatment on material degradation and crystallization. The variation of the sample mass when heating up from room temperature to 1000°C has been followed to find the optimal synthesis temperature to form the KFP_3 phase.

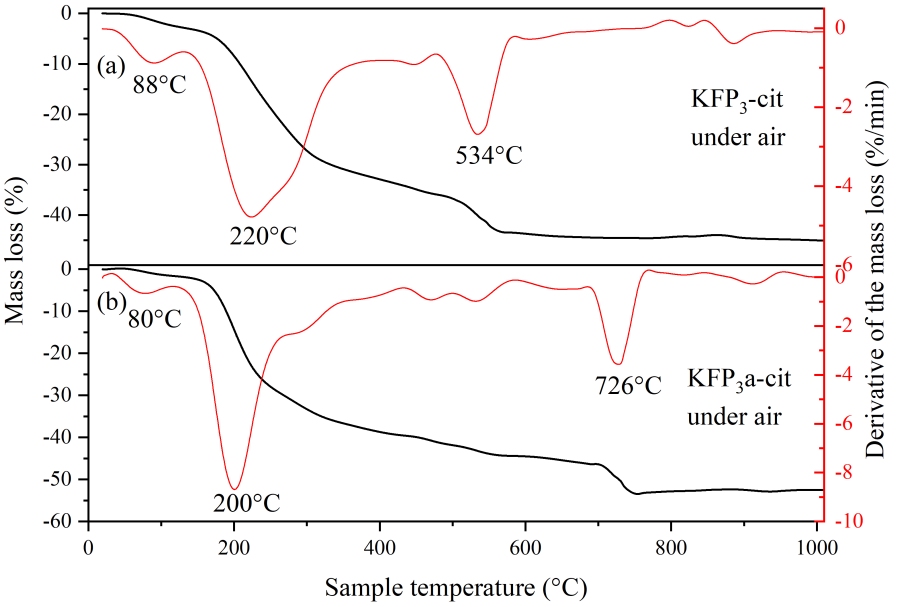

Figure V-8: TGA profile and its derivative curve for the spray-dried precursor of the KFP_3-cit powders (a) without or (b) with complexing agents.

TGA and derivative curves for the spray-dried precursors powders are presented in Figure V-8. The first mass loss observed for both samples is around 90°C and can be attributed to the loss of residual water. The main loss occurs between 200°C and 550°C, corresponding to the degradation of the different precursors. For the sample with complexing agents, an additional phenomenon is observed at 730°C that could be linked to partial degradation of the KFP_3 phase or degradation of the complexing agents. Nevertheless, this last assumption has a low probability as the measurement has been performed under air and both citric acid and ascorbic acid are completely degraded at this temperature. For this reason, the temperature of

600°C is conserved for the calcination of both powders. To verify the composition of the calcined powders, XRD measurements were conducted and the XRD patterns of these powders are presented in Figure V-9.

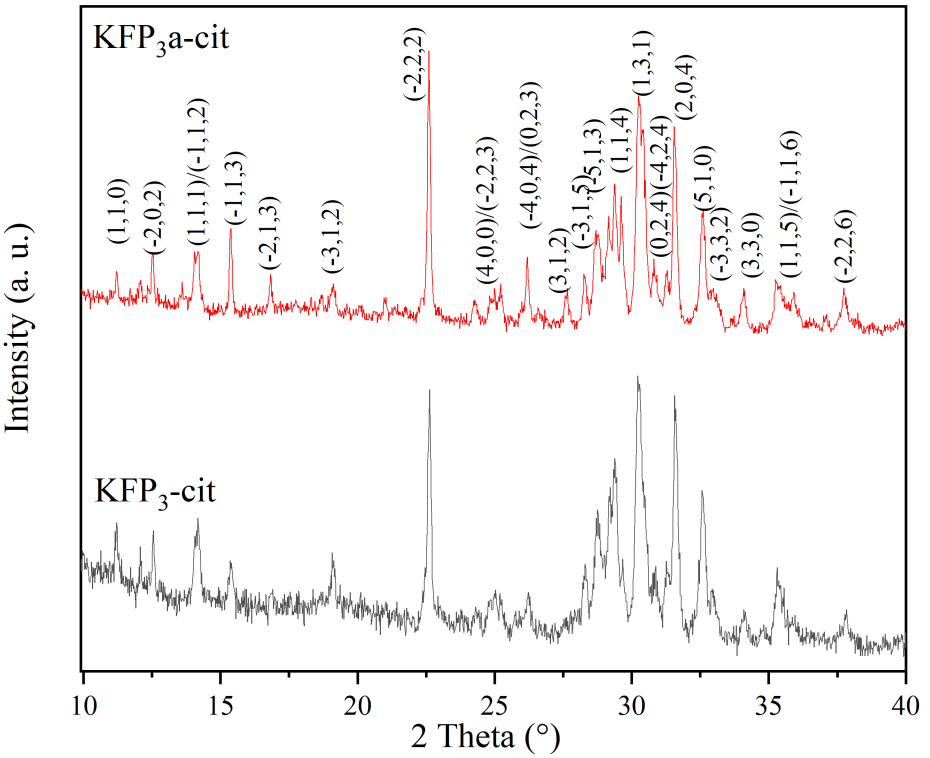

Figure V-9: XRD diffractograms of the KFP_3-cit powders with or without complexing agent obtained after heat treatment at 600°C 10 h under air.

The XRD patterns confirm that the desired pure phases in both cases were obtained. The KFP_3-cit sample seems to be slightly less crystalline than the KFP_3a-cit samples as the peaks are broader. Nevertheless, all the peaks can be attributed to the KFP_3 phase meaning that no crystallized impurities are detected in the sample. To further investigated the purity, oxidation state and local environment of iron in these samples, ^{57}Fe Mossbauer analysis has been performed on both samples.

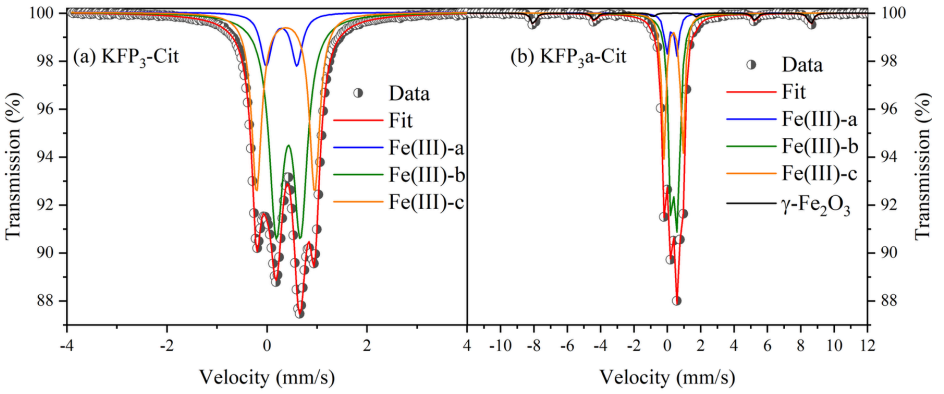

(c)	Fe(III)-a	Fe(III)-b	Fe(III)-c
δ (mm/s)	0.290(5)	0.429(2)	0.373(1)
ΔEq (mm/s)	0.61(1)	0.487(3)	1.161(3)
Γ (mm/s)	0.263(2)	0.543(3)	0.249(2)
Area (%)	11(1)	54(1)	35(1)

(d)	Fe(III)-a	Fe(III)-b	Fe(III)-c	γ-Fe_2O_3
δ (mm/s)	0.264(9)	0.432(2)	0.356(3)	0.36(2)
ΔEq (mm/s)	0.624(2)	0.382(1)	1.135(4)	0.16(4)
Γ (mm/s)	0.323(3)	0.350(3)	0.305(3)	0.334(3)
Field	/	/	/	51.6(2)
Area (%)	10(1)	51(1)	33(1)	6(1)

Figure V-10: ^{57}Fe Mössbauer spectrum of the (a) KFP_3-cit and (b) KFP_3a-cit samples after calcination at 600°C for 10 h in air. (c),(d) corresponding ^{57}Fe Mössbauer hyperfine parameters for KFP_3-cit and KFP_3a-cit.

The room temperature ^{57}Fe Mössbauer spectra of both KFP_3-cit and KFP_3a-cit materials after calcination at 600°C under air are presented in Figure V-10, and their corresponding hyperfine parameters are summarized in the tables in Figure V-10c, d. Mössbauer spectroscopy measurements at room temperature show the paramagnetic behavior of the prepared compounds. The spectra have a similar profile and consist of two asymmetric doublets. These spectra are quite different from their Li and Na analogous materials $Li_3Fe_2(PO_4)_3$ and $Na_3Fe_2(PO_4)_3$ where only a single doublet is observed [10,11]. This is due a high symmetry of NASICON-type rhombohedral structure compared to KFP_3 that crystalizes in monoclinic type structure. For KFP_3-cit materials a good fit has been obtained using three components; Fe(III)a, Fe(III)b and Fe(III)c. The three components have an isomer shift typical of Fe(III) high spin of 0.29, 0.42 and 0.37 mm/s, respectively. The quadrupole splitting of the two first components is slightly

different showing the two different environments of the iron in the octahedral site (0.61 mm/s and 0.48 mm/s). The last component has a huge quadrupole splitting (1.16 mm/s) meaning a highly distorted local environment of the iron. This is in good agreement with the crystal structure of the KFP_3-cit material as some iron octahedra are described as highly distorted and also not all the iron sites are octahedral since the structure is also formed with FeO_5 site [1]. The value of full width at half maximum (FWMH) confirms the good crystallinity state of the material. Regarding the KFP_3a-cit samples, Mössbauer spectra was fitted using the same components used in the case of KFP_3-cit with three Fe(III) component with an isomer shift of 0.26, 0.43 and 0.36 mm/s and a quadrupole splitting of 0.62, 0.38, and 1.14 mm/s respectively showing the same iron environment than the KFP_3-cit sample. A last magnetic component has also been detected corresponding to only 6% of surface area. This component exhibits an isomer shift of 0.36 mm/s and magnetic hyperfine field $B_{hf} = \mu 0 H_{hf}$ =51 T and thus can be attributed to γ-Fe_2O_3. This low impurity can be attributed to partial oxidation of the iron during the calcination step.

Figure V-11 presents the SEM images of the obtained KFP_3-cit and KFP_3a-cit particles before and after calcination. Similar to KFP_2 material, a spherical morphology is obtained after spray drying which was expected. After calcination, the morphology is completely different but contrary to the KFP_2, the observed morphology change seems to result from a breaking of the spheres more than a fusion of the sample. With the addition of complexing agents, the particles after calcination are no longer spherical and the obtained agglomerate seems to be less dense and agglomerated than for KFP_2 samples.

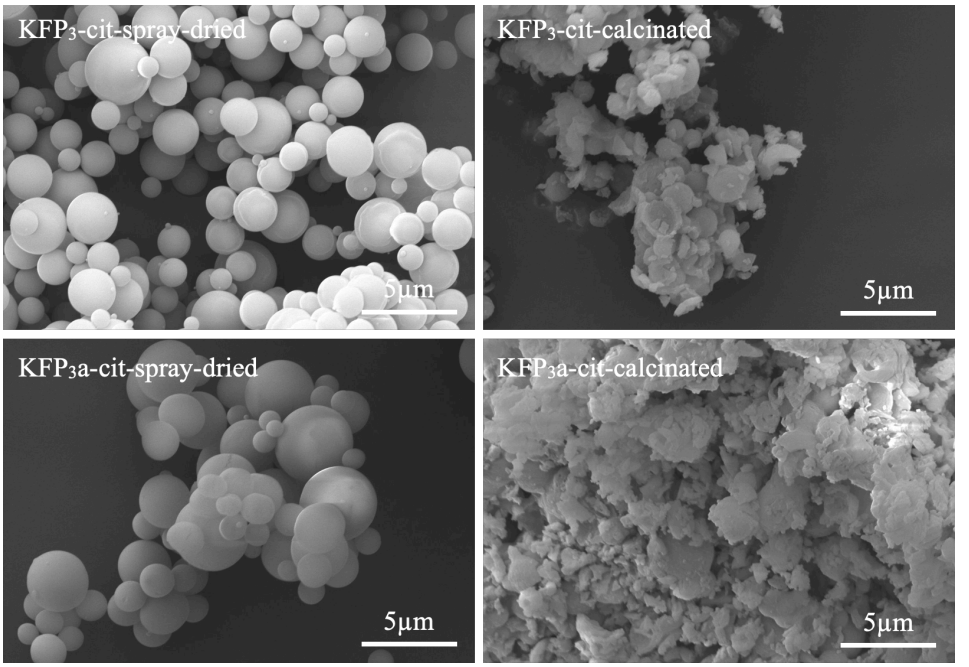

Figure V-11: SEM micrographs of spray-dried KFP_3-cit and KFP_3a-cit with complexing agents before and after calcination.

To determine the electrochemical properties of KFP_3-cit and KFP_3a-cit, K half-cells were assembled and tested at 25°C. Figure V-12a shows a cyclic voltammetry curve with a scan rate of 0.1 mV/s of the KFP_3-cit cathode material and Figure V-12b shows the evolution of the specific capacity upon cycling of the KFP_3-cit and KFP_3a-cit cathode material after calcination under air at 600C° for 10 h.

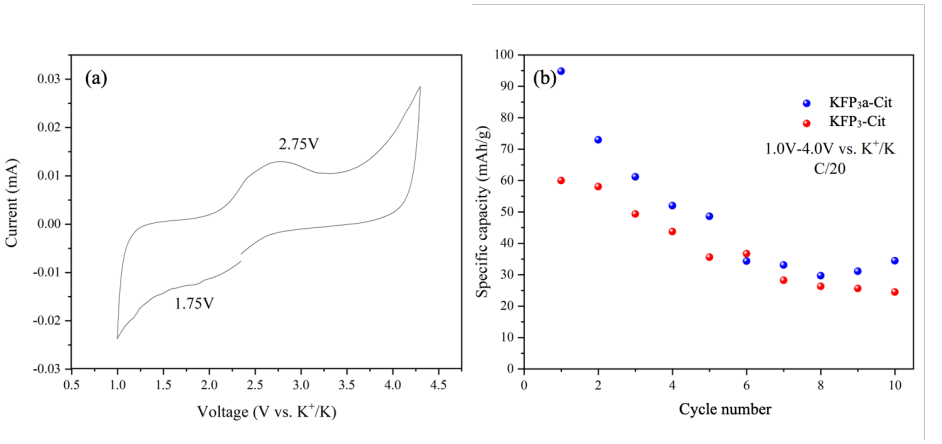

Figure V-12: (a) Cyclic voltammogram of KFP_3-cit materials with a scan rate of 0.1 mV/s between 1.0V and 4.5 V vs. K^+/K. (b) Evolution of the discharge capacity with cycle number of the KFP_3-cit and KFP_3a-cit cathode material at C/20 cycling rate between 1 V and 4 V.

As shown in Figure V-12a, only one broad peak of oxidation is observed around 2.75 V. On the reduction side, there are no well-defined peaks observed but a bump can be distinguished around 1.75 V. Figure V-12b presents the evolution of the discharge capacity with cycle number at C/20. Regarding the cycling performance (Figure V-12b), similar behavior is observed for both compounds. The initial obtained discharge capacities are: 95 mAh/g for KFP_3a-cit and 60 mAh/g for KFP_3-cit that decreases upon subsequent cycling. After 6 cycles, the obtained capacity stabilizes at around 35-40 mAh/g for both samples which is still far from the theoretical capacity of 104 mAh/g. This low capacity can be explained by a low conductivity of the active material and also by large agglomerated particles after calcination as observed by SEM (Figure V-11).

To enhance the electrochemical performance through improving the electronic conductivity of the cathode material, KFP_3a-cit/CNT composite materials were synthesized. The same synthesis protocol is used except that 20wt% of CNT is added to the precursor solution before the spray drying step. As mentioned earlier, we encounter some issues when calcination under argon is performed. This has

been evidenced in the KFP_2 sample, as such a TGA analysis was first performed under an argon atmosphere to analyze the thermal behavior of our samples.

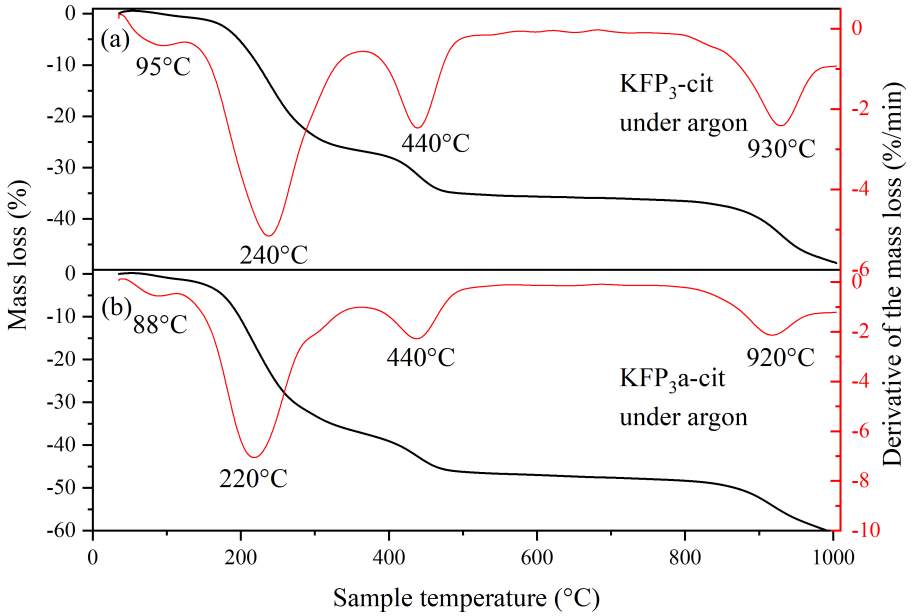

Figure V-13: TGA profile and its derivative curve for the spray-dried precursor of the KFP_3-cit powders (a) without or (b)with the complexing agent under argon atmosphere.

As shown in Figure V-13, both samples have a similar profile for mass loss. The first loss is due to water loss at around 100°C. The main loss is situated between 175°C and 400°C and corresponds to the degradation of the precursors, an additional loss that can be attributed to the same phenomenon occurring around 450°C [12]. The mass loss is negligible till 850°C and the final loss is present is attributed to partial degradation of CNT. According to the TGA analysis, also the temperature of 600°C should be suitable to obtain the desired phase under argon. The profile of thermal behavior is the same for both materials, the presence of a complexing agent should not induce any difference between the samples. Several temperatures have been tried from 600°C to 900°C and the XRD patterns

for the KFP_3-cit without complexing agents are presented and compared in Figure V-14.

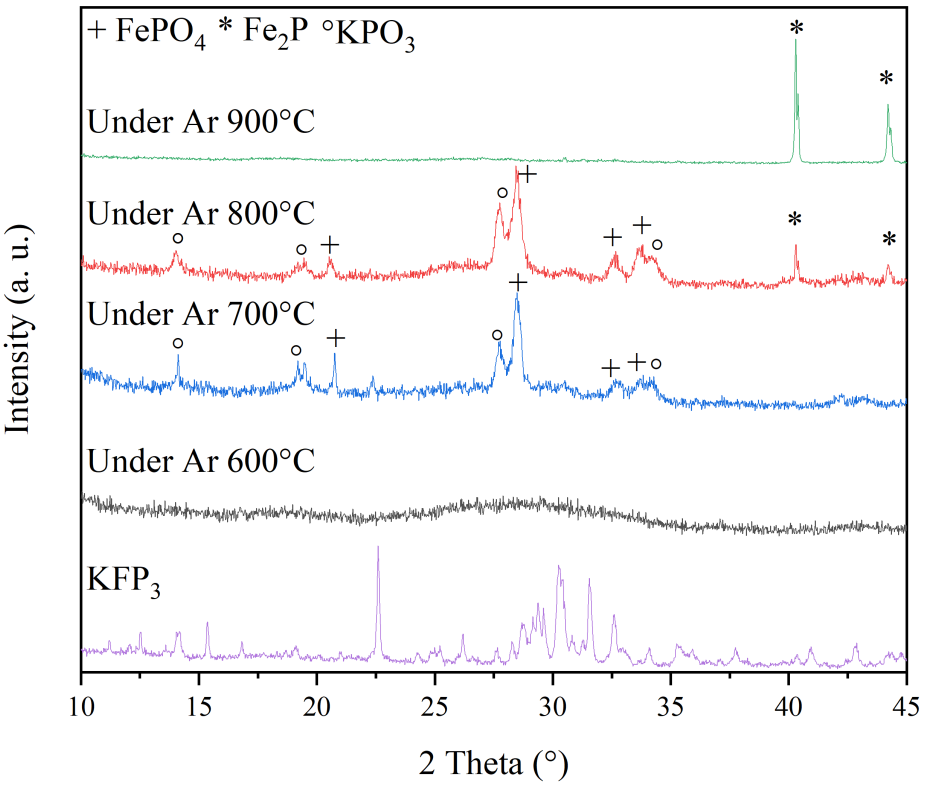

Figure V-14: XRD patterns of KFP_3-cit annealed under argon for 10 h at different temperatures.

Unfortunately, none of the annealing steps under argon has led to the formation of the desired phase. At 600°C, the obtained sample is completely amorphous, and no information can be extracted from the XRD analysis. At 700°C and 800°C, the same XRD patterns are observed where we observe the formation of $FePO_4$ and KPO_3, while the KFP_3 phase is absent. The sample annealed at 900°C is well crystallized, however, the obtained phase is Fe_2P and not KFP_3. As such, calcination under air is required also in the case of KFP_3.

The best strategy to enhance the electrochemical performance of the sample is to reduce the particle size by grinding and the *ex situ* addition of conductive carbon.

Thus, ball-milling has been performed on the calcinated sample with an addition of 20wt% of CNT during this grinding step.

As expected from the SEM micrographs, the particle size is quite large before the grinding (Figure V-15a). Both samples are mainly composed of secondary particles of more than 100 µm in size. The particle size for the KFP_3a-cit sample is higher as almost all the particles have a size of more than 10 µm while the KFP_3-cit sample has particles below 10 µm and a higher intensity of submicronic peak. The observations for the ground samples are completely different, indeed grinding during 90min seems to be quite efficient to reduce the particle size. For the KFP_3a-cit -ground sample, all the particles now have a size below 5 µm and the mean particle size of 250 nm is achieved. Regarding the sample, without complexing agent addition, the distribution of particle size is a bit different. Two peaks of equivalent intensity are observed one that is centered around particle size of 250 nm and the other one that has a mean size of 3 µm. This means that the ball-milling would have benefited from a longer duration to reduce the size of the particles more homogeneously. This also means, as already observed for the KFP_2 powder that the grinding is more efficient on the samples with complexing agent addition and so that these samples are more friable. As the grinding can also affect the crystallinity of the sample, the duration has been limited to 90 min. The SEM images related to the grinding of KFP_3a-cit are presented in Figure V-15c and confirm that the grinding has effectively reduced the size of the secondary particles but that some larger particles still remain.

The influence of the grinding step on the electrochemical performance of the material was investigated. The evolution of the discharge capacity with the cycle number is presented in Figure V-16.

The diminution of the particle size leads to an enhancement of the delivered capacity for both materials. KFP_3a-cit and KFP_3a-cit -ground cathode materials deliver nearly identical capacities of 90 and 95 mAh/g, respectively. However, a capacity fading is observed, and the capacity value stabilizes at 56 mAh/g after

10 cycles while the capacity without grinding is only 30 mAh/g for KFP_3a-cit and 25 mAh/g for KFP_3-cit. The capacity fading is still too important as the initial capacity of KFP_3a and KFP_3a-ground is about 90 mAh/g (90% of the theoretical capacity). This also means that the grinding is not efficient enough and that the conductivity of the material is still too low to allow a good electrochemical performance. Additionally, since the addition of CNT inside the particle before spray drying has not led to the formation of the desired phase, the electronic conductivity must be enhanced by exploring other strategies.

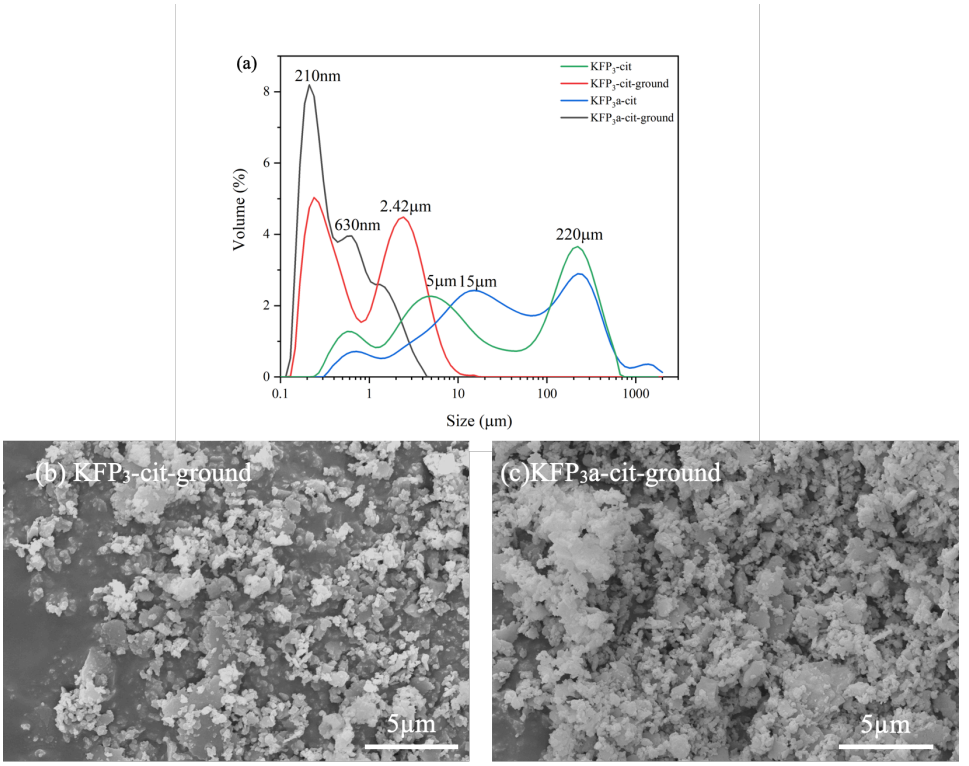

Figure V-15: (a) Particle size distribution of KFP_3-cit and KFP_3a-cit samples before and after grinding (90 min). SEM micrographies of ground powders of (a) KFP_3-cit and (b) KFP_3a-cit.

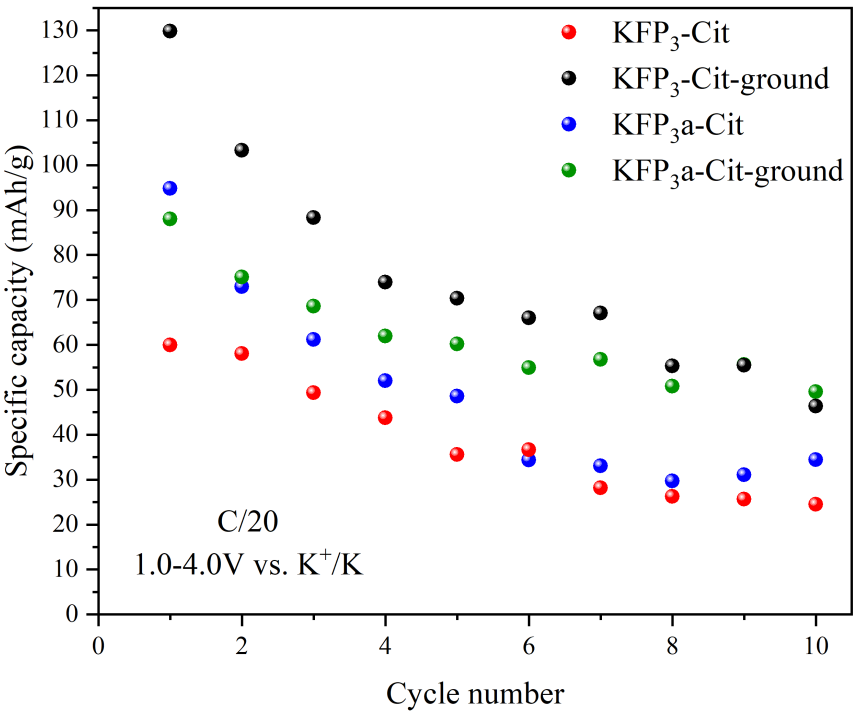

Figure V-16: Evolution of the discharge capacity with cycle number of KFP_3-cit and KFP_3a-cit materials before and after grinding at C/20 in the window voltage of 1.0-4.0 V vs. K^+/K.

3.3. Influence of the iron precursor on the synthesis and electrochemical performance of KFP_3 material.

To enhance the capacity and avoid the capacity fading observed in the last section, another strategy has been developed. New iron precursors have been used to form the solution of precursor before the spray drying step. We have tested 2 new precursors: iron(III) acetylacetonate and iron (III) nitrate with the same synthesis process as before. In addition, the influence of complexing agents on the synthesis

is studied. All the spray-dried materials were calcinated at 600°C for 10 h in air. XRD patterns of the different obtained materials are presented in Figure V-17.

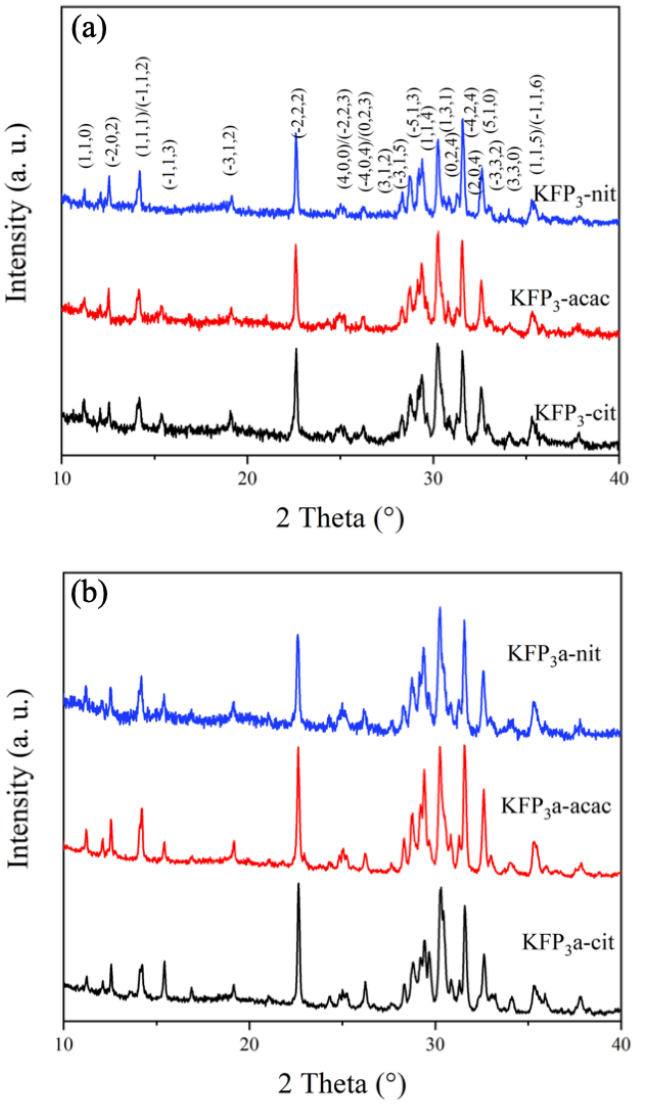

Figure V-17: XRD patterns of KFP_3 with different iron precursors (a) without and (b) with complexing agents.

As shown in Figure V-17, all of the obtained powders of KFP_3-cit, KFP_3-acac (with iron(III) acetylacetonate) and KFP_3-nit (with iron (III) nitrate) contain the

desired $K_3Fe_2(PO_4)_3$ phase as the main phase with the diffraction pattern corresponds to this material. This result proves the robustness of the synthesis method. In addition, the crystallite size calculated by the Scherrer formula reveals a similar value for all the samples which is around 66 nm based on the isolate (-2,2,2) peak. No significant difference is found between the samples with and without complexing agents, but the crystallite size is slightly higher for the KFP_3a sample with a mean value of 70 nm. The morphology of the obtained materials (Figure V-18) are investigated by SEM. After spray drying, the particles are spherical and have an average particle size of 5 µm, similar to the results with other iron precursors. KFP_3-nit seems to have slightly lower particle sizes, especially with the addition of complexing agents. KFP_3-acac has a more peculiar morphology, the obtained spheres seem to be an agglomeration of smaller particles. This particular shape is not conserved after the calcination step as for the citrate-based KFP_3 material, the spherical morphology of the particles is completely lost after calcination. Large agglomerates are formed, probably due to a partial melting during the calcination step. The only material with different morphology is the KFP_3-acac, in this case, we do not observe large agglomerated and the morphology is not spherical. The decomposition of the precursors leads to the formation of small irregular particles and some broken spheres are still visible. These results imply that a grinding step will probably be necessary to obtain good electrochemical performance. As for the KFP_3-cit sample, a grinding step is performed in anhydrous isopropanol for 90 min. The particle size distribution is presented in Figure V-19a. The obtained results are comparable to the obtained result from the KFP_3-cit sample. Before the grinding step, particles have a large and broad size distribution. KFP_3-nit has a mean particle size of 90 µm and KFP_3-acac has a mean particle size of 15 µm. These results are consistent with the observations made in SEM images (Figure V-18). After the grinding step, the KFP_3-nit sample exhibits the main peaks for size distribution which are centered around 200 nm and 1.5 µm, and in case of the KFP_3-acac sample, the mean diameter is 200 nm. The same results are obtained with addition

of complexing agents. This reduction of size should have an important influence on the specific surface area. To confirm this, specific surface area was measured by BET (Figure V-19b). First, as expected the surface area of the materials before grinding are low and all materials have a specific surface area below 4 m^2/g, and KFP_3-Nit has the lowest surface area with 0.39 m^2/g. This result is explained by both the larger particle size of the sample but also by the apparent density of the different materials. Indeed, only dense particles are observed by SEM. After grinding, the surface area is greatly enhanced with values from 12 to 20 m^2/g. The highest surface area is obtained for KFP_3-Acac material with a value of 20.5 m^2/g. This result is related to the reduction of particle size in the powder. Citrate-based KFP_3 has a slightly lower surface area of 15 m^2/g. The KFP_3-a-Nit material has the lowest surface area among the samples with 12.8 m^2/g, however, this specific surface area is still almost 10 times higher compared to before grinding. A SEM analysis (Figure V-20 a and c) confirms the great reduction of size after grinding. Additionally, the electrodes prepared with the powders before and after grinding are compared. No more agglomerates are visible after grinding, and the homogeneity of the obtained (electrode film see Figure V-20d) is greatly enhanced. Before grinding, the particle of the phosphate compounds is clearly distinguished in the electrochemical film which is no more the case after grinding (Figure V-20b and 20d)

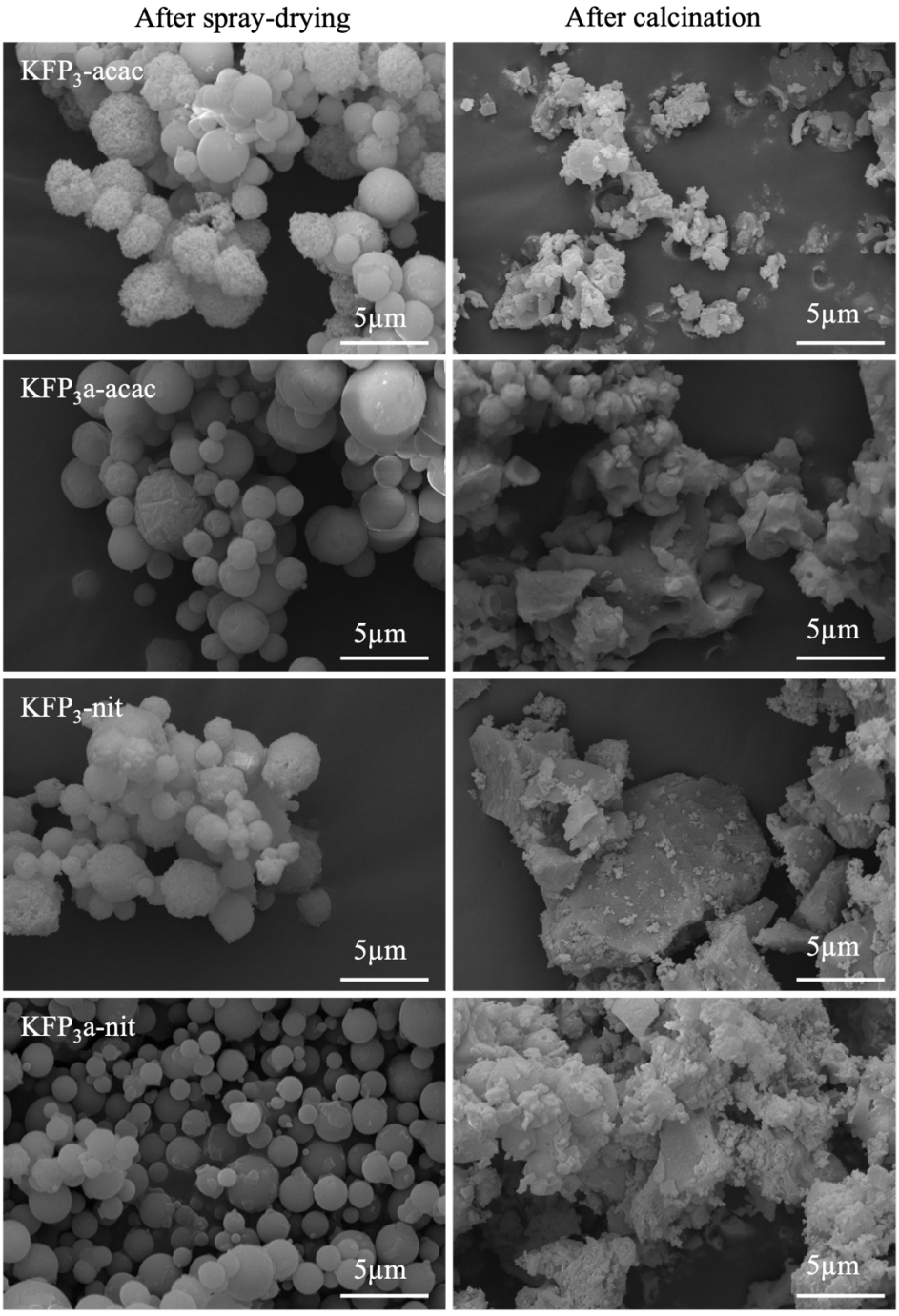

Figure V-18: SEM micrographs of KFP_3-acac, KFP_3a-acac, KFP_3-nit, and KFP_3a-nit materials obtained after spray drying and calcination.

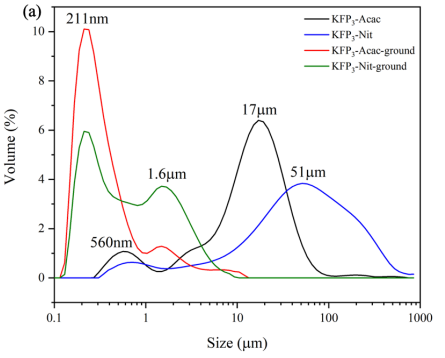

(b) Samples	Specific surface area after calcination (m^2/g)	Specific surface area after grinding (m^2/g)
KFP3-Cit	1.89	15.79
KFP3-a-Cit	3.72	15.82
KFP3-Acac	2.06	20.49
KFP3-a-Acac	1.80	17.51
KFP3-Nit	0.39	19.41
KFP3-a-Nit	1.38	12.83

Figure V-19: (a) Particle size distribution of the KFP_3-acac and KFP_3-nit materials before and after grinding step. (b) Specific surface area of the KFP_3-cit, KFP_3-acac and KFP_3-nit materials before and after grinding process.

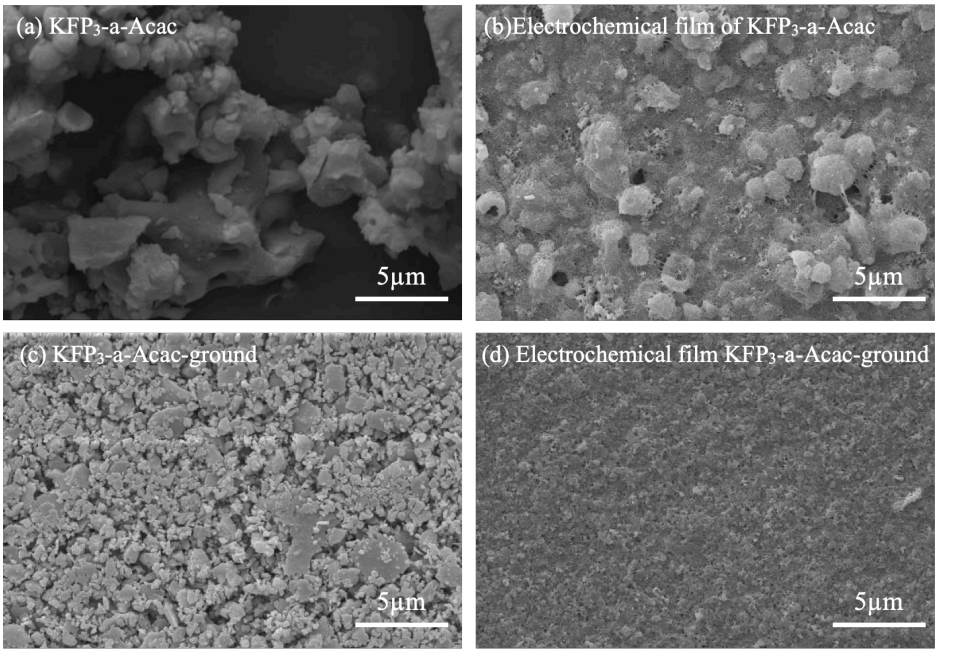

Figure V-20: SEM micrographs of KFP_3-a-Acac powders and their corresponding electrodes before (a,b) and after grinding (c,d).

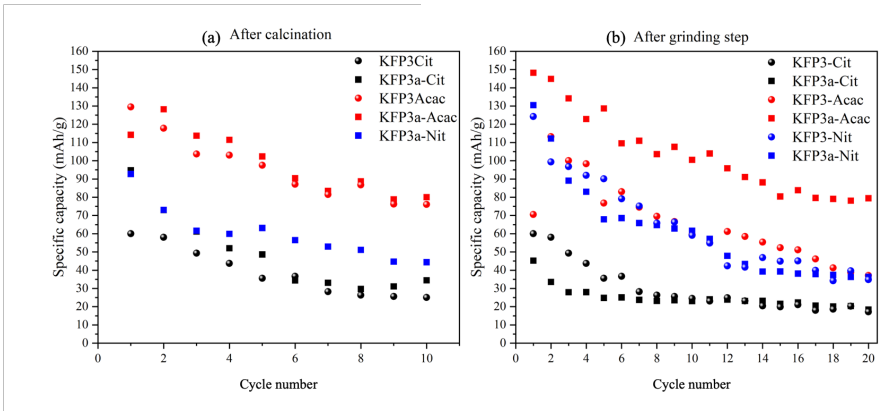

Figure V-21: Evolution of the capacity over the number of cycles for KFP_3's materials with different iron precursors (a) after calcination and (b) after grinding.

The influence of the precursor types on electrochemical performance was also studied. The evolution of the discharge capacity with cycle number of different prepared materials after calcination and after grinding is presented in Figure V-21a and Figure V-21b, respectively. The KFP_3-nit sample presented poor performance. which could be related to its huge particle size and low surface area; thus, it is not presented before grinding. Despite that, KFP_3a-Nit presents better performance compared to KFP_3a-cit and has a first discharge capacity of 95 mAh/g. However, like KFP_3a-cit a significant capacity fading behavior is observed after the first 10 cycles for KFP_3a-Nit, and then the capacity stabilizes at around 45 mAh/g. For the KFP_3-acac, both with and without complexing agents addition, improved performance with higher initial discharge capacity of 130 mAh/g was observed. KFP_3-acac material presents the best capacity among all other electrode materials. Although the issue of capacity fading is not resolved, but the obtained discharge capacity is still about 80 mAh/g before grinding for KFP_3-acac which represents about 77% of the theoretical capacity. There is no significant difference after the addition of complexing agents. Figure V-21b shows the same electrochemical test but for materials after the grinding step. The grinding step influences the specific capacity of the materials. Looking at the

capacity values after 10 cycles for the nitrate-based and acetylacetonate-based materials, the obtained capacity is higher than before grinding except for the KFP_3-Acac sample (without complexing agents) that has similar performance to the nitrate compounds. Despite this improvement, the capacity still fades quite rapidly to about 40mAh/g after 20 cycles. Regarding the KFP_3a-Acac materials, the conclusions are quite different. The initial discharge capacity is 145 mAh/g meaning that some side reactions occur during the first cycle. This is also confirmed by the first charge capacity which is more than 500 mAh/g. Despite this huge irreversibility in the first cycle, the capacity seems to stabilize after a few cycles to about 85 mAh/g which still represents 82% of the theoretical capacity and makes it the highest obtained capacity for this material.

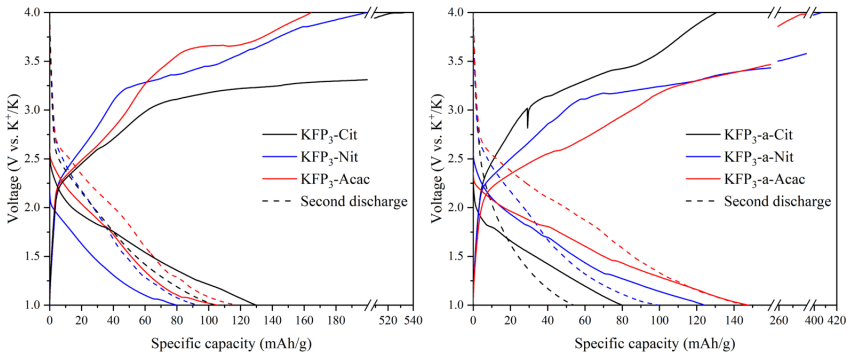

Figure V-22: Charge/discharge curves of the first cycle of (a) KFP_3 and (b) KFP_3a materials prepared by spray-drying with different iron precursors (nitrate in blue, citrate in black, acetylacetonate in red) after calcination and grinding step, cycled at C/20 rates (1.0-4.0 V vs. K^+/K) at room temperature. The dotted line presents the second discharge and the full line represents the first cycle of each sample.

Figure V-22a and b present the charge/discharge curves of the KFP_3 and KFP_3a materials after grinding. The full line represents the first cycle. As the initial oxidation state of the iron is +3, we first start with a discharge process to insert more potassium inside the structure which leads to the reduction of the iron.

The KFP_3 materials without acid all present a first discharge without any well-defined plateau. The insertion of the potassium ions seems to be continuous and could be explained by a solid solution mechanism. Regarding the first charge, the oxidation phenomenon begins around 2.5 V which is consistent with the cyclic voltammetry analysis presented in the Figure V-12a. All of the materials present a higher charge capacity than the first discharge capacity, meaning that there are side reactions that can occur at high voltage such as electrolyte degradation. This phenomenon is much more pronounced for the citrate-based materials where an initial charge capacity of 530 mAh/g is obtained. The KFP_3-acac seems to have lower irreversibility than other materials. The nitrate-based material is in between with an initial charge capacity two times higher than its initial discharge. The second discharge of the material leads to slightly higher capacity except for the citrate-based materials, this can be linked to the huge irreversibility of the first charge.

Regarding the materials with complexing agent addition, the same phenomena are occurring except that the discharge curve is flatter. The same phenomenon in the charge curve around 3.25 V is observed and it is now the nitrate sample that shows the highest irreversibility. The second discharge of the KFP_3a-Acac materials shows the best reproducibility compared to the first discharge. This can explain the better capacity retention of this material compared to the others presented in Figure V-21.

To avoid the presence of carbon in our synthesis process, another approach has been explored using this time $Fe(PO_4)$ and K_3PO_4 in a 2/1 ratio to respect the stoichiometric ratios. The same protocol for spray drying and calcination has been performed. The addition of CNT has also been performed and calcination under argon leads to the same problem as mentioned before. The result of the calcination in the air is presented in Figure V-23.

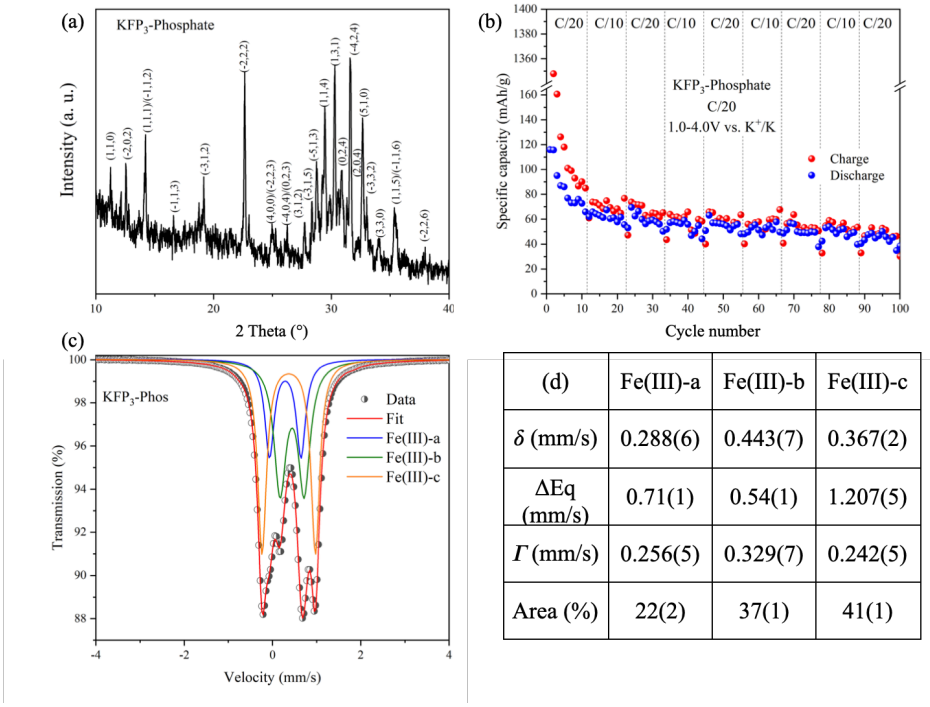

(d)	Fe(III)-a	Fe(III)-b	Fe(III)-c
δ (mm/s)	0.288(6)	0.443(7)	0.367(2)
ΔEq (mm/s)	0.71(1)	0.54(1)	1.207(5)
Γ (mm/s)	0.256(5)	0.329(7)	0.242(5)
Area (%)	22(2)	37(1)	41(1)

Figure V-23: (a) XRD diffractograms of the KFP_3-phosp materials after calcination at 600°C 10 h. (b) Evolution of the capacity over the number of cycles for KFP_3-phosp materials in K-ion half-cell. (c) ^{57}Fe Mössbauer spectrum of the KFP_3-phosp materials after calcination at 600°C for 10 h in air. (d)Associated ^{57}Fe Mössbauer hyperfine parameters for KFP_3-phosp.

All the peaks of the XRD diffractograms are attributed to the KFP_3 materials. The background is relatively high and the peak intensity is quite low meaning that the material is not completely crystallized and that amorphous contributions can also be present. To further analyze KFP_3-Phosp, ^{57}Fe Mössbauer spectroscopy analysis was performed and the obtained spectrum and associated fitted parameters are summarized in Figure V-23c,d. The spectrum has a similar profile to the previously obtained spectrum with two asymmetric doublets without any magnetic impurities. A good fit has been obtained with three components all with an isomer shift corresponding to high spin Fe(III) in octahedral site.

The quadrupole splitting is slightly higher than in KFP_3-cit materials showing a higher distortion of the local environment of the iron.

For the electrochemical performance investigations of the material a rate capability test has been performed and the result is presented in Figure V-23b. Significant irreversibility is observed at the first charge with over 1350 mAh/g. We currently have no other hypothesis for this phenomenon except that a formation cycle is necessary to allow the insertion and extraction of the potassium ions inside the materials and that this formation cycle consumes a huge amount of energy maybe due to a degradation of the electrolyte. The initial discharge capacity is 120 mAh/g at C/20. The loss of the capacity is still observed after 10 cycles with a discharge capacity of 74 mAh/g. This capacity decay can also be related to intrinsic properties of the materials, including its relatively low conductivity of 3 x 10^{-7} S/cm to 10^{-5} S/cm (from 573K to 673K) [1]. The change in cycling rate from C/20 to C/10 doesn't seem to have an impact on the obtained capacity. After 100 cycles the discharge capacity is still around 45 mAh/g which proves that this material is promising for future KIBs stationary applications when the problem of capacity fade and initial irreversibility will be solved. This confirms that we still face a challenging perspective to make a composite with carbon materials at the spray drying step.

4. Conclusions

The $K_3Fe(PO_4)_2$ has been successfully synthesized by a simple spray drying method. The pure and well crystalized compounds with and without acid addition are obtained after a calcination step at 600°C for 10 h in air. The two materials have been successfully tested as active cathode materials in K-ions half-cells for the first time in this work. KFP_2a with the addition of complexing agents shows the best discharge capacity of 70 mAh/g but the capacity rapidly decreased to 40 mAh/g after a few cycles. To enhance the performance a carbon nanotube addition has been tried, however, the crystalline and pure materials were not obtained under argon atmosphere.

$K_3Fe_2(PO_4)_3$ pure material has also been obtained by spray drying after calcination in air. Despite many trials, none of the materials can be obtained under argon atmosphere making the addition of *in situ* CNT very challenging and not feasible in the tested conditions. Different strategies have been explored to enhance the capacity of the different materials. Among them, the grinding step after calcination and addition of CNT during the grinding have led to an average capacity of 60 mAh/g. To further enhance the discharge capacity, four different iron precursors have been used in the synthesis (citrate, nitrate, acetylacetonate, and phosphate). For all materials, important irreversibility is observed during the first cycles. KFP_3a-Acac after grinding presents the best discharge capacity after 20 cycles with 80 mAh/g representing 77% of the theoretical capacity. The KFP_3-phosphate materials that removed all carbon sources from the synthesis method also led to the same phase formation problem under argon. However, the synthesis under air and with the addition of CNT during the grinding step has enabled us to prepare materials with long cycling performance (100 cycles) with an average discharge capacity of 52 mAh/g at the 95^{th} cycle. This preliminary study evidenced the interest in iron-based phosphate for K-ion batteries and shows promising performance. Further tests are still needed to enhance the

electrochemical performance of these materials and the most promising one is to successfully synthesize a composite material with carbon.

5. References:

[1] M. PINTARD-SCREPEL, F. D'Yvoire, Structure de l'Orthophosphate de Difer(III) et de Tripotassium, K3Fe2(PO4) a PAR, Acta Crystallographica Section C. 39 (1983) 9–12.

[2] B. Lajmi, M. Hidouri, A.K. ben Hammouda, A. Wattiaux, L. Fournés, J. Darriet, M. ben Amara, Synthesis and structural study of a new iron phosphate K3Fe(PO4)2, Materials Chemistry and Physics. 113 (2009) 372–375. https://doi.org/10.1016/j.matchemphys.2008.07.064.

[3] B. Lajmi, M. Hidouri, M. ben Amara, The iron phosphate K3Fe5(PO4)6, Acta Crystallographica Section C: Crystal Structure Communications. 58 (2002) 156–158. https://doi.org/10.1107/S0108270102015251.

[4] B. Lajmi, M. Hidouri, A. Wattiaux, L. Fournés, J. Darriet, M. ben Amara, Crystal structure, Mössbauer spectroscopy, and magnetic properties of a new potassium iron oxyphosphate K11Fe15(PO 4)18O related to the Langbeinite-like compounds, Journal of Alloys and Compounds. 361 (2003) 77–83. https://doi.org/10.1016/S0925-8388(03)00412-2.

[5] S. Patoux, C. Wurm, M. Morcrette, G. Rousse, C. Masquelier, A comparative structural and electrochemical study of monoclinic Li3Fe2(PO4)3 and Li3V2(PO4)3, Journal of Power Sources. 119–121 (2003) 278–284. https://doi.org/10.1016/S0378-7753(03)00150-2.

[6] Y. Cao, Y. Liu, D. Zhao, X. Xia, L. Zhang, J. Zhang, H. Yang, Y. Xia, Highly Stable Na3Fe2(PO4)3@Hard Carbon Sodium-Ion Full Cell for Low-Cost Energy Storage, ACS Sustainable Chemistry and Engineering. 8 (2020) 1380–1387. https://doi.org/10.1021/acssuschemeng.9b05098.

[7] Y. Liu, Y. Zhou, J. Zhang, Y. Xia, T. Chen, S. Zhang, Monoclinic phase Na3Fe2(PO4)3: Synthesis, structure, and electrochemical performance as cathode material in sodium-ion batteries, ACS Sustainable Chemistry and Engineering. 5 (2017) 1306–1314. https://doi.org/10.1021/acssuschemeng.6b01536.

[8] R. Rajagopalan, B. Chen, Z. Zhang, X.L. Wu, Y. Du, Y. Huang, B. Li, Y. Zong, J. Wang, G.H. Nam, M. Sindoro, S.X. Dou, H.K. Liu, H. Zhang, Improved Reversibility of Fe3+/Fe4+ Redox Couple in Sodium Super Ion Conductor Type Na3Fe2(PO4)3 for Sodium-Ion Batteries, Advanced Materials. 29 (2017). https://doi.org/10.1002/adma.201605694.

[9] J. Kim, G. Yoon, H. Kim, Y.U. Park, K. Kang, Na3V(PO4)2: A New Layered-Type Cathode Material with High Water Stability and Power Capability for Na-Ion Batteries, Chemistry of Materials. 30 (2018) 3683–3689. https://doi.org/10.1021/acs.chemmater.8b00458.

[10] A.S. Andersson, B. Kalska, P. Jonsson, L. Haggstrom, P. Nordblad, R. Tellgren, J.O. Thomas, The magnetic structure and properties of rhombohedral Li3Fe2(PO4)3, Journal of Materials Chemistry. 10 (2000) 2542–2547. https://doi.org/10.1039/b002218g.

[11] D. Beltran-porter, R. Olazcuaga, L. Fournès, F. Ménil, F.G. Le, Etude magnétique et par résonance Mössbauer de l ' orthophosphate Na 3Fe2 (PO4) 3 α et d ' une phase vitreuse dérivée, Revue de Physique Appliquée, Société Française de Physique. 15(6) (1980) 1155–1160.

[12] J. Bodart, N. Eshraghi, T. Carabin, B. Vertruyen, R. Cloots, F. Boschini, A. Mahmoud, Spray-dried K3V(PO4)2/C composites as novel cathode materials for K-ion batteries with superior electrochemical performance, Journal of Power Sources. 480 (2020). https://doi.org/10.1016/j.jpowsour.2020.229057.

Chapter VI

General Conclusions and Outlooks for Future Works

Global warming casts an apocalyptic shadow over our future. Facing these serious problems has become now the main emergency and priority for our generation. The solutions exist and are already in place to begin and ensure the energy transition. However, problems persist and in particular the storage of the new renewable energies and their mobility. Batteries are among the most advanced and promising solutions in tackling global warming and energy security. They have a wide range of applications, from mobile phones to mass storage, including electric vehicles, there is no shortage of applications. However, current commercial batteries are mainly based on the use of critical raw materials elements (CRM) such as lithium or cobalt.

In this work, we specifically focus on the development of the next generation cathode materials for Na-ion and K-ion batteries by spray-drying process, and the replacement of the CRM with abundant, cheap and eco-friendly elements and compounds such as phosphate and iron. The microstructure and the chemical composition of the electrode materials have a great impact on the electrochemical performance. Spray-drying as a synthesis and shaping method allows us to control both the morphology and composition of the desired materials at a pilot-scale in GREEnMat Laboratory. This work also proves its high versatility and its high ability to control and tune the electrode material morphology and composition.

1. Optimization of the synthesis of Na_2FePO_4F/CNT material and investigation of its electrochemical mechanism in Na-ion and K-ion batteries

In the first part of this work, we were interested in the investigation and improvement of the electrochemical performance of the Na_2FePO_4F as cathode for Na-ion batteries (NIB) and K-ion batteries (KIB). We successfully optimized its synthesis by the spray-drying process. By playing on the nozzle type, the particle size was reduced from 10 µm to 3 µm. Despite this reduction in particle size, the electronic conductivity of this phosphate-based materials was still insufficient to achieve decent capacities. Composite synthesis was made by *in situ* addition of 5, 10 or 15wt% of CNT in the precursors' solution before the spray-drying step. However, the addition of this carbon leads to the formation of metallic iron and iron carbide during the heat treatment at 600°C for 2 h under argon as clearly evidenced by ^{57}Fe Mössbauer spectroscopy analysis. The synthesis protocol was then investigated deeply to avoid the Fe^0 formation. The first hypothesis behind the metallic iron Fe^0 formation was that the oxidized iron during the spray-drying step does not lead to the formation of the desired phase and then was more susceptible to reduction during the annealing step. A fully controlled atmosphere synthesis process was tested using an ATEX spray-dryer under argon (less than 50 ppm of O_2) for two material compositions: without CNT and with 15wt% of CNT. However, the metallic iron in the composite material with CNT is still detected. The control of the Fe^{3+}/Fe^{2+} ratio in the precursors seems to be the key parameter to obtaining the desired phase without impurities. Indeed, a low Fe^{3+}/Fe^{2+} ratio after the spray-drying step leads to a huge amount of Fe^0 and a high Fe^{3+}/Fe^{2+} ratio leads to oxidation of the NFPF or in the worst case to the presence of Fe_2O_3 impurity. The pure phase was successfully obtained by

using degassed water during the acidic attack step and by spray-drying with hot airflow.

The optimized NFPF/CNT material delivers excellent specific capacity of 123 mAh/g at C/15 in the voltage window 2.2-4.5 V *vs.* Na^+/Na (99% of the theoretical capacity) as cathode in Na-ion batteries. The discharge capacity retention was 91% after 100 cycles. This shows that the grinding can be avoided by combining the addition of CNT and the reduction of the particle size induced by the use of a bifluid nozzle even if particles of about 3 µm are obtained due to a homogeneous distribution of carbon inside and at the surface of the NFPF particles. Despite this excellent performance, the coulombic efficiency was quite low of only 90%. The reduction of the potential window from 2.2-4.5 V to 2.0-4.2 V leads to a great enhancement of the coulombic efficiency to 99% with an excellent discharge capacity of 123 mAh/g.

The excellent performance of NFPF/CNT material in Na-ion batteries prompted us to test it in a K-ion batteries. For the first time, NFPF/CNT material was used as cathode materials in K-ion batteries. The first performed tests were carried out by simply replacing the metallic sodium with metallic potassium and the associated electrolyte in the half-cell. A discharge capacity of 80 mAh/g was obtained at C/15 in the voltage window 2.0-4.2 V *vs.* Na^+/Na which represents 71% of the theoretical capacity of $NaKFePO_4F$ with 0.8 M KPF_6 in EC:PC as the best-tested electrolyte. To further enhance the obtained capacity, a pre-charged Na_1FePO_4F material in a Na half-cell was tested in K half-cell. This leads to better electrochemical performance with a specific capacity of 114 mAh/g at C/15, i.e., 99% of the theoretical capacity. These results highlight the potential of NFPF/CNT prepared by spray-drying as a promising cathode material for both NIBs and KIBs and the robustness of this material.

The electrochemical reaction during charge and discharge processes of NFPF/CNT cathode material in Na-ion and K-ion batteries was deeply investigated using *operando* ^{57}Fe Mössbauer spectroscopy combined with

operando XRD techniques (using Co Kα radiation). The huge quantity of data obtained with these two techniques was treated using chemometric and more specifically Principal Component Analysis and Multivariate Curve Resolution-Alternating Least Square. In Na-ion batteries, a clear double biphasic mechanism was evidenced by both *operando* techniques as follows:

$$Na_2FePO_4F \xleftrightarrow{Dis/charge} Na_{1.5}FePO_4F \xleftrightarrow{Dis/charge} Na_1FePO_4F$$

The three components determined by the chemometrics analysis evidenced a great variation and reversibility of the iron oxidation state upon cycling. Also, the intermediate phase presents a mixed valence of iron between Fe^{2+} and Fe^{3+}. The XRD calculated components were also refined and show in this case a variation of the cell volume upon cycling from 851 $Å^3$ for the pristine material to 821 $Å^3$ for the end of charge electrode material, passing by the intermediate state with a cell volume of 832 $Å^3$. Both the pristine and EOC materials crystallize in Pbcn space group, however, the intermediate phase crystallizes in a primitive monoclinic $P2_1/c$ space group. This allows us to refute the idea of a "quasi-solid-solution" mechanism reported in the literature. In K-ion batteries, the *operando* ^{57}Fe Mössbauer spectroscopy analysis shows that the oxidation state of the iron follows a variation upon cycling. The PCA and MCR-ALS analysis only found two spectral components, one for the pristine and one for the EOC component. We were expecting four components for this material: the same three found in the case of cycling NFPF/CNT in NIB and one corresponding to the new $NaKFePO_4F$. Unfortunately, the XRD data have low resolution to evidence the mechanism. Indeed, the insertion of potassium to replace sodium in NFPF materials leads to the amorphization of the material during the charge process. Despite that, the pristine and EOC components are similar to the NIB mechanism and some clear differences have been evidenced, in particular the lower reversibility that is observed in the case of K-ion batteries, but also the absence of an intermediate phase during the first potassiation.

2. Development of new phosphate-based cathode materials for K-ions batteries.

In the second part of this work, three new cathode materials for KIB were developed: $K_3V(PO_4)_2$, $K_3Fe(PO_4)_2$ and $K_3Fe_2(PO_4)_3$. None of these materials were previously reported as cathode material in K-ion batteries. Also, these three materials were previously synthesized using a complex method or not easily up-scalable method. Here, we reported an easy and rapid synthesis method of the three materials using the spray-drying process.

$K_3V(PO_4)_2$ has been successfully obtained using spray-drying after annealing at 650°C for 8 h under an argon atmosphere. The cycling performance of this material was low due to the inherent low electronic conductivity of phosphate-based material. To improve the conductivity, we performed the synthesis of the three composite materials with 20wt% of CNT, 20% of GO, and a mix of 10wt% of CNT+10wt% of GO. The influence of the carbon addition was analyzed, and the results show a remarkable improvement in the electrochemical properties. Indeed, the obtained discharge capacity for the carbon-free material was only 25 mAh/g and the obtained capacity with CNT, GO or CNT+GO are around 60, 80 and 90 mAh/g respectively at C/40 in the voltage window of 2.0-4.5 V *vs*. K^+/K. Furthermore, the electrochemical impedance spectroscopy shows a great decrease of the charge-transfer resistance passing from 187 Ω in the carbon free material to 92 Ω for the CNT composite material. Despite this great enhancement, the increase of cycling-rate directly leads to a huge reduction of the obtained capacity. To solve this problem, a grinding step was performed and the ground KVP, KVP/20rGO, KVP/20CNT and KVP/10CNT+10rGO delivered reversible capacities of around 60, 50, 101 and 60 mAh/g, respectively (at C/40 in the voltage window of 2.0-4.5 V *vs*. K^+/K). KVP and KVP/20CNT exhibited higher discharge capacities after grinding thanks to the decrease of their particle size and the increase of the specific surface area. KVP/20CNT has a surface area

of 127 m2/g after grinding and only 36 m2/g before grinding with a decrease in particle size from 7 µm to 0.1 µm. The grinding of composite with graphene oxide leads to lower capacity retention and higher charge transfer resistance which is attributed to the destruction of the reduced-GO sheet that surrounds KVP particles. Finally, KVP/20CNT demonstrated excellent rate capacity which confirms its good electrochemical properties as cathode material in KIB.

In order to fulfill our objective of making low-CRM material, the use of vanadium has to be avoided. Two new materials were then developed as cathodes for KIB based on iron instead of vanadium. $K_3Fe(PO_4)_2$ and $K_3Fe_2(PO_4)_3$ have been successfully obtained using the spray-drying process followed by a heat treatment of 600°C under air, and both materials have been successfully used as active cathode materials in KIB. KFP_2 with the addition of complexing agents shows the best discharge capacity of 70 mAh/g but the capacity rapidly decays to 40 mAh/g after a few cycles. To enhance the performance a carbon nanotube addition has been tested, however the crystalline and pure material was not obtained under argon atmosphere.

KFP_3 material also requires calcination under oxygen atmosphere to obtain pure and crystalline phase. Other enhancement strategies have been tried and for example the change of iron precursor in the solution before spray-drying. Four different precursors were tested and compared: iron citrate, iron acetylacetonate, iron nitrate and iron phosphate. All investigated materials suffer from important irreversibility during the first cycles. Acac-based KFP_3 exhibits a more spongious morphology than the other electrodes and delivered the highest discharge capacity of 80 mAh/g after 20 cycles C/40 in the voltage window of 2.0-4.5 V *vs.* K^+/K. To remove all the carbon inside the precursors' solution in the hope of forming the KFP_3 phase under argon, a new synthesis using iron phosphate and potassium phosphate was investigated, however the heat treatment under argon does not lead to the formation of the desired phase. This phosphate-based KFP_3 material calcined under air still delivers a discharge capacity of 52 mAh/g after 100 cycles.

This preliminary study evidenced the interest of KFP_2 and KFP_3 as cathode materials in K-ion batteries.

3. Outlooks for Future Works

This PhD thesis is rich in perspectives and more efforts are still required to improve the electrochemical performance or to understand the formation and electrochemical mechanisms of the electrode materials investigated in this work. Here we present a non-exhaustive list of the possible strategies to enhance or complete the obtained results:

3.1. General outlooks

The first and main outlook for all the materials developed in this thesis is to test these materials in full cell configuration. For the K-ion materials, hard carbon or graphite can be used as the counter electrode. We have already performed some preliminary tests to use commercial graphite in KIB, the capacity obtained are still quite low and some optimization still need to be done (Figure VI-1).

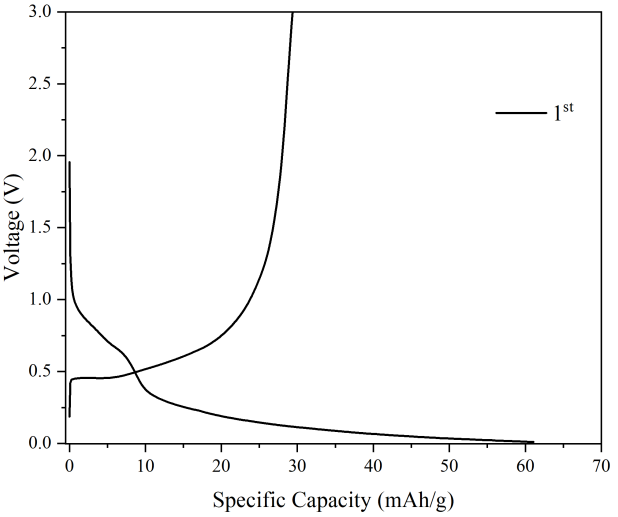

Figure VI-1: First charge and discharge curve of graphite in K-ion half-cell using KPF_6 0.8M in EC:DMC electrolyte.

For NFPF/CNT material hard carbon can be used as anode material. Another possibility is to use an alloying anode material such as Sb which has

already been reported as advanced anode material for NIB batteries[1,2]. The Sb active anode material was given by ICGM of Montpellier that has made plenty of works on it as anode material for NIB [1,3–6]. This approach has been investigated and some preliminary tests have been performed in pouch cell configuration. Figure VI-2a, b presents the evolution of the charge and discharge capacities with cycle number and their corresponding voltage profiles. Figure VI-2c shows a photo of the tested pouch cell in this work. Promising results have been obtained. Despite an important irreversibility during the first cycles which is probably due to the formation of the SEI layer, a good initial discharge capacity of about 95 mAh/g was obtained.

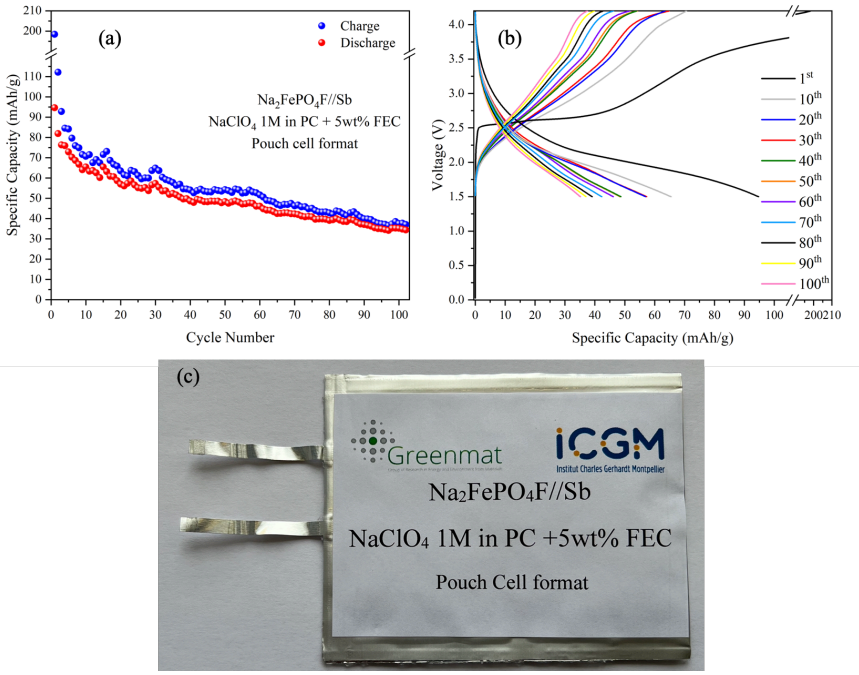

Figure VI-2: Charge and Discharge capacities along cycles of Na_2FePO_4F vs. Sb materials in pouch cell configuration. (b) Associated charge and discharge profiles. (c) Photography of a typical pouch cell assembly used for this experiment.

Another strategy regarding all the material is related to the reduction of the amount of *in situ* added carbon that leads to enhancement of the electrochemical performance. Indeed, the less added carbon, the more the mass of active material and the more energy density can be achieved.

3.2. More specific outlooks

- For NFPF materials, some complementary tests regarding the influence of the carbon addition on the presence of iron should be carried out to fully understand this phenomenon. Also, some improvement on the carbon addition content should be performed to further improve the capacity obtained at high cycling rate and the capacity retention for the long cycle term. Regarding its use in K-ion batteries, some long cycling tests should be performed to study the stability and life cycle of this material.
- Regarding the electrochemical mechanism analysis during cycling of this material in KIB, a pre-charge to remove the Na of the materials prior to the analysis should be performed in order to enhance the performance. Also some more powerful techniques should be used to better follow the evolution of the structure of the material such as performing the *operando* synchrotron based XRD measurements. Also regarding the *operando* ^{57}Fe Mössbauer spectroscopy, a longer acquisition time should be implemented to obtain better quality of dataset.
- For KVP materials, the capacity can be further enhanced to reach the theoretical capacity of this material of 150 mAh/g. Indeed, the best obtained capacity in this work is about 101 mAh/g meaning that there is still a lot of effort that is required to enhance the achieved electrochemical performance. The strategies can rely on a better crystallinity of the material after grinding but also to investigate new electrolyte compositions as it can have a huge influence on the obtained performance. Also, cycling these materials against carbon (either graphite or hard carbon) can help to obtain better performance due to the high reactivity of the potassium as anode material.

- For KFP_2, and KFP_3 materials, the first and main outlook is to succeed in forming a composite material, by *in situ* or *ex situ* addition of the carbon, to enhance the electronic conductivity and the electrochemical performance.
- Regarding KFP_2 itself, the low theoretical capacity of this material has led us to focus on KFP_3 material, but the obtained capacity is finally in the same range for both materials and the development with new precursors etc., should be done for KFP_2 material also.
- For KVP, KFP_2, and KFP_3 materials, the intrinsic properties of the materials should also be investigated, such as their ionic conductivity. Also, post-Mortem analyses should be performed to deeply investigate the capacity decay causes. Also, playing on the materials' porosities could improve the ionic conductivity, as shown by Orikasa et al.,.[7]
- Finally, the electrochemical mechanism of the new three cathode materials KVP, KFP_2 and KFP_3 should be investigated to understand their electrochemical mechanisms as for NFPF with other techniques such as solid-state nuclear magnetic resonance. This can help us understand the limitation of these materials and maybe how to enhance their performance.

4. References

[1] A. Darwiche, C. Marino, M.T. Sougrati, B. Fraisse, L. Stievano, L. Monconduit, Better cycling performances of bulk sb in na-ion batteries compared to li-ion systems: An unexpected electrochemical mechanism, J Am Chem Soc. 134 (2012) 20805–20811. https://doi.org/10.1021/ja310347x.

[2] B. Pandit, M.T. Sougrati, B. Fraisse, L. Monconduit, Exploration of a Na3V2(PO4)3/C –Pb full cell Na-ion prototype, Nano Energy. 95 (2022) 107010. https://doi.org/10.1016/j.nanoen.2022.107010.

[3] M. Chamas, A. Mahmoud, J. Tang, M.T. Sougrati, S. Panero, P.E. Lippens, Aging processes in lithiated FeSn2 based negative electrode for li-ion batteries: A new challenge for tin based intermetallic materials, Journal of Physical Chemistry C. 121 (2017) 217–224. https://doi.org/10.1021/acs.jpcc.6b11302.

[4] V. Gabaudan, R. Berthelot, L. Stievano, L. Monconduit, Inside the Alloy Mechanism of Sb and Bi Electrodes for K-Ion Batteries, Journal of Physical Chemistry C. 122 (2018) 18266–18273. https://doi.org/10.1021/acs.jpcc.8b04575.

[5] V. Gabaudan, R. Berthelot, M.T. Sougrati, P.E. Lippens, L. Monconduit, L. Stievano, SnSb: Vs. Sn: Improving the performance of Sn-based anodes for K-ion batteries by synergetic alloying with Sb, Journal of Materials Chemistry A. 7 (2019) 15262–15270. https://doi.org/10.1039/c9ta03760h.

[6] A. Darwiche, F. Murgia, M. Fehse, A. Mahmoud, A. Iadecola, S. Belin, C. la Fontaine, V. Briois, R.P. Hermann, B. Fraisse, R. Berthelot, M.T. Sougrati, L. Monconduit, L. Stievano, Operando X-ray absorption spectroscopy applied to battery materials at ICGM: The challenging case of BiSb's sodiation, Energy Storage Materials. 21 (2019) 1–13. https://doi.org/10.1016/j.ensm.2019.06.027.

[7] Y. Orikasa, Y. Gogyo, H. Yamashige, M. Katayama, K. Chen, T. Mori, K. Yamamoto, T. Masese, Y. Inada, T. Ohta, Z. Siroma, S. Kato, H. Kinoshita, H. Arai, Z. Ogumi, Y. Uchimoto, Ionic conduction in lithium ion battery composite electrode governs cross-sectional reaction distribution, Sci Rep. 6 (2016) 2–7. https://doi.org/10.1038/srep26382.

Appendix A

Preparation of Fe_3O_4@SiO_2 Core-shell particles by spray drying method for the detection of SARS-CoV-2 virus.

Abstract

In this chapter, we briefly present the work that has been carried out to help during the SARS-CoV-2 pandemic. This chapter is presented in the appendix because it represents a large part of my work during my Ph.D. thesis. During the first lockdown in March 2020, we developed a new synthetic technique for the reagents for extracting the RNA of the SARS-CoV-2 virus, which was sorely lacking for effective testing of any symptomatic person. Between March 2020 and December 2021, i.e. 21 months, we provided more than 10,000,000 reagents for carrying out the Reverse Transcription Polymerase Chain Reaction (RT-PCR) test for virus detection. We briefly present the patented synthetic technique, achievement and main results.

1. Introduction

In February 2020, the Covid-19 pandemic finally reached Belgian territory with its first detected case, and a few weeks later, Europe was confined to limit the explosion of cases. Quickly, the various equipment to manage this crisis ran out. Whether it was the masks, the protective suits for caregivers, the protective visors, and finally the detection test kits, equipment shortages were everywhere. The technique used for the detection of SARS-CoV-2 is the Reverse Transcription-Polymerase Chain Reaction commonly called the PCR test. If you have ever experienced a PCR test, an explanation of the different steps of this analysis, and an illustration of the procedure is presented in Figure A -VI-1.

The Covid-19 virus tends to congregate in the nose and throat of an individual, thus a sample is taken from those areas of the body. The sample is subjected to a series of chemical treatments that extract the sample's RNA from other components including proteins and lipids. If the virus is present, its RNA is mixed with the person's genetic material.

A certain enzyme is used to reverse-transcribe the RNA into DNA. Then, scientists incorporate other small DNA probes that complement particular regions of the transcribed viral DNA. These fragments bind to certain regions of the viral DNA if the virus is present in the sample. Some of the additional DNA probes are used to create DNA strands during amplification, while others are used to create label DNA with marker information that is used to identify the virus.

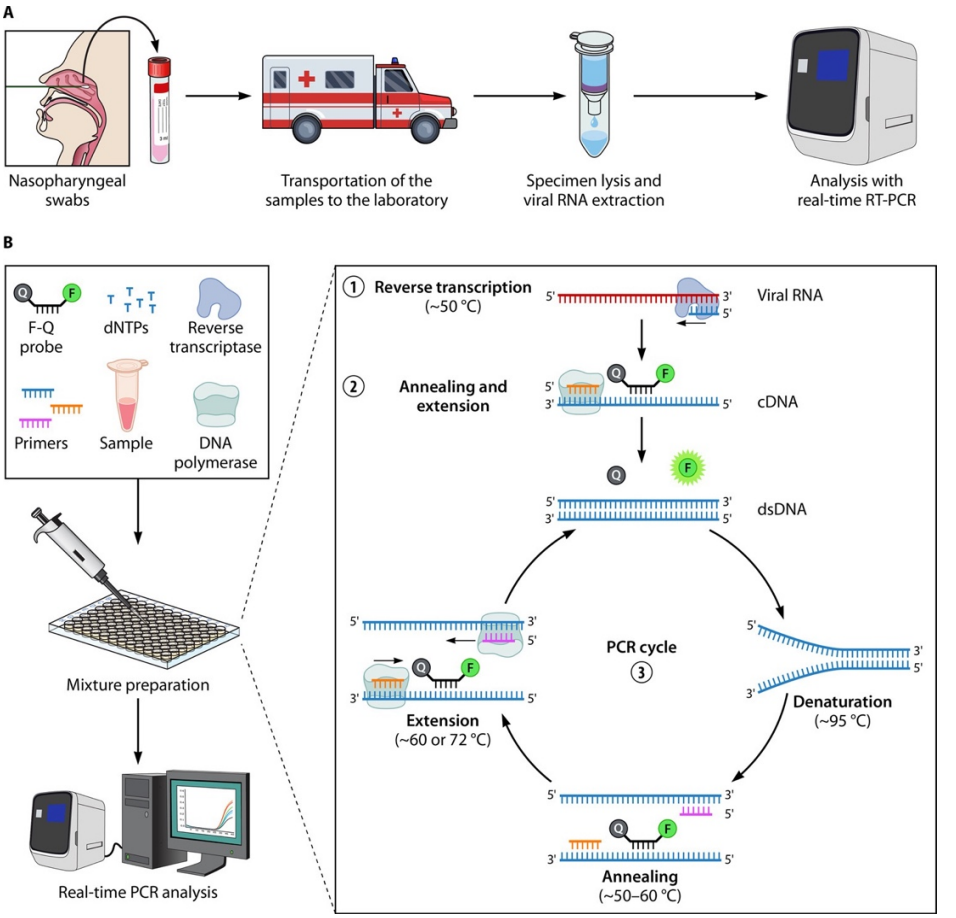

Figure A -VI-1: Real-time-RT-PCR-analysis. Typical steps required for the detection of SARS-CoV-2 reproduced from [1].

The RT-PCR apparatus is filled with the mixture. The device alternately heats and cools the sample to start precise chemical reactions that duplicate the targeted viral DNA segments in fresh, identical copies. To keep duplicating the targeted viral DNA regions, the cycle is constantly repeated. The previous number is doubled with each cycle: two copies become four, four copies become eight, and so forth. By the time a typical real-time RT-PCR setup has completed 35 cycles, each strand of the virus present in the sample has produced approximately 35 billion additional copies of the viral DNA segments.

The marker labels bind to the DNA strands as fresh copies of the viral DNA sections are created, releasing a fluorescent dye that is monitored by the machine's computer and displayed in real-time on the screen. After each cycle, the computer keeps track of the sample's fluorescence levels. Fluorescence above a specific threshold indicates the presence of the virus. To judge the intensity of the infection, researchers also keep track of how many cycles are required to reach this threshold. The fewer cycles required, the more serious the viral infection is.

In this context, we have worked on the critical component for testing which was reagent to extract the RNA from the sample and purified it from other contaminants.

The use of core-shell particles containing Fe_3O_4 as the core for DNA or RNA extraction or purification has received a lot of attention in recent years [2–4]. Fe_3O_4 particles make excellent candidates in biotechnology for RNA extraction from viruses due to their low toxicity and magnetic features. These magnetite particles must, however, be functionalized in this type of application using certain coatings like glass or silica. To generate core-shell particles with regulated surface properties, several synthesis methods have been explored. Colloid silica particles can be prepared using the Stober method: tetraethyl orthosilicate (TEOS) is used as a reagent. Ammonia can be used as a catalyst to hydrolyze and condense TEOS in an alcohol-water system. If this procedure is used with nanometric particles suspended in solution, a silica coating is created on the particles [5–7].

Using this method, core-shell Fe_3O_4 particles covered in SiO_2 can be prepared. However, there are several issues with this wet procedure. First, it calls for using a huge quantity of solvents. Second, depending on the required shell thickness, it takes a long time to react: between 4 and 24 hours. Thirdly, several variables, including reactant concentration, stirring speed, stirring style, and reaction temperature, can have an impact on the process' ability to produce a high-quality coating and prevent particle aggregation. As a result, process control is never easy,

and the process needs to be closely controlled to prevent any variations in the end product. After the reaction, the fresh core-shell particles must also be thoroughly washed with an organic solvent to get rid of the TEOS that hasn't been hydrolyzed and with lots of water to get rid of any excess colloidal silica particles in the suspension and/or TEOS that wasn't used to coat the particles. To prevent oxidation, pure core-shell particles must be dried by lyophilization following the drying stage. Consequently, the wet process is a time and reactant-consuming procedure with many steps. Core-shell particle manufacturing on a pilot scale is not practical. To create magnetic glass particles, Roche Diagnostics described a spray drying procedure in WO 01/37291 A1. However, to produce such particles, a sintering process is required. The document states that the sintering temperature is around 750°C. This energy-intensive procedure prevents the synthesis of significant amount of core-shell particles quickly and effectively.

The objective of our work was to resolve previously described issues. Here, we present a method for preparing core-shell particles without washing, purification, or sintering steps at a pilot scale .

2. Results and discussion:

The developed procedure is summarized in Figure A -I-2. The procedure can be described briefly as follow:

- The first step consists in grinding Fe_3O_4 particles to obtain nanoparticle materials of about 100 nm or less. The magnetite powder is suspended in dry ethanol to perform ball-milling between 60-120 minutes this step is done under an inert atmosphere to prevent the oxidation of the iron. Another possibility that has also been tried is to synthesize the Fe_3O_4 by coprecipitation from iron (II) sulfate and iron (III) chloride by a sodium hydroxide solution. This second approach led to a lower production rate and was therefore set aside in favor of grinding strategy.
- The second step is to suspend the Fe_3O_4 nanoparticles in a solution of SiO_2 precursors. To do this, Fe_3O_4 particles obtained at the first were suspended in isopropanol with an ultrasonic probe. The precursors of SiO_2 are then added to the suspension and thoroughly stir. The amount is fixed to obtain a ratio in the final product of Fe:Si 1:1.16 after spray-drying.
- A hydrolyzing agent is then added, and the solution/suspension is directly injected into the spray dryer.
- The core-shell Fe_3O_4@SiO_2 particles are recovered at the cyclone using special magnet mounting developed for this specific application.

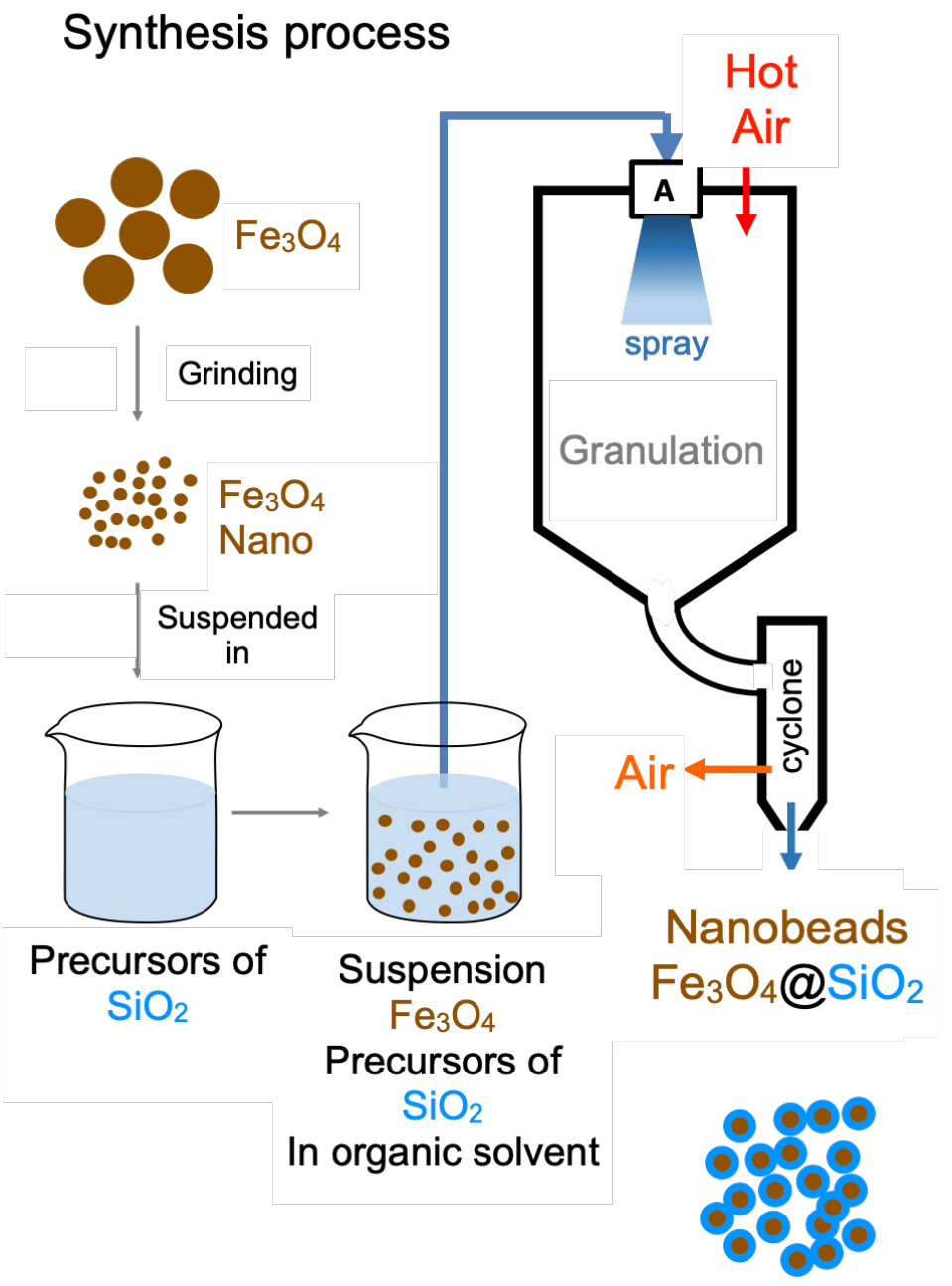

Figure A -I-2: Schematic representation of the synthesis process of Fe_3O_4@SiO_2 nanobeads.

The obtained particles can then be used to extract the RNA from the matrix sample and purify it. Briefly, the nanobeads are suspended in the sample where the virus is deactivated. The RNA of the virus is linked to the nanobeads by hydrogen interactions. The beads are recovered magnetically, and the rest of the sample is dismissed. After careful cleaning of the beads, the RNA strands are unhooked from the nanobeads using elution solvent as in conventional chromatography. The obtained sample can then be used in conventional RT-PCR as explained before.

The purpose of this chapter is not to go into detail into scientific details but to illustrate our work, and to briefly show the developed method and present our contribution in limiting SARS-CoV-2 cases.

Figure A -I-3 shows a macrophotography, TEM and SEM micrographies of the obtained nanobeads.

As we can see the core-shell is well defined on the TEM micrography with the Fe_3O_4 core darker and surrounded by SiO_2 which is slightly transparent. The SEM micrography reveals like a spongious grain of rice with a lot of porosity, which is counter intuitive to what is expected when speaking about beads. This porosity was confirmed by BET measurement and shows a relatively high porosity of more than 50 m^2/g.

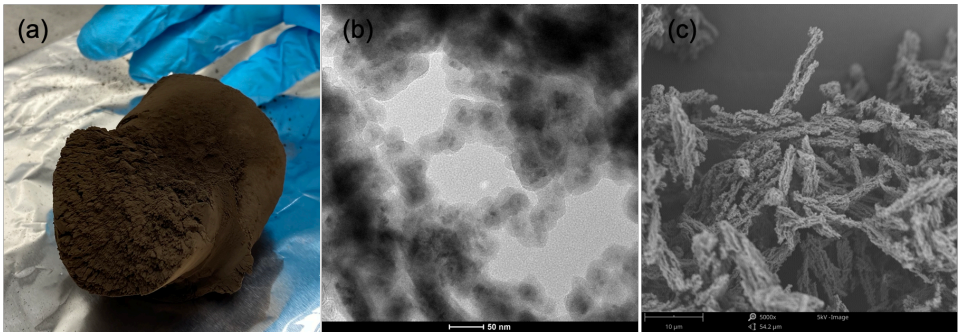

Figure A -I-3: (a) Macrophotography (b) TEM micrography, and (c) SEM micrography of the obtained nanobeads.

2.1. Some numbers

Using this technique, we have been able to develop an independent technology from other industries (for reactant supply) and an automated method of extraction of the viral RNA with the help of GIGA, FARAH, and University Hospital. We have provided the nanobeads that were the most critical materials, but we also provided the inactivation material (Guanidine isothiocyanate). This allowed the university to perform on April 2020 more than 3000 tests per day. At the beginning of the new academic year in September 2020, the GIGA developed a salivary test using our reagent to both deactivated the virus and extract the viral RNA. This monitoring allows us to prevent any cluster in the University and in total, more than 400,000 tests have been performed during 18 months until June 2022.

The crisis reactant doesn't only affect us but the whole Belgium and other countries. As so, we have provided multiple other countries such as Sweden, Canada, Luxembourg, Romania, and Senegal. The new strategy of the federal government was to create a federal platform of testing. For this platform, we have provided more than 8,000,000 tests reagents for the second, third, and fourth wave of Covid cases until January 2022 with the help of a local company Diagenode that provides the quality assurance of our products.

2.2. What about batteries?

Fe_3O_4 is known to be used as anode material for alkali-ions batteries [8,9]. This material suffers from volume expansion as all conversion active electrode materials, Among the solutions to reduce the destructive effect of the volume expansion and thus enhancing the electrochemical performance is the realization of a coating [10,11]. This material has been used in Li-ion batteries and the result is presented in Figure A -I-4. All materials present a quick decrease in capacity during the first cycle. The capacity of Fe_3O_4 materials without coating decay

rapidly after 40 cycles. For the core-shell materials, different Fe:Si ratio were tried 1:1, 1:0.5, and 1:0.1. As can be seen, material with 10% of Si shows the best performance, and the capacity obtained is increasing along the cycle reaching 450 mAh/g after 500 cycles. This is not the main purpose of this material, but enhancement can be done to stabilize this material. Also, it should be interesting to test it in K-ion batteries.

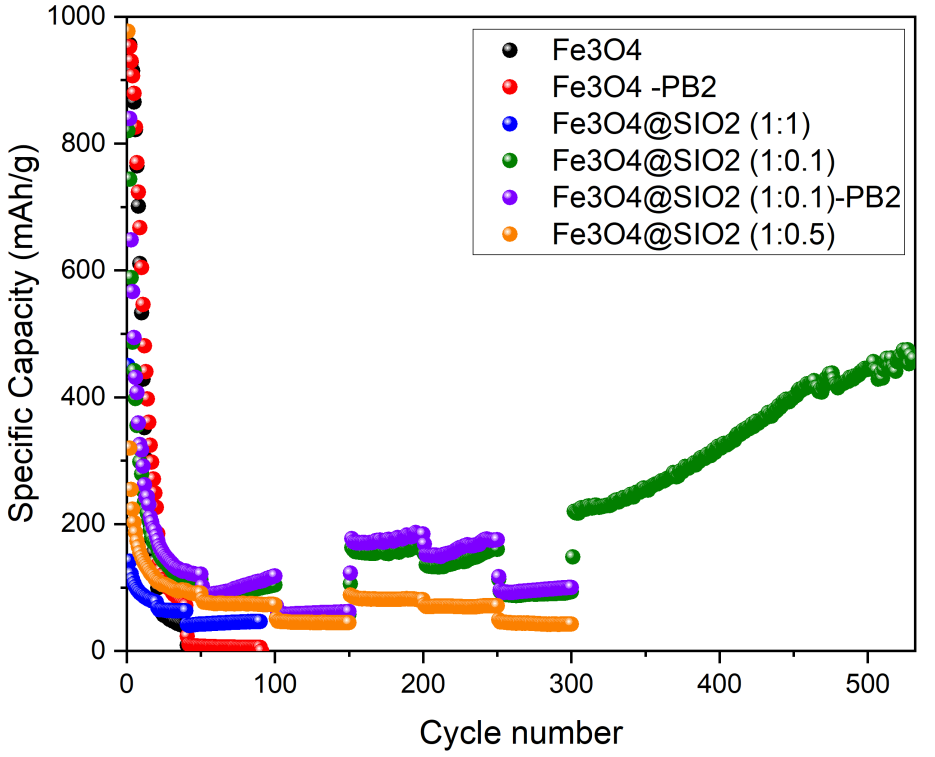

Figure A -I-4: Evolution of discharge capacity of Fe_3O_4@SiO_2 materials with cycle number in Li-ion half-cell using LP30 electrolyte.

3. Conclusions

To conclude this brief chapter about the implication of the GREEnMat in the Covid-19 crisis, we have shown of our reactivity and contribution against a health crisis and this is also the role of a chemist. Within only one month we have established, optimize, validate and provide a new technology to synthesize core-shell Fe_3O_4@SiO_2 particles for medical applications of viral-RNA detection. During one year and a half, we have produced more than 10,000,000 reagents of which more than 8,000,000 were used by the Belgian federal platforms for Covid-19 detection. In some ways, we have allowed the testing to pass from a few hundred per day at the beginning of the crisis to more than 150,000 at the peaks of January 2022. Systematic testing has always been evidenced as the main strategy to control of the Covid-19 crisis. Nowadays, antigenic testing is widely spread, and the PCR test is not the only testing strategy. Nevertheless, our nanobeads reagents are not exclusive to Covid-19 and can be used for the extraction of any type of DNA or RNA, or other applications such as pollutant removal or battery.

4. References

[1] S.H. Safiabadi Tali, J.J. LeBlanc, Z. Sadiq, O.D. Oyewunmi, C. Camargo, B. Nikpour, N. Armanfard, S.M. Sagan, S. Jahanshahi-Anbuhi, Tools and techniques for severe acute respiratory syndrome coronavirus 2 (SARS-CoV-2)/COVID-19 detection, Clinical Microbiology Reviews. 34 (2021). https://doi.org/10.1128/CMR.00228-20.

[2] A. Ribeiro-Silva, H. Zhang, S.S. Jeffrey, RNA extraction from ten year old formalin-fixed paraffin-embedded breast cancer samples: A comparison of column purification and magnetic bead-based technologies, BMC Molecular Biology. 8 (2007) 1–10. https://doi.org/10.1186/1471-2199-8-118.

[3] C.J. Liu, K.Y. Lien, C.Y. Weng, J.W. Shin, T.Y. Chang, G. bin Lee, Magnetic-bead-based microfluidic system for ribonucleic acid extraction and reverse transcription processes, Biomedical Microdevices. 11 (2009) 339–350. https://doi.org/10.1007/s10544-008-9240-1.

[4] N.M. Adams, H. Bordelon, K.K.A. Wang, L.E. Albert, D.W. Wright, F.R. Haselton, Comparison of three magnetic bead surface functionalities for RNA extraction and detection, ACS Applied Materials and Interfaces. 7 (2015) 6062–6069. https://doi.org/10.1021/am506374t.

[5] Z. Sharafi, B. Bakhshi, J. Javidi, S. Adrangi, Synthesis of silica-coated iron oxide nanoparticles: Preventing aggregation without using additives or seed pretreatment, Iranian Journal of Pharmaceutical Research. 17 (2018) 386–395.

[6] Z. Lu, J. Dai, X. Song, G. Wang, W. Yang, Facile synthesis of Fe3O4/SiO2 composite nanoparticles from primary silica particles, Colloids and Surfaces A: Physicochemical and Engineering Aspects. 317 (2008) 450–456. https://doi.org/10.1016/j.colsurfa.2007.11.020.

[7] H. Uematsu, K. Daimon, S. Yoshiga, Nucleic acid-bondable magnetic carrier and method for isolating nucleic acid using the same, EP0757106A2, 1997.

[8] Z. Zeng, H. Zhao, J. Wang, P. Lv, T. Zhang, Q. Xia, Nanostructured Fe3O4@C as anode material for lithium-ion batteries, Journal of Power Sources. 248 (2014) 15–21. https://doi.org/10.1016/j.jpowsour.2013.09.063.

[9] W.M. Zhang, X.L. Wu, J.S. Hu, Y.G. Guo, L.J. Wan, Carbon coated Fe3O4 nanospindles as a superior anode material for lithium-ion batteries, Advanced Functional Materials. 18 (2008) 3941–3946. https://doi.org/10.1002/adfm.200801386.

[10] Z. Hu, H. Cui, J. Li, G. Lei, Z. Li, Constructing three-dimensional Li-transport channels within the Fe3O4@SiO2@RGO composite to improve

its electrochemical performance in Li-ion batteries, Ceramics International. 46 (2020) 18868–18877. https://doi.org/10.1016/j.ceramint.2020.04.207.

[11] J. Zhang, L. Huang, J. Zheng, J. Xu, A.M. Asiri, H.M. Marwani, M. Zhang, SiO2-assisted synthesis of Fe3O4@SiO2@C-Ni nanochains for effective catalysis and protein adsorption, Journal of Magnetism and Magnetic Materials. 497 (2020). https://doi.org/10.1016/j.jmmm.2019.166011.

Appendix B

Characterization techniques

1. Mössbauer spectroscopy

1.1. Principle

Mössbauer spectroscopy is a technique based on a nucleus's recoil-free emission and absorption of γ-rays. It makes it possible to obtain information on the local environment of the atom (degrees of oxidation, magnetic state, nature of the ligands, etc.). γ rays are emitted by metastable nuclei (source), which pass from an excited state to a ground state. They can only be absorbed by nuclei of the same isotope in an energetically lower state. Thus, only part of the elements of the periodic table can be analyzed by this technique (the most studied elements are iron and tin). Mössbauer spectroscopy depends on the lattice's vibrational state since only a fraction of the nuclei will likely undergo a nuclear transition without recoil effect. This fraction is called the Lamb Mössbauer factor (f). It is, therefore, possible to play on factor f by decreasing the temperature to freeze the network.

Mössbauer spectroscopy consists of exposing a solid sample to a beam of γ rays and detecting the intensity transmitted through the sample. The source, which emits radiation of constant energy, is placed on an oscillating support to modulate its energy (Doppler effect). The Mössbauer spectrum represents the energy transmitted as a function of the speed of the source (figure B-1).

The spectrum is characterized by four hyperfine parameters, which make it possible to obtain information on the structure of the material:

The isomeric shift δ.

The quadrupole splitting Δ.

The width at half height Γ.

The magnetic interaction H (only for the magnetic component).

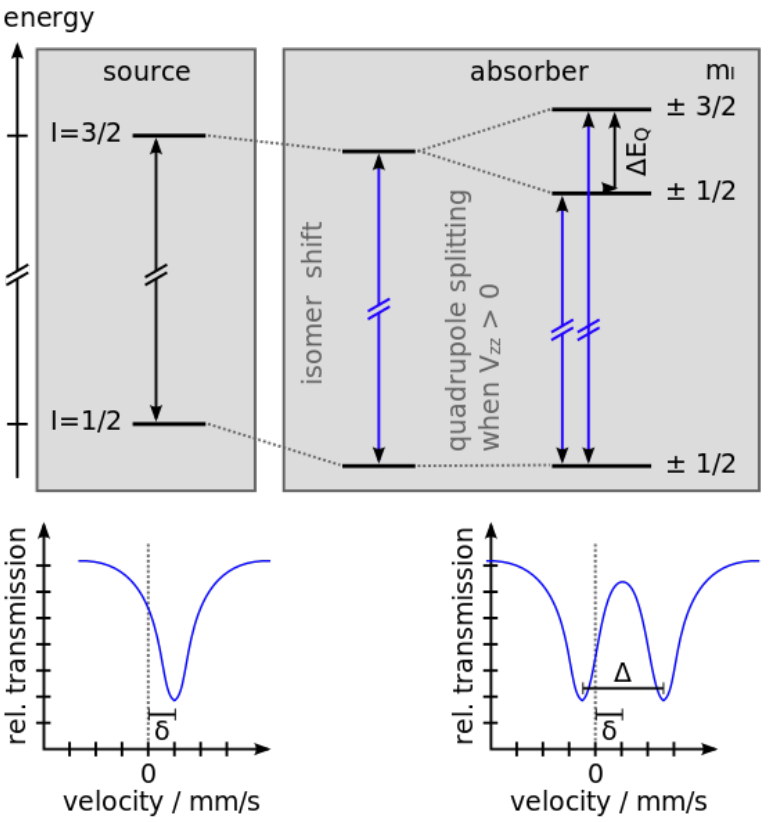

Figure B-1:Example of Mössbauer spectrum and associated hyperfine parameters. [1]

1.2. Spectrometer

A schematic of a typical spectrometer is shown in Figure B-2. It is composed of a source mounted on a Doppler vibrator which emits a radiation beam γ, a sample, and a detector.

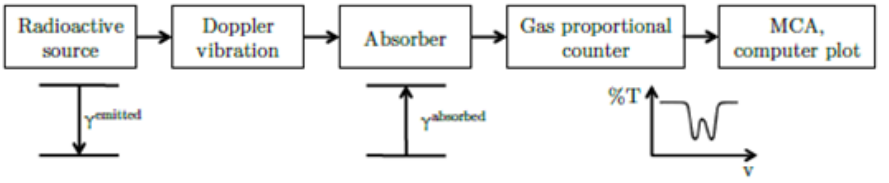

Figure B-2: Scheme of a Mössbauer spectrometer.[2]

^{57}Co (source diffused in a rhodium matrix) decays by electron capture to an excited state of ^{57}Fe, part of which transits from the excited state with spin 3/2 at an energy of 14.4 keV above the ground state. This 14.4 keV transition gives rise to the emission of a γ Mössbauer photon, which is absorbed by the ^{57}Fe nuclei in the sample.

As the ^{57}Fe nuclei presents in the source and the absorber are in different electrical and magnetic environments, the energy of the emitted radiation differs from that required for absorption. It is, therefore, necessary to vary the emission wavelength. The energy variation is obtained by moving the source at a relative speed v with respect to the absorber (Doppler effect). Most spectrometers operate in constant acceleration mode: the speed varies linearly with time between $-v_{max}$ and $+v_{max}$ and reverse. The energies are, for Mössbauer spectroscopy, expressed in units of velocity. A detector finally counts the radiation γ transmitted through the absorber. The latter records the spectrum (intensity transmitted by the sample as a function of the wavelength emitted by the source).

The spectrometer used in this thesis is a constant acceleration spectrometer. Samples are prepared with ~40 mg/cm^2 of powder mixed with boron nitride. The acquisition time is generally 24 hours. The spectrometer was calibrated at room temperature with the magnetically split sextet spectrum of a high-purity α-Fe foil as the reference absorber.. Fitting the experimental data, the spectral parameters such as isomer shift (δ), quadrupole splitting (Δ), linewidth (Γ), magnetic field (B_{hf}) and relative resonance areas of the different spectral components were

determined. The validity of fits was judged on the basis of minimizing the number of parameters and χ^2 values (χ^2 =~1).

2. X-ray diffraction technique

The principle is to expose a sample with X-rays and measure the diffracted intensity as a function of orientation in space. When X-rays irradiate a crystalline sample, constructive interferences are observed in specific orientations. Bragg's law dictates this phenomenon:

$$n\lambda = 2d\sin\theta$$

Where n is an integer called the "diffraction order", λ is the wavelength of the X-rays, d is the distance between the planes, and θ is half the angle of deviation. The diffractometer used is a D8 Discover Twin-twin from BrükerTM. The X-ray source is the Kα line of copper with a wavelength of 1.54Å. This diffractometer is of the Bragg-Brentano type. The sample, a cup filled with perfectly flat powder or a wafer, is horizontal. The tube and the X-ray detector move symmetrically. The sample can also rotate on itself to increase the sampling area. The Bragg-Brentano assembly is shown in Figure B-3. Using this assembly, it is possible to scan the angles **θ** with the source and the detector and to measure the intensity of diffraction at certain angular positions characteristic of the sample analyzed.

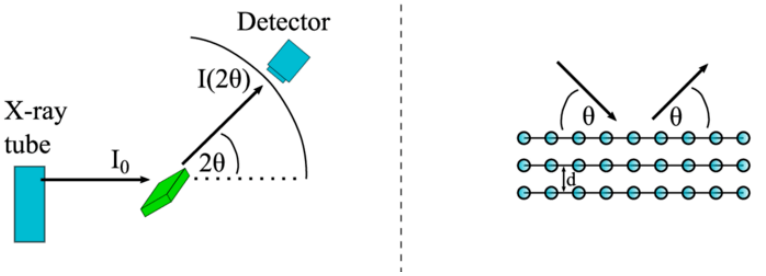

Figure B-3: Left: Scheme of the Bragg Brentano geometry for XRD analysis. Right: Visualization of the Bragg equation

3. Scanning electron microscopy

This apparatus allows the direct observation of the samples and, therefore, the determination of the synthesized powders' morphology, particle size, composition and thickness. This microscope operates based on the emission of electrons and the detection of signals due to the interaction of these electrons with the sample. The microscope has three detectors: a secondary electron detector, a backscattered electron detector, and an X-ray detector. A schematic representation of a scanning microscope is shown in Figure B-4.

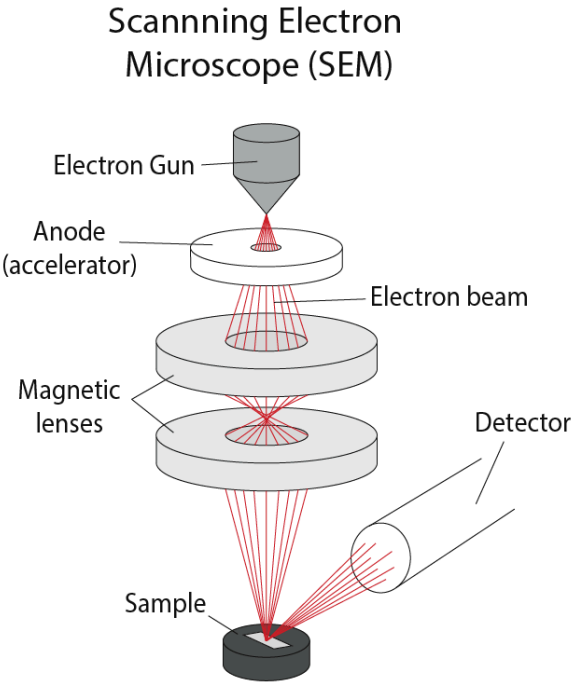

Figure B-4: Schematic representation of a scanning electron microscope. [3]

Secondary electrons are generated when an electron passes near an atom. The latter transmits part of its energy to an electron in the conduction band, which implies an ejection of this electron from the atom. These electrons cannot have a

kinetic energy greater than 50eV. Because of this low energy, only electrons close to the surface will be detected. This provides information on the sample's topography since topographic variations imply a change in the number of secondary electrons detected.

The backscattered electrons are due to the collision between an electron of the incident beam and an atom. The incident electrons have much higher energy and can penetrate deeper into the sample. The backscattered electrons have no topographic information. The information provided by these electrons is composition information. The number of backscattered electrons is directly proportional to the atomic number of the atoms in the sample.

A phenomenon of relaxation creates X-rays. Indeed, when a beam of electrons bombards an atom, an internal electron of the atom can be ejected. To reduce its energy, the atom will fill this loss with a more external electron, which generates an X-ray. These have a wavelength specific to the element that emitted them, providing information on the sample's composition.

Due to the use of electrons, the analyzed film or powder must be conductive. The sample is therefore metalized with gold. The microscope is a Phillips ESEM-FEG XL30.

4. Electrochemical characterization

4.1. Cell assembly protocol

Electrochemical measurements were performed on the electrodes in Swagelok or coin cell (2032 type) configurations (Figure B-5). Both settings were used to assemble the Na- and K-ion batteries.

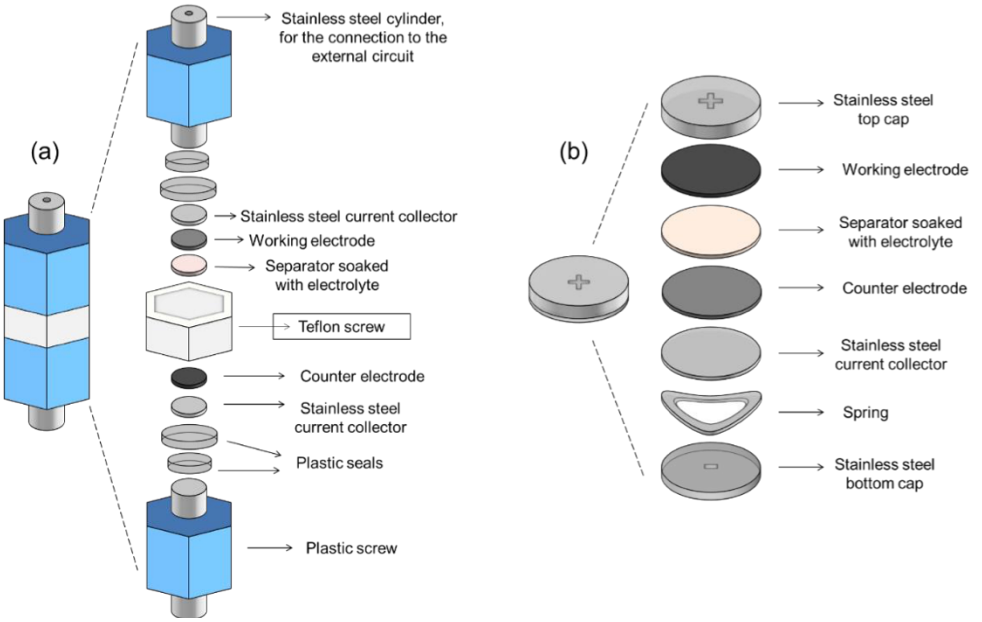

Figure B-5: Schematic representation of (a) Swagelok battery and (b) Coin-cell battery. [4]

4.2. Electrochemical measurement

4.2.1. Chronopotentiometry

This technique is also called galvanic cycling, galvanostatic cycling, or even charge/discharge technique. It consists in applying a constant current to the terminals of the accumulator and monitoring the evolution of the potential as a

function of time. Depending on the sign of the applied current, a phenomenon of deintercalation of A+ ions (charge) or intercalation of A+ ions (discharge) will occur for a positive and negative current, respectively. The direction of the current is reversed when the potential reaches a value set by the user. Chronopotentiometry is regularly used in electrochemical tests because it makes it possible to approach conditions close to reality. The battery completes a cycle when it undergoes a charge and a discharge. The performance of the accumulator is deduced from the analysis of the potential curves as a function of time for a fixed value of current. The properties that can be extracted are essentially the specific capacity and the cycle life, i.e., the resistance of the accumulator to a high number of charge/discharge cycles.

Two kinds of tests can be carried out. The first is a rate capacity test, which applies the accumulator to increasingly intense currents to analyze the capacity that can be extracted at different speeds. To be more precise, it is necessary to explain the cycling speed: depending on the intensity of the current applied, the time required for a complete (dis)charge will be different. Therefore, the higher the current, the higher the speed will be. The current intensity to be applied also depends on the quantity of active material in the accumulator. The intensity of the current can be calculated as follows:

$$\mathrm{I(A)} = \mathrm{C}_{\mathrm{Specific}}^{\mathrm{Theoretical}} \left(\frac{\mathrm{Ah}}{\mathrm{g}}\right) . \mathrm{m}_{\mathrm{active}}(\mathrm{g}) . \mathrm{v}(\frac{\mathrm{cycles}}{\mathrm{h}})$$

Where v represents the desired cycling speed. We will speak of rate C/10 when it takes 10 hours to perform a complete (dis)charge. This thesis performed throughput capacity tests at speeds between C/40 and 1C.

The second type of test is used to assess cycling resistance. It consists of carrying out a high number of cycles at a constant current and monitoring the evolution of the experimental specific capacity as a function of the number of cycles. The specific capacity is calculated using the following formula:

$$C_{Specific}^{Theoretical}\left(\frac{Ah}{g}\right) = \frac{I(A).t(h)}{m_{active}(g)}$$

The time, in hours, corresponds to the time required to perform a full (dis)charge (set by the user-defined potential limit values) according to the applied current. The cycling life is considered good if the capacity does not fade along the cycle's number.

4.2.2. Cyclic voltammetry

Potential with a linear variation is applied in a predetermined voltage window during a cyclic voltammetry experiment, and the resulting current is monitored. Redox peaks can be seen by plotting the current vs. the potential. Positive current (increasing potential) causes oxidation phenomena, whereas negative current causes reduction phenomena (decreasing potential).

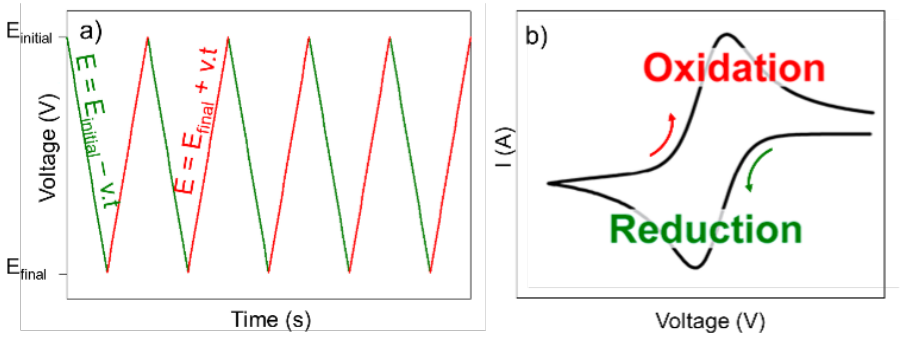

Figure B-6: (a) Evolution of the potential with the time (5 cycles). v is the scanning rate in mV/s, and t is the time in s. (b) Voltammogram: evolution of the measured current as a function of the applied potential.[5]

4.2.3. Electrochemical impedance spectroscopy

In a typical electrochemical cell, in addition to the resistance of the electrolyte, interactions between matter (redox species) and the electrode also involve the concentration of electroactive species, charge transfer, and mass transfer from the bulk solution to the electrode surface.

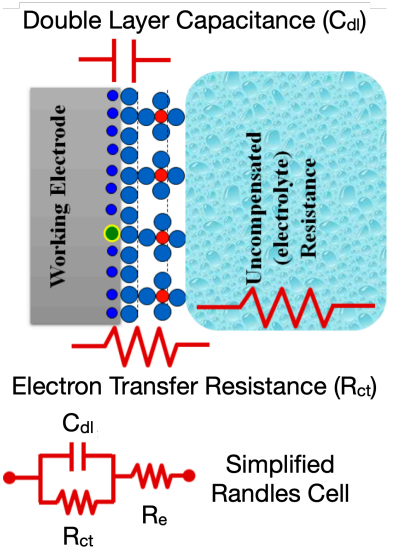

Figure B-7: Simplified scheme describing an EIS circuit and the redox reaction at the surface of working electrodes in a conventional-electrochemical cell (i.e., three-electrode system). [6]

As illustrated in Figure B-7, each of these characteristics is represented by an electrical circuit consisting of resistances, capacitors, or constant phase elements coupled in parallel or series to create an equivalent circuit. Therefore, processes including mass transfer, charge transfer, and diffusion could be studied using the EIS. As a result, the EIS can research intrinsic material characteristics or particular processes that may affect an electrochemical system's conductance, resistance, or capacitance. The difference between impedance and resistance is that the

resistance in DC circuits directly follows Ohm's Law. The impedance response is measured using a modest signal stimulation. The current response to a sinusoidal potential is a sinusoid at the applied frequency, whereas the electrochemical cell response is pseudo-linear in that a phase shift is acquired. Thus, the excitation signal is presented as a function of time :

$$E_t = E_0 . \sin(\omega t)$$

where E_t is the potential at time t, E_0 is the signal's amplitude, and ω is the radial frequency.

The following equation links the radial frequency ω and the applied frequency (f):

$$\omega = 2\,\pi\,f$$

In a linear system, there is a shift of the signal in phase (Φ) with a different amplitude than I_0 that can be expressed as :

$$I_t = I_0 . \sin(\omega t + \Phi)$$

The whole system impedance is then expressed as :

$$Z = \frac{E}{I} = Z_0 . \exp(i\Phi) = Z_0 . (\cos\Phi + i \sin(\Phi))$$

Where Z is the impedance, E is the potential, I is the current, ω is the frequency, and Φ is the phase shift between E and I.

Impedance is measured by applying a potential wave to the working electrode and observing the current wave that results. Z, Φ, Z_{real}, and Z_{imag} are extracted from these two waves and sketched. These parameters are measured for potential waves of various frequencies to produce the spectrum. An EIS experiment is carried out in a three-electrode system by setting the applied voltage perturbation. The generated Warburg impedance (W), charge transfer resistance (Rct), and solution resistance (Rs) are gathered and shown in the Nyquist plots (figure B-8).

To extract the targeted value, the electrochemical process associated with the electrolyte, redox reaction, interface, are simulated using an equivalent electric circuit using the resistance of the electrolyte (Rs), double layer capacitance at the

surface of the electrode (C_{dl}), charge transfer resistance (R_{ct}), and Warburg resistance (Z_w), this last is the result of a diffusion process occurring at the electrode-electrolyte interface. As the experiment is never a perfect capacitor, a constant phase element is generally added to solve the non-ideal capacitance of the real system.

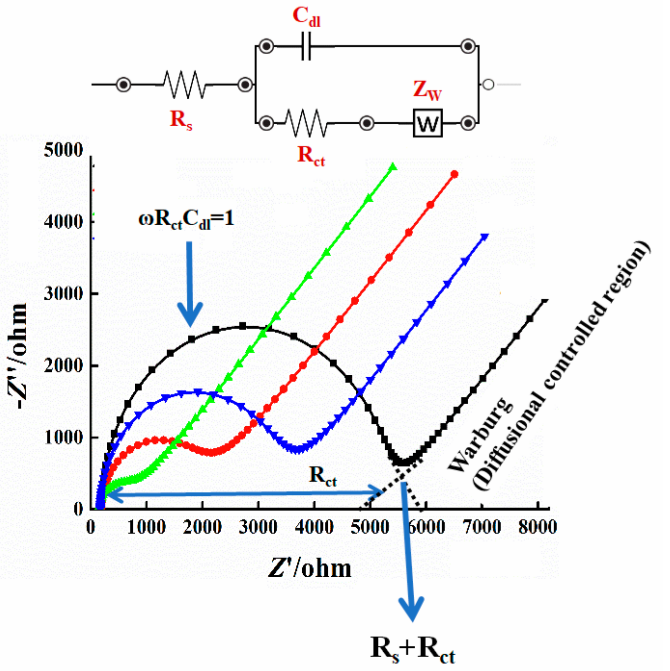

Figure B-8: Experimental and simulated impedance spectra of a simplified Randles equivalent circuit for an electrochemical system. [6]

5. References

[1] Joël Gubler, Isomer Shift and Quadrupole Splitting with iron 57. Energy levels and schematic spectra. Naming of quantities according to IUPAC recommendations., Pure & Appl. Chem. 45 (1976) 211—216. https://en.wikipedia.org/wiki/Mössbauer_spectroscopy#/media/File:Mossbauer_Isomer_Shift_and_Quadrupole_Splitting_for_57Fe.svg.

[2] Long G.J., Mössbauer Spectroscopy Applied to Inorganic Chemistry, 1987.

[3] University of Cambridge, The Scanning Electron Microscope, (n.d.). https://www.eng-atoms.msm.cam.ac.uk/RoyalSocDemos/SEM (accessed October 2, 2022).

[4] C. Piffet, Spray-drying synthesis of Ti-based materials for Li / Na-ion batteries : development of Li 4 Ti 5 O 12 flexible electrodes and in-situ characterizations of Na 2 Ti 3 O 7, University of Liege, 2021.

[5] N. Elgrishi, K.J. Rountree, B.D. McCarthy, E.S. Rountree, T.T. Eisenhart, J.L. Dempsey, A Practical Beginner's Guide to Cyclic Voltammetry, J Chem Educ. 95 (2018) 197–206. https://doi.org/10.1021/acs.jchemed.7b00361.

[6] H.S. Magar, R.Y.A. Hassan, A. Mulchandani, Electrochemical impedance spectroscopy (Eis): Principles, construction, and biosensing applications, Sensors. 21 (2021). https://doi.org/10.3390/s21196578.